REMOTELY CONTROLLED DRUG DELIVERY SYSTEMS

by

Amir Zaher

A THESIS SUBMITTED IN PARTIAL FULFILLMENT OF
THE REQUIREMENTS FOR THE DEGREE OF

DOCTOR OF PHILOSOPHY

in

THE COLLEGE OF GRADUATE STUDIES

(Engineering)

THE UNIVERSITY OF BRITISH COLUMBIA

(Okanagan)

March 2016

The undersigned certify that they have read, and recommend to the College of Graduate Studies for acceptance, a thesis entitled:

Remotely Controlled Drug Delivery Systems

Submitted by Amir Zaher in partial fulfillment of the requirements of

The degree of Doctor of Philosophy .

Dr. Ian Foulds, School of Engineering
Supervisor, Professor (please print name and faculty/school above the line)

Dr. Jürgen Kosel, King Abdullah University of Science and Technology
Supervisory Committee Member, Professor (please print name and faculty/school in the line above)

Dr. Keekyoung Kim, School of Engineering
Supervisory Committee Member, Professor (please print name and faculty/school in the line above)

Dr. Rudolf Seethaler, School of Engineering
University Examiner, Professor (please print name and faculty/school in the line above)

Dr. Bethanie Stadler, University of Minnesota
External Examiner, Professor (please print name and university in the line above)

April 1, 2016
(Date submitted to Grad Studies)

Abstract

Implantable drug delivery is becoming an increasingly important field of research, providing great potential for a wide range of flexible and low cost solutions for localized treatment of chronically debilitating diseases. This dissertation presents work that encompasses several approaches for the remote triggering, powering, and control of micro drug delivery devices and systems, designed with remote-controllability, minimal power requirements, biocompatibility, and the potential for minimally invasive implantation in mind. The control mechanisms used rely on microtechnology, nanotechnology, and electromagnetic power transfer to magnetic nanoparticles and magnetic nanowires, for the heating and actuation of thermoresponsive Poly(N-isopropylacrylamide) hydrogels (PNIPAm) in the form of nanoparticles in membranes and stand-alone microdroplets, and actuation of flexible membranes for drug pumping.

Thermoresponsive PNIPAm, in any form such as nanoparticles, microdroplets, or mezzo scale bulk material shapes, has the property of swelling with water in its hydrophilic state below a critical temperature. At higher temperatures, a sharp change occurs, the polymer network becomes hydrophilic, and the water molecules in the network is expelled, causing the overall material to shrink in size, while the released water or aqueous solution is left free to flow around or away from the material.

When embedded in membrane matrices used as drug delivery gates, PNIPAm nanoparticles act as diffusion and flow blockers below the critical temperature. When PNIPAm surpasses the critical temperature, induced by heat from local magnetic iron oxide nanoparticles (exposed to a 62 mT, 450 kHz magnetic field), it shrinks in size and increases the drug flow through membrane pathways. The combination of this membrane design with osmotic pumping and methods for tailoring the drug release profile is reported. Simulation supports experimental results while describing interactions between the osmotic pump and the thermoresponsive membranes. A sensitivity analysis based on a fluidic circuit analogy gives insight into the contributions of the components of the device, in particular those of membranes affecting the displacement of fluid.

PNIPAm microdroplets, spherical microparticles larger than the PNIPAm nanoparticles discussed above, are fabricated with embedded magnetic iron oxide

nanoparticles or magnetic iron nanowires and pre-loaded with an aqueous drug. Upon magnetic heating, these microdroplets shrink in size and expel the drug. Magnetic nanowires have much lower power requirements when compared with widely-used iron oxide magnetic nanoparticles for triggering PNIPAm, due to their ability to generate losses via physical vibration within the microdroplets. A model is used to corroborate the experimentally observed low power (1 mT, 20 kHz magnetic field) required to induce PNIPAm microdroplet shrinkage. This model for nanowire loaded microdroplet design is compared with the well-established theory for power generation from magnetic iron oxide nanoparticles, and associated experiments (using a 72 mT, 600 kHz magnetic field) in order to confirm the validity of the calculated power generated by iron nanowires.

The findings in this work offer several flexible options for the application of PNIPAm as a remotely triggerable drug delivery controller or carrier, using relatively simple fabrication methods, permitting several degrees of customization of the delivery rate or profile by adjusting the PNIPAm material, its magnetic content, and the applied magnetic field, all the while demonstrating the use of magnetic nanowires as a more efficient power transfer material when compared to traditionally used magnetic nanoparticles. The findings associated with the efficient triggering of PNIPAm microdroplets can be implemented in a more power-friendly design of magnetic, remotely triggered membranes which, although implemented in conjunction with osmotic pumps here, can be coupled with other pressure sources.

Preface

The content of chapter 2 has been published:

Zaher, A., Li, S., Wolf, K. T., Pirmoradi, F. N., Yassine, O., Lin, L., Khashab, N.M., & Kosel, J, "Osmotically driven drug delivery through remote-controlled magnetic nanocomposite membranes." *Biomicrofluidics*, 2015. **9**(5): 054113.

I conducted the manuscript writing, most of the experimental work, and most of the data analysis and part of the simulation analysis.

The content of chapter 3 has been submitted:

Yassine, O., Zaher, A., Li, E.Q., Alfadhel, A., Perez, J.E., Kavaldzhiev, M., Contreras, M.F., Thoroddsen, S.T., Khashab, N.M., & Kosel, J., "Highly Efficient Thermoresponsive Nanocomposite for Controlled Release Applications," under review, *Nature Scientific Reports*, 2016.

I conducted part of the manuscript writing, part of the experimental work, most of the theoretical work, and all of the theoretical work related to nanowires.

The content of Appendix B will be submitted and has been presented:

Contreras, M.F., Zaher, A., Perez, J.E., Alfadhel, A., de Oliveira, L.A.S., Pirota, K.R., Ravasi, T., Kosel, J., "Magnetic Nanowires and Hyperthermia: the Influence of Geometry on and Material on Heat Production Efficiency," (in preparation).

Contreras, M.F., Zaher, A., Pérez, J.E., Alfadhel, A., de Oliveira, L.A.S., Pirota, K.R., Ravasi, T., Kosel, J. "Specific Absorption Rate Magnetic Nanowires: How Geometry and Material Affect Heat Production Efficiency", ASME 2015 4th Global Congress on Nano Engineering for Medicine and Biology.

Contreras, M.F., Zaher, A., Perez, J.E., Ravasi, T., Kosel, J., "Magnetic Nanowires and Hyperthermia: How Geometry and Material Affect Heat Production Efficiency," *Magnetics Conference* (INTERMAG), 2015 IEEE, 1-1

I conducted part of the writing, part of the experimental work, and part of the theoretical work.

The content of Appendix E has been published and presented:

Yi, Y., Zaher, A., Yassine, O., Kosel, J., & Foulds, I. G., "A remotely operated drug delivery system with an electrolytic pump and a thermo-responsive valve." *Biomicrofluidics*, 2015. 9(5): 052608.

Yi, Y., Zaher, A., Yassine, O., Buttner, U., Kosel, J., & Foulds, I.G., "Electromagnetically powered electrolytic pump and thermo-responsive valve for drug delivery," in *Nano/Micro Engineered and Molecular Systems (NEMS), 2015 IEEE 10th International Conference on* , vol., no., pp.5-8, 7-11 April 2015

I conducted part of the manuscript writing, part of the experimental work, and part of the theoretical work.

Underlined authors contributed equally to the work.

Table of Contents

Abstract ..... **ii**

Preface ..... **iv**

Table of Contents ..... **vi**

List of Tables ..... **x**

List of Figures ..... **xii**

List of Abbreviations ..... **xxiii**

Glossary ..... **xxiv**

Acknowledgements ..... **xxix**

Dedication ..... **xxx**

Chapter 1 Introduction **1**

1.1 Dissertation Objectives 1

1.2 Introduction to Drug Delivery Systems 1

1.2.1 Osmotic Pumps for Drug Delivery 4

1.3 Stimuli-Responsive Drug Delivery 9

1.3.1 Poly(N-isopropylacrylamide) Hydrogels and Drug Delivery 9

1.3.2 Thermoresponsive Membranes 11

1.3.3 Thermoresponsive Microdroplets 13

1.3.4 Thermoresponsive Microvalves 14

1.4 Magnetically-Induced Heating for Drug Delivery Applications 16

1.4.1 Introduction to Magnetism 16

1.4.2 Magnetic Induction and Ferromagnetic Materials 21

1.4.3 Magnetic properties of single domain nanoparticles and nanowires 22

1.4.3.1 Magnetization switching and the Stoner-Wohlfarth model 24

1.4.4 Superparamagnetic Nanoparticles for Heat Generation 27

1.4.4.1 Preparation of Superparamagnetic Nanoparticles 27

1.4.4.2 Introduction to Superparamagnetism 28

1.4.4.3 Magnetic Nanoparticles in Thermoresponsive Systems 32

1.4.5 Magnetic Nanowires for Remote-Controlled Heat and Motion 33

1.4.5.1 Nanowires in Therapeutic and Thermal Applications 33
1.4.5.2 Nanowires in Translation and Vibration 34
1.4.5.3 Modeling of Nanowire Vibration in Viscous Media 35
1.4.5.3.1 Derivation of Equation of Motion of Nanowires in PNIPAm 37
1.4.5.4 Nanowire Fabrication 39
1.5 Research Motivations and Objectives 43
1.6 Chapter Outline 48

Chapter 2 Magnetic Composite Membranes for Osmotic Drug Delivery 49

2.1 Synopsis 49
2.2 Methods 49
2.2.1 Device Design 49
2.2.2 Fabrication of the Osmotic Pump 52
2.2.3 Fabrication of Magnetic Nanocomposite Membranes 53
2.2.3.1 PNIPAm Hydrogels 53
2.2.3.2 Superparamagnetic Iron Oxide (SPIO) Nanoparticles 54
2.2.3.3 Magnetic Nanocomposite Membranes 55
2.2.3.4 Cyanoacrylate Layer Treatment 58
2.2.3.5 Mechanical and Surface Area Characterizations of Membrane Types 59
2.2.4 Modeling and Numerical Simulations 60
2.2.5 Sensitivity Analysis using Fluidic Circuit Analogy Model 62
2.3 Results and Discussion 71
2.3.1 Individual Membrane and Device Characterization 71
2.3.2 Controlled Release of Model Drug 79
2.3.3 Simulation-Based Device Characterization and Discussion 80
2.3.4 Device Discussion 83
2.4 Chapter Summary 86

Chapter 3 Magnetic Nanowires in PNIPAm Microdroplets for Drug Delivery 89

3.1 Synopsis 89
3.2 Methods 91
3.2.1 Chemical Components of Magnetic PNIPAm Microdroplets 91
3.2.1.1 Selection of Crosslinker Concentration 92
3.2.2 Fabrication of Magnetic PNIPAm Microdroplets 93
3.2.3 Fabrication of Magnetic Iron Nanowires 95

3.2.4 Characterization of Magnetic PNIPAm Microdroplets 98
3.2.4.1 Normalized Swelling-deswelling Ratio 98
3.2.4.2 Drug Loading 99
3.2.4.3 Drug Release 99
3.3 Results and Discussion 100
3.3.1 Thermoresponsive Behavior Magnetic PNIPAm Microdroplets 100
3.3.2 Magneto-Thermoresponsive Behavior Magnetic PNIPAm Microdroplets 101
3.3.3 Modeling of Nanowire Vibration in PNIPAm Microdroplet 104
3.3.4 Drug Release 107
3.3.4.1 Continuous Drug Release 107
3.3.4.2 Pulsatile Actuation Drug Release 108
3.4 Nanowire and Nanoparticle SAR Measurements 110
3.5 Chapter Summary 111

Chapter 4 Conclusion 113

4.1 Summary 113
4.2 Contributions 114
4.2.1 Journal Publications 114
4.2.2 Conferences 115
4.2.2.1 Conference Oral Presentations 115
4.2.2.2 Conference Paper and Poster Contributions 115
4.2.3 Patent 116
4.3 Recommendations and Future Directions 117
4.4 Final Word 118

Bibliography or References 119

Appendices 137

Appendix A Modeling and Numerical Simulation of Osmotically Driven Drug Delivery through Remote-Controlled Magnetic Nanocomposite Membranes 138
A.1 Modeling and Numerical Simulations 138
A.2 Derivation of Pressure Applied to PDMS Membrane by Osmotic Process 145
A.3 Determining Magnitude of Donor Chamber Pressure 148
A.4 Approximation of Ratio of Permeability Values of Magnetically Triggered Membrane (Magnetic Field ON/OFF) 151
A.5 Summary of Simulation Specific Settings 154

Appendix B Nanowire and Nanoparticle SAR Measurements 155
B.1 Specific Absorption Rate of Magnetic Materials 155
B.2 Methods 156
B.3 Results 158
B.4 Summary 162
Appendix C Nanowire Fabrication System 163
C.1 Details of Constructed Nanowire Fabrication System 163
Appendix D Modeling of Iron Nanowire Vibration in PNIPAM microdroplets 173
D.1 Matlab Script for Modeling the Vibration of Iron Nanowires 173
Appendix E Magnetic PNIPAm Microvalves for Electrolytic Drug Delivery 174
E.1 Synopsis 174
E.2 Methods 175
E.3 Results and Discussion 178
E.4 Summary 186

List of Tables

Table 1.1 Reservoir based and drug infusion pump based passive and active devices with highlighted features for comparison. 45
Table 1.2 Magnetic material-based micro and nano-sized particle drug carriers. 46
Table 1.3 Non-magnetic stimuli responsive particle drug carriers. 47
Table 2.1 Thicknesses measurements of different nanocomposite membranes after casting and curing. 57
Table 2.2 Mixture volumes for the two types of membranes before and after membrane drying: (ii) 1 g of 8 wt% Ethyl Cellulose in Ethanol, 40 mg of PNIPAm hydrogel, and 75 mg of SPIO nanoparticles, (ii) 1 g of 10 wt% Cellulose Acetate in Acetone, 40 mg of PNIPAm hydrogel, and 75 mg of SPIO nanoparticles. 58
Table 2.3 Mean flexural stress at breaking point for dry and wet cellulose acetate and ethyl cellulose based membranes. 59
Table 2.4 The Brunauer–Emmett–Teller (BET) specific surface area results for physical adsorption of gas molecules in untreated ethyl cellulose and untreated cellulose acetate membranes: 60
Table 2.5 Summary of calculated values using circuit model and experimental data. All resistances are in units of kg/[m s (m^3)]. 67
Table 2.6 Symbolic expression for the sensitivity of I_{out} to each circuit element. 68
Table 2.7 Summary of conditions, durations, and associated labels for EC, CA, and treated EC membrane device stages. 74
Table 2.8 Simulation-derived values of porosity and permeability for the cyanoacrylate treated ethyl cellulose-PNIPAm-SPIO composite membrane, RhB transport rate of simulated and experimental data. 82
Table 3.1 List of constituents of the solution phases used in the microfluidic droplet generation process. 92
Table 3.2 Efficiencies of NW and SPIO microdroplets with respect to max shrinkage time and local field power. 104
Table S1 Magnetic nanowires and nanoparticles used in the experiments. 158

Table S2 Relevant magnetic quantities of the studied samples Abbreviations: M_R, remanence magnetization; M_S saturation magnetization; $H_{C\parallel}$, in-plane coercive field; $H_{C\perp}$, out-of-plane coercive field. * Observed trend for NWs was not observed for the iron oxide nanoparticles. $^{+}H_{SW}$ is the coercive field of single nanowires as reported elsewhere [164]. 160
Table S3 SAR values of the samples tested, along with temperature and concentration information. 161

List of Figures

Figure 1.1 Schematic of a typical Medtronic intrathecal drug delivery pump system, 25 mm thick and 76 mm wide. The device is typically implanted subcutaneously in the anterior abdominal wall. Reprinted by permission from The Journal of Bone and Joint Surgery, copyright 2012 [12]. 2

Figure 1.2 Example profiles of a constant drug delivery profile and a completely arbitrarily controlled ideal profile. 3

Figure 1.3 Schematics of (a) fundamental operation of an elementary osmotic pump and (b) a state of the art osmotic pump design developed by Theeuwes et al., (c) simplified diagram of a basic osmotic pump design with either a movable or flexible partition. 5

Figure 1.4 Duros osmotic pump design. Osmotic pressure drives the piston against a drug formulation, which in turn is ejected out of the orifice. Reprinted by permission from DURECT Corporation [http://www.durect.com/wt/durect/page_name/duros]. 7

Figure 1.5 Schematic of PNIPAm thermoresponsive behavior, transitioning from hydrophilic to hydrophobic and expelling aqueous content from the PNIPAm network chain shown. 10

Figure 1.6 Schematic of the triggering a PNIPAm hydrogel membrane. Magnetically heating superparamagnetic iron oxide (SPIO) nanoparticles within the membrane matrix cause the thermoresponsive PNIPAm hydrogel particles in the matrix to reduce in volume, widening diffusion pathways for the drug to flow through at an increased flux rate. 13

Figure 1.7 Illustration of the relationship between magnetic field strength H, magnetic flux density B, and a material's internal magnetization M when placed in free space and an externally applied magnetic field. 17

Figure 1.8 (Left) (a) H field and (b) B field of a permanent magnet, the vectors detail magnitude and direction of B, H_d, and M (cgs units) at the center of the material (where H_d is minimized). (Middle) Variation of H_d with respect to the length of the material. (Right) (c) Effect of placing (b) a magnetized bar

in (a) a uniform field. Figures reprinted with permission from John Wiley and Sons, 2008 [159]. 18
Figure 1.9 Example of a magnetization hysteresis loop depicting magnetic saturation, remanence, coercivity, and susceptibility. 19
Figure 1.10 Examples of hysteresis loops predicted by Stoner–Wohlfarth model for angles θ_0 between the applied field and magnetic material's easy axis. 26
Figure 1.11 (a) TEM image of iron oxide nanoparticles, (b) cluster of iron oxide nanoparticles in solution, (c) individual sub-domain iron oxide nanoparticle. Figure reprinted with permission, © 2009 IEEE [169]. 28
Figure 1.12 (a) Ferromagnetic material (FM) exhibit a single coercivity value and hysteretic behavior, if the FM size is reduced enough, to the point where thermal energy k_BT can randomize the magnetization orientation, resulting in a zero measured magnetization within a time interval that is typically 100 s, giving rise to superparamagnetic material (SPM), and paramagnetic material (PM) exhibits linear susceptibility that has an inverse dependence on temperature. These particles act as paramagnets with large moments and have no coercivity. (b) Randomization of the superparamagnetic particle's magnetization occurs with excitations that meet or exceed the energy barrier given by the product KV, or the magnetic anisotropy energy density times the volume of the particle. (c) Superparamagnetic nanoparticles are ferromagnetic while under a blocking temperature T_B, and superparamagnetic above this temperature. The value of T_B changes with change in volume V, as shown with V_1, V_2, and V_3. Figure reprinted with permission, © 2010 IEEE [171]. 30
Figure 1.13 Schematic of the angular position $\theta_l(t)$ of a nanowire during the first and second half of an applied alternating magnetic field. M points in the direction of magnetization of the nanowire. The subscripts i and f, and i2 and f2, refer to the initial and final angles of θ_l at the start and end of the first half and the second half of the cycle shown, respectively. 36
Figure 1.14 (a) Schematic of the anodization equipment used to create pores in aluminum which result in anodic aluminum oxide templates. The same setup is used for

growing dendrites underneath each pore (openings, smaller than pore diameter, serving as an electrical links between electrodeposition solution when placed in pores, and bottom un-oxidized aluminum potion of the aluminum disc), and for electrodeposition into pores, replacing the acid with the desired electrodeposition solution (no cooling). (b) Model of anodization setup with devices and custom built equipment, showing here a parallel anodization of two aluminum substrates. 40

Figure 1.15 Summary of nanowire fabrication process steps (a) through (f). Scanning electron microscopy images are those of samples imaged during fabrication of iron nanowires. 41

Figure 1.16 Illustration of dendrites grown at the bottom of each pore during the oxide barrier reduction process. The dendrites permit electrodeposition solutions in the pores to be in electrical contact with the aluminum portion at the bottom of the sample, which in turn is in electrical contact with the power supply. 42

Figure 2.1 Schematic diagram of the drug delivery system with magnetic composite membrane and osmotic pump. The structural material is made of laser-etched and chloroform bonded PMMA stacks. Reprinted with permission from [228]. Copyright 2015, AIP Publishing LLC. 50

Figure 2.2 PNIPAm hydrogel undergoing swelling (left) and shrinking (right) before and after an AC magnetic field is applied. SPIO particles react to the AC magnetic field to generate heat and the shrinkage of PNIPAm hydrogel. This shrinkage induces the large flux shown. Reprinted with permission from [228]. Copyright 2015, AIP Publishing LLC. 50

Figure 2.3 Test setup used to characterize the basic operations of the osmotic pump. The drug reservoir is filled using a sealable fill tube, and the initial height of dye in the glass capillary is recorded. After the activation of the osmotic pump, the height of the dye is recorded over time to calculate the pumped volume. Reprinted with permission from [228]. Copyright 2015, AIP Publishing LLC. 51

Figure 2.4 Summary of PNIPAm copolymerization method used to synthesize hydrogel. 54

Figure 2.5 Summary of high-temperature organic-phase decomposition method used to synthesize superparamagnetic iron oxide nanoparticles. 55
Figure 2.6 Scanning electron microscopy (SEM) images of the cross-sections of different nanocomposite membranes, (a) ethyl cellulose with PNIPAm, (b) ethyl cellulose with PNIPAm and SPIO, (c) cellulose acetate with PNIPAm, (d) cellulose acetate with PNIPAm and SPIO. (e) Vibrating sample magnetometer (VSM) measurement of iron oxide particles, shown near the magnetic field range of experiments. The graph is zoomed in to show enclosed area of loop, (M_s is at approximately 1500 mT). (f) Transmission electron microscopy image of synthesizes SPIO nanoparticles prior to membrane fabrication. (g) PNIPAM particles in water, 800 nm at 37°C and (h) 400 nm at 45°C (using direct heating). (i) Image of ethyl cellulose magnetic composite membrane (a)-(d) and (f)-(h) Reprinted with permission from [228]. Copyright 2015, AIP Publishing LLC. 56
Figure 2.7 Summary of the fabrication of ethyl cellulose and cellulose acetate magnetic membranes.....57
Figure 2.8 Circuit analogy of complete device with osmotic pump and magnetically triggered membrane.....63
Figure 2.9 Circuit analogy of (a) the isolated osmotic pump without a magnetically triggered membrane, (b) the osmotic driving mechanism without a flexible PDMS membrane at the outlet. 64
Figure 2.10 (a) Curve fit of volume displaced over time of osmotic pump under operation without a magnetic membrane. 65
Figure 2.11 Plot of S_{Rin} and $S_{Rcontrol}$ over time. $S_{Rcontrol}$ remains negative in this design for over ~40 days, and has an absolute value greater than or equal to 0.8 for around 8 days (~200 hr). 69
Figure 2.12 Total delivered mass curves over time, as predicted by the circuit analogy model for different magnetic field application conditions, along with experimentally recorded mass delivery for the cyanoacrylate treated EC

membrane device with osmotic pumping ON and modulation of magnetic field application (62 mT, 450 kHz). 70
Figure 2.13 Zoom in view of stage B of total delivered mass curve, during which the magnetic field is modulated first 30 min ON then 30 min OFF, and repeated, showing total delivered mass curves over time, as predicted by the circuit analogy model, along with experimentally recorded mass delivery for the cyanoacrylate treated EC membrane device with osmotic pumping ON. 71
Figure 2.14 (a) Absorbance of PNIPAm hydrogels at different temperatures. Diffusion profiles of RhB through (b) ethyl cellulose with PNIPAm and SPIO and (c) cellulose acetate with PNIPAm and SPIO composite membranes at room temperature and at 45°C. (d) Diffusion profiles of RhB through ethyl cellulose with PNIPAm and SPIO composite membranes treated with 0.06 ml of cyanoacrylate, at room temperature and at 45°C. Reprinted with permission from [228]. Copyright 2015, AIP Publishing LLC. 72
Figure 2.15 The EC membrane (ethyl cellulose with PNIPAm and SPIO) testing results with average delivery rates of RhB sampled for each test stage (A-D). (A) Room temperature diffusion, (B) applied magnetic field (62 mT, 450 kHz, cycled on/off every 30 minutes) and no osmotic pumping, (C) applied magnetic field with osmotic pumping, (D) osmotic pumping with no applied magnetic field. Reprinted with permission from [228]. Copyright 2015, AIP Publishing LLC. 75
Figure 2.16 3 kW inductive heater solenoid, experimental setup, control panel, power and frequency settings. 76
Figure 2.17 The CA membrane (cellulose acetate with PNIPAm and SPIO) testing results with average delivery rates of RhB sampled for each test stage (A-D). (A) Room temperature diffusion, (B) applied magnetic field (62 mT, 450 kHz, cycled on/off every 30 minutes) and no osmotic pumping, (C) applied magnetic field with osmotic pumping, (D) osmotic pumping with no applied magnetic field. Reprinted with permission from [228]. Copyright 2015, AIP Publishing LLC. 76

Figure 2.18 The cyanoacrylate treated EC membrane (cyanoacrylate treated ethyl cellulose with PNIPAm and SPIO) testing results with average delivery rates of RhB sampled for each test stage (A-H). (A) Applied magnetic field without osmotic pumping, (B, D, F) applied magnetic field with osmotic pumping, (C, E, G) osmotic pumping without applied magnetic field, (H) without magnetic field and locking of osmotic pump in its deflected position. Red plot indicates simulation results, with point α indicating the simulated value for room temperature diffusion rate, whose mass value is too low to measure experimentally. Although H is lower than α, it is a measurable diffusion rate due to the larger amount of RhB present in the receptor chamber. (b) (c) Reprinted with permission from [228]. Copyright 2015, AIP Publishing LLC. 77

Figure 2.19 Vibrating sample magnetometer (M/M_s) measurements of 2 to 3 millimeter square pieces of (a) CA magnetic membrane (M_s = 5.40 memu) and (b) EC magnetic membrane (M_s = 4.26 memu). Small differences in M_s may be attributed to difference in sample size, a result of error during manual slicing, as well as local non-homogeneity of the iron oxide distribution within the initial membrane, whose effects are aggravated when sampling very small pieces.....84

Figure 3.1 Schematic of the fabrication and drug release actuation principles for remotely triggered magnetic PNIPAM microdroplets (MPMs) with embedded iron nanowires or iron oxide nanoparticles (nanowires illustrated here). The MPMs are synthesized in a glass capillary microfluidic system and are loaded with the test drug by diffusion in an aqueous solution after post-synthesis washing. The heat generated by the nanowires or nanoparticles upon application of an alternating magnetic field AMF triggers the PNIPAm hydrogel structure, causing it to shrink and expel the aqueous drug content. Two AMFs are mainly used, one significantly lower than the other and resulting in comparable release rates.....91

Figure 3.2 Maximum percentage shrinkage of MPM volume during magnetic triggering with respect to PNIPAm hydrogel crosslinker concentration. 93

Figure 3.3 (a) Schematic the microfluidic system and synthesis process of MPMs. The inner and middle water phase and the outer oil phase flow rates are Q1 (20 µL/min), Q2 (20 µL/min) and Q3 (120 µL/min), respectively. (b) Image of the outlet of the first capillary as it generates a continuous laminar flow of the two streams Q1 and Q2. (c) Image of flow focus generation of the microdroplets. (d) Microscope image of several MPMs after fabrication. The MPM size distribution can be described by a PDI index, defined as PDI = (δ/d_{av} x 100) %, where δ is the standard deviation and d_{av} is the MPM diameter average. Over 500 MPMs are imaged and a PDI value of 3.9 % is found, indicating high monodispersity of droplet generated MPMs. (e) Image of the microfluidic system. (f) Scanning electron microscopy imaging of iron nanowires. Scale bars are 400 µm in (b) and (c), 200 µm in (d) 2 cm in (e) and 2 µm in (f).....95

Figure 3.4 (a) Voltage and current profiles for electrodeposition of iron nanowires in aluminum oxide templates. (b) Schematic of electrodeposition process, nitrogen purge protects oxidation of iron electrodeposition solution.....97

Figure 3.5 Magnetization of ~500 nm – 2 µm iron nanoparticles (not iron oxide) and un-sonicated 5.5 µm iron nanowires. Nanowires are measured with applied field parallel (red) and perpendicular (blue) to the wires. Due to shape anisotropy, regardless of the orientation of the nanowires relative the applied field, the remanent magnetization M_r will always be higher than that of the spherical particles, and the average of which for some disordered dispersion of nanowires will lie between the M_r values for aligned iron nanowires parallel to the field and iron nanoparticles (y-intercept of red and black curves here).....98

Figure 3.6 Under direct heating, normalized swelling-deswelling ratio (SR) of pure PNIPAm [PNIPAM(0)] microdroplets containing no magnetic material as well as that of magnetic PNIPAm microdroplets (MPMs) magnetic compositions using superparamagnetic iron oxide nanoparticles and (SPIO) iron nanowires (NW). Measurements are taken while MPMs are under direct external heating in a temperature controlled water bath with no magnetic field application.....100

Figure 3.7 (a) Normalized swelling-deswelling SR ratio of superparamagnetic iron oxide (SPIO) nanoparticle filled MPMs (higher field, 73 mT 600 kHz) and iron nanowire (NW) filled MPMs (lower field, 1 mT 20 kHz), responding to applied alternating magnetic fields (AMF), along with control tests including pure PNIPAm [PNIPAM(0)]. The rapid decrease near 200 seconds and 550 seconds, respectively, corresponds to the time required for the lower critical solution temperature to be achieved. (b) Average temperature of the MPMs caused by NW and SPIO heating, at lower power and higher power AMFs as indicated, over time. 102
Figure 3.8 (a) Time-dependent imaging of SPIO filled MPM under the lower AMF condition, showing no notable shrinkage and hence the negligible SR change in Fig. 3.7a. (b) Time-dependent imaging of NW filled MPMs under the lower AMF condition, showing shrinkage. (c) Unheated and heated SPIO filled MPMs under the higher AMF condition, showing shrinkage. (d) Imaging of heated and cooled pure PNIPAm microdroplets. 103
Figure 3.9 (a) Release profile of RhB with respect to time from control non-magnetic pure PNIPAm microdroplet, iron oxide nanoparticle loaded MPM, and iron nanowire loaded MPM, when a low power and high power alternating magnetic field is applied for continuous release (as indicated in legend). (b) Effect of nanowire concentration on the time required to release 4% of RhB using low-power AMF conditions (B = 1 mT, f = 20 kHz). 107
Figure 3.10 (a) Pulsatile AMF generated release profiles of RhB from non-magnetic control pure PNIPAm, iron oxide nanoparticle loaded MPM, iron nanowire loaded MPM, by consecutive alternating magnetic field (AMF) applications. MPMs are exposed to an AMF for 12 minutes separated by 5 minute intervals. (b) Effect of AMF frequency on time required for 4% RhB release using lower power AMF (B = 1 mT, f = 20 kHz). 109
Figure S1 (a) Diagram of simulated device assembly with osmotic pump, with components used summarized as follows: (i) donor chamber houses test drug to be transferred to receptor chamber, (ii) the osmotic chamber under the PDMS membrane is replaced by applied fluid pressure profile

for simplicity, (iii) the relief at the top of the assembly marked as "Flow/Drug Outlet" indicates the atmospheric boundary, (iv) dotted parallelogram indicates the part of the full osmotic pump assembly examined in a separate simulation model for closer understanding of flexible PDMS membrane's behavior (applied pressure test). (b) 2D axisymmetric model of the device. (c) Close up views of PDMS membrane and inlet membrane. Reprinted with permission from [228]. Copyright 2015, AIP Publishing LLC. 142
Figure S2: Simulated applied pressure on PDMS membrane (a) and volume deflected by PDMS membrane (b) over time. Note that the applied pressure plot is cubic over time, while the resulting volume deflection in almost linear. Reprinted with permission from [228]. Copyright 2015, AIP Publishing LLC. 153
Figure S3 Experimental setup for SAR measurements....157
Figure S4 Morphology of magnetic nanowires. Cross-section and top SEM images of the anodized aluminum oxide templates used to later deposit NWs. Pore size is determined by the acid used, averaging 35 nm for oxalic acid (A) and 190 nm for phosphoric acid (B). SEM images of released magnetic NWs on top of a silicon wafer with an average diameter of 35 nm (C) and 180 nm (D). .158
Figure S5 Magnetization loops of arrays of nanowires (NWs) embedded in the anodized aluminum oxide template. For all NW measurements the field is applied parallel the NWs (black curves) and perpendicular to the NWs (red curves). In the case of the iron oxide nanoparticles, only one curve is shown as the particle-solution suspensions are isotropic during measurement. 159
Figure S6 Temperature curves for nanowire and nanoparticles under a 60 mT, 425 kHz AMF over time. 161
Figure S7 Branson B-200 Ultrasonic cleaner used in the initial cleaning process of aluminum substrates. 164
Figure S8 Electropolishing platinum mesh on Teflon plate. 164
Figure S9 Images of custom Teflon cell on Thermo Scientific cooled cooling plate, chiller, Keithley sourcemeter used for anodization and electrodeposition, and Agilent DC power supply for stirrer....165

Figure S10 Images of 4-hole Teflon cell with O-rings and aluminum substrates. Diameter of exposure of holes is ~15 mm (depending on O-ring design). 165
Figure S11 The opaque cloudy aluminum oxide layer on the initially mirror-like aluminum substrate is removed in a chromium oxide and phosphoric acid solution, rendering the surface mirror-like again, with nano indentations on the surface.....166
Figure S12 Scanning electron microscopy images before and after the removal of the 1st anodization oxide layer. 166
Figure S13 Scanning electron microscopy images taken after the second anodization, which use the nano indentations of the previous step, results in a more ordered array of pores.....167
Figure S14 The electrodeposition solution is heated during the deposition process for Co and Ni. For more precaution, a smaller hole of ~7 mm diameter (depending on O-ring design) exposure for the substrate may be used. 168
Figure S15 Electrodeposited samples may be diced into smaller pieces for experiments, imaging, magnetic measurements, or storage, prior to release and use. Partially released nanowires connected to aluminum oxide. 169
Figure S16 Schematic illustration of the solid drug in reservoir (SDR) based device and its cyclic operation. Reprinted with permission from [279]. Copyright 2015, AIP Publishing LLC. 175
Figure S17 (a) photographs of the experimental apparatus and the prototypes of the major components: (b) assembled electrolytic pump; (c) image of Nafion coated Pt/Ti electrodes; (d) sputtered platinum coated carbon fiber mesh; (e) inductive coil; (f) the serpentine PNIPAm valve mixed with iron micro-particles (g) the glass capillary PNIPAm valve surrounded by iron micro-particles. Reprinted with permission from [279]. Copyright 2015, AIP Publishing LLC. 177
Figure S18 Magnetic field controlled flow rates (mean ± standard error, *n*=3) of the electrolytic pump with one catalytic reformer element and without a catalytic reformer under the same conditions. Reprinted with permission from [279]. Copyright 2015, AIP Publishing LLC. 179

Figure S19 Dye displacement of electrolytic pump with one catalytic reformer element and without a catalytic reformer under the same conditions. An electromagnetic field of 40.5 mT is applied. Reprinted with permission from [279]. Copyright 2015, AIP Publishing LLC. 180
Figure S20 Pumping profile under an electromagnetic field of 40.5 mT when the thermo-responsive valve was used in combination with a pump with three catalytic reformer elements. The insets illustrate the states of the valve at different time points and the corresponding temperatures. Black particles are the iron micro-particles. Scale bars are 3 mm. Reprinted with permission from [279]. Copyright 2015, AIP Publishing LLC. 182
Figure S21 Cyclic liquid displacement of the dye when a device with a pump, three catalytic reformer elements and a PNIPAM valve is operated with an electromagnetic field of 40.5 mT that is periodically turned on and off. Reprinted with permission from [279]. Copyright 2015, AIP Publishing LLC. 183
Figure S22 (a) PNIPAm polymer valve sealed at room temperature; (b) The valve opens under magnetic field, due to shrinking of PNIPAm. Figure reprinted with permission [278], © 2011 IEEE. 184
Figure S23 Throughput of the valve under different magnetic fields, used to calculate the corresponding valve opening time. Figure reprinted with permission [278], © 2011 IEEE. 185
Figure S24 Single pumping pulse under magnetic field with PNIPAm polymer valve installed. Figure reprinted with permission [278], © 2011 IEEE.....185

List of Abbreviations

AAO, anodic aluminum oxide

AC, alternating current

AMF, alternating magnetic field

B, magnetic flux density (scalar)

B, magnetic flux density (vector)

CA, cellulose acetate

EC, ethyl cellulose

H, magnetic field strength (scalar)

H, magnetic field strength (vector)

H_c, magnetic coercivity or coercive field

H_s, switching field

H_{sat}, saturation field

LSR, loop-squareness ratio

m, magnetic moment (scalar)

m, magnetic moment (vector)

m_h, reduced magnetization

M, magnetization (scalar)

M, magnetization (vector)

M_r, remanence magnetization

M_s, saturation magnetization

MPM, magnetic PNIPAm microdroplet

NW, nanowire

PNIPAm, poly(N-isopropylacrylamide)

R, aspect ratio

SAR, specific absorption rate

SPIO, superparamagnetic iron oxide

VSM, vibrating sample magnetometer

μ, magnetic permeability

μ_0, magnetic permeability of free space vacuum

χ_m, magnetic susceptibility (aka volumetric susceptibility)

Glossary

- Anodization: process used to increase the thickness of the oxide layer of a metal surface, generating nanopores in the process. During anodization, the metal to be anodized is the anode electrode in the electric circuit, hence the name. The oxide layer is grown when a direct current passes through an electrolytic solution and the metal, such as an aluminum anode. The cathode electrode submerged in the electrolyte releases hydrogen, while the anode releases oxygen, and this oxygen release results in the growth of metal oxide, such as aluminum oxide. The oxide layer is porous by virtue of the chemical process forming the layer; nanopores allow the current carrying electrolytic solution to reach the non-oxidized metal substrate, and the longer the anodization, the more parallel the pore growth with increasing oxide layer depth.
- Apoptosis: the process of biochemical events leading to characteristic changes in living cells, changes resulting in their deaths.
- Block copolymer: a block copolymer results from a special kind of copolymerization (see copolymerization), in which the resulting polymer is built from different blocks of polymerized monomers (see monomer).
- Coercivity: the coercivity, or coercive field (denoted by H_c), indicates the applied magnetic field strength required to cause a material to reach zero magnetization after having reached magnetic saturation.
- Colloid: mixture in which small particles of one species (dispersed phase) are distributed evenly throughout another species that acts as the liquid suspension medium (continuous phase). Colloidal mixtures do not settle, or take very long to appreciably settle.
- Copolymer: see copolymerization.
- Copolymerization: when a monomer of one species (i.e. a molecule that chemically binds, or polymerizes, with others to form a polymer), unites with one or more monomers of (a) different species, the resulting polymer is referred to as a copolymer, and the processes is called copolymerization.

- Demagnetizing field: the demagnetizing field, also referred to as the stray field, is the magnetic field produced by a material's own magnetization. Its name is associated with its tendency to reduce the total magnetic moment of a material. The demagnetization field is responsible for such phenomena as shape anisotropy and magnetic domain generation.
- Easy-axis (magnetic): the direction in a magnetically anisotropic material that is energetically favorable for spontaneous magnetization. This tendency is in contrast to what occurs in magnetically isotropic materials and objects that have no directional preference for magnetic moment when under no externally applied magnetic field. A magnetic hard-axis is similar, but refers to a direction of unfavorable maximum energy.
- Electrodeposition: the process of generating a material deposition on a surface using electrolysis.
- Hard-axis: see easy-axis.
- Hyperthermia (magnetic): magnetic hyperthermia is an experimental technique used for the treatment of cancer, and is based on the principal of heat generation occurring when magnetic nanoparticles are placed in an applied alternating magnetic field. When such nanoparticles are inserted in a tumor, or injected in the body and designed to target a tumor, the required magnetic field amplitude and frequency can be applied remotely from the treatment area, increasing the temperature of the treatment zone, increasing the efficiency of chemotherapy or potentially inducing cell death in the tumor.
- Hysteresis (magnetic): When a magnetic field is applied to a ferromagnetic material, the material becomes magnetized, and the relationship between the magnetic field strength and the magnetization is non-linear, following a hysteretic path. In other words, applying a field in one direction results in a change in magnetization, while applying an equal and opposite field will result in a change that is unequal in magnitude to the first. This is because of a lag between the applied field and the magnetization of the material. This irreversibility in the magnetization path is seen in the plot of a material's magnetic hysteresis loop, which graphs the magnetic response of the material versus an applied external magnetic field. The response differs

according to material properties and their dependence on field strength and frequency, and the area enclosed by the hysteretic path is the energy lost by the system in the process of going through one loop cycle.

- Intrathecal: administered to or occurring within the spinal theca (loose spinal cord sheath).
- Liposome: spherically shaped microscopic vesicle made of phospholipid molecules (class of lipids, or naturally occurring molecules, that are a major component of the cell membrane composition), enclosing water or an aqueous solution. These can be used to transport an aqueous drug in the human body.
- Lyophilization: the process by which a material is freeze-dried by freezing the wet samples and subliming the formed ice directly to vapor when exposed to low pressure.
- Magnetic dipole moment: the quantity determining the torque that a magnetic object will experience when exposed to an externally applied magnetic field.
- Magnetization: a scalar vector that characterizes, at the macroscopic scale, the magnetic behavior of a material. It is a measure of the density of induced (permanently or not) magnetic dipole moments in the material (see magnetic dipole moment).
- Magnetocrystalline anisotropy: a ferromagnetic material exhibits magnetocrystalline anisotropy if the axes of its crystal lattice induce directions in which the energy required to magnetize the material are unequal. This inequality results in preferential directions for magnetization, and originates primarily from the spin-orbit coupling of the orbital motion of electrons coupled with the electric field of the crystal structure.
- Magnetoelastic anisotropy: also known as the “inverse magnetostrictive” effect, the magnetoelastic effect refers to the change in a material’s magnetic susceptibility in response to a mechanical stress. When a uniaxial mechanical stress is applied, the value of the magnetic flux density B will increase or decrease for a given field strength H. The response in the material is anisotropic, as the applied stress is uniaxial, resulting in magnetoelastic magnetic anisotropy along that axis (e.g. easy-axis, see above).

- Micelle: aggregate of surfactant molecules dispersed within a liquid colloidal solution (see colloid).
- Monomer: a molecule that chemically binds, or polymerizes/undergoes polymerization, with others to form a polymer.
- Parenteral: administered or occurring somewhere in the body other than the mouth and alimentary canal.
- Permeability: the measure of a material's degree of magnetization when exposed to an externally applied magnetic field. In other words, a measure of a material's ability to sustain the internally formed magnetic field when responding to an applied field.
- Polymer: see monomer.
- Polymerization: the chemical binding process resulting in the creation of polymers (see monomer).
- Remanent magnetization: remanent magnetization, also known as remanence, is the value of the magnetization which remains in a material after the removal of any externally applied magnetic field.
- Saturation magnetization: magnetic saturation is reached when a material's magnetization no longer changes with increasing magnetic field strength (in magnitude). When the magnetic domains in a material are as aligned as possible with the applied field, they can no longer augment the global magnetization of the material. This condition results in a flat, horizontal segment, in a plot of magnetization versus applied magnetic field H, where magnetization remains constant and has a value referred to as the magnetization saturation value. H_{sat} is the associated magnetic field value required to achieve saturation.
- Shape anisotropy: the demagnetization field (see above) of a non-spherical particle is not equal in all direction of the material, resulting in one or more magnetic easy-axes (see above). This geometric effect is referred to as shape anisotropy.
- Superparamagnetism: a behavior of magnetic materials when in the form of nanoscale particles. When sufficiently small, the magnetization of a particle can spontaneously reverse under the influence of temperature. In the absence of an applied magnetic field, if the measurement time used to measure the magnetization of these nanoparticles is much larger than the average time between spontaneous reversals

(known as Néel relaxation time), then their magnetization appears to be zero, and this is referred to as a superparamagnetic state. The application of a magnetic field can magnetize the nanoparticles, as occurs with paramagnetic materials, but the frequency dependent magnetic susceptibility of superparamagnetic materials is larger than that of paramagnetic materials.

- Susceptibility: dimensionless proportionality constant that indicates the degree of the *response* of a material's magnetization to an externally applied magnetic field. The magnetization of a material can be calculated by multiplying the applied magnetic field strength by the susceptibility of the material.
- Vibrating sample magnetometry: the measurement of magnetic properties, including magnetic hysteresis (see above), of a material by placing it in a uniform magnetic field, magnetizing the sample, vibrating it sinusoidally, and measuring the voltage it induces in a pickup coil (which is proportional to its magnetic moment and independent of the applied magnetic field strength).

Acknowledgements

I would like to show my deepest gratitude to my co-supervisors, Dr. Ian G. Foulds and Dr. Jürgen Kosel, for their invaluable insight, advising, support, patience, instruction, guidance, unrestrained constructive questioning, shared experience and personal attention. Their knowledge, intuition, collaborative spirits, and multi-disciplinary visions have been great sources of inspiration throughout my research, and have continuously helped increase my capacity to transform creativity into application.

I would also like to express my thanks to my committee member Dr. Keekyoung Kim for his help through general advising with regards to my research, and for the time and attention invested in reviewing my dissertation. Special thanks go to Dr. Liwei Lin and Dr. Niveen Khashab, who collaborated with me on much of my research, providing invaluable input and opportunities for achieving our multidisciplinary objectives.

My sincerest gratitude goes out to collaborating colleagues and group members. Song Li, María Fernanda Contreras, Ahmed Alfadhel, Mincho Kavaldzhiev, lab manager Ulrich Buttner, and Dr. Omar Yassine. Dr. Yassine's expertise and significant experience with polymers and microfluidics as proven invaluable to our research, and I am very grateful for having the opportunity to work together.

My heartfelt appreciation goes to my parents and sister, whose abundance of love and support throughout the years have served as fundamental constants among the multi-variables of scientific research.

Dedication

This work is dedicated to my mother, father, sister, as well as my family and all the friends, mentors, and colleagues who have become a part of it over the years.

Chapter 1 Introduction

1.1 Dissertation Objectives

To assist the reader in understanding this work through the appropriate lens, a brief overview of the scope and objectives of this dissertation will be covered prior to delving into the background of the field of drug delivery systems.

This work seeks to diversify and optimize several drug delivery solutions that focus on remote and repeatable triggering of devices or carriers, as well as passive and active drug dose control. This is achieved by building upon present technologies that include thermoresponsive PNIPAm polymers and implantable osmotic pumps, and implementing new electromagnetic applications of nanostructure and nanowire composites in several previously unexplored combinations, in order to reduce the power requirements.

Due to the interdisciplinary nature of the research presented in this dissertation, Chapter 1 will cover a broad range of introductory and background information regarding drug delivery systems (section 1.2), stimuli-responsive drug delivery (section 1.3), magnetically- induced heating for drug delivery applications (section 1.4), which includes an introduction to magnetism and how it applies to the work presented, and finally an overview of the research motivations and objectives (section 1.5). The subsections, particularly those within section 1.4, provide information for understanding the principles governing the physical phenomena reported.

1.2 Introduction to Drug Delivery Systems

Drug delivery is the set of technologies and approaches for delivering therapeutic treatments to targeted locations in a patient, for the facilitation of pharmaceutical compound release in a patient's system, or for the control over the kinetics and profiles of these compounds' release. Drug delivery technology includes implantable micro-engineered devices and systems, on a scale larger than molecular systems, that contain a liquid drug of a certain concentration, and that provide a certain drug release profile over lifespan of the system.

Implantable drug delivery systems are one of the most difficult medical devices to develop because of the requirements of surgical installation, replacement, long-term reliability issues, and complications involving reactions to implanted foreign objects [1-3]. However, this is also a high-risk high-reward research area, as the technology entry-level is

high, and successful developments of new implantable drug delivery systems will lead to direct impacts on various medical treatments [1, 2, 4]. In light of this, implantable drug delivery systems are playing an increasingly important role in therapeutic treatments [1-4].

Drug delivery systems have been used in many applications, such as morphine delivery for the treatment of cancer-related pain and nonmalignant ailments [5-7], or intrathecal delivery of baclofen for the treatment of severe spasticity [8-10]. For example, a drug delivery system from Medtronic Inc. (Figure 1.1) can store drugs up to 18 ml and the average delivery rate is 48μl per day: a refill is required every 375 days [8]. Because medications are delivered locally, where they are most effective, smaller volumes of concentrated dosages can substantially control chronic pain and severe spasticity without side effects [8-10]. As a result, current research efforts include extending battery life and reducing the drug delivery rates to minimize surgical replacement or refill requirement [5-7, 9-11].

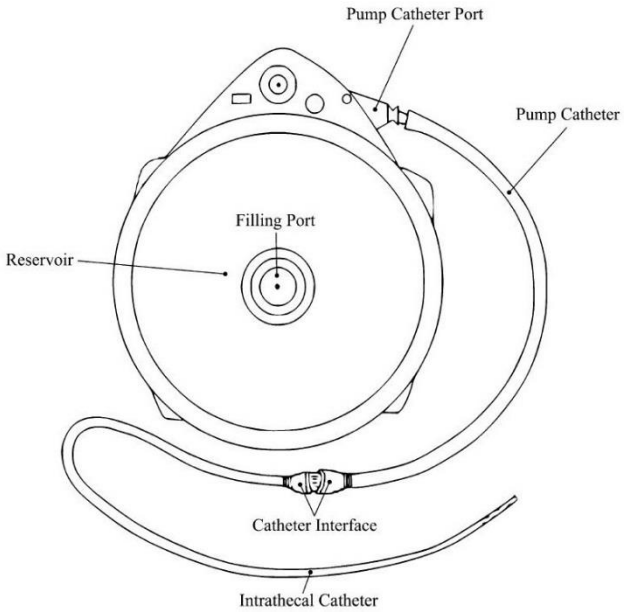

Figure 1.1 Schematic of a typical Medtronic intrathecal drug delivery pump system, 25 mm thick and 76 mm wide. The device is typically implanted subcutaneously in the anterior abdominal wall. Reprinted by permission from The Journal of Bone and Joint Surgery, copyright 2012 [12].

The majority of therapeutic treatments require some predetermined ideal drug concentration profile to be maintained for the duration of an effective therapeutic period of time examples of which are illustrated in Figure 1.2. Many conventional drug delivery approaches do not easily accomplished this [13], methods including oral ingestions of time

release capsules, eye drop solutions, and standard parenteral subcutaneous injections. Implantable drug delivery systems, in contrast to such conventional methods, have therapeutic advantages in terms of their ability for controlled locally targeted drug dosing. In particular, devices with reliable and tunable remote controllability are pushing the boundaries of treatments for chronically debilitating diseases, such as in the case of brain tumor treatment [14].

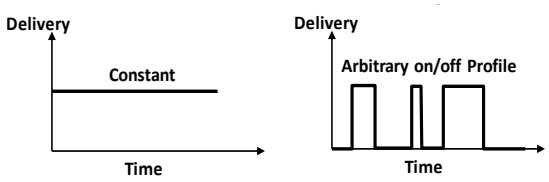

Figure 1.2 Example profiles of a constant drug delivery profile and a completely arbitrarily controlled ideal profile.

Sustained drug release technology has been applied in many medical fields [3], and over the past several years, significant advancements have been made with regards to the synthesis and tunability of functionalized drug carriers [15-18], switches [4, 19], membranes [4, 15, 20, 21], containers [4, 15, 22-26], pumps [22, 27], and valves [4, 15, 19, 21]. State of the art implantable micro-devices include reservoir-based systems [4, 22, 28-30], controlled-release microchips [28-30], and various electrically powered microsystems [4, 28-30]. Near-infrared responsive nanoparticles composed of a mixture temperature-sensitive poly(N-isopropylacrylamide) polymer (PNIPAm) and gold−gold sulfide nanoshells are capable of on demand release of protein molecules, but eventually suffer from inconsistent dosages after several trigger cycles [31]. Ferrofluid-loaded polymer sheets [32], liposomes [33], microspheres [34, 35], microcapsules [36, 37], and nanospheres [38-40] can be remotely activated using magnetic induction.

Osmotic pumps present a convenient and reliable cost-effective drug delivery method capable of replacing repeated injections of soluble and poorly soluble drugs [41, 42] for the treatment of chronically debilitating diseases [27, 43-46]. These marketed pumps use the principle of osmotic pressure for the delivery of pharmaceutical ingredients at a predetermined rate [47], and will be discussed in more detail in the following section.

There has been an increased interest in the development of remotely modulated drug delivery from implantable devices. Examples of the need for such systems, where short

bursts of increased delivery are highly optimal, include insulin delivery and osteoporosis therapy [45, 48]. For these cases, a lower, sustained bias delivery rate, driven by a pressure source, would address the need for continuous treatment. This is then supplemented by intermittent on-demand rate increases. Similarly, switchable transdermal nicotine delivery rates are pursued to address the varying therapeutic demand levels for nicotine cessation treatments [49]. Chronic diseases that present symptom flare up, including diabetes [50, 51], hemophilia [52, 53], hypertension [54], high cholesterol [55], asthma [56], seasonal allergies [57], and chronic seizures [58], may potentially be addressed using variable dosing. Furthermore, in the case of diseases that affect specific locations in the body (e.g. internal bleeding at joints in hemophiliacs), localized device implantation can allow for significant reductions in the required drug mass delivery by bypassing untargeted organs such as the stomach, small intestine, liver, and kidney, which cause unnecessary loss of drugs.

1.2.1 Osmotic Pumps for Drug Delivery

Osmotic pumps are a sub category of infusion pumps, which typically infuses a treatment in the form of nutrients or medication into a patient's body via intravenous, arterial, epidural or subcutaneous infusion [27, 43, 59]. The need for miniaturization of a pump typically requires the use of a pressurizing system that functions reliably despite the scale-down, hence the development of osmotic pumps, the smallest of the infusion pump family, in which osmotic power drives the system. A chamber containing a salt solution absorbs water through a semi-permeable membrane, and the swelling in volume induces a deflection of a flexible membrane which in turn pushes out the contents of a syringe-filled drug chamber. The rate of delivery is controlled by the salt concentration and the geometry of the pump and its chambers, membranes, and the type of delivery port used. A semi-permeable membrane is a type of membrane, either biological or synthetically produced, that selectively permits certain molecules to travel though it by diffusion or forced convection flow.

In the early work by Theeuwes et al., the fundamentals of an elementary osmotic pump were introduced [60]; an elementary osmotic pump is defined as a device containing an osmotic core, serving as both the osmotic agent and the drug carrier, surrounded by a semi-permeable membrane housing equipped with at least one drug delivery outlet (Figure 1.3a).

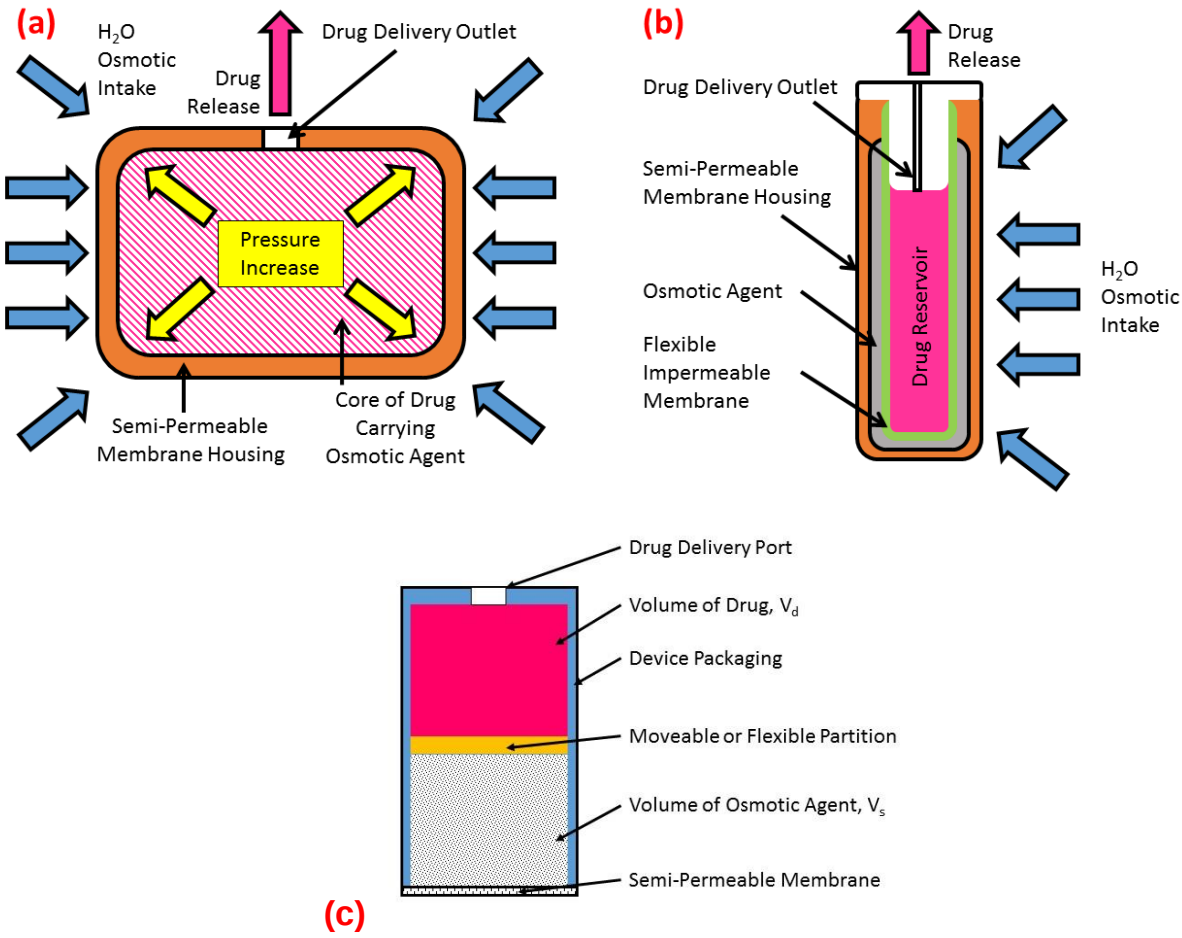

Figure 1.3 Schematics of (a) fundamental operation of an elementary osmotic pump and (b) a state of the art osmotic pump design developed by Theeuwes et al., (c) simplified diagram of a basic osmotic pump design with either a movable or flexible partition.

Water exposure is then required for triggering an osmotic reaction which releases the inner drug. When the inner volume of the device is fixed, the osmotically imbibed volume of water passing through the semi-permeable membrane replaced an equal volume of saturated solution from the core, which in turn is expelled from the drug delivery outlet. The delivery rate drops parabolically to zero when the concentration of the osmotic solid falls below saturation.

Later, Theeuwes develops an osmotic pump design that allows for a complete separation between the osmotic agent and the drug to be delivered [44]; a drug reservoir is in contact with a flexible impermeable membrane and has one drug delivery outlet, the impermeable membrane is surrounded by an osmotic agent, which is encapsulated by a semi-permeable membrane housing (Figure 1.3b). Just as with the elementary osmotic pump,

water is absorbed through the semi-permeable membrane and works to increase the volume contained in the osmotic agent section, but now acts as a pressurizer by pushing against the impermeable membrane that contains the drug, which in turn is expelled from the drug delivery outlet (the phenomena is detailed after the next paragraph). This is the basic principal of the osmotic pump used in this research to achieve pressurized forced convection (coupled with diffusion) through magnetically controlled membranes, and the combination of these two components in a device are envisioned for subcutaneous implantation.

The latest osmotic pumps provide reliable and convenient cost-efficient drug delivery solutions that replace multiple injections of soluble or poorly soluble drugs [41, 42], for treating chronic debilitating diseases [26, 27, 43-45, 59, 60]. The pumps utilize principles of osmotically generated pressure to deliver pharmaceutical agents at pre-calculated rates [47], while eliminating the need for several instances of device manipulations and injections using external leads and connectors. DUROS osmotic pumps (Figure 1.4), for example, are used for parenteral therapy, for local or systemic drug delivery, while spanning durations of days to years [43]. Additionally, osmotic drug delivery systems may be used in animal testing for research including but not limited to central nervous system disorders treatment [61, 62], spinal cord injury treatment [63], cerebral malaria treatment [64], peripheral arterial disease treatment [65], and the treatment of Parkinson's disease [66]. Furthermore, discrete or daily dosing of anabolic osteoporosis medication for human treatment, via implantable wirelessly controlled microchips, has been pursued [45]. However, such current systems are typically limited to single-event release or constant drug release that does not benefit from real time on-demand wireless control for dose varying.

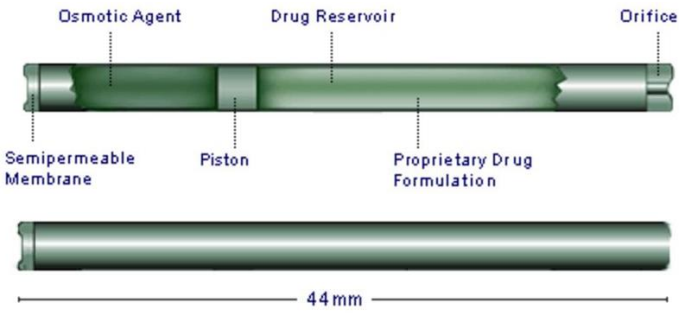

Figure 1.4 Duros osmotic pump design. Osmotic pressure drives the piston against a drug formulation, which in turn is ejected out of the orifice. Reprinted by permission from DURECT Corporation [http://www.durect.com/wt/durect/page_name/duros].

The osmotic pumps used in this research are coupled with remotely controlled membranes used as valve mechanism, discussed later, with the goal of overcoming the aforementioned limitations.

The phenomena occurring in the osmotic pump can be summarized as based on the early work by Theeuwes et al (1976). Figure 1.3c shows the simplified diagram for a basic drug delivery osmotic pump design, in which a drug reservoir contains a homogeneous drug solution (of volume V_d), in contact with a drug delivery exit port. The flexible or movable partition separates the drug reservoir from the osmotic driving agent that provides the driving force against the partition. A semi-permeable membrane allows water to flow through it, but is impermeable to the volume of osmotic driving agent in the osmotic chamber (of volume V_s).

By placing the osmotic pump in an aqueous solution or moist environment, a net flux of water occurs through the semi-permeable membrane and into the osmotic chamber. This flux is controlled by the semi-permeable membrane, which holds back the osmotic agent while pressure is exerted on the moveable or flexible partition. The drug solution contained on the other side of the partition is then expelled through the drug delivery port. The pump packaging and the semi-permeable membrane are non-deformable, therefore the volume of incompressible water entering the device is equal to the volume of solution delivered via the drug delivery port.

Water flow for a single osmotic driving agent solute is written as:

$$J = K \cdot A \cdot (\sigma \Delta\pi - \Delta P), \tag{1-1}$$

where K is the permeability of the semi-permeable membrane [m^2s/kg] to water specifically (alternatively expressed in terms of hydraulic permeability L_p [m^3s/kg] and membrane thickness h [m] as $K=L_p/h$), J is the water volume transport rate [m^3/s], A is the semi-permeable membrane's effective surface area [m^2], σ is the membrane's osmotic reflection coefficient (unitless), Δπ is the difference in osmotic pressure between the osmotic chamber and the outside of the device (Pa), and ΔP is the difference in hydrostatic pressure between the osmotic chamber and the outside of the device (Pa). The latter two are defined as follows.

With all internal components and solutions considered incompressible, the volume rate of drug delivery from the device is equal to that of the water transferring across the semi-permeable membrane, given by Eqn. (1-1). When the pump operates in an environment with an osmotic pressure, denoted by π_e, Δπ is expressed as:

$$\Delta\pi = \pi_s - \pi_e, \tag{1-2}$$

where π_s is the osmotic pressure of the water solution in the osmotic chamber (consisting of the single solute osmotic agent and the water accumulated). ΔP, the hydrostatic pressure difference, is then expressed as:

$$\Delta P = \Delta P_d + \Delta P_e, \tag{1-3}$$

where ΔP_d is the increase in internal pressure caused by the flow of the drug solutions through the drug delivery port. ΔP_e is the pressure that would be required to deform the drug reservoir in the imploding direction.

Constant drug delivery and constant pumping can be achieve by taking Eqn. (1-1) and setting ($\sigma\Delta\pi - \Delta P$) as constant. This can be achieved by ensuring that the right hand sides of Eqn. (1-2) and Eqn. (1-3) are constant.

By maintaining continuous saturation in the osmotic solution with an excess of NaCl, as done in the pump used in the magnetically controlled drug delivery devices reported in Chapter 2, and given that the external solution pulled into these devices' osmotic pumps has both constant and negligible osmotic pressure (water relative to saturated NaCl solution), Eqn. (1-2) is ensured to remain constant. The magnetically controlled membranes used with the osmotic pumps in Chapter 2 essentially increase or decrease in porosity, depending on whether a magnetic field is applied to the membranes or not. Furthermore, ΔP_d, ΔP_e, and therefore Eqn. (1-3), are constant in each steady state of operation with the osmotic pump active; ΔP_d stabilizes while the magnetically controlled membrane is in the increased

porosity state or decreased porosity state, and ΔP_e is unchanging given the rigidity of the devices and the magnetically controlled membrane. Therefore, in each of the devices' steady states, the volume transport rate J in Eqn. (1-1) is constant, representing the incoming and the outgoing aqueous solutions.

1.3 Stimuli-Responsive Drug Delivery

Materials that react to external stimuli are of great interest in the fields of biochemistry and biomedical engineering, in particular for their potential for controlled drug delivery solutions in therapeutic applications [67].

The study of stimuli-responsive based drug delivery is of great interest for academic and industry research aimed at optimizing targeted, smart, and remotely controllable on-demand systems [4, 21, 27-29, 43, 68-70]. Stimuli-responsive functionalized organic composites that react to magnetization, heating, lighting, pH changes, or ultrasound application are particularly focused on for potential biomedical solutions [15, 18, 20].

For example, Poly(N-isopropylacrylamide) (PNIPAm) hydrogels are employed in many applications for sensing [71, 72], electrochemical switching [73], bio-membranes [74], cell attachment and cell culturing [75-77], color tuning [78], radiotherapy [79], and optics [80]. Additionally, the embedding of micro and nanoparticles in stimuli-responsive materials like PNIPAm during synthesis can add functionality the material, such as what has been achieved with irradiation-responsive composites which can be used in photodynamic therapy [80], catalysis [81], and water desalination [82].

1.3.1 Poly(N-isopropylacrylamide) Hydrogels and Drug Delivery

PNIPAm has been implemented as a thermoresponsive polymer hydrogel in drug delivery systems. PNIPAm grafted with other polymers [67, 83-86], inorganic particles [67, 87-93], or PNIPAm in the form of micelles [67, 94], core-shell structures [67, 95, 96], liposomes [97, 98], or nanoparticles and nanogels [99-101], can achieve different drug delivery functionalities.

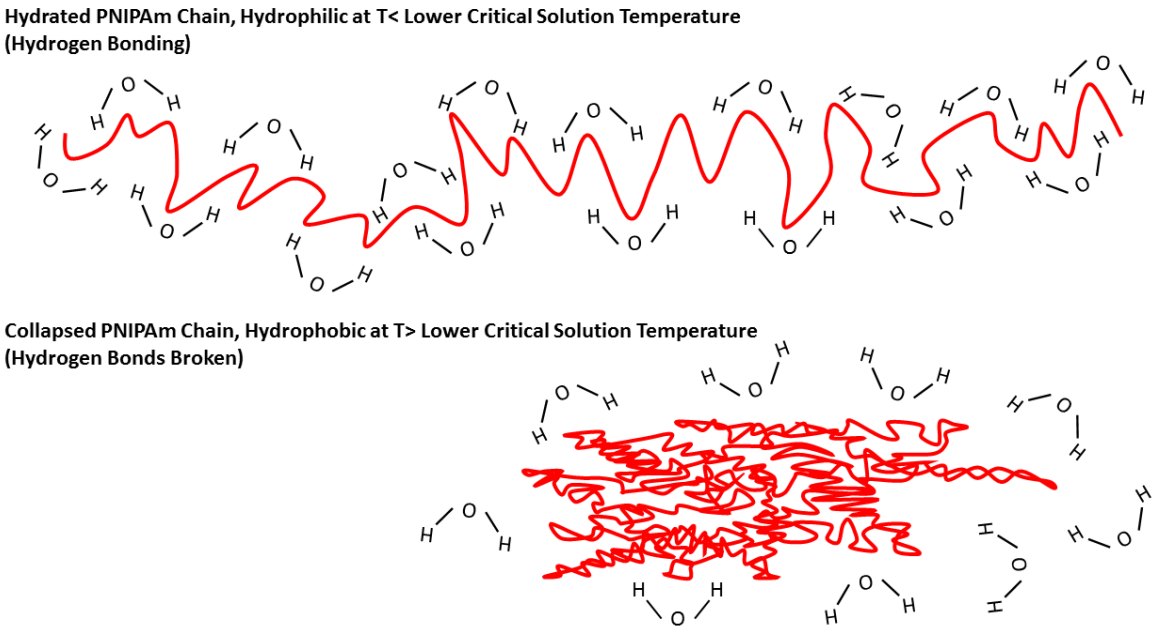

Figure 1.5 Schematic of PNIPAm thermoresponsive behavior, transitioning from hydrophilic to hydrophobic and expelling aqueous content from the PNIPAm network chain shown.

PNIPAm is thermoresponsive (reacting to the stimulus of temperature change), as illustrated in Figure 1.5, making it one of the most widely used smart polymers [102-104]. Its NIPAM water soluble monomer component can polymerize as a structure in the form of a gel network. This work relies on the gel network form and its properties, a form in which PNIPAm consists of 3D polymer chain networks that are highly water absorbent, thus classifying it as a "hydrogel" whose network contains a vast majority of water content when hydrated [67]. In addition to the thermoresponsive nature of the PNIPAm hydrogel, its viscoelasticity or water content can be exploited by using the motion of magnetic materials embedded in its network to generate heat, as will be demonstrated in this work.

PNIPAm hydrogels undergo volume phase and hydrophilicity changes at a temperature transition point, referred to as the lower critical solution temperature (LCST). The LCST influences the hydrogen bonds formed within the polymer network, thus determining the hydrogel's swelling state. Below LCST, a PNIPAm hydrogel is hydrophilic, swelling with water molecules when in an aqueous environment. Above LCST, the hydrogel increases in hydrophobicity, expelling water molecules and shrinking in volume.

Specifically, below LCST, the PNIPAm polymer chains become more water soluble, a phenomenon caused by the water molecules' hydrogen atoms undergoing H-bonding with

the amide moieties in the polymer network (containing ammonium). Above LCST, the hydrogen bonding is severed, and Van der Waal forces between the hydrophobic groups in the polymer network attract them to each other and dominate in bonding, leading to a physical collapse in the network structure and an expulsion of the previously hydrogen bonded water molecules from the network [67].

PNIPAm has an LCST close to the temperature of the human body, which can be adjusted by changing its monomer composition (see below), is relatively insensitive to low salt concentrations, and is biocompatible, making it a suitable candidate for medical applications [75]. It can be molded when synthesized to take any shape, including films and spherical particles on the micro and nanoscale, making it very flexible as a valving material for drug delivery control. The geometry and size of a PNIPAm gel may be adjusted to match application requirements by tuning the chemical reaction temperature, agitation and stir levels [105], as well as the crosslinker concentrations [106], initiator concentrations [107], and the addition of surfactants [107, 108].

PNIPAm can be prepared by the copolymerization method [109], in which different monomers bind and result in a copolymer. PNIPAm may also consist solely of a single type of monomer, NIPAm, in which case the process is simply a polymerization. In this work, the constituents of a copolymerized PNIPAm hydrogel are N-isopropylacrylamide (NIPAm), N-isopropylmethacrylamide (NIPMAm), and acrylamide (AAm). N,N'-Methylenebisacrylamide (also known as bisacrylamide, BA, or MBAm) is used to crosslink (i.e. polymer bond) the generated PNIPAm polymers, resulting in a 3D hydrogel in the shape of spherical particles. These copolymer hydrogel PNIPAm particles are used in the magnetically triggered composite membranes reported in this research. The non-copolymer, single monomer PNIPAm polymer, can be cross-linked using the same crosslinker as copolymerized PNIPAm, also resulting in a 3D hydrogel. This single monomer PNIPAm is used in the fabrication of remotely triggered magnetic PNIPAm microdroplets, reported in this research. The difference in monomer compositions results in a difference in the LCST of the hydrogels.

1.3.2 Thermoresponsive Membranes

Several materials have been explored for their application in temperature sensitive membrane design. For example, thermoresponsive porous membranes in ethyl cellulose (EC), cellulose

acetate (CA), nylon-6 and commercially available films [109-117] have been developed for maximizing the control over reversible changes in membrane properties for drug delivery. In addition, models have been used to explain the diffusion processes in such membranes [118]. Grafting techniques have been used to further customize the functionality of PNIPAm and PNIPAm-polymer combinations used in composite and surface treated membranes [119-125], which includes radiation-induced grafting and synthesis [126-128], photo-grafting of N,N-diethylacrylamide (DEAAm) onto microfiltration membranes [129], grafting of PNIPAm on commercially available membranes [130, 131], poly(vinylidene fluoride) membranes with grafted PNIPAm chains [132-139], and microfluidic capillary grafting for the control of fluid flow [140]. For even smaller versions of such capillary systems, membranes have been developed with functional gates grafted onto the side-walls of the membrane micropores using PNIPAm [141-143] or poly(oligo(ethylene glycol) methacrylates) (pOEGMA) macromolecules [144]. Grafting consists of the chemical bonding of the PNIPAm to the matrix or structure functioning as a valve. This approach is particularly effective when higher levels of control over the designed dimensions of the valve openings are necessary. While grafting may be used to effectively functionalize materials for various applications, this work focuses on thermoresponsive membrane composites containing PNIPAm, whose integration does not rely on grafting techniques.

PNIPAm treatments have been used on surfaces and membranes to allow for hydrophilic-hydrophobic reversible switching [123, 145]. UV-photopolymerization of PNIPAm [146, 147] has increased the level of design possibilities for membrane surface treatments, and opened up the doors for microfabrication integration.

Membranes utilizing PNIPAm particles have been demonstrated as effective switchable valve or gate controllers for on-off drug diffusion profiles [15, 20, 109, 117, 125]. In the off state, PNIPAm particles below LCST in a membrane will occupy the majority of the volume in the diffusion pathways available for the drug to pass through, significantly limiting its mass transport. In the on state, these particles shrink in volume when heated above LCST, permitting higher mass transport rates though the membrane.

The first works to achieve remote control of PNIPAm hydrogel based membranes for drug delivery are those of Hoare *et al* [109, 117], in which superparamagnetic iron oxide (SPIO) nanoparticles (the magnetic triggering element) and PNIPAm nanogels (the switching

element) are mixed into EC (the matrix, after casting and drying), to create cast and dried thin film membranes which are studied for their drug release profiles from one side of a membrane to the other, undergoing repeatable and reversible switching of the embedded PNIPAm using an alternating magnetic field.

Figure 1.6 shows the general dynamics involved in triggering a hydrogel PNIPAm-based membrane by magnetically heating particles within the membrane matrix, causing the thermo-sensitive PNIPAm particles in the matrix to reduce in volume, widening diffusion pathways for the drug to flow through with an increased flux.

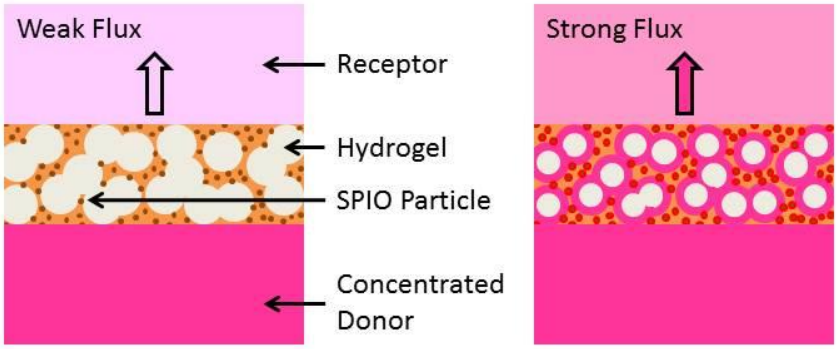

Figure 1.6 Schematic of the triggering a PNIPAm hydrogel membrane. Magnetically heating superparamagnetic iron oxide (SPIO) nanoparticles within the membrane matrix cause the thermoresponsive PNIPAm hydrogel particles in the matrix to reduce in volume, widening diffusion pathways for the drug to flow through at an increased flux rate.

1.3.3 Thermoresponsive Microdroplets

PNIPAm hydrogel micro-sized particles, referred to as PNIPAm microdroplets here, for distinction from the previously discussed PNIPAm hydrogel particles embedded in membranes, and to avoid confusion with other particles discussed, are made of 3D polymer chain networks. As with the PNIPAm used in membranes and microfluidic valves, these microdroplets are swollen with an aqueous solution (such as water and a known concentration of aqueous drug) when their temperature is below the LCST. Above the LCST, the microdroplets shrink in size while expelling the solvent [148-150], and the LCST can be tuned by the copolymer molar ratio composition or the molecular weight of the PNIPAm hydrogel [151, 152].

The first ever reported PNIPAm hydrogel was in the form of micro-sized particles, developed in 1986 by Pelton *et al* [153]. These microdroplets were made of two moieties,

namely isopropyl hydrophobic groups and amide hydrophilic groups, the combination of which determines the phase transition phenomena with change in temperature. The balance between the two types of moieties is such that, when the PNIPAm is below the LCST, the hydrophilic amide groups undergo hydrogen bonding with proximate water molecules, resulting in the swelling of the PNIPAm structure, while above the LCST, hydrogen bonding is severed, PNIPAm becomes poorly soluble in the water molecules, and the latter are expelled from the structure [75]. Due to the high tunability of PNIPAm in water, its applications as a biocompatible material [154], and the simplicity of its synthesis, it has become one of the most applied hydrogels in medical solutions and drug delivery applications requiring customizable controlled delivery. The LCST of PNIPAm can be tuned with the addition of co-monomers to be used in the synthesis of the PNIPAm hydrogel [155].

Methods for synthesizing PNIPAm droplets at the micron and sub-micrometer scale with incorporated magnetic iron oxide nanoparticles have been reported [156-158]. First, Ding *et al* [156] used a dispersion copolymerization method to synthesize PNIPAm microparticles incorporated with iron oxide nanoparticles, and the effects that the synthesis parameters had on the formation of the PNIPAm structures, inhomogeneous in size, were studied. Next, Sauzedde *et al* [157] synthesized PNIPAm microparticles incorporated with iron oxide nanoparticles via a two stage process; an absorption step which allowed the iron oxide to diffuse into a synthesized PNIPAm hydrogel, followed by a polymerization process that generated PNIPAm microparticles containing up to 30 %w/w of iron oxide. And finally, Purushotham *et al* [158] achieved drug release from PNIPAm microparticles synthesized with iron oxide nanoparticles using a two-step co-precipitation method. By exposing the spheres to a magnetic field of 50 mT, 375 kHz, for 50 min, the PNIPAm was capable of releasing approximately 15% of its loaded aqueous drug solution.

In this research, PNIPAm microdroplets are synthesized with magnetic iron oxide nanoparticles on the one hand, and iron nanowires (NWs) on the other, for comparison and in the effort of achieving magnetically controlled drug release, using much lower power than previously reported. The mechanism for heat generation is discussed in section 1.4.

1.3.4 Thermoresponsive Microvalves

Magnetically controlled PNIPAm-based valves allow for thermal control of drug release, while being triggered remotely or by a physiologically apparent temperature change.

Previous work includes PNIPAm grafting on microfluidic capillary for the control of fluid flow [140], and PNIPAm monoliths used as valve plugs for magnetically triggered flow control [152]. Compared to aforementioned approaches, this is the simplest form of external, remote actuation of a microvalve, as reported by Ghosh et al. [152], relying on the use of magnetism as a stimuli. In their work, they prepared ferromagnetic nanoparticles encapsulated in PNIPAm, polymerized within 300μm and 1500μm diameter tubes. By applying an AC magnetic field ranging from 20 to 125Oe, at 100-1000 kHz, heat was induced in the particles, thus heating the PNIPAm, causing it to shrink and the valves to open. Flow rates were measured for various valve shapes and temperatures of PNIPAm under inductive heating.

Applying similar design principles to our drug delivery systems makes sense, due to the reliably and remotely triggerable nature of the robust PNIPAm-microvalve-magnetic material combination, the potentially transportable nature of a magnetic source for triggering the device, the possible field strengths that can be achieved within the human body at the device location, and, most importantly, the rapid reported swelling/deswelling response times of PNIPAm valves.

To prevent drug diffusion and flow from a device outlet to the patient, while the electrolytic pump used in this research is not in operation, a PNIPAm thermoresponsive polymer-based valve is integrated into the system, sealing the outlet during the device off-state, after the required solid drug reservoir refill, while opening the outlet channel with the application of an external magnetic field. This is of particular importance in treatments using highly potent and highly concentrated drugs and drug solutions, in which excess dosing may lead to harmful side-effects and health risks. While previously reported PNIPAm valves loaded with superparamagnetic iron oxide nanoparticles are triggered by inductive heating using a high frequency magnetic field, they demonstrate the valves' capacity for remote control and resistance to pressure that is higher than that produced by the electrolytic pump used in this research [152]. The thermoresponsive hydrogel polymer reacts to temperature changes by expelling water molecules and shrinking in volume when above its LCST, allowing for fluid flow in the microchannel it occupies. Below LCST, the process is reversed, water is reabsorbed from the polymer surroundings and into the polymer network chains, and the microchannel in which it resides is sealed.

1.4 Magnetically-Induced Heating for Drug Delivery Applications

1.4.1 Introduction to Magnetism

Prior to the discussion of the properties and applications of magnetic nanoparticles and NWs used in this research, we review the general principles of magnetism. A magnetic flux density **B**, produced by an electric current, has an effect on the total force **F** on a moving charge q with velocity vector ***v*** inside an electric field **E,** in the Lorentz force law

$$F = qE + q\boldsymbol{v} \times \boldsymbol{B}. \tag{1-4}$$

When a current-generated **B** field, measured in Tesla [T] or Oersted [Oe] (1mT = 10 Oe), originated outside a magnetic material and passes through the material, which itself contributes an internal magnetic field (demagnetizing field) when magnetized, there must be a differentiation between the part of the field that originates from an external current, and the part which is a contribution from the material itself. To do so, the magnetic field strength **H** (amperes per meter, [A/m]) is defined, allowing for a differentiation between a driving magnetic influence from external currents on a material (from **B**), and the material's internal magnetic response, or magnetization, **M**. Furthermore, the definition of a magnetic field strength **H** allows for the discussion of the field originating outside a material in free space, passing through the material, and taking into account the resulting change in the magnetic behavior of the material, including a change in its **M** and potentially in its magnetic permeability (a measure of a material's ability to form an internal magnetic field). **B** also changes depending on the medium it passes through. This, along with the definition of **H**, is seen in Eqn. (1-5) which relates **B**, **H**, and **M** with magnetic permeability, namely the magnetic permeability of free space vacuum μ_0

$$B = \mu_0(H + M). \tag{1-5}$$

This equation and the following are illustrated in Figure 1.7. As can be seen, **H**, can be used to describe **B**, when combined with **M**, as **H** and **M** permeate free space. Furthermore, the magnetic susceptibility χ_m (dimensionless) specifies how a material responds to an applied field by relating **M** to **H**, and is itself a material dependent term

$$M = \chi_m H. \tag{1-6}$$

The permeability of a specific material, μ (inductance per length, [H/m]), is a measure of its ability to form a magnetic field inside itself, and is therefore a degree of magnetization

obtained when responding to an externally applied magnetic field. Typically materials are described by their relative permeability (relative to free space), defined as $\mu_r = \mu/\mu_0$. For a field applied to an isotropic material, μ is a scalar and the relationship for **B** and **H** is as follows

$$B = \mu H. \tag{1-7}$$

Therefore, **H** field can be used to describe **B** (i) using only the total magnetic permeability of a material and all the space enclosed within it (μ), or (ii) using the permeability of free space (μ_0) while in combination with the magnetization of the material **M**, also essentially existing in free space. The former approach contains information about **M** within μ, as $\mu_r = \chi_m + 1$ by definition, and as discussed $\mu_r = \mu/\mu_0$.

Inside a magnetic material, there is a demagnetizing field $\mathbf{H}_d$, shown in Figure 1.7 for a magnetic material within an externally applied field, and in Figure 1.8 for a standalone permanent magnet, that tends to demagnetize the material while pointing in the opposite direction of **B** and **H**.

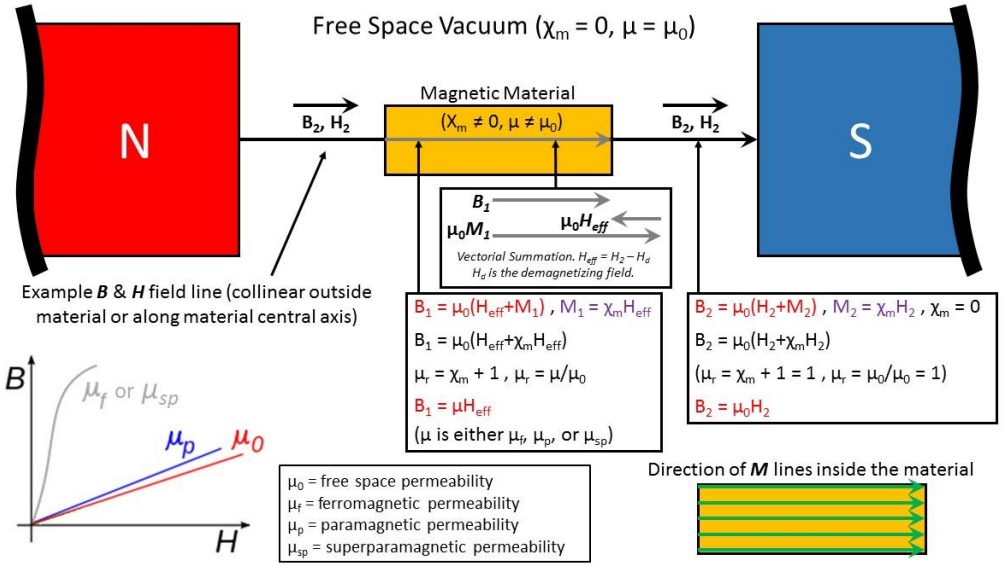

Figure 1.7 Illustration of the relationship between magnetic field strength H, magnetic flux density B, and a material's internal magnetization M when placed in free space and an externally applied magnetic field.

At the exact center of the material, it points in the exact opposite direction of **B** and **H**. The importance and effects of $\mathbf{H}_d$ on magnetization are discussed in more detail in section 1.4.3.

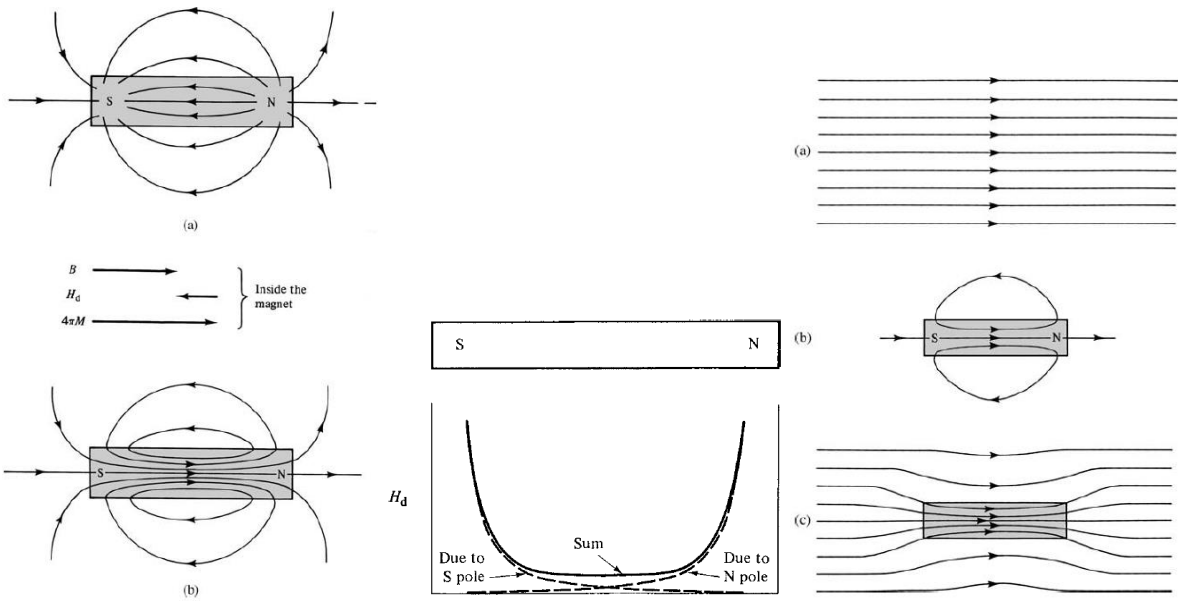

Figure 1.8 (Left) (a) H field and (b) B field of a permanent magnet, the vectors detail magnitude and direction of B, H_d, and M (cgs units) at the center of the material (where H_d is minimized). (Middle) Variation of H_d with respect to the length of the material. (Right) (c) Effect of placing (b) a magnetized bar in (a) a uniform field. Figures reprinted with permission from John Wiley and Sons, 2008 [159].

A magnetic hysteresis loop can graph the magnetic response of a material under an applied external magnetic field, as well as that of a permanent magnet, and differs according to material anisotropy terms, including magnetocrystalline, magnetoelastic, and shape anisotropy [160]. The x-axis corresponds to the applied magnetic field strength **H**, while the y-axis corresponds to the material-dependent **B**, **M**, or **M/M$_s$** (magnetization normalized with respect to saturation magnetization M_s), as shown in Figure 1.9. In general, the overall global magnetic response of a material can be categorized as, among others, (i) paramagnetic, where $\mu_r \geq 1$, because the induced magnetic field in the material is in the direction of the external field, permitting or promoting permeation of the field through the material, and (ii) ferromagnetic, where $\mu_r >> 1$, because the magnetic field response in the material is even more pronounced than that of paramagnetic materials, to the extent that it can be sustained even after the removal of the external field, in the form of the internally induced regions of permanent uniform magnetic alignment, or magnetic domains (Figure 1.7, Figure 1.8). These are the two magnetic responses that this research relies on, a complete coverage of magnetic responses is found elsewhere [159]. Inside a magnetized material, the **B** and **H** fields are quite different, and **H** is in the opposite direction of **B** and of **M** (this internal **H** is defined

above as $\mathbf{H_d}$, see Figure 1.7 and Figure 1.8**)**. Ferromagnetic materials are limited to iron, cobalt, nickel, their alloys, and some rare earth metals. Each possible overall response discussed will affect the shape of the hysteresis loop of a material.

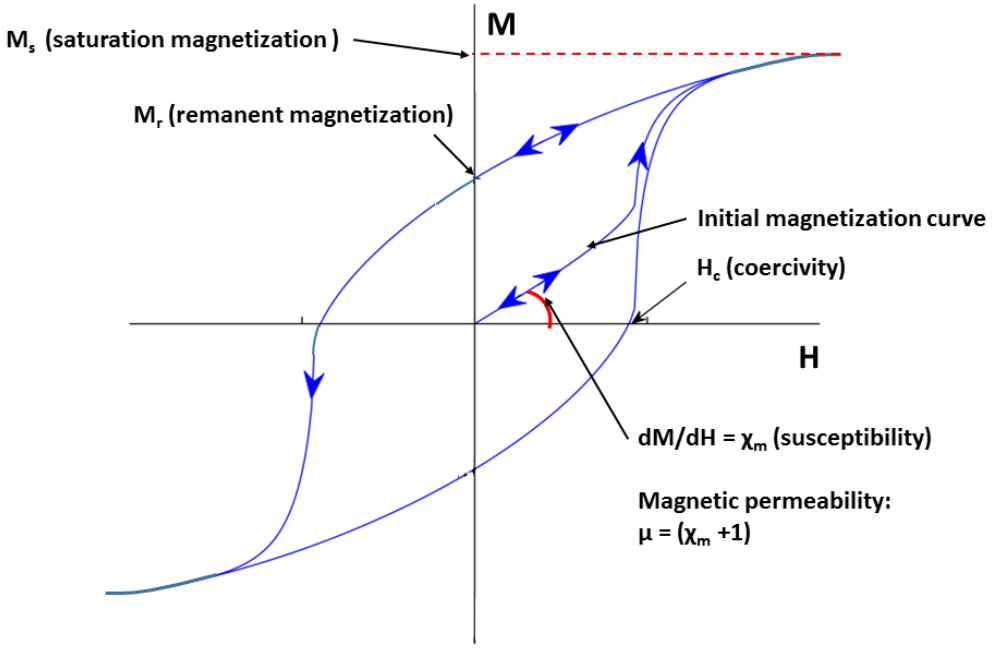

Figure 1.9 Example of a magnetization hysteresis loop depicting magnetic saturation, remanence, coercivity, and susceptibility.

The application of an external magnetic field of strength **H** induces atomic dipole alignment within a magnetic material such as ferromagnetic iron. Iron retains this magnetization **M** after the removal of the magnetic field by maintaining the atomic dipole alignment. When the magnetic field is removed after the material has reached its magnetic saturation asymptote, M is now offset from the origin in an M vs H curve and the associated value is referred to as the material's remanence or remanent magnetization (M_r, stable magnetization value when external magnetic field is removed, Figure 1.9). Any application of a magnetic field in one direction until saturation is reached, followed by an application of the field in the opposite direction until saturation, will result in a hysteresis loop, the curve in and M vs H plot, that is formed by the two magnetization paths followed. This loop is the main loop, while other smaller loops can be formed by applying the field using reduced strengths that do not magnetically saturate the material. For the main loop, the value of H when M is zero is called the coercivity of the material (H_c, magnetic field value required to

return from saturation back to zero magnetization, Figure 1.9). After the removal of an applied field, the material remains magnetized unless a demagnetization process is used to bring the material back to zero magnetization (M = H = zero) through a series of applied and successively reduced magnetic field strengths, in reversing directions, that bring the magnetization hysteresis curve closer and closer to the origin in an M vs H plot.

From a measured hysteresis loop of a material, we can obtain properties such as saturation magnetization M_s (maximum magnetization value at which all magnetic dipoles align with external magnetic field), remanent magnetization M_r, coercivity H_c, and loop-squareness ratio, LSR (defined as M_r/M_s). The closer the hysteresis loop is to a square shape (such as when M_r and M_s are close in value), the closer LSR is to unity, while the further it is, the closer LSR is to zero.

The aforementioned types of anisotropy energy manifest themselves in every magnetic material to a certain extent, and can generate what is known as a magnetic easy-axis in a material. A magnetic easy-axis is a direction in a magnetically anisotropic material that is energetically favorable for spontaneous magnetization; this is in contrast to magnetically isotropic materials that have no directional preference for magnetic moment when under no applied field [160]. Magnetocrystalline anisotropy occurs when a material's crystallographic directions have aligned components with the magnetic easy-axis of a material. In other words, if the crystal lattice structure of the material induces directions in which the energy required to magnetize the material are unequal, some directions will be energetically and magnetically preferred (hence the term "easy-axis"). Magnetoelastic anisotropy occurs when there is elastic strain and tensions in the material's lattice structure. Here, the easy-axis is the direction of magnetization that minimizes the strain energy of this term. When a mechanical stress is applied, for example, the positions of the atoms in the structure will move, affecting the magnetic domains and the interaction between the magnetic domains, thus changing the material's ability to hold a magnetic moment in a given direction. And finally, shape anisotropy can occur when one dimension is particularly larger than the rest, such as with high aspect ratio NWs, whose easy-axis is typically in the direction of the NW length. This dimension imbalance results in a material's stray field (aka demagnetizing field) to act unevenly in space, causing the magnetic moment of domains to typically align with the direction of the large dimension. The overall magnetic behavior of a

material is determined by the combination of these energy terms, which will typically have one term that overcomes the rest and determines the general magnetic response, such as shape anisotropy in NWs [161], which renders the hysteresis loop square-shaped when measured with the applied field parallel to the NWs.

1.4.2 Magnetic Induction and Ferromagnetic Materials

This research applies principles of magnetic induction heating to generate losses in the form of heat from magnetic material, including ferromagnetic iron particles. Induction heating typically requires a high power source running at hundreds of kHz frequency and supplying several kW of power, which drives an alternating current though an air core coil (copper) that can be designed with varying diameters, number of coil turns, and coil heights. The power supply primarily produces a high current (on the order of several to tens of amps) at high frequency, and therefore circulating water cooling through both the power supply and the coil prevent the system from overheating and also from transferring bias heating to the experimental setup in research applications. Industrial applications typically use induction heating for the heat treatment of metals. The coil design and power supply determine the magnetic field amplitude, only the power supply determines the frequency.

When a magnetic material, like ferromagnetic iron, is placed in the magnetic field of such a system, heat is generated from the irreversible nonlinear hysteretic response of the material as it undergoes magnetization [160]. The path of the magnetization hysteresis curve is affected by the field characteristic, and the curve will always have an enclosed area for ferromagnetic materials. This enclosed area, which can be observed in the case of the iron material used in this research, is the energy loss generated in one cycle of magnetization of the material being measured or being used for heat generation.

Magnetic materials typically provide higher heating than conductive materials because the magnetization losses they generate are a combination of Joule heating (resistive heating which occurs in conductive materials as a result of field-induced Eddy currents) and the magnetization process itself (described in section 1.4.1). Materials with higher permeability provide more heat, and their magnetic properties are maintained while the material is below the Curie temperature. The Curie temperature of iron is 1043 K and its relative permeability μ/μ_0 is around 200,000 [160, 162], among the highest know for any material. Since the experiments conducted in this research do not reach such exceedingly

high temperatures, iron's high permeability can be utilized while remaining under the Curie temperature, making it a suitable choice for magnetic heating.

1.4.3 Magnetic properties of single domain nanoparticles and nanowires

The magnetic properties of nanomaterials and how they can be exploited strongly depend on the magnetic anisotropy energies discussed above. This section focuses on magnetocrystalline anisotropy and shape anisotropy, which apply to both single domain nanoparticles and NWs. This single domain state is possible below a critical diameter value (sub micrometer), at which it is energetically unfavorable to generate one or more domain walls for the existence of multiple magnetic domains within the material [163]. Under this condition, the magnetization of a single domain particle, or that of a superparamagnetic nanoparticle, is a single large magnetic moment, summed of the individual magnetic moments of the nanoparticle's atoms. Above this critical diameter, the energy of the system is minimized by the formation of multiple domains, within which magnetic moments of atoms are aligned. From micromagnetic simulations and experimental studies, magnetic NWs with diameters on the order of tens of nanometers have been shown to exhibit a single domain state at remanence [164], with **M** pointing in the direction of the NWs' length.

The total energy in a magnetic material, such as a nanoparticle or NWs, can be written as

$$E = E_{ex} + E_H + E_{EA} + E_{ca} + E_D, \quad (1\text{-}8)$$

where E_{ex} is the exchange energy (related to the interaction between spins of atoms), E_H is the Zeeman energy (magnetic potential energy given by externally induced magnetization), E_{EA} is the magnetoelastic energy, E_{ca} is the magnetocrystalline anisotropy energy, and E_D is the demagnetization energy (or magnetostatic energy), related to the shape of the material [163]. The two last terms make the total energy dependent on the angle of the magnetization **M** with respect to the crystal lattice, and with respect to the three dimensional axes of the material (shape dependency).

Iron and iron oxide, the materials used to fabricate the NWs and nanoparticles in this research, respectively, have a face-centered cubic (fcc) crystal structure. This structure gives rise to three crystalline easy axes, for which the magnetocrystalline anisotropy energy, E_{ca}, is given by [163]

$$E_{ca} = K_0 + K_1(\cos^2\theta_1\cos^2\theta_2 + \cos^2\theta_2\cos^2\theta_3 + \cos^2\theta_3\cos^2\theta_1) + K_2(\cos^2\theta_1\cos^2\theta_2\cos^2\theta_3) + \cdots \quad (1\text{-}9)$$

where the anisotropy energy constants K_0, K_1, K_2, are in J/m^3, and the angles $\boldsymbol{\theta_1}$, $\boldsymbol{\theta_2}$, and $\boldsymbol{\theta_3}$ are the angles between M and the three easy axes. These magnetocrystalline easy axes are in the <100> crystal directions, and the value of K_1 is 48000 J/m^3 for iron [163], while K_0 and K_2 can typically be ignored, as the former represents the difference in energy between the crystal orientations and is independent of angle, and the terms involving K_2 are small.

Moving up in scale (from particle crystal structure to particle geometry), the magnetization of a non-spherical magnetic material is easiest along its longest axis, and more difficult along its short axis, due to shape anisotropy. This shape anisotropy derives from the demagnetizing field inside a material, H_d (Figure 1.8), which tends to demagnetize the material, given by [163]

$$\boldsymbol{H_d} = -N_d\,\boldsymbol{M}, \quad (1\text{-}10)$$

where N_d is the demagnetizing factor, and depends on the shape of the material. Calculations for N_d can be made for ellipsoidal shapes, where the magnetization is uniform in the entire sample, and the associated demagnetization energy E_D [J/m^3] is given by

$$E_D = \frac{1}{2}\mu_0 N_d \boldsymbol{M_s^2}, \quad (1\text{-}11)$$

For an ellipsoid of a, b, and c semi axes, N_a, N_b, and N_c are the demagnetizing factors along the three axes, and are related by

$$N_a + N_b + N_c = 1, \quad (1\text{-}12)$$

For the case of a nanoparticle with a large aspect ratio R = c/a, a prolate spheroid can be used to approximate the associated demagnetization factors, which, for c > a = b, are given by [163]

$$N_a = N_b = \frac{R}{2(R^2-1)} \times \left[R - \frac{1}{2(R^2-1)^{1/2}} \times \ln\left(\frac{R+(R^2-1)^{1/2}}{R-(R^2-1)^{1/2}}\right)\right], \quad (1\text{-}13)$$

$$N_c = \frac{1}{R^2-1} \times \left[\frac{R}{2(R^2-1)^{1/2}} \times \ln\left(\frac{R+(R^2-1)^{1/2}}{R-(R^2-1)^{1/2}}\right) - 1\right], \quad (1\text{-}14)$$

For large values of c/a, the demagnetization factor is $N_a = 1/2$ along the hard axis (the a or b

semi-axes), and $N_c = 0$ along the easy axis (the c semi-axis), the axis parallel to a NW's length for example. This approximation holds for NWs with aspect ratios greater than 10 [163]. From Eqn. (1-10), this results in a non-zero value of $\mu_0 (1/4) M_s^2$ for E_D in the a and b semi-axes directions, and a value of zero in the c direction, making c the energetically favorable easy axis for magnetization. The shape anisotropy energy difference between the easy and hard axes is $K_u = \Delta E_D = E_{Da} - E_{Dc} = \mu_0 (1/4) M_s^2 - 0$, where K_u is known as the uniaxial shape anisotropy constant. Values of K_u may range from less than 1 kJ/m^3 to more than 20 MJ/m^3 [160]. For an iron NW, E_D can be calculated using $M_s = 1.71E6$ A/m, and is found to be 918633 J/m^3 (equivalent units to the calculation derived units of N/m^2), which is larger than the value of $K_1 = 48000$ J/m^3 discussed above, making shape anisotropy dominate over magnetocrystalline anisotropy in iron NWs.

1.4.3.1 Magnetization switching and the Stoner-Wohlfarth model

For a material to reach magnetic saturation M_s (Figure 1.9), a saturation field H_{sat} must be applied in order to overcome the anisotropy energy. For the case of high aspect ratio materials like NWs, it is a reasonable approximation to consider only the shape anisotropy and estimate the H_{sat} field using Eqn. (1-10) in both the easy and hard axis directions [163]. The work presented in Chapter 3 uses the vibration of NWs to generate heat within PNIPAM. The reason why single domain NWs vibrate is their high remanence magnetization M_r and large switching field H_s (not to be confused with saturation field H_{sat}) [164]. H_s is the field required to begin the reversal of the direction of magnetization of the domain in a particle, and because H_s is large in the case of NWs, the NWs presented here physically rotate and vibrate in their medium instead of undergoing a rotation of the direction of magnetization of its single domain. Because of the large value of M_r, the NWs experience a higher torque in the presence of a magnetic field.

For a sufficiently large viscosity (or solid) media and/or large enough field (i.e. greater than H_s), the magnetization **M** of a NW switches by first nucleating a vortex domain wall at the ends of the NWs followed by domain wall motion along the NW. Only in the theoretical case of an exactly 90° angle between the applied magnetic field **H** and the length of the NW, will the NW's single domain undergo coherent rotation of **M**. Simulations and summaries of the magnetization reversal process in single domain magnetic NWs can be

found in the work by Ivanov et al [164].

Briefly, for perfectly cylindrical NWs approximated as spheroid shaped, or for spheroid particles, the Stoner-Wohlfarth model for coherent rotation describes the change in **M** with respect to **H** for single domain ferromagnets, considering only the demagnetization energy E_D and the Zeeman energy E_H

$$E_H = -\boldsymbol{M} \cdot \boldsymbol{H}, \tag{1-15}$$

in the total energy of a particle E, such that

$$E = E_D + E_H, \tag{1-16}$$

The coherent rotation mode corresponds to a homogeneous rotation of the magnetization **M** in unison along the whole length of the NW. If the angle between the external field and the easy axis is θ_0, and the angle between the external field and the direction of magnetization **M** is θ, then E_D can be written as

$$E_D = K_u \sin^2(\theta - \theta_0), \tag{1-17}$$

And combining this with E_H gives

$$E = K_u \sin^2(\theta - \theta_0) - \boldsymbol{H} \cdot \boldsymbol{M}_s = K_u \sin^2(\theta - \theta_0) - HM_s \cos\theta, \tag{1-18}$$

When the derivative of E with respect to θ is zero, the total energy is minimized. By defining the reduced magnetization $m_h = M / M_s$, the reduced field $h = H/(2K_u/M_s)$, from Eqn. (1-18) $M = M_s \cos\theta$, and finally applying trigonometric identities to the derivative of E, the following equation is acquired [163],

$$\tan^3(\theta_0 - \theta_s) = -\tan\theta_0, \tag{1-19}$$

When the applied field is closer to the easy axis, this corresponds to $0° < \theta_0 < 45°$, and when the applied field is closer to the hard axis, this corresponds to $45° < \theta_0 < 90°$. Plots of m_h versus h for values of θ_0 (Figure 1.10) show that when the field is aligned with the easy axis ($\theta_0 = 0$), $H_s = H_c$, and the hysteresis loop has a very high LSR and is quite rectangular. As θ_0 increases, the shape of the loop shears and H_s become larger than H_c (e.g. at 80°).

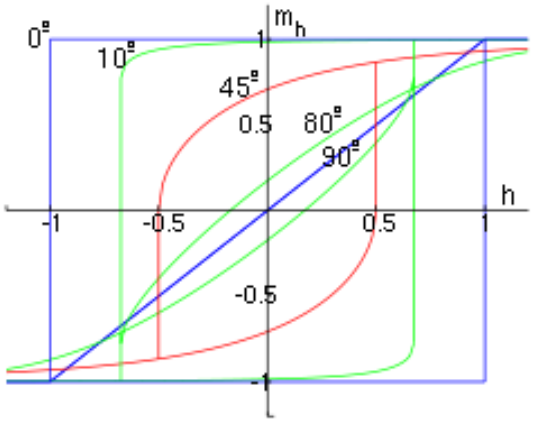

Figure 1.10 Examples of hysteresis loops predicted by Stoner–Wohlfarth model for angles θ_0 between the applied field and magnetic material's easy axis.

The Stoner-Wohlfarth model in its standard form, however, cannot be used to fully describe NW magnetization reversal, but can be used to describe the basics of magnetization reversal for single domain materials (e.g. the shape of the magnetization loop, H_s and H_c). Studies of individual NWs show that, as the angle between a NW's easy axis and the applied field changes, the magnetization curve remains rectangular in shape, and the switching field H_s and the coercive field H_c increase together and are approximately equal [165]. Furthermore, the sharp transitions between magnetization states indicate the single domain nature of the NWs [165].

As mentioned for NWs specifically, the magnetization switches by first nucleating a vortex domain wall at the ends of the nanowires followed by domain wall motion along the NW. Recall that the switching field H_s varies with the angle between the field and the NW; the closer to the hard axis (i.e. perpendicular to the NW), the larger H_s becomes [163, 165]. Also, practically speaking, as the angle tends to zero (i.e. closer to the easy-axis, parallel to the NW), H_s approaches the value of the coercivity or coercive field H_c [163]. These two points are true for an array of NWs parallel to each other. However, for individual, isolated NWs, with no magnetic dipole interactions between them, as the angle increases, the magnetization curve remains rectangular in shape and therefore H_s and H_c both increase and are the same [165]. This results in a square shaped loop for isolated NWs that maximizes the value of the remanent magnetization M_r and hence also the magnetic torque experienced by a NW in an applied field. As long as the applied field does not surpass H_s or H_c, which are equal in the case of isolated NWs (such as the low concentration NW-PNIPAm composite

used in this work), then the vortex domain wall motion, followed by transverse domain wall motion, will not initiate, and the power transferred from the applied field will primarily go into the vibration of the NW instead of changing its magnetization. Even in cases when the magnetization switches direction, a NW will vibrate, but to a lesser extent, and a repelling force becomes an attractive one, and vice versa, for a given orientation at the switching time.

1.4.4 Superparamagnetic Nanoparticles for Heat Generation

When exposed to a high frequency alternating magnetic field, superparamagnetic nanoparticles generate heat as a result of two magnetic mechanisms contributing to hysteresis, called Néel and Brownian relaxations [166-168]. The Néel relaxation mechanism relies on the reorientation of the material's internal magnetic moments, while the Brownian relaxation mechanism involves the reorientation of a suspended particle in its media.

Because superparamagnetic iron oxide has been studied extensively for its potential as a hyperthermia treatment solution, extensive work has been dedicated to explaining the magnetism involved in the heat generation such nanoparticles in a high frequency magnetic field, as discussed in subsequent sections.

1.4.4.1 Preparation of Superparamagnetic Nanoparticles

The iron oxide nanoparticles discussed in the following sections can be purchased as powders, suspensions, or composites with other polymers such as Dextran, forming nanobeads that are also typically stored in liquid suspensions [169] (Figure 1.11). Centrifuging or magnetic separation is used to isolate, manipulate, or wash the nanoparticles as necessary. Iron oxide nanoparticles can be prepared using a high-temperature organic-phase decomposition method [170], and are also separated from solutions by centrifuge or magnetic separation. This synthesis method allows for size tuning of particles, resulting in diameters between 3 and 20 nm, which is controlled by varying the concentration of oleic acid and oleylamine used in the decomposition into iron oxide, or the reaction temperature.

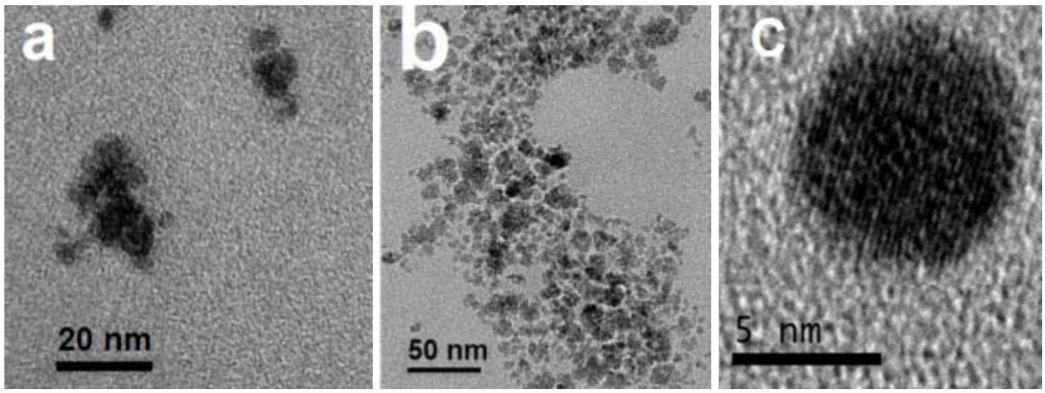

Figure 1.11 (a) TEM image of iron oxide nanoparticles, (b) cluster of iron oxide nanoparticles in solution, (c) individual sub-domain iron oxide nanoparticle. Figure reprinted with permission, © 2009 IEEE [169].

1.4.4.2 Introduction to Superparamagnetism

Superparamagnetic behavior can be observed in ferromagnetic nanoparticles that are of a single magnetic domain due to their size [160] (Figure 1.12a). This single domain and superparamagnetic state is possible below a critical diameter value, which typically falls between 3 nm and 50 nm depending on the material [160]. Under this condition, the magnetization of a superparamagnetic nanoparticle is a single large magnetic moment summed of the individual magnetic moments that the nanoparticle's atoms possess. However, above a critical diameter, a nanoparticle may still be single domain without being superparamagnetic (e.g. NWs) [163]. Superparamagnetic nanoparticles are ferromagnetic while under a blocking temperature T_B (Figure 1.12c), and superparamagnetic above this temperature. While above T_B, the magnetic moments of individual nanoparticles can rotate freely, and an agglomeration of them would act like a paramagnet. The value of T_B changes with change in volume V. Unlike the individual ferromagnetic state of the nanoparticles (below T_B), the paramagnetic agglomeration retains no magnetization when no magnetic field is applied. Based on the combined Néel-Brown theory, superparamagnetic nanoparticles do not interact with one another magnetically, and hence are only affected by temperature and applied magnetic field.

A single domain superparamagnetic nanoparticle exhibits magnetic anisotropy, having at least one easy-axis along which two stable magnetic moment orientations can lie. The two orientations, anti-parallel to each other, can flip when their energy barrier is overcome while above T_B. From Néel-Brown theory, an expression of τ_N, the Néel relaxation

time, and τ_0 (time constant that is characteristic of a material), describes the time between two flips, or reversals, of the magnetization direction of a nanoparticle above T_B.

$$\tau_N = \tau_0 e^{\left(\frac{KV}{k_B T}\right)}, \tag{1-20}$$

Here, k_B is the Boltzmann constant, T is the temperature, K is the magnetic anisotropy energy density, and V is the volume of nanoparticle. The product k_BT is the thermal energy of the nanoparticle, and the product of KV is the energy barrier (Figure 1.12b). It is clear that, as the size of a particle increases, V increases and heavily affects the value of τ_N, an exponential function of V, which would increase. Similarly, the higher the temperature T, the lower the value of τ_N, again with an exponential relation between the two. Therefore, smaller nanoparticles at higher temperature have shorter relaxation times. Brownian relaxation specifically is expressed as:

$$\tau_B = \frac{3\eta V_H}{k_B T}, \tag{1-21}$$

Here, η is the viscosity of the medium and V_H is the hydrodynamic volume of the nanoparticle. While Neel relaxation, τ_N, is associated with the reorientation of magnetic moments, Brownian relaxation, τ_B, is associated with the reorientation of the entire particles.

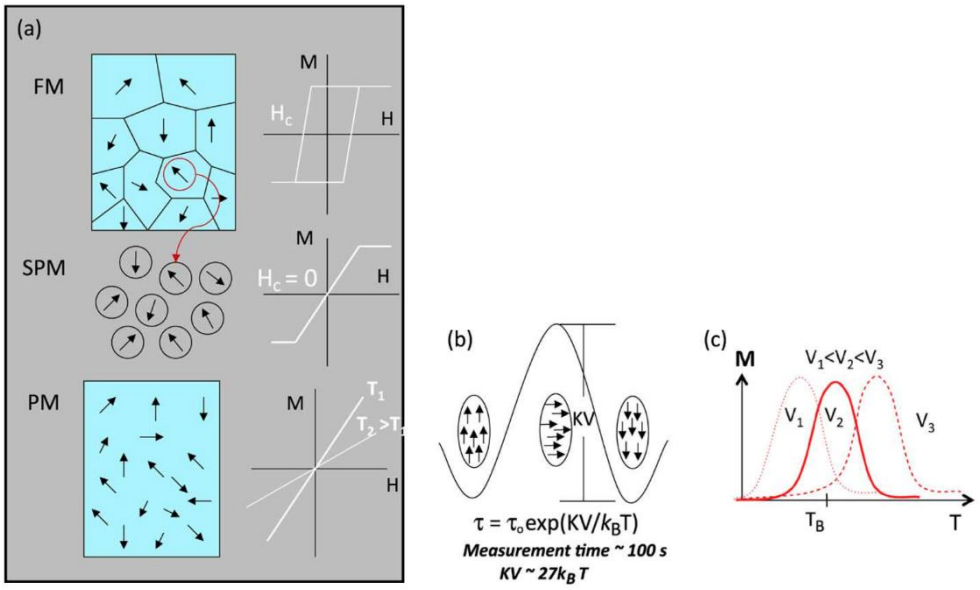

Figure 1.12 (a) Ferromagnetic material (FM) exhibit a single coercivity value and hysteretic behavior, if the FM size is reduced enough, to the point where thermal energy k_BT can randomize the magnetization orientation, resulting in a zero measured magnetization within a time interval that is typically 100 s, giving rise to superparamagnetic material (SPM), and paramagnetic material (PM) exhibits linear susceptibility that has an inverse dependence on temperature. These particles act as paramagnets with large moments and have no coercivity. (b) Randomization of the superparamagnetic particle's magnetization occurs with excitations that meet or exceed the energy barrier given by the product KV, or the magnetic anisotropy energy density times the volume of the particle. (c) Superparamagnetic nanoparticles are ferromagnetic while under a blocking temperature T_B, and superparamagnetic above this temperature. The value of T_B changes with change in volume V, as shown with V_1, V_2, and V_3. Figure reprinted with permission, © 2010 IEEE [171].

The volumetric power, P, depends on the change in internal energy of the particle, ΔU, and is time dependent because of the frequency of the field causing this change. The first law of thermodynamics states that $dU = \delta Q + \delta W$ for internal energy U, heat added to system Q, and work done to system W. For the adiabatic system containing the particle, $\delta Q = 0$, and the magnetic work is expressed as [168]:

$$\delta W = \boldsymbol{H} \cdot d\boldsymbol{B}, \tag{1-22}$$

resulting in

$$\delta U = \boldsymbol{H} \cdot d\boldsymbol{B}. \tag{1-23}$$

These last two fields are collinear, and therefore the expression can be reduced to magnitudes and becomes:

$$\delta U = H \cdot dB. \tag{1-24}$$

B = μ_0 (H+M), as discussed before in Eqn. (1-5). Combining B with the expression for dU from Eqn. (1-24), and integrating by parts, yields the expression for the cyclic internal energy change

$$\Delta U = -\mu_0 \oint M\, dH. \tag{1-25}$$

This result provides an integrable expression for P, where P = f ΔU, expressed using the real and imaginary parts of the complex susceptibility of the material: first, by expressing the magnetization in terms of the complex susceptibility χ and re-writing the applied magnetic field, H(t),

$$\chi = \chi_r - i\chi_i. \tag{1-26}$$

$$H(t) = H_0 \cos \omega t = Re[H_0 e^{i\omega t}], \tag{1-27}$$

where χ_r and χ_i are the real and imaginary components, then magnetization M(t) becomes

$$M(t) = Re\left[\chi H_0 e^{i\omega t}\right] = H_0(\chi_r \cos \omega t + \chi_i \sin \omega t), \tag{1-28}$$

and we can substitute H and M from Eqn. (1-28) into Eqn. (1-25), which yields

$$\Delta U = 2\mu_0 {H_0}^2 \chi_i \int_0^{2\pi/\omega} (\sin \omega t)^2\, dt, \tag{1-29}$$

This results in the energy generated via Néel and Brownian mechanisms, which dissipates from the superparamagnetic particles to their surroundings while exposed to each AC magnetic field cycle. P is proportional to the frequency, f, of the applied AC magnetic field, of magnitude H, and the internal energy of the particles, ΔU [168], and by multiplying both sides of Eqn. (1-29) by the cyclic frequency f = $\omega/2\pi$, we achieve:

$$P = f\Delta U = \pi\mu_0 \chi_i f H^2, \tag{1-30}$$

χ_i is the imaginary part of the material's complex susceptibility (AC susceptibility). The susceptibility is affected by the frequency of the magnetic field, as well as Néel and

Brownian relaxations [168]. The complete AC susceptibility of a material is expressed by a combination of the real, in-phase components, χ_r, and the above imaginary, out-of-phase, component, χ_i.

$$\chi_i = \chi \sin \varphi, \tag{1-31}$$

$$\chi_r = \chi \cos \varphi, \tag{1-32}$$

Here, φ is the phase shift caused by the lag angle between the direction of the applied AC field and the direction of the magnetization of a nanoparticle. This lag occurs when the frequency is no longer low enough to simply cause static magnetization behavior, and instead causes dynamic effects in the material. It is clear that when $\varphi = 0$, $\chi_m = \chi_r$ and $\chi_i = 0$, hence resulting in the susceptibility of the material having only the real component. However, this is not the case during the high frequency magnetization of superparamagnetic iron oxide nanoparticles. Because $\chi_i \neq 0$, and is a function of f, the shape of the hysteresis loop that the nanoparticles follow changes with increasing f, and the width of the loop widens (LSR heads towards unity). As the magnetization loop widens, the area enclosed in the loop (Figure 1.9) increases, and the power losses generated by the nanoparticles increase (area enclosed represents all magnetization losses). However, the full hysteresis curve is not used in practice due to the high field and power requirements for doing so, and instead smaller portions of the loop are used in applications such that comparatively much lower field strengths are required for heat generation [152]. In other words, applying lower fields results in the creation of minor loops (traced inside the major loop), which still enclose an area representing power generation.

1.4.4.3 Magnetic Nanoparticles in Thermoresponsive Systems

The incorporation of magnetic materials can add controllability to thermoresponsive systems with neither the need for physical connections nor line of sight. PNIPAm may be tailored for magnetic and remote controlled triggering through the incorporation of particles into the drug delivery system [15, 20, 87, 90, 91, 93, 109, 117]. In this manner, magnetic particles such as Fe_3O_4 can transfer power from an alternating magnetic field (AMF) into the system, providing thermal energy to the PNIPAm via Néel and Brownian relaxations. This transfer of heat induces a temperature change and shrinkage in the hydrogel. The shrinkage opens up

pathways through a permeable membrane matrix, increasing the flux of drug through it, as shown in Figure 1.6.

Iron oxide nanoparticles which are embedded in PNIPAm systems are considered biocompatible and therefore heavily used in biomedical applications [166, 172-181]. Heat generation from nanoparticles in a fluid medium not only relies on Néel relaxation, but also Brownian motion, which creates a lag between the applied magnetic field and the magnetization directions of the particles; this is caused by the particles' physical, random rotation.

Nanoparticles made of materials such as cobalt and iron have higher magnetization than iron oxide nanoparticles, allowing for a potentially larger power transfer through the material and from the magnetic field (which is measured as Specific Absorption Rate, discussed in Chapter 3 and Appendix B). However, such magnetic nanoparticle materials present concerns with regards to oxidation and toxicity, and must therefore have careful integration methods into drug delivery systems and devices, in order to avoid such issues, e.g. isolation, insulation, anti-oxidation treatment layers [182]. Due to these potential complications, the more widely used and approved iron oxide nanoparticles remain a major focus for heat generation in biomedical treatments.

1.4.5 Magnetic Nanowires for Remote-Controlled Heat and Motion

Magnetic NWs have been studied for their reactions and behavior in response to the application of magnetic fields, be it in the form of hysteresis losses or physical motion and rotation of the NWs in a medium. Such reactions to remotely applied magnetic fields have several applications in the fields of biological and chemical studies, as well as in biomedical research, some of which will be discussed in the following section.

1.4.5.1 Nanowires in Therapeutic and Thermal Applications

Non-magnetic NWs have been studied for their potential in photothermal therapy using Au based NWs [183-185]. Thermal characterization and enhanced thermoelectrics using NWs [186-189], as well as NW based heat pumps and engines converting temperature into useable work and enhancing thermal conduction via high surface tension forces of liquids have also been studied [190, 191].

Furthermore, the potential for tapping into magnetic NW-generated heat has been

pursued in hyperthermia related research for the inactivation of living cells [192], as well as more specific studies on the influence of morphology of iron NWs and iron nanoparticles on the heating efficiency of hyperthermia treatments [192, 193]. Iron oxide NWs were tested for their specific heating power using magnetic fields close to those typically used in medicine (100 kHz, 20 mT field) [194].

Macro-sized PNIPAm gels have been synthesized with micrometer scale iron and iron oxide particles to study the combined potential for drug delivery and hyperthermia applications (375 kHz, 1.7-2.5 kA/m or 2.1-3.1 mT) [195]. However, no work has been done to take advantage of magnetic NW manipulation. This approach is pursued in this research for the design of a more efficient PNIPAm microsphere-based drug delivery system, requiring low power and low frequency (20 kHz, 1 mT field) for drug delivery from locally and minimal-invasively implantable microsystems.

NWs made of Ni have been demonstrated as effective cell manipulators, separators, and purification agents [196-202], as well as in the delivery of macro size biological particle cargo [203]. Later, in addition to the hyperthermia applications discussed [192], NWs are used for inducing cell inflammation in embryonic cell cultures [204], and as apoptotic agents in cancer cells of the pancreas [205].

1.4.5.2 Nanowires in Translation and Vibration

NWs made of magnetic or non-magnetic metals have been developed for potential biomedical applications, among which are methods for cell manipulation and cell delivery [197, 206], bacteria capture and colloidal cargo transport in solution [207, 208], and cell cytoplasm mechanical characterization [209]. Furthermore, more in depth studies on the magnetic orientation, rotation, and alignment of magnetic NWs show potential for NEMS based biomedical applications using magnetic manipulations of NWs [210, 211]. Magnetic NWs have been shown to be able to induce cell death for cancer treatment through the physical agitation of NWs internalized in fibroblasts, with the application of low power external magnetic field [212].

For applications utilizing power transfer through mechanical motion of a nano material, as opposed to pure magnetic losses induced by an applied field, magnetic NWs provide an advantage over magnetic nanoparticles in the form of higher magnetic moments

per unit volume [197, 198]. Furthermore, the larger the NW length, the higher the total magnetic moment [207]; this increases the possibilities for generating high torques by changing NW lengths (limited by a given cell medium's volume and internalization process), while magnetic losses in nanoparticles cannot be tuned through the size and geometry of the nanoparticles. Superparamagnetic nanoparticles, as discussed above, must remain below a maximum size to retain the single domain state.

1.4.5.3 Modeling of Nanowire Vibration in Viscous Media

When a magnetic field is applied to a magnetized material at time t, the material experiences an instantaneous torque which causes it to rotate. If the field is applied in the same direction long enough, the material's magnetic moment will align with the field. However, the material can be made to vibrate in some medium, if the field direction or polarity is changing over time at some frequency f [210, 213].

Previously, Sun *et al* applied a model to explain the angular displacement of magnetic NWs of specific magnetic saturation M_s, density ρ, and geometry (radius r and length L) under an applied magnetic field **H** in an environment of viscosity η [210]. A geometric constant of approximately C= 0.15 for a single NW is typically used [213], and depends on the aspect ratio of a NW and the number of segments N of the wire being modelled (e.g. a solid NW rotating around its center only results in N=2, one segment for each side of the NW from its center). Here we use a simplified form for a uniaxially applied field:

$$\frac{d^2\theta_l(t)}{dt^2} + \frac{4\eta C}{r^2\rho}\frac{d\theta_l(t)}{dt} + \frac{12M_s\boldsymbol{H}}{\rho L^2}\sin\theta_l(t) = 0 \tag{1-33}$$

where $\theta_l(t)$ is defined to be the angle with respect to time between a NW and the applied magnetic field direction. The latter's direction does not change for the AC field used in the work reported here, only polarity and magnitude change (and therefore **H** is of the form $H\cdot\sin(2\pi f)$, where $2\pi f$ is the angular frequency of the uniaxially applied field). If, however, the applied field is not uniaxial, but rather rotates with an angular velocity ω_H around the sample, then the equation is of the following form originally reported, where the last term on the left hand side describes the contribution of the field's rotation:

$$\frac{d^2\theta_l(t)}{dt^2} + \frac{4\eta C}{r^2\rho}\frac{d\theta_l(t)}{dt} + \frac{12M_s\boldsymbol{H}}{\rho L^2}\sin\theta_l(t) - \frac{4\eta C}{r^2\rho}\omega_H = 0 \quad (1\text{-}34)$$

The behavior of a NW during the first and second half of one cycle of the uniaxial AC field is shown in Figure 1.13. Since the NWs used here are magnetically saturated prior to their integration with a drug delivery system (magnetic PNIPAm microdroplets, MPMs), the value of M_s represents the NW's magnetic state appropriately. When solving Eqn. (1-33) above, simplified for a single direction AC magnetic field, the total angle traveled by one NW in one AC magnetic field cycle can be determined. This total angle is the absolute value of double the angle traveled between a NW's start position and its position at half of an AC magnetic field cycle.

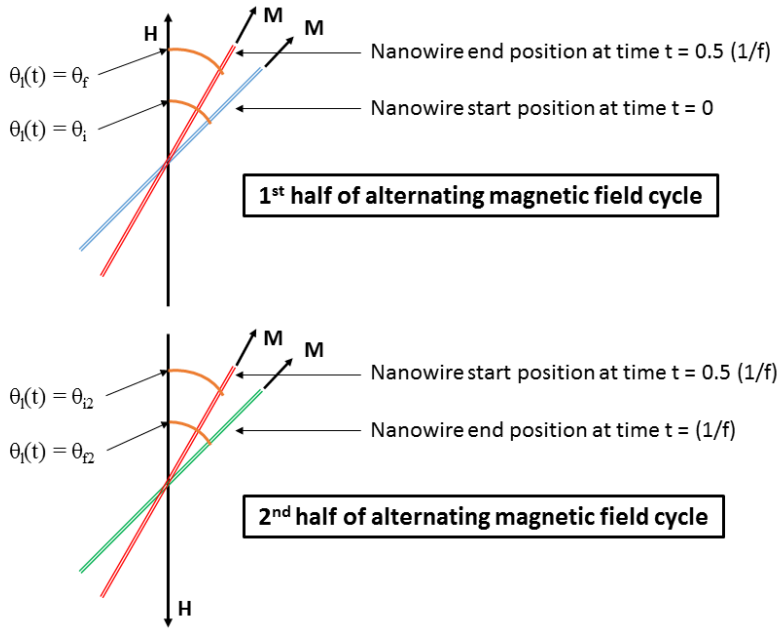

Figure 1.13 Schematic of the angular position $\theta_l(t)$ of a nanowire during the first and second half of an applied alternating magnetic field. M points in the direction of magnetization of the nanowire. The subscripts i and f, and i2 and f2, refer to the initial and final angles of θ_l at the start and end of the first half and the second half of the cycle shown, respectively.

An appropriate selection of a single NW's angle with respect to the field is required to properly represent the system of NWs being modeled. Fortunately, for randomly oriented NWs in a medium used in this study, it is simple to deduce that a single NW, regardless of orientation of magnetic polarity, will be somewhere between perpendicular and parallel to the field (i.e. 0º or 90º). Any NW parallel to the field will experience no magnetic torque,

while those perpendicular will experience the maximum torque possible. Therefore, it is assumed that the average NW in PNIPAm is oriented at a 45° angle at its start position.

The work input into the system containing a single NW during half a cycle is as follows, where V is the NW's volume, m·V is the NW magnetic moment (Am^2), m is the magnetic moment per unit volume, and θ_f is the final angle found from the above model results and θ_i is the start angle

$$W_1 = \int \tau \, d\theta = \int \boldsymbol{m}V \times \boldsymbol{H} \, d\theta = \int_{\theta_i}^{\theta_f} mVH \sin\theta \, d\theta = mVH \, (\cos\theta_f - \cos\theta_i). \quad (1\text{-}35)$$

The work in the second half of the cycle is equal to that of the first, therefore

$$W_{total} = W_1 + W_2 = 2 \cdot mVH \cdot \cos(\theta_f - \theta_i). \quad (1\text{-}36)$$

Work input into the system is converted into heat through friction from the kinetic motion of the NW surrounded by viscous PNIPAm. The power generated by a system of NWs is then determined by multiplying the total work in one cycle by the total number of NWs and the frequency of the magnetic field.

In the case of NWs in a fixed volume, such as the PNIPAm microdroplet reported in this research, such a model can be used to determine the power density in the volume (power per unit volume of the microdroplet). In this work, modelling of the vibration of NWs in PNIPAm is corroborated by comparing it to theoretical and experimental findings for the power density of SPIO filled PNIPAm microdroplets, (determined using well established equations for superparamagnetism).

1.4.5.3.1 Derivation of Equation of Motion of Nanowires in PNIPAm

In the rotational motion of a NW, the torques counteracting each other are that of the fluid drag and that of the magnetic moment, expressed as τ_D and τ_M respectively. I is the moment of inertia of a wire, while ρ, r and L are its density, radius and length. The angular acceleration is α_{NW} (derivative of angular velocity ω_{NW})

$$\tau_M - \tau_D = I\alpha_w(t), \quad (1\text{-}37)$$

$$I = \pi r^2 \rho L^3/12. \quad (1\text{-}38)$$

Below, M_s is the NW's magnetization at saturation, H is the amplitude of the applied magnetic field, C is the geometric factor based on r, L, the dynamic viscosity of the fluid η, and the number of segments N used to describe the portions on a wire that are rotating around a fixed midpoint in our case (N=2). We use C_1 and D to represent constant in order to clean up and simplify the appearance of the equations.

$$\tau_M = \boldsymbol{M}_s \times \boldsymbol{H} = M_s \pi r^2 HL \sin\theta_l, \tag{1-39}$$

$$\tau_D = \frac{1}{3}\omega_w \pi \eta L^3 C, \tag{1-40}$$

$$C = \frac{N^3 - N}{N^3\left[ln\left(\frac{L}{Nr}\right) + \frac{1}{2}\right]}, \tag{1-41}$$

$$I\alpha_w(t) = I\dot{\omega}_w(t) = I\ddot{\theta}_w(t) = M_s \pi r^2 HL \sin\theta_l - \frac{1}{3}\dot{\theta}_w \pi \eta L^3 C$$
$$= C_1(\sin\theta_l \, H \sin\omega_M t) - D(\dot{\theta}_w)$$

$$0 = -I\ddot{\theta}_w(t) + C_1(\sin\theta_l \, H \sin\omega_M t) - D(\dot{\theta}_w)$$

Here $\theta_l(t)$ is defined as the angle between the NW and the fixed magnetic field direction, and $\theta_w(t)$ the angle between the NW and its original position, and ω_M is the magnetic field angular velocity. C, C_1 and C_2 are unrelated to each other.

$$\dot{\theta}_w = \dot{\theta}_l$$

$$\ddot{\theta}_w = \ddot{\theta}_l$$

$$C_2 = C_1 H$$

$$\frac{C_2}{I} = \frac{HM_s \pi r^2 L}{\pi r^2 \rho L^3/12} = \frac{12HM_s}{\rho L^2}$$

$$\frac{D}{I} = \frac{\frac{1}{3}\pi \eta L^3 C}{\pi r^2 \rho L^3/12} = \frac{4\eta C}{\rho r^2}$$

$$I\ddot{\theta}_l + C_2(\sin\theta_l \sin\omega_M t) + D\left(\dot{\theta}_l\right) = 0$$

$$\frac{d^2\theta_l(t)}{dt^2} + \frac{D}{I}\frac{d\theta_l(t)}{dt} + \frac{C_2}{I}(\sin\omega_M t)(\sin\theta_l) = 0$$

or

$$\frac{d^2\theta_l(t)}{dt^2} + \frac{4\eta C}{r^2\rho}\frac{d\theta_l(t)}{dt} + \frac{12M_s\boldsymbol{H}}{\rho L^2}\sin\theta_l(t) = 0$$

In this form of Eqn. (1-33), one can solve for $\theta_l(t)$, which in the result using Matlab is a sinusoidal shaped graph.

1.4.5.4 Nanowire Fabrication

Typically, metallic NW fabrication consists of the electrodeposition of a metal or alloy into a porous insulation layer. Many methods have been used to date for the fabrication of NWs in such a manner, including electron beam lithography and nano imprint lithography, but the simplest and cheapest approach is the use of porous anodic aluminum oxide templates (AAO). AAO is a widely used approach for the growth of highly ordered nano pores, allowing for chemical control over diameter (from tens to hundreds of nanometers) and pore length, with a closely packed hexagonal arrangement [214-217].

The AAO templates are created using a two-step anodization process, carried out on high purity aluminum substrates. After the preparation of the templates, the desired conductive material is electrodeposited into the AAO pores. Typical metals used for their magnetic properties include Co, Ni, Fe, and alloys [161, 214-218].

Anodization consists of exposure of the metal to an electrolytic solution (oxalic, phosphoric or sulfuric acid), with a constant voltage and temperature to regulate the anodization (Figure 1.14). Chemical reactions form the AAO template, which grows into the metal substrate, while stirring removes bubbles generated at the surface of the AAO, bubbles that impede the process. The first anodization forms long hexagonally packed non-parallel pores in AAO. The further down the pore growth advances, the more ordered and aligned they become. Next, this AAO layer is dissolved, leaving behind hexagonally ordered indentations. The second anodization presents pore growth that preferentially starts at the indentations created in the previous step, and parallel aligned pores are generated for any desired length smaller than the aluminum substrate thickness. Figure 1.15 shows the summary of the NW fabrication process.

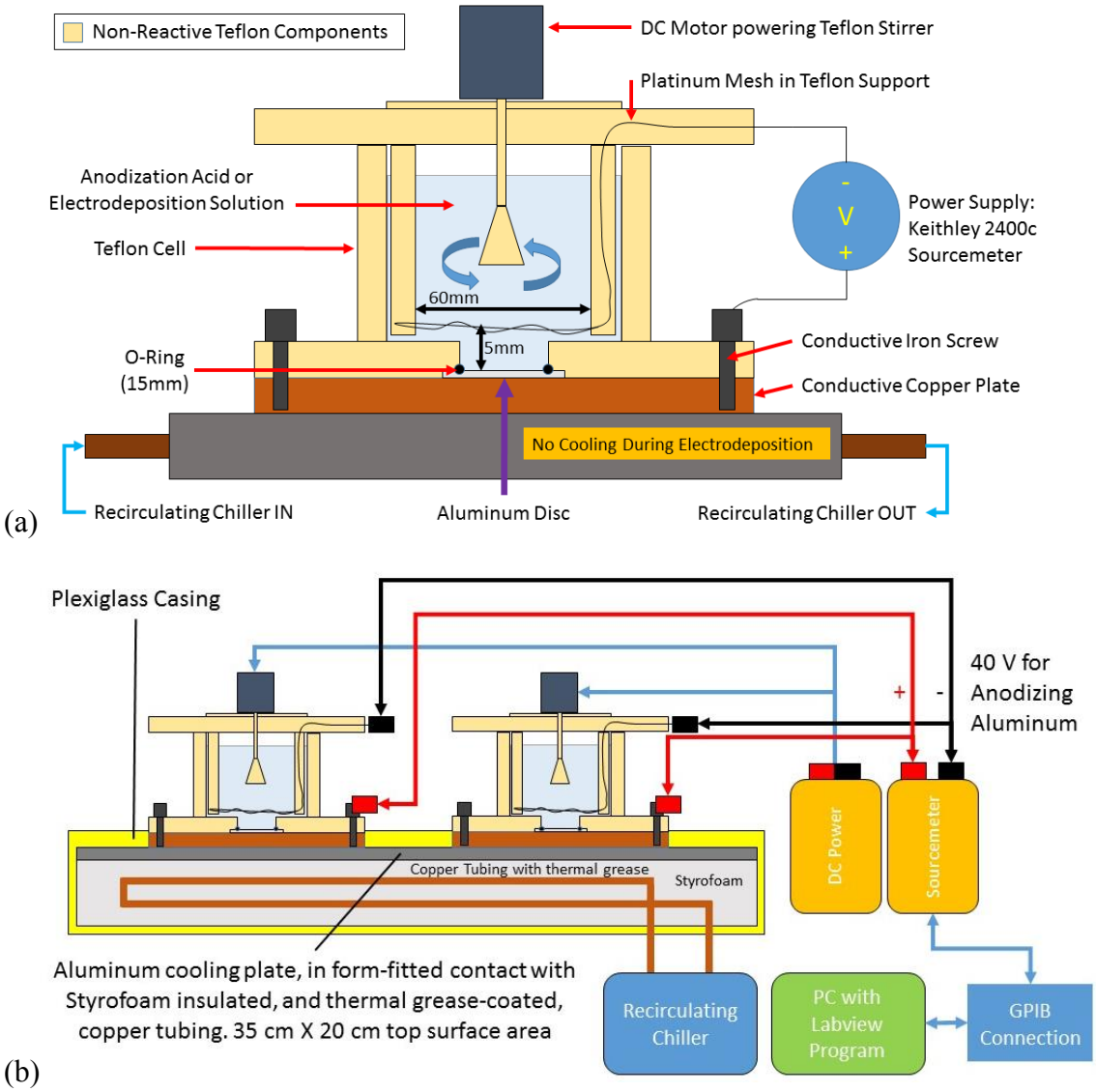

Figure 1.14 (a) Schematic of the anodization equipment used to create pores in aluminum which result in anodic aluminum oxide templates. The same setup is used for growing dendrites underneath each pore (openings, smaller than pore diameter, serving as an electrical links between electrodeposition solution when placed in pores, and bottom un-oxidized aluminum potion of the aluminum disc), and for electrodeposition into pores, replacing the acid with the desired electrodeposition solution (no cooling). (b) Model of anodization setup with devices and custom built equipment, showing here a parallel anodization of two aluminum substrates.

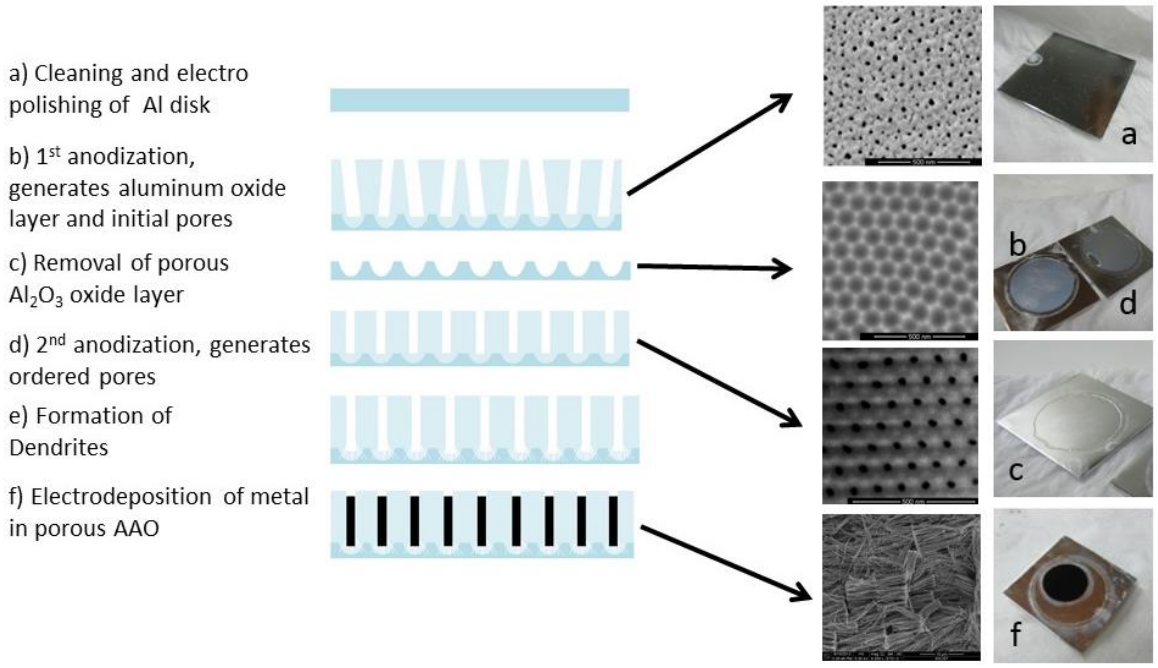

Figure 1.15 Summary of nanowire fabrication process steps (a) through (f). Scanning electron microscopy images are those of samples imaged during fabrication of iron nanowires.

For the first anodization step, the 24 hour anodization results in the ordering of pores of homogeneous diameters [214, 216, 217]. Longer times result in an increase in hexagonal array domain area, but also a decrease in pore diameter homogeneity [161]. Phosphoric acid (1 wt%, 0-1 ºC) at 195V results in an interpore distance of 105 nm, and a pore diameter of 180nm. Oxalic acid (0.3 M, 3-5 ºC) at 40V results in an interpore distance of 105 nm, and a pore diameter of 35 nm. Alternatively, sulfuric acid at 25V results in an interpore distance of 65nm, and a pore diameter of 25 nm for relatively smaller pores [161]. This work uses anodization processes relying on phosphoric and oxalic acid solutions.

The second anodization, which determines the pore length, will have a growth rate of 1µm/hr for 0.3M oxalic acid at 2°C and 40V [217], and 2µm/hr for 0.3M oxalic acid at 4°C and 40V [214, 216, 217]. Upon pore growth completion, dendrites are formed at the bottom of the pores of the oxide layer for electrical contact between electrodeposition solution and Al substrate, using the same experimental setup shown in Figure 1.14. The growth of dendrites consist of the reduction of the oxide barrier at the bottom of each pore, and is achieved by applying a step-wise exponential decaying voltage such that $V_{final}=V_{initial} \cdot e^{-t/\tau}$, where t is time, and where the start and end voltages, V_{final} and $V_{initial}$, as well as the time

constant τ, depend on the solution used (experimentally determined in the previously reported work). $V_{initial}$ and V_{final} when using oxalic acid is 40V to 4.5V, and using phosphoric acid is 195V to 75V. The resulting reduction of the oxide material and dendrite growth is more closely illustrated in Figure 1.16.

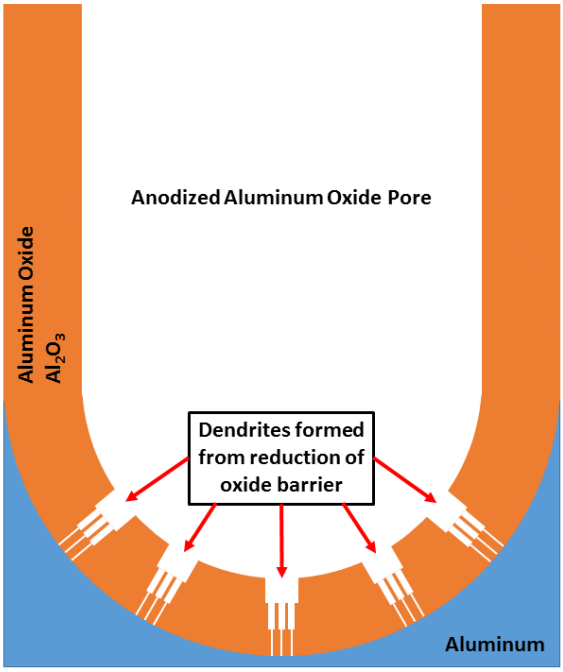

Figure 1.16 Illustration of dendrites grown at the bottom of each pore during the oxide barrier reduction process. The dendrites permit electrodeposition solutions in the pores to be in electrical contact with the aluminum portion at the bottom of the sample, which in turn is in electrical contact with the power supply.

During the final electrodeposition step in NW fabrication, the positive metal ions in the electrolytic solution are propelled towards the cathode-linked Al substrate, depositing at the bottom of the pores. This is achieved while maintaining uniform pore filling by applying a pulsed voltage-current profile to the sample [214, 216, 217], which maintains a balanced ion distribution in the solution, provides better control over the metal deposition, and prevents damage to the AAO membrane by rebuilding the pores [214, 216, 217, 219].

Alternatively to this pulsed electrodeposition process, a direct current deposition with a constant voltage can be used for faster NW growth rates and potentially more reliable deposition without failure when attempting to grow particularly long NWs (> 10 μm) [220-222]. By monitoring and controlling the acidity of the electrolytic solutions typically used in pulsed deposition, these solutions can be tailored to optimize the NW deposition quality

while minimizing the risks associated with higher deposition rates (e.g. inhomogeneous structure growth) when such solutions are used for direct current deposition.

1.5 Research Motivations and Objectives

Today's implantable and controllable drug delivery pump-based systems offer low power and low volume reservoir-based devices that are miniaturized with the goal of implantation in areas where conventionally scaled systems cannot be implanted [28]. These systems typically rely on actuators and valves driven by onboard power. Moving mechanical structures may contribute to problems of long-term reliability due to potential mechanical wear. Therefore, advancements in the form of drug delivery solutions that allow for remote magnetic powering of, and repeatable drug dosing from, battery-free and actuator-free systems, may improve the longevity and the efficiency of treatment delivery for a variety of medical conditions. Furthermore, such features can potentially have a large impact on the biotechnology market.

An ideal system should contain a large enough quantity of drug, be switchable between the on and off states, and be triggered remotely to release a controlled dose triggered by the user or the prescribing physician. Such a system would be optimal for the treatment of conditions such as chronic pain, diabetes, and cancer [223]. Many systems offer viable medical solutions that address several of these criteria. However, given the demand for such criteria, there remains potential for improvement in the development of drug delivery systems. One particular area of interest for improving existing technologies is adding the ability to dynamically modify drug dosing from an active device, depending on the patient's changing physiological requirements, and to do so remotely using solid state valving. Therefore, this work pursues magnetically triggered thermoresponsive polymer valving of a pump design based on osmotic pumps that excel at constant drug delivery [27, 43, 59]. A brief review of pump and reservoir based drug delivery systems have been tabulated in Table 1.1 for ease of reference and comparison with the work reported here.

Other delivery systems based on micro and nano-sized particles and vesicles, discussed above, can successfully deliver single burst dosing (e.g. rupturing of the polymer interface used as the flux trigger in a device reservoir or vesicle), or several dose bursts over a period of time. Usually such systems require high power (on the order of 10 mT and/or 100 kHz) to activate electromagnetically using the superparamagnetic effect of iron oxide [158,

224-227]. Therefore, an alternative composite polymer is pursued in this research, using trigger mechanisms based on the remote heating using magnetic NW vibrations in microparticles, for the repeated release of a drug. A brief review of micro and nano-sized particle-based drug delivery systems have been tabulated in Table 1.2 and Table 1.3 for ease of reference and comparison with the work reported here.

This research develops several approaches for remotely powered drug delivery, to be used with high-concentration drug solutions in some cases, targeting long-term treatments, while minimizing the aforementioned issues by focusing on the elimination of mechanical moving components and internal power sources, as well as a reduction of the required electromagnetic power supply. One of the approaches pursued is in the form of pumps regulated by a remotely controlled valve-membrane design based on a thermoresponsive polymer, while another entails the low power and remotely triggered release of a drug from potentially injectable microdroplets based on the same thermoresponsive polymer. Additionally, this work seeks to take advantage of the particular properties of high aspect ratio magnetic NWs as they apply to heat generation and triggering of drug release. Therefore, a study is pursued in which the material and geometry of NWs is varied, and their power transfer capabilities are measured.

The NW vibration triggered thermoresponsive microparticles are envisioned to replace the thermoresponsive nanoparticle polymer element in the remotely controlled valve-membrane design, potentially increasing power transfer and valve efficiency, thus permitting orders of magnitude of reduction of the power requirements for controlling the release of drugs driven by osmotic pumps, or any equivalent pressure sources.

Table 1.1 **Reservoir based and drug infusion pump based passive and active devices with highlighted features for comparison.**

Sub-category, applicable to set	Reference	Wireless Control	Valving	Valve Control	Cyclic Delivery/ Valving	Pump or Pressure Assisted/Driven	Release Type	Tested Drug/Compound	e.g. Disease/Treatment Area	Release Rates	Stimuli/Delivery Mechanism	Stimuli Intensity	Stimuli Transducer	Comments or Features
Reservoir-based drug-delivery devices														
Active and passive delivery, reservoir-based devices														
	Zaher, Li et al [228]	**Yes**	**Yes**	**Yes**	**Yes**	**Yes**	Continuous	Rhodamine-B (RhB)	Potential for chronic treatment, pain relief, emergency dosing	Order of 0.5-2 μg/hr for higher release rate designs, and 12–40 ng/hr for lower release rates	Thermoresponsive particles in magnetic membrane, AC magnetic field induced heating	62 mT 450 kHz magnetic field (variable)	Iron oxide nanoparticles in membrane matrix, NaCl (osmotic agent in pump)	Nanoporous magnetic membrane allows for pressure assisted delivery and magnetic porosity control
Passive diffusion-based reservoir devices														
	Desai et al [229]	No	No	No	No	No	Continuous	Transplanted pancreatic islet cells	Diabetes	100-150 μIU/mL in response to stimulatory (16.7 mM) glucose	Diffusion through nanoporous membrane	—	Glucose-responsive insulin	Nanoporous membrane protects islet cells from external antibodies
	Santini et al [30, 230]	No	No	No	No	No	Pulsatile	Lyophilized test drug	—	0-300 ng <1min	Electrochemical dissolution of membrane	1.04 V	Passage of a threshold level of electric current	Pulse per container
	Maloney et al [231]	No	No	No	No	No	Pulsatile	14C-labeled mannitol model drug	—	99% loaded drug in 4 hr (per reservoir)	Electrothermal degradation of membrane	0.31-1.4 A (for 80-95% membrane opening)	Passage of a threshold level of electric current	Individually sealed and actuated reservoirs
	Prescott et al [232]	**Yes**	No	No	No	No	Pulsatile	Polypeptide leuprolide in dogs (6 months)	—	7 ng/mL blood ~2.5hr (in vivo), 100% release ~10hr (vitro/ vivo)	Electrothermal degradation of membrane	Onboard battery	Passage of a threshold level of electric current	100 addressable 300 nL reservoirs
	Rahimi et al [147]	**Yes**	**Yes**	**Yes**	**Yes**	No	Pulsatile	Fluorescent dye	—	Dye release intensity of 290 (65kHz), 230 (20kHz)	Thermoresponsive polymer valve	~800 mW magnetic field, device resonance 10-100 MHz	Wireless resonant heater shrinks PNIPAm valve	Resonant frequencies of 10–100 MHz achieving ~40-% size reduction in PNIPAm
	Grayson et al [233]	No	No	No	No	No	Pulsatile	Dextran/heparin/growth/hormone/glucose/glycerol	—	100% loaded drug in ~60 days	Physicochemical dissolution of membrane	—	Biodegradable poly(L-lactic acid) or poly(lactide-co-glycolide) membrane seals	120-130 nL reservoirs with degradable caps differing in opening times
Active actuation-driven reservoir devices														
	Chung et al [234]	No	No	No	No	**Yes**	Pulsatile	Vasopressin	Hemorrhagic shock (not studied)	15 μL in 20s, single opening	Electrochemical dissolution of membrane and electrolytic pressure expulsion	5 mW (0.13 mW steady state)	Metal membrane dissolves	Only 37% of drug (15 μL) released, chemical degradation of drug during electrolysis observed
	Elman et al [235]	No	No	No	No	**Yes**	Pulsatile	Vasopressin	Cardiac resuscitation (not tested)	20 μL in 45s, single pulse	Resistive heating induced bubbles break membrane and then pumps solution	9 V (gives 650 mA)	Metal resistor boils liquid	85% of active drug recovered upon release, minimal thermal degradation
	Pirmoradi et al [236]	**Yes**	No	No	**Yes**	**Yes**	Pulsatile	Low solubility docetaxel (DTX)	Intraocular delivery for diabetic retinopathy	171 ± 16.7 ng per pulse (over 35 days)	DC deflection of magnetic membrane	255 mT DC magnetic field	Iron oxide nanoparticles in PDMS membrane	Background leakage of drug solution through the aperture was negligible at 0.053 +/- 0.014ng/min
Drug-infusion micropumps														
Passive micropumps														
Osmotic micropumps—	Su YC et al [70, 237]	No	No	No	No	**Yes**	Continuous	—	—	Slow, < 2 μL/hr from 2 mL volume	Osmotic pressure against deflecting membrane	—	NaCl (osmotic agent)	Stacked, planar arrangement of osmotic chamber, drug reservoir and delivery port
	Su YC et al [238]	No	No	No	No	**Yes**	Continuous	Bone morphogenetic proteins	Bone growth (maxillofacial distraction osteogenesis)	3.6 μL/day	Osmotic pressure against piston	—	NaCl (osmotic agent)	Larger cylindrical osmotic piston pump
	Ryu et al [239]	No	No	No	No	**Yes**	Continuous	Basic fibroblast growth factor (bFgF)	Tissue Regeneration	40 ng/day (for four weeks)	Osmotic pressure expels both drug and osmotic agent	—	Polyethylene glycol (osmotic agent)	Biodegradable pump design. Downside: drug and osmotic agent are in the same reservoir
Spring-powered micropumps—	Evans et al [240-242]	No	**Yes**	**Yes**	**Yes**	**Yes**	Continuous	—	—	0.51-2.30 mL/hr	Spring-loaded pressure on (electrostatic) valve	3-4 V DC	Metal springs	Multidrug capability of dual reservoir pump
Active micropumps														
Electrostatic micropumps—	Bourouina et al [243]	No	**Yes**	No	**Yes**	**Yes**	Pulsatile	—	—	0-1200 nL/min	Pressure from coulombic pulsing of plates	10 V DC	Oppositely charged plates	Single reciprocating diaphragm
	Teymoori et al [244]	No	**Yes**	**Yes**	**Yes**	**Yes**	Pulsatile	—	—	9.1 μL/min	Pressure from coulombic pulsing of plates	18-23 V, 50 Hz	Oppositely charged plates	Peristaltic pumping (multiple reciprocating diaphragms)
Piezoelectric micropumps—	Schneeberger et al [245]	No	**Yes**	No	**Yes**	**Yes**	Pulsatile	Insulin	Diabetes	60 μL/h (sum of cycles)	Electric field mechanically deforms material	_ (not reported)	Silicon piezoelectric actuator	Passive one way check valving controls flow
	Geipel et al [246]	No	**Yes**	**Yes**	**Yes**	**Yes**	Continuous	Antiangiogenic drugs	Cancer	10–1,000 μL/hr	Electric field mechanically deforms material	100-250 mW	Silicon piezoelectric actuator	Can preset voltage controlled stroke volume (10-200 nL)
Electrochemical micropumps—	Li PY et al [247, 248]	No	**Yes**	No	**Yes**	**Yes**	Pulsatile	Trypan blue solution (0.06%)	Ocular drug delivery	2.0 μL/min delivery when using 0.4 mW	Pressure on membrane from electrolysis	0.4 mW	Electrodes reversibly generate O2 and H gas from H2O	Low power consumption, large mechanical displacement, linear rel. to power (large range)
	Gensler et al [249]	No	**Yes**	No	**Yes**	**Yes**	Pulsatile	Local delivery gene therapy, RNA-targeting SPHK1 & Au nanorods	Cancer tumor	50 μL over 30 min, 1-34 uL/min	Pressure on membrane from electrolysis	~3mW	Electrodes reversibly generate O2 and H gas from H2O	Low power consumption, large mechanical displacement, linear rel. to power (large range)
	Sheybani et al [250-252]	**Yes**	No	No	**Yes**	**Yes**	Pulsatile	Cocaine	Drug addiction	~100 μL/min, 141.95 ± 0.46 μL/min (13mA)	Pressure on membrane from electrolysis	1.63–51.31 mW	Nafion-coated electrochemical actuators	Low power consumption, large mechanical displacement, linear rel. to power (large range)
Thermal micropumps—	Cooney and Towe [253]	No	No	No	**Yes**	**Yes**	Pulsatile	—	—	1.4 μL/min for 4.5 hr	Thermopneumatic liquid-vapor expansions	~200 mW	Perfluoro carbon	Downside: long thermal time constant limits response time, high power, battery
	Samel et al [254]	No	**Yes**	No	No	**Yes**	Pulsatile	NMDA-receptor antagonist	Visual attention and impulsivity	0.3 μL per packet	Thermooneumatic expansion of particles	~600 mW, expansion in 5 s	Expandable microspheres (XB) in PDMS	Single use pump, valve, battery. Intracerebral.

Table 1.2 Magnetic material-based micro and nano-sized particle drug carriers.

Reference	Magnetic material (MM)	MM concentration in composite	MM size(s) [nm]	Field strength [kA/m]	Field strength [mT]	Field frequency [kHz]	Composite size	Composite type	Composite SAR [W/g] (or power generation)	Composite SR	Magnetic Heating T max [°C]	Magnetic Heating T max time [min]	Magnetic Heating T start	Released drug or material	Initial drug concentration pre-loading	Initial % loading of drug in composite	Release %
Yassine, Zaher et al [under review]	Fe nanowires	2.54 %v/v in ~10 wt% PNIPAM solution	Length ~500nm Diam. ~45nm	~0.477-0.796	~0.6-1	20	~100µm	PNIPAM µparticle composite with Fe nanowires	52.5 kW/m^3 of Fe in PNIPAM, or 6.667 mW/g	~0.3 normalized	34	14	28	Rhodamine-B (RhB)	1 mg/mL	[3.5% loading efficiency]	~6% in 30 min with continuously applied field. ~70% in 200 min with pulsatile field application (both values are plateaued)
Purushotham et al [158]	gamma-Fe_2O_3 (maghemite) 25, 45, 58 emu/g	~6wt% PNIPAM in composite	14, 19, and **43** nm	1.7	2.14	375	–	Magnetic core - PNIPAM coating	22.4, 30.1, **42.8** W/g 10 mg/mL ferrofluid in PBS	–	41 (10 mg/mL Fe_2O_3 loading in water)	2	30	anti-cancer doxorubicin-(dox)	0.18 mg/ml	2.5 wt%	14.7% within 30 min heating and 17 min cooling (continuous field) or 0.001 mg/min 14.6% (37C), 14.9% (42C) in 45 min (direct heating)
Yao et al [226]	Fe_3O_4 (magnetite), 23 emu/g	15 wt% Fe_3O_4	10 nm	6.5	8.183	65	50 nm	Magnetic core - P(NIPAAm-co-Am) coating	–	–	41, 46 (15wt% Fe_3O_4 loading in water)	20, 60	27	Vitamin B-12	30 mg/ml	[65% drug loading efficiency]	50% in 1 hr (continuous field) 69% in 6 hr. ~45% in 1hr pulse #1 (pulsatile field). ~20% in 1hr pulse #2, ~10% in 1hr pulse #3. 2.5% (25C), 5.5% (37C), 49% (42C) in 1.5hr (direct heating). 19 (25C), 22.5% (37C), 65% (42C) in 24hr (direct heating).
Yang et al [225]	Zn0.8Mn0.2Fe2O4 (self-regulating with T_{Curie})	[particle cores are coated with PNIPAm]	62 nm	6.5	8.183	80	125 nm >LCST, 100 nm > LCST	Magnetic core P(NIPAAm-co-HMAAm)–Zn0.8Mn0.2Fe_2O_4	47 W/g of ferrite (in water)	–	44, 45 (10mg/mL ferrofluid in water)	06, 18	22	–	–	–	–
Liu et al [227]	$MnFe_2O_4$	"High" and "Low", Vol fraction is 0.04 (high 6nm), 0.02 (low 6nm), 0.24 (high 18nm), 0.12 (low 18nm)	6, 18 nm	4	5.036	435	~100 nm hydrodynamic size	MnFe2O4 loaded in PBMA-g-C12 amphiphilic copolymer	83 W/g (6nm) 580 W/g (18nm) 0.3 mg/mL in (1) water or (2) 5% agarose gel	–	35 (6 nm hi and lo), 45 C (18 nm lo) and 40 C (18 nm hi)	3.33 (800 sec)	32	–	–	–	–
Frimpong et al [255]	Fe_3O_4 (magnetite)	[particles are coated with PNIPAm-PEG400DMA]	~6-10 nm	–	–	–	290nm <LSCT (20C), 250~220> LCST (50C)	Magnetic core - PNIPAm-PEG400DMA coating	–	–	–	–	–	–	–	–	–
Regmi et al [256]	Fe_3O_4 (magnetite)	50 wt% composite particles	12 nm	10.345	13	380	270nm T<LCST, 225nm T>LCST, LCST is 311 K	Iron oxide loaded composite PNIPAM–SA–Fe_3O_4	–	–	50 (323 K)	4	25 (297 K, room temp.)	Mitoxantrone	1 mg/ml of mitoxantrone and 25 mg/ml of microgel	–	4% release in 4 min with T final 323 K average 0.010 mg/min (1%/min)

Table 1.3 Non-magnetic stimuli responsive particle drug carriers.

	Stimuli Transfer Material (STM)	STM concentration in composite	STM size(s) [nm]	Stimuli Type	Stimuli Frequency [kHz]	Stimuli Result	Composite size	Composite type	Composite SAR [W/g]	Temperature T max [C]	Temperature T max time [min]	Temperature T start	Released drug or material	Initial drug concentration pre-loading	Initial % loading in composite
Ma et al [18]	N/A	N/A	N/A	pH of 7.4, 5.0, 4.0	N/A	release of 5, 48, 67 % at 5 hours and 9, 60, and 80 % at 24 hours	100 nm	pH-responsive poly(acrylic acid) (PAA) with magnetic colloid nanocrystal cluster (MCNC) core (for MRI tracking)	N/A	37 °C	N/A	37 °C	doxorubicin (DOX)	5 mg of DOX were dispersed in 5 mL of deionized water and 5 mL of phosphate buffer (pH 7.4)	up to 44.6 wt %
Qi et al [257]	N/A	N/A	N/A	Glucose concentration	N/A	release of 55% loaded insulin in 400 min (28% in 100 min, 40% in 3 hr) in glucose solution	~6 μm	core-shell microcapsule of insulin particle coated with glucose oxidase and catalase	N/A	37 °C	N/A	37 °C	Insulin	N/A (core of insulin particle)	_
Mamada et al [258]	bis(4-(dimethylamino)phenyl)(4-~inylphenyl)methyl leucocyanide	N/A	N/A	Ultraviolet irradiation	N/A	Gels discontinuously swell and de-swell in response to irradiation when compared to swelling-deswelling without irradiation	1.73 millimeter	Copolymer gels of NIPA and the listed STM	N/A	N/A	N/A	N/A	N/A	N/A	N/A

1.6 Chapter Outline

This dissertation is comprised of four chapters. Chapter 1 presents the background to the drug delivery devices and systems used in this work, as well as the electromagnetism and thermoresponsive material chemistry required to understand the phenomena reported.

Chapter 2 discusses the design, simulation and testing of several variations of a drug delivery system with (1) remote magnetic triggering and no onboard power source requirements, (2) potential for further reduction in size for minimally invasive implantation (or microcapsule "injection"), (3) controlled activation to achieve higher delivery rates (for treatments that require it) or rates much lower than the state-of-art systems, in order to have no-refill requirements in long-term use with highly concentrated dosages. In order to achieve these goals, this chapter covers the investigation of osmotic pumping [70] combined with magnetically activated membrane valving. In the on-state, thermoresponsive PNIPAm based membranes are permeable to a drug (whose molecules are larger than those of water), while in the off-state, there is no drug release, or low drug release, depending on the treatment. Using this approach, release rates on the order of ng/hr to µg/hr are achieved and controlled magnetically. The system must meet biocompatibility requirements, and hence the selection of appropriate materials is taken into account.

Chapter 3 covers the magnetic triggering of PNIPAm microdroplets loaded with a test drug, heated by either iron oxide magnetic nanoparticles or iron NWs. These microdroplets are fabricated by two phase droplet generation, each solution containing chemicals which, when combined, polymerize into PNIPAm, hydrated by the water in both solutions. One of the two solutions contains a suspension of iron oxide nanoparticles or iron NWs. Both materials are compared for their viability as heating methods, and the low power requirements of the NW loaded microdroplets are explained. Options for continuous drug release and pulsatile drug release, depending on the nature of the applied magnetic field, are presented and further vary the option available for release profiling. Specific absorption rate studies are conducted on different magnetic materials for determining and comparing heat generation potential via magnetic losses, and the selection process is discussed.

Chapter 4 concludes the work presented in this dissertation and draws links between the findings and future work in the field of drug delivery systems.

Chapter 2 Magnetic Composite Membranes for Osmotic Drug Delivery

2.1 Synopsis

Implantable drug delivery systems can provide long-term reliability, controllability, and biocompatibility, and have been used in many applications, including cancer pain and non-malignant pain treatment. However, many of the available systems are limited to constant rate, inconsistent, or single burst event drug release. To address these potential limitations, we demonstrate several variations of a remotely operated drug delivery device that offers controllability of drug release profiles, using osmotic pumping as a pressure source and magnetically triggered membranes as a switchable on-demand valve. The membranes are made of EC or CA polymers mixed with thermosensitive Poly(N-isopropylacrylamide) hydrogel and superparamagnetic iron oxide (SPIO) particles. The prototype devices' drug delivery rates are on the order of 0.5-2 µg/hr for higher release rate designs, and 12–40 ng/hr for low release rates, with maximum on-off ratios of 4.19 and 3.15, respectively. The devices exhibit increased drug delivery rates with higher osmotic pumping rate or with magnetically-increased membrane porosity. Furthermore, a vapor deposition of biocompatible cyanoacrylate [259, 260] demonstrates a drastic reduction of the drug delivery rate from micrograms down to tens of nanograms per hour. By utilizing magnetic membranes as the valve-control mechanism, triggered remotely by means of induction heating, the demonstrated osmotic drug delivery devices benefit from having the power source external to the system to eliminate the need for a battery. These designs multiply the potential approaches towards increasing the on-demand controllability and customizability of drug delivery profiles in the field of implantable drug delivery systems, with the future possibility of remotely controlling the pressure source (at the inlet).

2.2 Methods

2.2.1 Device Design

The main design consists, from bottom to top, of (i) an osmotic pump that resides underneath (ii) a donor chamber containing the model drug, 1 mg/mL of Rhodamine-B (RhB), (iii) a magnetically triggered nanocomposite membrane separating the donor chamber from (iv) a receptor chamber containing pure water (Figure 2.1).

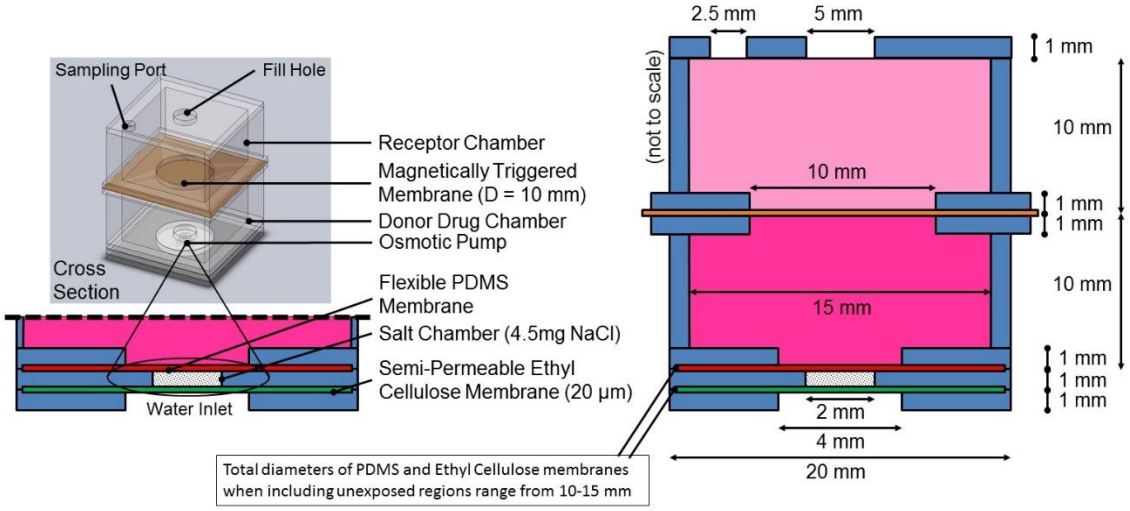

Figure 2.1 Schematic diagram of the drug delivery system with magnetic composite membrane and osmotic pump. The structural material is made of laser-etched and chloroform bonded PMMA stacks. Reprinted with permission from [228]. Copyright 2015, AIP Publishing LLC.

The osmotic pump contains NaCl salt and, when its water inlet is wetted, its volume expands with the influx of water against its flexible poly(dimethylsiloxane) (PDMS) membrane, pressurizing the donor solution towards the receptor. The water inlet membrane is made of pure EC, permeable to water and preventing the loss of undissolved NaCl. The nanocomposite membrane consists of either EC or CA as a matrix with embedded PNIPAM and superparamagnetic iron oxide (SPIO) particles. When an alternating magnetic field is applied, the SPIO particles generate heat via magnetic losses, which results in the shrinkage of the thermosensitive PNIPAM (Figure 2.2).

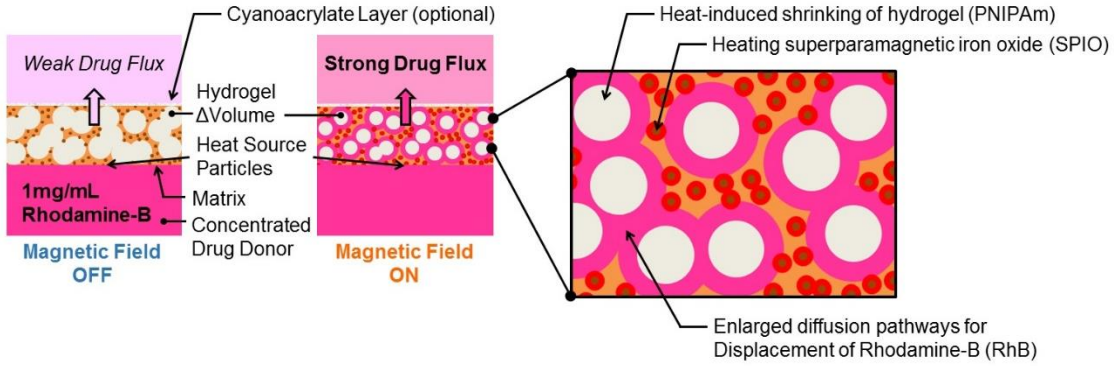

Figure 2.2 PNIPAm hydrogel undergoing swelling (left) and shrinking (right) before and after an AC magnetic field is applied. SPIO particles react to the AC magnetic field to generate heat and the shrinkage of PNIPAm hydrogel. This shrinkage induces the large flux shown. Reprinted with permission from [228]. Copyright 2015, AIP Publishing LLC.

This increase in porosity of the membrane allows for higher diffusion and flow rates of RhB, through the membrane and into the receptor chamber. A combination of increased porosity and osmotic pressure results in higher RhB dosing. The effect of a cyanoacrylate layer on top of the nanocomposite membrane (Figure 2.2) on the drug release is also studied to address the need for delivery rate reduction when applications depend on a small release of highly concentrated, high potency, drug solutions.

The main body is 20x20x26 mm and is made of six 1 mm and two 10 mm thick laser-etched and chloroform bonded PMMA substrates (Figure 2.1). Both the donor and receptor chambers have a volume of 2.3 ml to have enough solutions for spectrophotometric analysis. The 5 mm in diameter fill hole on top of the system is used to fill water into the receptor and the 2.5 mm in diameter sampling port is used to extract fluid samples for solution analysis. The donor chamber has two 1 mm fill holes drilled through one wall (one used for RhB intake, the other for air outflow) for accurate filling of the chamber with RhB and evacuation of air bubbles. The magnetically triggered nanocomposite membrane has an opening of 10 mm in diameter.

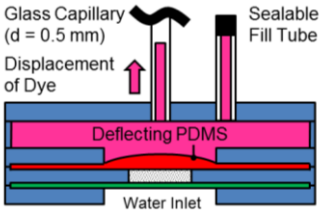

Figure 2.3 Test setup used to characterize the basic operations of the osmotic pump. The drug reservoir is filled using a sealable fill tube, and the initial height of dye in the glass capillary is recorded. After the activation of the osmotic pump, the height of the dye is recorded over time to calculate the pumped volume. Reprinted with permission from [228]. Copyright 2015, AIP Publishing LLC.

The osmotic pump, depicted in Figure 2.1, consists of three 1 mm thick layers of structural PMMA that hold a semi-permeable membrane made of 20 µm-thick EC underneath the salt chamber, which is 2 mm in diameter and 1 mm in height containing 4.5 mg of powdered NaCl, which is in turn underneath a 63 µm-thick PDMS membrane, separating the NaCl from the donor chamber. Figure 2.3 shows the schematic diagram of an assembled osmotic pump with the addition of a fill tube and a glass capillary of 0.5 mm in diameter attached to the donor drug reservoir for basic

characterization of the pump operations. The vertical displacement of the dye is measured over time and data is collected to determine the pump flow rates that occur before (priming phase) and during drug delivery operations. This assembly configuration (Figure 2.3) is not used during the complete drug delivery device (Figure 2.1) operation and characterization, and only serves to study the osmotic pump alone. A large osmotic gradient occurs between the semi-permeable membrane and the salt when the pump is wetted [43]. The osmotic chamber is filled with NaCl and water is continuously drawn through the semi-permeable membrane due to the concentration differences. The PDMS membrane is in direct contact with the RhB solution in the donor cell. When the pump is activated, the volume of the salt chamber expands and pushes against the donor cell solution by deflecting the PDMS, hence increasing the pumping pressure. When an AC magnetic field is applied to the device, the embedded SPIO particles within the nanocomposite membrane generate heat via magnetic losses (section 1.4.4) and cause the PNIPAm hydrogel in the CA matrix to shrink (Figure 2.2) for an increase of porosity and larger flow passage rates. An optional cyanoacrylate control layer is used to achieve a significant reduction of drug delivery rates when desirable. A combination of increased porosity and increased pressure in the donor cell (by applying both osmotic pumping and magnetic heating) results in higher dosage states.

2.2.2 Fabrication of the Osmotic Pump

A 20 µm-thick, semi-permeable membrane made solely of EC is cast on a glass slide using a micrometer adjustable film applicator (Sheen Instruments, Elektron Technology Group, Cambridge, UK). This material is selected for its ability to allow water permeation while preventing the loss of NaCl from the salt chamber. This membrane is then released in water and left to dry while compressed between filter paper sheets (>16 hr). A buffered oxide etch (BOE) and Piranha Etch treated silicon wafer is used to spin coat 63 µm-thick PDMS, from which membranes of approximately 10-15 mm in diameter are laser cut as the top deformable pump membrane. Adhesive (Loctite 401 glue) is used to ensure watertight sealing between osmotic NaCl chamber, donor, and exterior. The osmotic NaCl chamber is filled with finely powdered NaCl, and sealed from the pump's bottom with an adhered EC

membrane. The PMMA layer with a water intake hole of 4 mm in diameter at the bottom defines the intake opening of water inlet. When attached to the donor chamber, an additional PMMA-chloroform mixture is used to prevent possible leakages of the system. Upon evaporation of the chloroform content, the remaining structural material is composed only of PMMA.

2.2.3 Fabrication of Magnetic Nanocomposite Membranes

2.2.3.1 PNIPAm Hydrogels

The PNIPAm hydrogels are prepared by copolymerization [109] of N-isopropylacrylamide (NIPAm), N-isopropylmethacrylamide (NIPMAm) and acrylamide (AAm) by adding 300 ml DI water, 4 g NIPAm (35.5 mmol), 7.44 g NIPMAm (58.5 mmol), 0.5 g AAm (7.0 mmol), and 0.78 g bisacrylamide (BA, crosslinker, 5.6 mmol) at 40°C under continuous stirring and nitrogen purging. After 1 hr, the reaction is initiated by adding 1 g potassium persulfate and increasing the temperature to 70°C. The mixture is kept at this temperature for 12 hr to obtain a white suspension which is then allowed to cool at ambient conditions. To remove the unreacted monomers and small polymer molecules, this mixture is purified by dialysis in DI water for 2 days using 25kDa MWCO dialysis bag (filtration system used to separate out smaller particles from larger ones). White PNIPAm hydrogel powders are obtained by lyophilization (freeze drying of particles by subliming frozen water directly to vapor in a vacuum). The volume phase transition temperature of PNIPAm hydrogels is observed by monitoring the absorbance of PNIPAm aqueous suspension on UV/Vis spectrum (UV-Vis-NIR system, Cary 5000, Agilent, Santa Clara, CA, United States) under different temperatures. From 35°C to 50°C, the temperature is gradually increased by 1°C increments, and each temperature is held for 10 min before the absorbance at 500 nm (A_{500}) is recorded. The A_{500}-T curve is established to determine the transition temperature. The synthesis process is summarized in Figure 2.4.

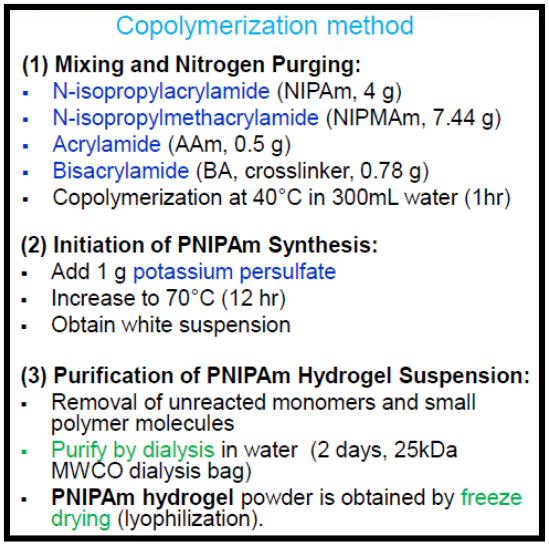

Figure 2.4 Summary of PNIPAm copolymerization method used to synthesize hydrogel.

2.2.3.2 Superparamagnetic Iron Oxide (SPIO) Nanoparticles

The synthesis of Fe_3O_4 SPIO particles is performed using a high-temperature organic-phase decomposition method [170, 261, 262], a method that produces highly uniform and monodisperse crystalline SPIO particles [255, 261, 262], and that the author and collaborators have the most experience with. $Fe(acac)_3$ (2 mmol), 1,2-hexadecanediol (10 mmol), oleic acid (6 mmol), oleylamine (6 mmol), and phenyl ether (20 mL, or 126 mmol) are mixed under nitrogen purging. The mixture is heated on a hot plate to 200°C for 2h and then to 300°C for another 1h. After the chemical reaction, the mixture is allowed to cool at ambient conditions, followed by precipitation in 40 mL of ethanol. To purify the resulting precipitate, the solution is dissolved into hexane with 0.05 mL (0.157 mmol) oleic acid and 0.05 mL (0.152 mmol) oleylamine, and then centrifuged at 4000 rpm for 15 min to remove any undispersed residue. The SPIO dispersion is precipitated again in ethanol and re-dispersed into hexane for storage or use. The synthesis process is summarized in Figure 2.5.

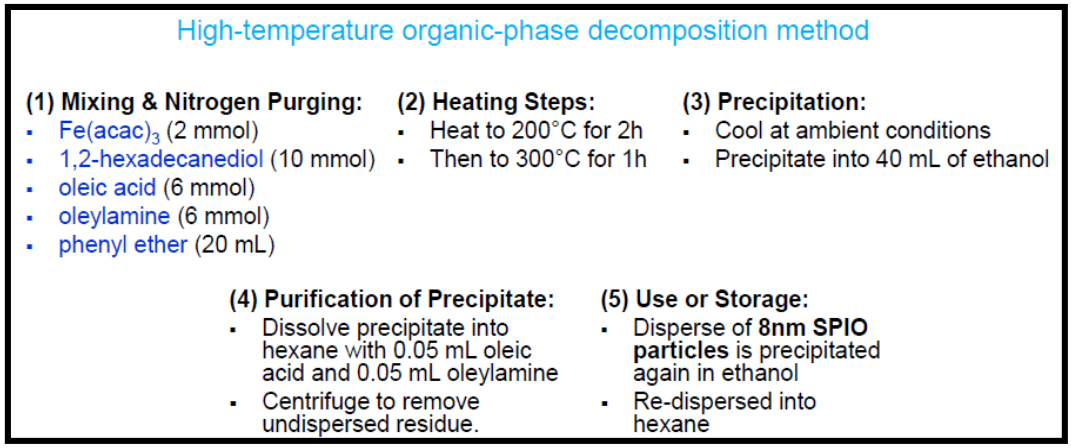

Figure 2.5 Summary of high-temperature organic-phase decomposition method used to synthesize superparamagnetic iron oxide nanoparticles.

2.2.3.3 Magnetic Nanocomposite Membranes

The nanocomposite membranes used in the prototype systems are based on either CA or EC as the porous matrices, with PNIPAm hydrogel and inter-dispersed SPIO particles. Membranes are fabricated for basic characterizations (by diffusion testing using direct heating), and for implementation in the drug delivery devices. These membranes have thicknesses between 16 μm and 21 μm after cast-set (by film applicator). The magnetic field amplitude and frequency are chosen as activation variables. It should be noted that inductive heating of single domain nanoparticles such as SPIO particles has been found to depend little on particle aggregation and heavily on particle size [263]. The composite membranes with base matrices of either EC or CA are fabricated by casting the mixture dispersion on glass slides. The EC-PNIPAm-SPIO membrane is fabricated by adding 1 g of 8 wt% of EC in ethanol with 40 mg of PNIPAm with stirring over 12 hr to homogenize the mixture. The SPIO dispersion (containing 75 mg SPIO) is precipitated in equal volume of ethanol and washed with ethanol before it is mixed with the previous dispersion. The resulted mixture containing EC, PNIPAm and SPIO is utilized to make the final composite membranes on glass slides. The fabrication of the CA-PNIPAm-SPIO membrane follows the same procedure, except that 10 wt% CA in acetone is used in the mixture. All membranes are allowed to dry at ambient conditions overnight and observed by scanning electron microscopy as shown in Figure 2.6.

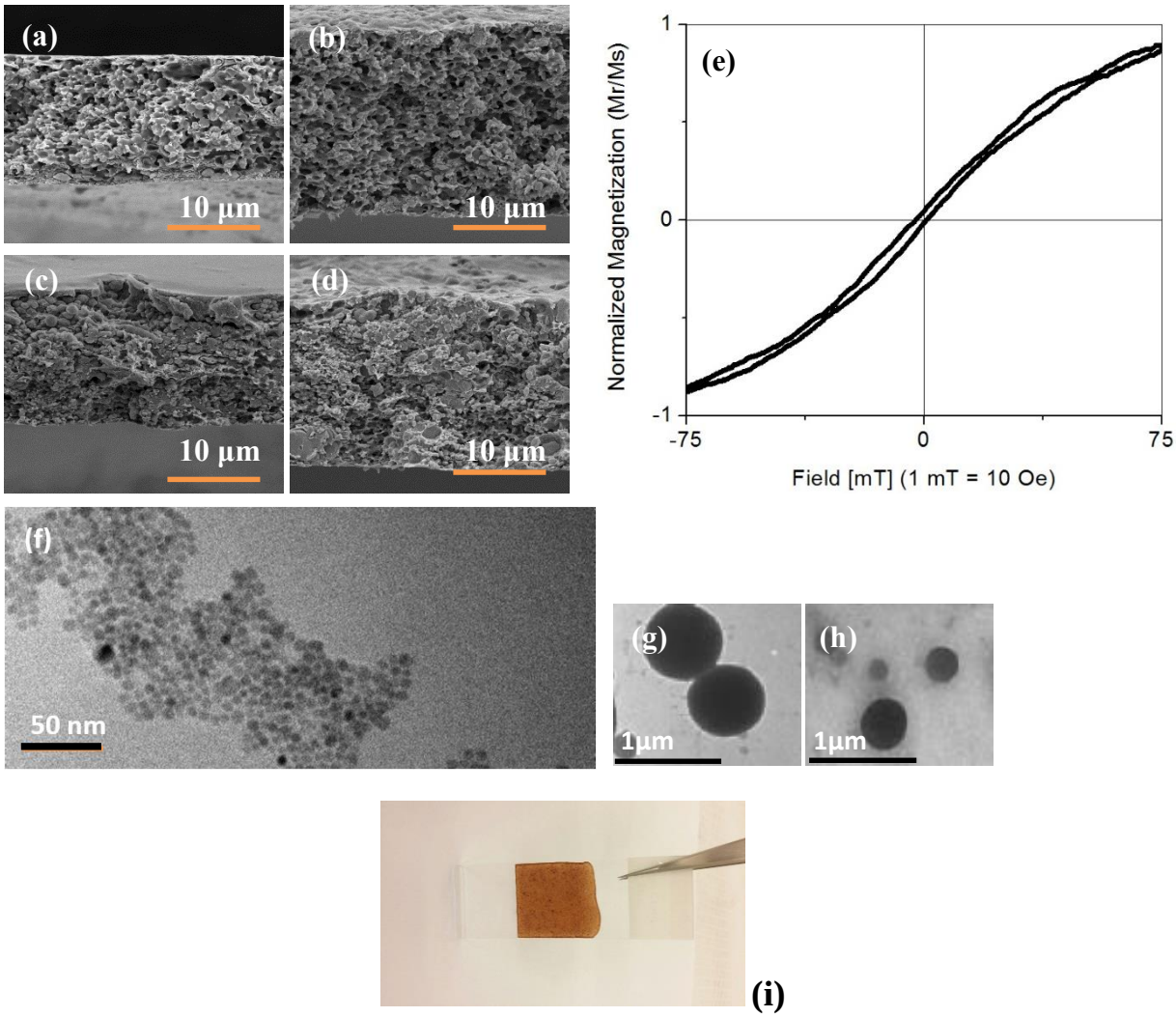

Figure 2.6 Scanning electron microscopy (SEM) images of the cross-sections of different nanocomposite membranes, (a) ethyl cellulose with PNIPAm, (b) ethyl cellulose with PNIPAm and SPIO, (c) cellulose acetate with PNIPAm, (d) cellulose acetate with PNIPAm and SPIO. (e) Vibrating sample magnetometer (VSM) measurement of iron oxide particles, shown near the magnetic field range of experiments. The graph is zoomed in to show enclosed area of loop, (M_s is at approximately 1500 mT). (f) Transmission electron microscopy image of synthesizes SPIO nanoparticles prior to membrane fabrication. (g) PNIPAM particles in water, 800 nm at 37°C and (h) 400 nm at 45°C (using direct heating). (i) Image of ethyl cellulose magnetic composite membrane (a)-(d) and (f)-(h) Reprinted with permission from [228]. Copyright 2015, AIP Publishing LLC.

The average thicknesses of the membranes are obtained as the mean value of 8 different positions along the cross-sections as listed in Table 2.1. The membrane

fabrication process is summarized in Figure 2.7.The drying process of a membrane is the gelation of polymers in the mixture and the exclusion of the solvent from the solid components. For the membrane composed of EC with PNIPAm, there is an abundance of solvent evaporating from around and among the polymer network, causing a collapse of solid components in the gelation. When SPIO particles are present, they form rigid structures that allow some solvent to reside in the spacing between them, which results in thicker membranes. This solvent eventually evaporates, but only after larger pockets of solvent do, and may not create a large enough negative pressure in their cavities to fully collapse the space between SPIO particles. In a similar manner, the sponge-like structure of CA is accentuated in the composite membranes, as the hydrophilic PNIPAm hydrogel particles disperse in the network, expanding the porous structures.

Table 2.1 Thicknesses measurements of different nanocomposite membranes after casting and curing.

Membrane types	Thickness
Ethyl cellulose with PNIPAm	15.48 ± 1.43 µm
Ethyl cellulose with PNIPAm and SPIO	18.78 ± 2.03 µm
Cellulose acetate with PNIPAm	12.97 ± 2.12 µm
Cellulose acetate with PNIPAm and SPIO	18.73 ± 3.45 µm

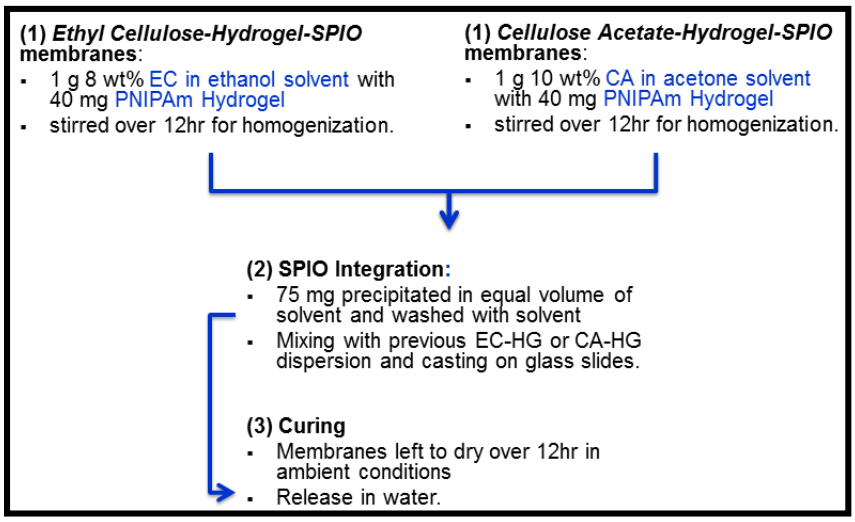

Figure 2.7 Summary of the fabrication of ethyl cellulose and cellulose acetate magnetic membranes.

The final values of material content in each type of membrane are tabulated in Table 2.2, and the final mixture volumes are found to be quite close after drying (approximately equal to

122 mm^3 for both membranes). Since magnetization is discussed as being per unit volume of magnetic material, it is of interest to note that the SPIO volumetric content is equal as well (approximately 12.3 % v/v), while the small difference in weight percent of SPIO between the two membranes is a result from the difference in densities of EC and CA.

Table 2.2 Mixture volumes for the two types of membranes before and after membrane drying: (ii) 1 g of 8 wt% Ethyl Cellulose in Ethanol, 40 mg of PNIPAm hydrogel, and 75 mg of SPIO nanoparticles, (ii) 1 g of 10 wt% Cellulose Acetate in Acetone, 40 mg of PNIPAm hydrogel, and 75 mg of SPIO nanoparticles.

Membrane types	Ethyl cellulose with PNIPAm and SPIO	Cellulose acetate with PNIPAm and SPIO
Mixture volume before casting & curing	1288.193 mm^3	1259.586 mm^3
Membrane volume before cutting (dry)	122.160 mm^3	121.786 mm^3
Volume percent SPIO (wet)	1.164 % v/v	1.190 % v/v
Volume percent SPIO (dry)	12.279 % v/v	12.317 % v/v
Weight percent SPIO (wet)	6.726 % w/w	6.726 % w/w
Weight percent SPIO (dry)	38.462 % w/w	34.884 % w/w

2.2.3.4 Cyanoacrylate Layer Treatment

Vapor deposition of inert and biocompatible pure cyanoacrylate [259, 260] (402 bonding formula, Henkel Corp, USA) is used to drastically reduce the drug delivery rate from micrograms per hour down to tens of nanograms per hour. The process consists of enclosing one side of the nanocomposite membrane in a 10x10x5 mm^3 enclosure with a 5 mm in diameter hole on the top. The cyanoacrylate is placed on the lower inner edges of the enclosure and spread along the four sides using a needle tip to ensure a well distributed vapor source. The setup is left for over 12 hr. As the cyanoacrylate polymerizes, its vapor deposits on the surface of the membrane, creating a permeable barrier, whose permeability depends on the amount of cyanoacrylate placed on the enclosure's bottom edges. The purpose of the 5 mm hole is to allow the vapors to exit the enclosure as they flow atop and past the membrane. Only this one condition is tested, the aim being to establish proof of concept of the use of cyanoacrylate as a secondary treatment of the magnetic membrane.

Cyanoacrylate is an acrylic resin that cures in the form of long fiber-like chains. It rapidly polymerizes when in contact with water, and exposure to normal levels of air humidity is enough to generate a thin layer of monomer chains. Its vapors travel across neighboring surfaces, depositing a thin layer of material, a process which has its own set of

applications, such as in forensics for capturing fingerprints on smooth surfaces. In this study, the thin layer of material is used for partially blocking pores at the top surface of the membrane, hence increasing the time required for permeating RhB molecules to find their way through the composite membrane and to diffuse into the receptor; the thicker the deposited material, the slower the rate. Such an approach to tuning the magnetic membrane allows for modification of drug delivery rates by changing the effective permeability of the membrane, based on patient or research requirements, without more drastic modifications to already mass-cast membranes.

2.2.3.5 Mechanical and Surface Area Characterizations of Membrane Types

The ASTM D 790-07 standard test method was used to mechanically characterize EC-PNIPAm and CA-PNIPAm membranes, both dry and wet, as they yield under a 3-point loading system (Instron, Illinois Tool Works, Glenview, Illinois, United States). Table 2.3 summarizes the mean flexural stress at the breaking point measured for each of the four conditions described. Five samples were studied for each condition. CA membranes exhibit larger flexural stress when compared to EC membranes, which is consistent with the experience of a higher failure rate for EC membrane devices and individual membranes studied. Some EC membranes would crack or leak during device assembly or at the start of diffusion cell testing, while no CA membranes did so. This suggests that CA is a more viable polymer to use as a membrane matrix for drug delivery applications. Membranes are broken into approximately 5 mm wide segments (length is 10 mm and has no effect on measurements). The formula for a rectangular sample under a load in a 3-point loading system is given by Eqn. (2-1), where F is the load force at the fracture point [N], L is the length of the span between the two supports on which the sample rests, b is the width of the sample (mm), and d is the thickness (mm).

$$\sigma = \frac{3FL}{2bd^2} \tag{2-1}$$

Table 2.3 Mean flexural stress at breaking point for dry and wet cellulose acetate and ethyl cellulose based membranes.

Membrane types	Mean Flexural Stress at Breaking point (MPa)
Cellulose Acetate and PNIPAm, dry	7.850
Cellulose Acetate and PNIPAm wet	7.210
Ethyl Cellulose and PNIPAm, dry	5.610
Ethyl Cellulose and PNIPAm, wet	3.480

The Brunauer–Emmett–Teller (BET) surface areas of the EC–PNIPAm–SPIO and CA–PNIPAm–SPIO membranes are measured to be roughly equal, as is desired for comparison of the two membranes (Table 2.4). BET specific surface areas were measured using nitrogen gas for adsorption, and the technique relies on measuring the difference between the amount of gas exposed to the sample, and the amount of gas measured after exposure and adsorption.

Table 2.4 The Brunauer–Emmett–Teller (BET) specific surface area results for physical adsorption of gas molecules in untreated ethyl cellulose and untreated cellulose acetate membranes:

Ethyl Cellulose – PNIPAm – SPIO	1.5 m^2/g
Cellulose Acetate – PNIPAm – SPIO	1.6 m^2/g

2.2.4 Modeling and Numerical Simulations

Finite element simulation software (COMSOL) is used to simulate the drug delivery device focusing on the osmotically pressurized cyanoacrylate treated EC membrane with PNIPAM hydrogel and SPIO particles (see Appendix A for details regarding simulation work carried out largely by collaborators at the University of California, Berkeley). The numerical model is developed based on three modules in the software: fluid-structure interaction (FSI) for the flexible PDMS, free flow and flow through porous media for the magnetically triggered membrane, and species transport through free and porous media for the RhB diffusion. The FSI module combines the Navier-Stokes equation that applies to water with the structural mechanics equation for isotropic linearly elastic material that is nearly incompressible (PDMS), while Brinkman's equation is utilized for porous regions. The transport of RhB solution through porous and free media can be solved with a module in COMSOL. In this work, the governing equation of the module is transferred to a mathematical module and simplified for the simulation (see Appendix A):

$$\varepsilon\frac{\partial c}{\partial t} + \nabla\cdot(cu) = \nabla\cdot\left(\left(\varepsilon^{\frac{4}{3}}D\right)\nabla c\right) \tag{2-2}$$

where εε is the porosity, c is the concentration, u is the velocity profile, and D is the diffusion coefficient of the diffusing species.

An analytical approximation is used to find the return force-induced pressure from the osmotic chamber on the flexible PDMS membrane, P_{PDMS}. The analytical equation for this applied pressure on the PDMS membrane is derived from two basic equations that describe

the elastic deflection of a membrane and the fluid flow through a semi-permeable membrane, namely the equation of deflection of a circular plate with clamped edges and under uniform lateral load [264], and Darcy's law [265]. By combining these and the boundary conditions, an approximation of the applied pressure on the PDMS membrane is derived:

$$P_{PDMS} = \alpha V^3 + \frac{\mu h}{kA}\dot{V} \tag{2-3}$$

where,

- P_{PDMS} is the applied pressure on the PDMS membrane by the osmotic chamber in the pump,
- α is a parameter determined when solely examining the PDMS membrane deflection,
- V is the fluid volume displaced due to PDMS deflection,
- μ is the dynamic viscosity of the fluid,
- h is the thickness of the magnetically responsive membrane,
- k is the mechanical permeability of the magnetically responsive membrane,
- A is the cross-sectional area of the magnetically responsive membrane and
- $\dot{v}$ is the rate of volume displacement over time.

The second term appears only with the existence of the magnetically responsive membrane, while the first term represents the contribution of the osmotic pump's displaced volume via the deflection of the PDMS membrane.

An approximated applied pressure on the PDMS membrane, used to simulate its behavior alone, shows an interesting behavior of the input pressure profile. Since the magnetic membrane's permeability is low in general, the small displacement of the PDMS membrane reduces the influence of the αV^3 term on P_{PDMS}, causing the pressure profile applied onto the donor chamber to be dominated by the volume displacement rate $\dot{v}$ through the magnetic membrane and the permeability k of the magnetic membrane in the second term.

The approximation of the permeability of the magnetic membrane is based on work done on fluid transport and permeability of water vapor through EC [266]. From such a basis, the magnitude of P_{donor} is determined. The permeability of the magnetic membrane is calibrated with this applied pressure, and the permeability difference between the magnetically activated and deactivated states is approximated by comparing the two states

(magnetic field on and off), which gives a ratio of the magnetic membrane's permeability values for the two states.

The simulation process is divided into four parts, namely (1) direct pressure test (PDMS membrane behavior without simulating osmotic process), (2) magnetic membrane porosity calibration, (3) magnetic membrane permeability calibration, and (4) simulation of the full osmotic pump and magnetic membrane assembly.

2.2.5 Sensitivity Analysis using Fluidic Circuit Analogy Model

The fully assembled device which includes the osmotic pump, the drug chamber, the magnetically triggered membrane, and the receptor chamber (Figure 2.1), can be modeled using a circuit analogy that represents the forced-convection fluidic system, and the sensitivity of the output fluid flow with respect to each circuit component can then be determined. Pressure is represented by voltage and flow rate by current. Figure 2.8 shows the resulting circuit analogy, where the grounded part of the circuit represents atmospheric pressure at the inlet and outlet of the device, and:

- I_{in} [volume/time] is the flow rate of water into the device at the osmotic pump inlet.
- I_{out} ($I_{out} = I_{in}$) is the water flow rate out of the device (water which contains an amount of RhB).
- I_{oc} is the osmotic chamber current, or flow rate, generated by the osmotic pump.
- I_{PDMS} is the flow rate through the osmotic pump's PDMS membrane ($I_{PDMS} = I_{out} = I_{in}$).
- R_{in} is the resistance of the osmotic pump's semi-permeable membrane at the inlet [pressure / (volume/time)].
- I_{Rin} is the water flow rate through R_{in} and is defined in the direction shown.
- C_{PDMS} is the fluidic capacitance of the osmotic pump's flexible PDMS membrane [volume/pressure].
- $R_{control}$ is the resistance of the magnetically triggered membrane, controlled by the magnetic field.
- V_{oc} is the osmotic chamber pressure to the right of R_{in} and to the left/behind the capacitor element C_{PDMS} when present.
- V_{dc} is the drug chamber pressure, located between C_{PDMS} and $R_{control}$ when both are installed.
- Q_{out} ($Q_{out} = Q_{in}$) [volume] is the time integral of flow I_{out}.

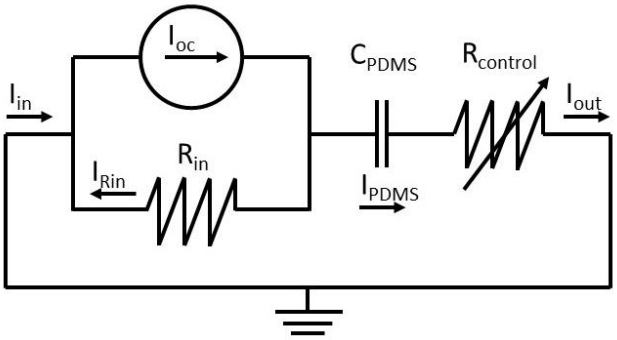

Figure 2.8 Circuit analogy of complete device with osmotic pump and magnetically triggered membrane.

To determine the osmotic pump's components prior to their assembly with the inclusion of $R_{control}$, the analogous osmotic pump, and its internal mechanism, shown in Figure 2.9a and Figure 2.9b, are analyzed. In Figure 2.9a, the flow, I_{oc} [m^3/s], can be described by the equation for an osmotically driven fluid shown in Eqn. (2-4) (rewritten from Eqn. (1-1)), where A is the area of the osmotic pump's semi-permeable membrane, h is it's thickness, L_p is its hydraulic permeability (inverse of flow resistivity, or [m^3s/kg]), σ is the reflectivity coefficient (unitless), Δπ and ΔP are the osmotic and hydrostatic pressure differences, respectively (Pa).

$$I_{oc} = \left(\frac{A}{h}\right) L_p(\sigma\Delta\pi - \Delta P) \tag{2-4}$$

The configuration shown in Figure 2.9a for t=0 (isolated osmotic pump without a magnetically triggered membrane) and Figure 2.9b (osmotic driving mechanism without a flexible PDMS membrane at the pump's actuation side) can be used to confirm that I_{oc} is determined by Eqn. (2-4), i.e. I_{in}" = I_{out}" = I_{oc}, I_{Rin}" = 0, ΔP = 0 (all potentials in the Figure 2.9b circuit are equal), and hence, I_{oc} = (A/h) L_p σ Δπ.

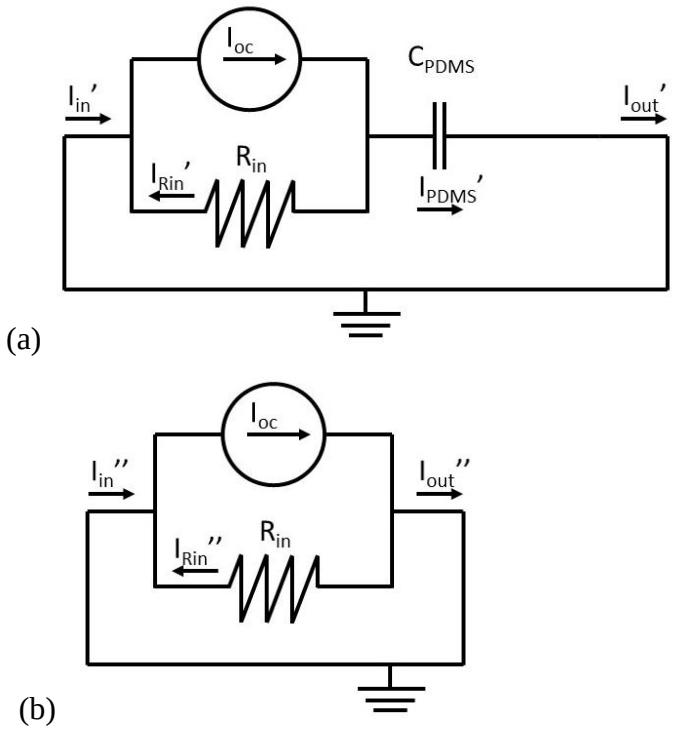

Figure 2.9 Circuit analogy of (a) the isolated osmotic pump without a magnetically triggered membrane, (b) the osmotic driving mechanism without a flexible PDMS membrane at the outlet.

From Figure 2.9a, we also see that $I_{in}' + I_{Rin}' = I_{oc}$, $V_{oc} / R_{in} = I_{Rin}'$, and $V_{oc} = \int (1/C_{PDMS})\, I_{in}'\, dt$. Combining these expressions gives the following.

$$\int \left(\frac{1}{C_{PDMS}}\right) I_{in}' dt = R_{in}(I_{oc} - I_{in}') \tag{2-5}$$

I_{oc}, unlike I_{in}', is constant and not time dependent, therefore taking the derivative of both sides of Eqn. (2-5) yields a 1st order ordinary differential equation (Eqn. (2-6)) and its solution (Eqn. (2-7)).

$$\frac{dI_{in}'}{dt} = -\left(\frac{1}{R_{in}C_{PDMS}}\right) I_{in}' \tag{2-6}$$

$$I_{in}' = c_1 e^{-t/(R_{in}C_{PDMS})} \tag{2-7}$$

To determine c_1 and $R_{in}\, C_{PDMS}$, a curve fit is done to the data recorded for the volume displaced over time of an osmotic pump under operation without a magnetic membrane

(Figure 2.10). Taking the indefinite integral of Eqn. (2-7) with respect to time gives an expression for Q_{out}', used in fitting the data, where c_1 (R_{in} C_{PDMS}) is the constant resulting from the integration and knowing that at t = 0, $Q_{out}' = 0$.

$$Q'_{out} = -c_1(R_{in}C_{PDMS})e^{-t/(R_{in}C_{PDMS})} + c_1(R_{in}C_{PDMS}) \tag{2-8}$$

Here it can be verified that at t=0, $Q_{out}' = 0$. It is found that $c_1 = I_{oc} = 6.32\text{x}10^{-13}$ m^3/s (or 2.3 mm^3/hr), R_{in} C_{PDMS} = 21755 s (or 6 hr).

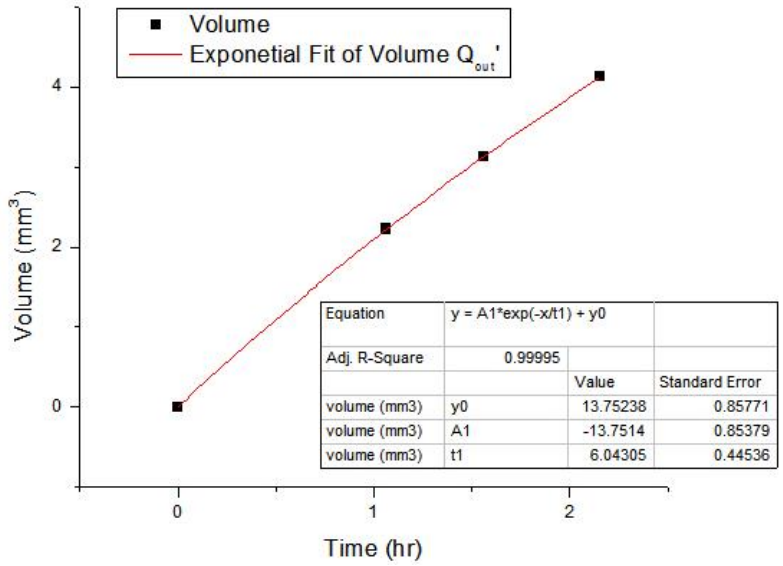

Figure 2.10 (a) Curve fit of volume displaced over time of osmotic pump under operation without a magnetic membrane.

For individually tested pumps (Figure 2.10), the flow rate dramatically increases from zero when a constant supply of water is introduced to the pump's water inlet. Priming is performed on all osmotic pumps used in this study, and allows for the NaCl in the salt chamber to contain an initial volume of water, promoting a more rapid activation of the pump upon introduction of water at the inlet.

To determine R_{in}, we need $\Delta\pi$ and we use Figure 2.9a and re-write Eqn. (2-4) for expressing I_{in}' (or I_{out}'), where $\Delta P \neq 0$ for t>0 with the presence of the PDMS membrane (C_{PDMS}), and ΔP is time dependent.

$$I'_{in} = \left(\frac{A}{h}\right) L_p(\sigma\Delta\pi - \Delta P) \tag{2-9}$$

At time $t=0^+$, Eqn. (2-7) gives $I_{in}' = c_1 = I_{oc}$, and $\Delta P_{t=0} = 0$ in Eqn. (2-9) (the PDMS membrane experiences no deformation in zero time, while the instantaneous current I_{in}' matches I_{oc}). Therefore:

- $I_{oc} = 6.32 \times 10^{-13}$ m^3/s

The osmotic pressure $\Delta\pi$ is calculated using the Morse equation, Eqn. (2-10), where i is the dimensionless van't Hoff factor (1.8 for NaCl), M is molarity (mol NaCl per L water), R is the gas constant (0.08206 L atm/mol K), T is the temperature (taken as 298 K).

$$\Delta\pi = iMRT \tag{2-10}$$

The molarity M is given by the solubility of NaCl in water (359 g/L), as the water content is fully saturated in the osmotic chamber during all experiments, divided by molar mass (58.44 g/mol), resulting in 6.14 mol/L. $\Delta\pi$ is 270.26 atm, or 2.738×10^7 Pa. Knowing that $I_{oc} = c_1$ and $I_{oc} = (A/h)\, L_p\, \sigma\, \Delta\pi$ (Eqn. (2-9) at t=0), we see that to achieve the "voltage" of $\Delta\pi$ and "current" I_{oc} from the osmotic process, the resistance R_{in} in the salt chamber is found to be as follows:

- $R_{in} = \Delta\pi / I_{oc} = 6.17 \times 10^{19}$ kg/[m s (m^3)] [dynamic viscosity/volume, or pressure/flow rate].
- $L_p\, (\sigma) = 1.032 \times 10^{-19}$ m^3s/kg [inverse of flow resistivity], from $R_{in} = [(A/h)\, L_p\, \sigma]^{-1}$, using h = 20 um and $A = \pi\, (1\text{ mm})^2$.
- $C_{PDMS} = 3.53 \times 10^{-16}$ m^3/Pa [volume change/pressure change], knowing R_{in} and $R_{in}\, C_{PDMS}$.

The data recorded in ng or µg of RhB delivered to the receptor chamber can be converted to the associated volume of water delivered, knowing that the concentration of RhB in water is 1 mg/mL, as long as the concentration gradient-driven diffusion data component that is recorded while the pump is off, is subtracted from the data recorded while the pump is on. In this manner, the circuit models the forced convection component of the drug delivery, driven by the pump over time, but not the diffusion component, which cannot be considered in a lumped system due to the nature of the combination of RhB species diffusing within the water species. Next, the only circuit element remaining to solve for is $R_{control}$ in Figure 2.8, which is constant within each device state (i.e. magnetic field on or off), but changes with the application of the magnetic field and the removal thereof. Using the

data from the treated EC membrane device and determining the volume of water delivered, the values for $R_{control}$ per test period can then be determined.

When $R_{control} \neq 0$, circuit analysis similar to that done using Figure 2.9a, this time using Figure 2.8 of the complete circuit, results in the following:

$$\frac{dI_{in}}{dt} = -\left(\frac{1}{R_{in}C_{PDMS}}\right)I_{in} \tag{2-11}$$

$$I_{in} = c_2 e^{-t/((R_{in}+R_{control})C_{PDMS})} = I_{OC}\left(\frac{R_{in}}{R_{in}+R_{control}}\right)e^{-t/((R_{in}+R_{control})C_{PDMS})} \tag{2-12}$$

When t = 0, $I_{in} = c_2 = I_{oc}\,(R_{in} / (R_{in} + R_{control}))$. Integrating I_{in} to find Q_{in}, where $Q_{out} = Q_{in}$, results in the following:

$$Q_{out} = I_{OC}R_{in}C_{PDMS}\left(1 - e^{-t/((R_{in}+R_{control})C_{PDMS})}\right) \tag{2-13}$$

Rearranging to solve for $R_{control}$ results in the following equation where all other terms have been found above and Q_{out} is determined from experimental data; this is achieved while having compensated for baseline concentration gradient-driven diffusion components (pump & field OFF, and pump OFF field ON) in order to work with only the forced convection component, by subtracting the experimental baselines from the total Q_{out} experimental data:

$$\frac{t}{C_{PDMS}\ln\left(\frac{I_{OC}R_{in}C_{PDMS}}{I_{OC}R_{in}C_{PDMS} - Q_{out}}\right)} - R_{in} = R_{control} \tag{2-14}$$

The unaltered experimental Q_{out} is the result of a sum of forced-convection and concentration gradient-driven diffusion. Tabulated below are the determined values when fitting the circuit to the data.

Table 2.5 Summary of calculated values using circuit model and experimental data. All resistances are in units of kg/[m s (m^3)].

I_{oc}	R_{in}	C_{PDMS}	$R_{control}$ Magnetic Heating on #1	$R_{control}$ Magnetic Heating off #1	$R_{control}$ Magnetic Heating on #2	$R_{control}$ Magnetic Heating off #2	$R_{control}$ Magnetic Heating on #3	$R_{control}$ Magnetic Heating off #3
6.32×10^{-13} m^3/s	6.17×10^{19}	3.53×10^{-16} m^3/Pa	6.5354 E+21	9.3705 E+21	7.1838 E+21	9.5355 E+21	5.8136 E+21	9.7503 E+21

Let S_n denote the relative sensitivity of the circuit output flow rate I_{out} to circuit component n.

$$S_n = \left(\frac{dI_{out}}{dn}\right)\left(\frac{n}{I_{out}}\right) \tag{2-15}$$

This value represents the percent change in I_{out} over the percent change in n. The sign of the value indicates the direction of the change: a positive or negative S_n means an increase in n gives an increase or decrease in I_{out}, respectively. The symbolic expression of S_n also indicates the effect of the magnitude of each component on, specifically, the sensitivity of I_{out} to any given n. Symbolic expressions for the sensitivity of I_{out} ($I_{out} = I_{in}$) are tabulated below.

Table 2.6 Symbolic expression for the sensitivity of I_{out} to each circuit element.

S_{Rin}	$1+ [R_{in}/(R_{in} + R_{control})]$ x $[-1 + t/(C_{PDMS} (R_{in} + R_{control}))]$	Sign depends on time constant $C_{PDMS}(R_{in} + R_{control})$, and both resistors separately
$S_{Rcontrol}$	$[R_{control}/(R_{in} + R_{control})]$ x $[-1 + t/(C_{PDMS} (R_{in} + R_{control}))]$	Sign depends on time constant $C_{PDMS}(R_{in} + R_{control})$
S_{Cpdms}	$1 / C_{PDMS}(R_{in} + R_{control})$	If C_{PDMS} is increased, I_{out} is less sensitive to the value of C_{PDMS}
S_{Ioc}	1	Constant over time: *relative* change does not occur with change in Ioc
S_{time}	$-time / C_{PDMS}(R_{in} + R_{control})$	Negative: as time increases, the value of I_{out} decreases

A plot of sensitivity over time can be used to determine the period of usefulness of the controllable element(s), in this case $R_{control}$ (Figure 2.11). Calculations are made using the average $R_{control}$ with no magnetic field application for the treated EC membrane device. $S_{Rcontrol}$ must be negative in order for a *decrease* in $R_{control}$ to result in an *increase* in I_{out}.

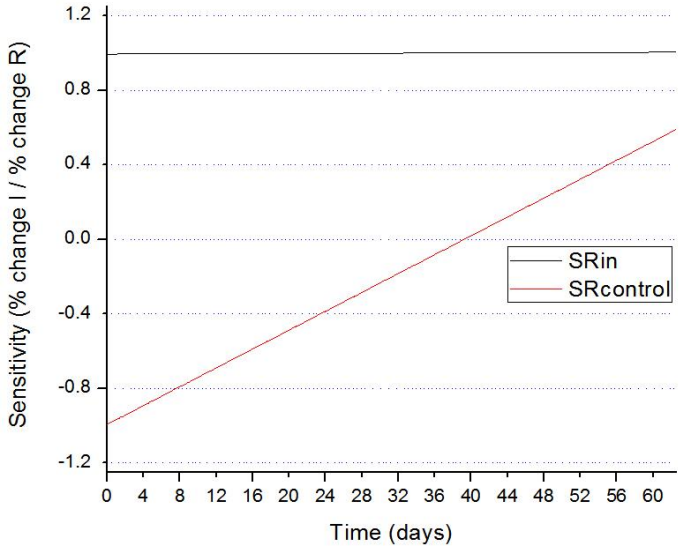

Figure 2.11 Plot of S_{Rin} and $S_{Rcontrol}$ over time. $S_{Rcontrol}$ remains negative in this design for over ~40 days, and has an absolute value greater than or equal to 0.8 for around 8 days (~200 hr).

It can be seen from Figure 2.11 that, although the effect of the inlet membrane S_{Rin} is more stable over time, only $S_{Rcontrol}$ remains negative for approximately the first 1000 hr of operation, confirming the validity of selecting this membrane to control when to objective is to increase drug output by magnetically decreasing the membrane's resistance to flow. If, on the other hand, a *reduction* of the baseline drug delivery profile is needed, then magnetically inducing a reduction in the flow resistance of R_{in} would achieve this. Therefore, this sensitivity analysis based on the fluidic circuit model permits the customization of the device, depending on the application requirements, where the flow rate can be modified to go above or below a set baseline value by manipulating one or both of the membranes of the device. The parameters for each component would change depending on the required design, and would affect sensitivity and device lifetime of effective operation.

The total mass delivered (ng) associated with the total flow Q over time is shown in Figure 2.12 as predicted by the circuit model, along with the experimentally recorded mass associated with the rates reported in Figure 2.18. Baseline delivery rates taken from the experimental results during both pump & field OFF, and during pump OFF field ON, are added to the circuit model prediction wherever the field is OFF, and ON, respectively, since these conditions are both a result of concentration gradient driven diffusion (as opposed to circuit modeled forced convection). Also shown in Figure 2.12 are curves for predicted delivery with the magnetic field always ON, and always OFF, for all stages B-G.

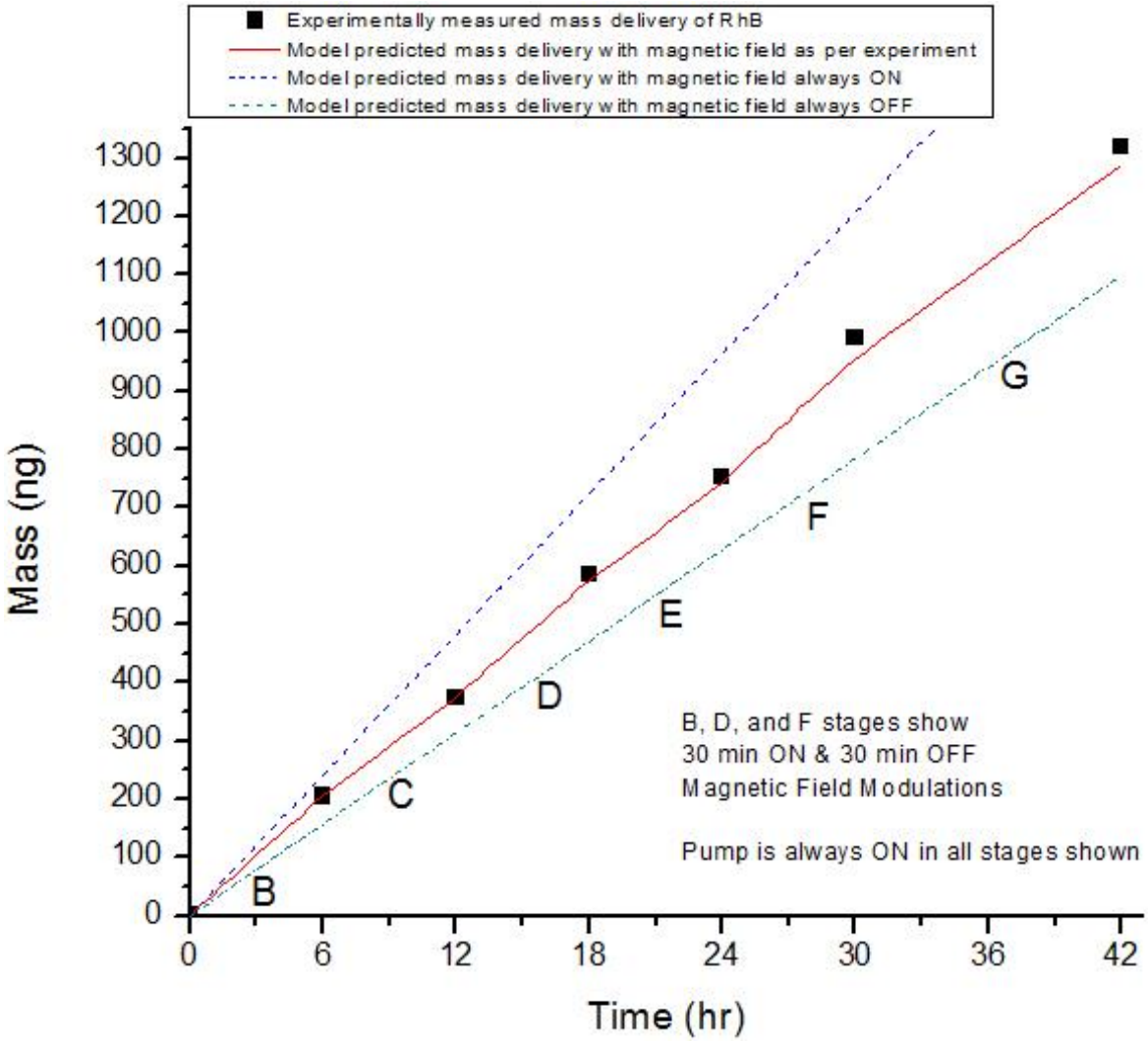

Figure 2.12 Total delivered mass curves over time, as predicted by the circuit analogy model for different magnetic field application conditions, along with experimentally recorded mass delivery for the cyanoacrylate treated EC membrane device with osmotic pumping ON and modulation of magnetic field application (62 mT, 450 kHz).

Figure 2.13 shows a close-up plot of stage B from Figure 2.12, where the magnetic field is modulated ON for 30 min and OFF for 30 min, and repeated this within this stage (as well as in stages D and F), resulting in the rounded-jigsaw shapes seen in the B, D, and F sections of the complete curve. Steeper slopes are the result of increased drug delivery due to the increased permeability of the magnetic membrane with each 30 min application of the magnetic field. Subsequent periods with no magnetic field show drops in slope, the result of reduced delivery rates during the 30 min OFF (and during stages C, E, and G).

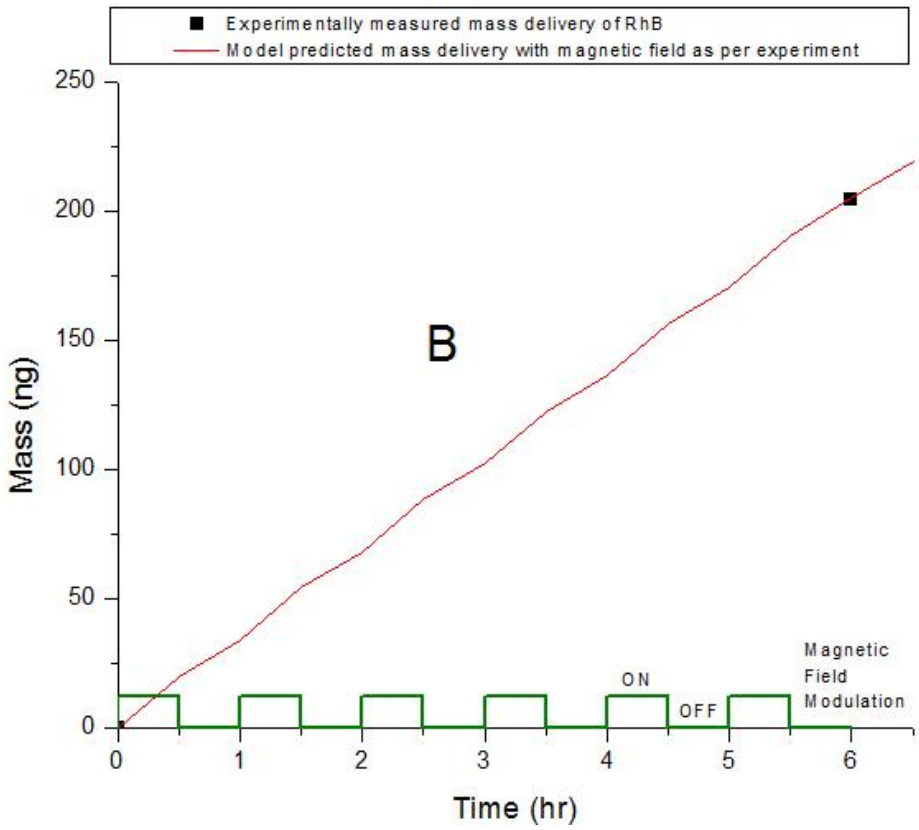

Figure 2.13 Zoom in view of stage B of total delivered mass curve, during which the magnetic field is modulated first 30 min ON then 30 min OFF, and repeated, showing total delivered mass curves over time, as predicted by the circuit analogy model, along with experimentally recorded mass delivery for the cyanoacrylate treated EC membrane device with osmotic pumping ON.

2.3 Results and Discussion

2.3.1 Individual Membrane and Device Characterization

The continuous change of absorbance of the PNIPAm hydrogel at 500 nm wavelength during heating is shown in Figure 2.14a, where a clear inflection point was observed on the continuous curve. This point indicates that the volume phase transition temperature of tested hydrogels was around 40°C, which is slightly higher than the regular 37°C in human physiological conditions. The plot is generated by heating (hotplate) PNIPAM hydrogel particles in water, and measuring the absorbance using the UV-VIS spectrophotometer at each temperature shown. As the size of the hydrogel particles changes, the amount of light transferred across the sample solution changes due to the increase in opacity of the hydrogel as it shrinks and expels water content. The chemistry of PNIPAM hydrogels is very well established especially in terms of their

thermo-responsivity [91, 93, 158, 267-274]. This concept is applied in this platform where hydrogel particles embedded in the polymer matrix undergo size transition to increase cargo efflux through the heterogeneous membrane. This thermoresponsive size transition is highlighted in Figure 2.6g-h, where a clear size transition from around 800 nm to 400 nm occurs after heating the hydrogel particles in solution to 45 °C. The same transition is hypothesized to be taking place in the composite membranes.

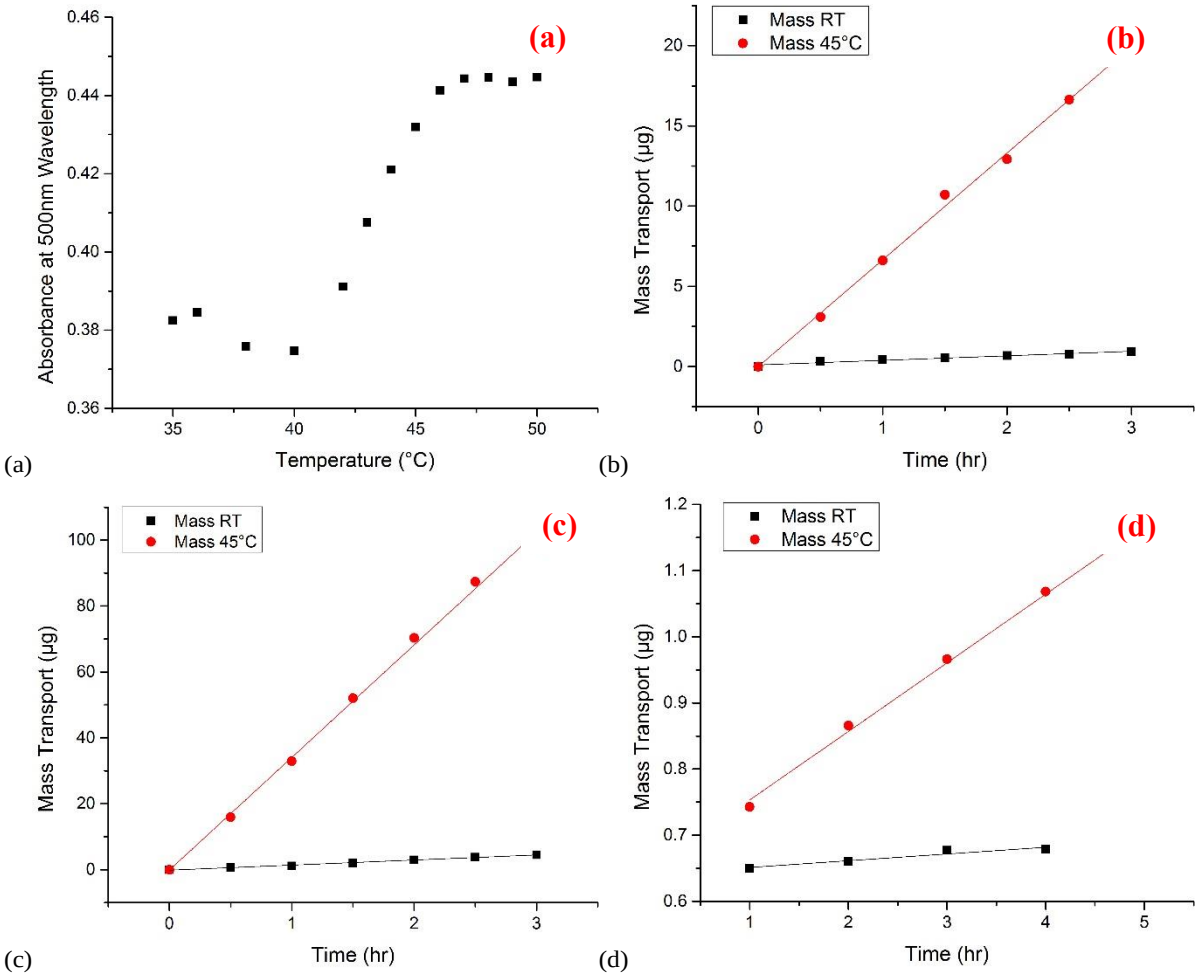

Figure 2.14 (a) Absorbance of PNIPAm hydrogels at different temperatures. Diffusion profiles of RhB through (b) ethyl cellulose with PNIPAm and SPIO and (c) cellulose acetate with PNIPAm and SPIO composite membranes at room temperature and at 45°C. (d) Diffusion profiles of RhB through ethyl cellulose with PNIPAm and SPIO composite membranes treated with 0.06 ml of cyanoacrylate, at room temperature and at 45°C. Reprinted with permission from [228]. Copyright 2015, AIP Publishing LLC.

With RhB as model drug molecules, its diffusions through composite membranes at different temperatures were studied as shown in Figure 2.14b-c. During

3 hr experiments, EC with PNIPAm and SPIO membranes diffused at an average rate of 0.28 µg/h, while those at 45°C diffused at an average rate of 6.65 µg/h. This indicates that the diffusion increases by 23.75 times when the temperature is increased to 45°C. For CA with PNIPAm and SPIO membranes, the diffusion also increased from room temperature to 45 °C, with the corresponding diffusion rate changing from 1.48 µg/h to 34.14 µg/h, which indicates an increased diffusion of approximately 23 times. Figure 2.14d shows the diffusion rates measured at room temperature and at 45°C for a cyanoacrylate treated EC with PNIPAm and SPIO membrane. As expected the addition of the layer impedes the diffusion, resulting in rates of only 0.01 µg/h and 0.1 µg/h, respectively, hence increasing relative diffusion by 10 times with the addition of direct heat over the room temperature state. These rates are measured after a prolonged initial diffusion over several hours to ensure that the small amount of RhB passing through the cyanoacrylate-impeded membrane can be detected and reliably measured to create the plot reported.

The essential reason for the significant difference between diffusion at <40°C and that at >40°C is that the PNIPAm hydrogel occupies different spaces in the diffusion pathway at these two temperature conditions. At room temperature, owning to the swelling state of hydrogel under its transition temperature, where the intermolecular H-bonds were mainly formed to increase the occupied spaces of the hydrogel particles and to block the diffusion pathway, the diffusion was highly inhibited. However, when the temperature was increased to 45°C, which was high enough to introduce the hydrogel's volume phase transition, the intermolecular H-bonds tended to be broken, but the intramolecular ones were preferred and formed. In this case, the shrinkage of the hydrogel particles increases the diffusion pathways around them, resulting in higher diffusion through membranes than that at room temperature. From the diffusion profiles it is also clear that the thermosensitive behavior of the hydrogel can be maintained no matter which membrane matrix, either EC or CA, is surrounding it. Moreover, the hydrophobicity of the SPIO type utilized in the membranes might help limit the diffusion at temperatures below LCST, which increases the difference of mass transport between temperatures above and below LCST.

We report three different devices in this study, using either an EC membrane, a cyanoacrylate treated EC membrane, and a CA membrane, each containing PNIPAm and SPIO, and undergoing similar test conditions. For convenience, all the stages described in the following three paragraphs, one for each device, are tabulated below along with conditions, durations, and associated labels in each device's figure.

Table 2.7 Summary of conditions, durations, and associated labels for EC, CA, and treated EC membrane device stages.

Stage Number and Condition	EC Device (label and duration)	CA Device (label and duration)	Treated EC Device (label and duration)
# 1-1: Baseline measure	No label/not shown, 2hr	No label/not shown, 2hr	No label/not shown, 2hr
# 1-2: Room temperature	A, 3 hr	A, 3 hr	α, 3 hr
# 2: Magnetic cycling*	B, 2.25 hr	B, 3 hr	A, 3 hr
# 3: Pump & Mag. cycling*	C, 4 hr	C, 3 hr	B, 6 hr
# 4: Pump only	D, 1.25 hr	D, 1.5 hr	C, 6 hr
# 5: Pump & Mag. cycling*			D, 6 hr
# 6: Pump only			E, 6 hr
# 7: Pump & Mag. cycling*			F, 6 hr
# 8: Pump only			G, 12 hr
# 9: Room temperature (after locking pump)			H, 7 hr

*Magnetic cycling: 30 min with AC magnetic field on first, followed by 30 min with field off, cycling repeated till end of stage.

The EC membrane device (Figure 2.15) is tested over a span of 10.5 hr, split into four test stages. In stage 1 (A label in figure), the donor and receptor are carefully loaded with RhB and DI water, respectively. The donor's fill holes are then sealed with several layers of PMMA-chloroform mixture that quickly dry while under a fume extraction system. The device is left upright at room temperature on a dry stand with the deactivated osmotic pump on the bottom for a total of 2 hr, after which a small amount of the receptor fluid is immediately analyzed via UV spectrophotometry to determine the total amount of RhB initially diffused, then slowly re-injected into the

receptor such that the membrane does not experience any excess force. UV analysis is conducted in such a manner for every device. With the baseline concentration gradient-driven diffusion process fully initiated, this measurement is used as the zero point for a second room temperature measurement taken after 3 hr (as shown in Figure 2.15).

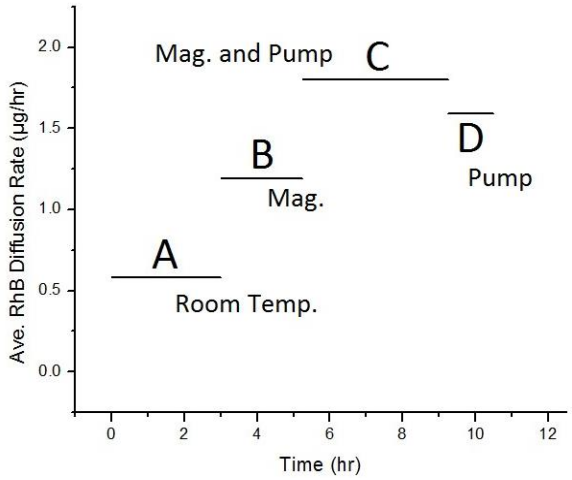

Figure 2.15 The EC membrane (ethyl cellulose with PNIPAm and SPIO) testing results with average delivery rates of RhB sampled for each test stage (A-D). (A) Room temperature diffusion, (B) applied magnetic field (62 mT, 450 kHz, cycled on/off every 30 minutes) and no osmotic pumping, (C) applied magnetic field with osmotic pumping, (D) osmotic pumping with no applied magnetic field. Reprinted with permission from [228]. Copyright 2015, AIP Publishing LLC.

In stage 2 (B label in figure), while maintaining the same orientation as before, the device is placed in the center of a vertically oriented magnetic solenoid (Figure 2.16) of a water cooled 3kW inductive heater (Induktive Erwärmungsanlagen GmbH, Austria), and cycled through approximately two 1hr-long on-off cycles, each including 30 minutes of exposure to a 62 mT, 450 kHz magnetic field, totaling ~2 hr prior to UV analysis. The device is positioned such that no part (of either the device or its holder) is in physical contact with the coil. During this entire process, high flow rate room temperature air (pressurized at 2.5 bar) is applied along the device holder, ensuring that no heat generated from the coil can dissipate to the device or the membrane during experimentation. Continuous air cooling is performed in such a manner and for every device, during every stage involving inductive heating. Stage 3 (C label in figure) repeats the steps performed in stage 2 for the duration of 4 hr, with the addition of the activation of the osmotic pump at the start of this step. While ensuring not to

agitate the device, the water inlet is wetted with a drop of DI water, held in place by surface tension with the device in the upright position. The device is then placed in a small water holder used to partially submerge the donor and fully submerge the pump in more DI water, such that no air remains in the pump's water inlet. Stage 4 (D label in figure) consist of a 1.25 hr period during which the device is left at room temperature with the osmotic pump still running and positioned as described above. The measurements of RhB diffused by the end of each stage are used to determine each stage's average delivery rate.

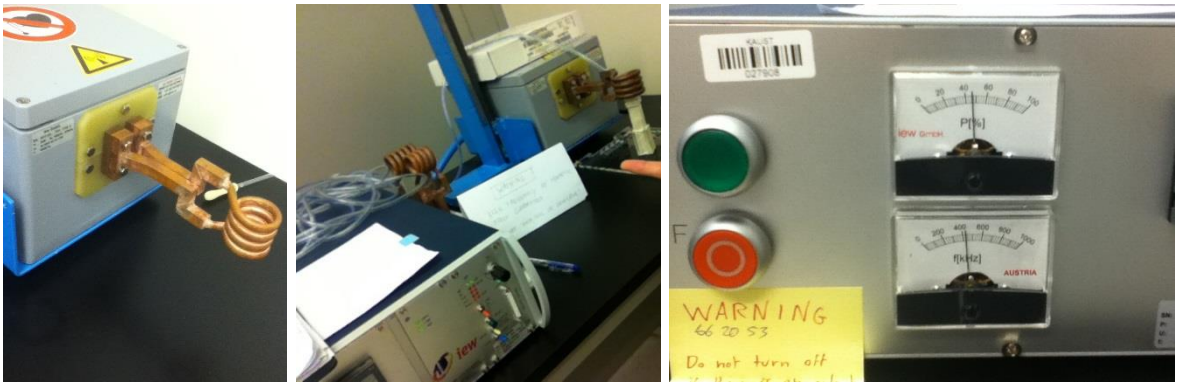

Figure 2.16 3 kW inductive heater solenoid, experimental setup, control panel, power and frequency settings.

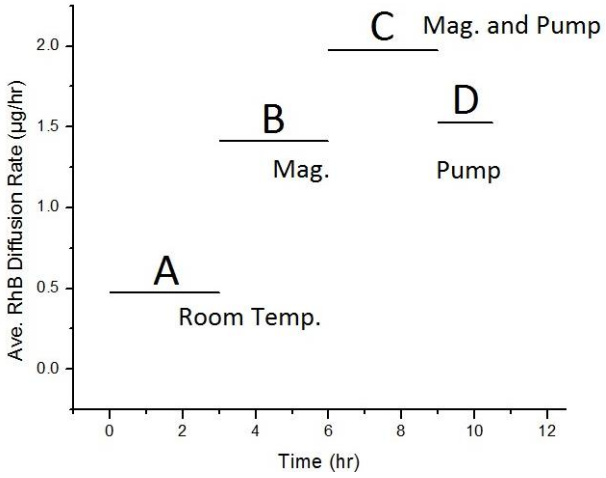

Figure 2.17 The CA membrane (cellulose acetate with PNIPAm and SPIO) testing results with average delivery rates of RhB sampled for each test stage (A-D). (A) Room temperature diffusion, (B) applied magnetic field (62 mT, 450 kHz, cycled on/off every 30 minutes) and no osmotic pumping, (C) applied magnetic field with osmotic pumping, (D) osmotic pumping with no applied magnetic field. Reprinted with permission from [228]. Copyright 2015, AIP Publishing LLC.

The same testing procedures (stages 1-4) are used to characterize the CA membrane device over a span of 10.5 hr as reported in Figure 2.17. In stage 1 (A label in figure), a total of 3 hr are used to determine the total diffused amount of RhB at room temperature. In stage 2 (B label in figure), the device is cycled through three 1hr long on-off cycles, each including 30 minutes of applied magnetic field exposure, and 30 minutes of rest time, totaling 3 hr prior to UV analysis. Stage 3 (C label in figure) repeats the steps performed in stage 2 for the duration of 3 hr, with the addition of the activation of the osmotic pump at the start of this step. Stages 4 (D label in figure) consists of a 1.5 hr period during which the device is left at room temperature with the osmotic pump still running and positioned as described above.

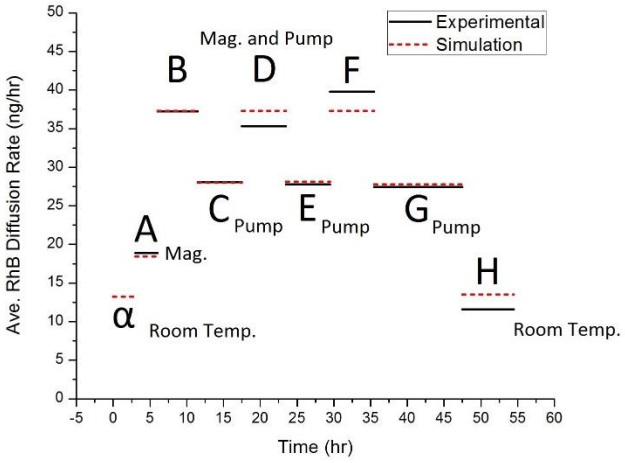

Figure 2.18 The cyanoacrylate treated EC membrane (cyanoacrylate treated ethyl cellulose with PNIPAm and SPIO) testing results with average delivery rates of RhB sampled for each test stage (A-H). (A) Applied magnetic field without osmotic pumping, (B, D, F) applied magnetic field with osmotic pumping, (C, E, G) osmotic pumping without applied magnetic field, (H) without magnetic field and locking of osmotic pump in its deflected position. Red plot indicates simulation results, with point α indicating the simulated value for room temperature diffusion rate, whose mass value is too low to measure experimentally. Although H is lower than α, it is a measurable diffusion rate due to the larger amount of RhB present in the receptor chamber. (b) (c) Reprinted with permission from [228]. Copyright 2015, AIP Publishing LLC.

The prototype device made of the cyanoacrylate treated EC membrane is tested over a span of ~55 hr. In stage 2 (A label in figure), the device is cycled through three 1hr on-off cycles with applied magnetic field as described above. In stage 3 (B label in figure), the device is cycled through six 1hr on-off cycles with the osmotic pump

activated at the start of this step. Stage 4 (C label in figure) consists of leaving the device for 6 hr while under the effect of osmotic pumping. Next, stages 5-8 (D-G label in figure) are obtained by repeating stages 3 and 4 two more times, providing four more data points. Stage 8 (osmotic pumping, G label in figure) is undergone over a 12 hr period in contrast to the previous 6 hr cycles. And finally, stage 9 (H label in figure) consist of a prolonged period of diffusion, over the course of approximately 7 hr, with the osmotic pump locked in its deflected position at the end of stage 8 (i.e. not forced convection process). To achieve this locked state, the device was removed from the small water holder, the pump's bottom EC membrane was carefully dried with the edge of KimWipes (Kimberley-Clark Corporation, Irving, Texas, United States), and the dry water inlet was completely sealed off using a carefully adhered wide area of Kapton tape (DuPont, Wilmington, Delaware, United States), in contact with the entire bottom and sidewalls of the exterior of the device.

In order to test for non-specific heating during the application of the magnetic field, an experiment was performed with an EC membrane in one case and a CA membrane in another, both fabricated as described in sub-section C, but with zero iron oxide content (Fig. 2a and 2c). The membranes were assembled into the device configuration, and after reaching a steady baseline value of RhB concentration gradient-driven diffusion from the donor chamber to the receptor chamber, the diffusion rates for a 6 hr period with no magnetic field application, and a 6 hr period with magnetic field application, were measured. Temperature monitoring by infrared thermometer and temperature probe, as well as air cooling, were performed to corroborate the findings. No measurable difference in diffusion rates was observed before and after the applications of the magnetic field for each membrane, and no measureable changes in temperature were observed using the thermometer.

One concern in using a PDMS membrane is the possibility of water permeating from the donor to the salt chamber. However, over a total of 55 hr of testing, 0.65 μL are over-estimated to have flowed into the 4mm diameter PDMS, at a rate of 11.78 nL/hr, which is calculated using a previously reported PDMS study [275]. Permeation occurs across the entire surface area of a membrane, as opposed to an isolated location, the total volume of the PDMS membrane is approximately 1 μL, and, given the overestimation of 11.78 nL/hr flow, none of the permeating water makes it out of

the bottom of the PDMS and into the salt chamber. It simply remains soaked in the PDMS and potentially permeates into the salt chamber well beyond the experiment time. Furthermore, we have found in the experiment that the salt chamber has not been dyed with any traces of RhB at the end of the 55-hr test. RhB has approximately the same molecular size as water and appears not able to penetrate the PDMS membrane used in the test.

2.3.2 Controlled Release of Model Drug

The drug release results in Figure 2.15, Figure 2.17, and Figure 2.18, show expected behavior qualitatively with regards to the effects of RF magnetic heating and osmotic pumping. In the case of the EC membrane (Figure 2.15), there is a clear increase of rate of delivery between the room temperature state at 0.58 µg/hr (stage A, this is diffusion with no pressure applied by pump), the magnetic heating state at 1.19 µg/hr (stage B), and the coupled magnetic heating and osmotic pumping state at 1.80 µg/hr (stage C). Removal of the magnetic heating, with the pump still on, drops the delivery rate to 1.59 µg/hr (stage D). Receptor concentration at its maximum is less than 1% of the donor's concentration during experimentation; therefore, the device's results are not significantly affected by the change in concentration of the two solutions, and remain a function of RhB delivery caused by the concentration gradient between the chambers, membrane properties, magnetic increase of membrane porosity, and pressurization by the pump (forced convection).

For the CA membrane (Figure 2.17), there is a clear increase of rate of diffusion between the room temperature state at 0.48 µg/hr (stage A), to the magnetic heating state at 1.41 µg/hr (stage B), and the coupled magnetic heating and osmotic pumping state at 1.97 µg/hr (stage C). Removal of the magnetic heating, with the pump still on, drops the delivery rate to 1.53 µg/hr (stage D). Again, receptor concentration at its maximum is less than 1% of the donor's concentration during experimentation.

For the cyanoacrylate treated (0.08 mL evaporation) EC membrane device with drug delivery tests recorded in Figure 2.18, there is a clear increase of delivery rate from 18.9 ng/hr in stage A with magnetic heating to 37.2 ng/hr in stage B with both magnetic heating and osmotic pumping. Without the magnetic heating but with the active osmotic pump, the delivery rate drops to 28.0 ng/hr in stage C. Stages E and

G are repetitions of stage C, over two different time intervals (6hr and 12hr), and are in good agreement with the expected value achieved in stage C (27.8 and 27.4 ng/hr, respectively). Stages D and F are repetitions of stage B, in which the magnetic field is applied together with osmotic pumping, and demonstrate repeatable and controllable pulsatile release. And finally, stage H is held for approximately 7 hr with only the diffusion process and with neither magnetic heating nor osmotic pumping, resulting in the lowest rate at 11.6 ng/hr. All measured delivery rates are on the nanogram scale and hence receptor concentration falls well below 1%.

Spectrometers have a set detection range, any concentration above that will not be measured and anything below that will be highly inaccurate; in this case α represents a simulated value of a concentration that is highly inaccurate if the measured value (which erroneously suggests that the concentration of RhB at point α is higher than at point A) is used. The reason for this is that a spectrophotometer measures both the test sample and a blank reference sample (nearly but not instantaneously) and calculates absorbance $A=\log(P_0/P)$, or $-\log(P/P_0)$, where P_0 is the reference intensity of the specific wavelength of light, and P is that of the sample. If the absorbance A is very low, it is due to the ratio of two very high numerically close values, namely P_0/P, which increases the relative error and makes it difficult for the machine to differentiate between the two values. Alternatively, if the P/P_0 ratio is too low, A is very large, and there is hardly any light that reaches the detector, making it difficult to measure the unabsorbed light at a specific wavelength.

2.3.3 Simulation-Based Device Characterization and Discussion

The simulation data is in good agreement with the experimental results, and supports two important aspects of the analytical approximation, namely the cubic volume relation and the volume displacement rate relation with the applied pressure (see Appendix A for details regarding simulation work carried out largely by collaborators at the University of California, Berkeley). First, the simulated direct pressure test on the PDMS membrane supported the cubic volume-pressure relation by observing only the PDMS membrane under externally applied pressure. With no magnetic membrane present during this test, a near-linear volume deflection under cubic pressure over time supports the αV^3 term in Eqn. (2-3) with reliable accuracy.

Under the same condition, the relation Pressure $\propto$ Time^3 is shown by plotting the applied pressure to the PDMS membrane over time, as well as the relation Volume ~ Time, by plotting volume deflection of PDMS over time. These two result in the relation Pressure $\propto$ Volume^3. The results from the direct pressure test support the analytical approximation. The simulation results of RhB transport through magnetic membrane over time are plotted along with experimental values, and all simulated parameters, along with derived results, show consistency with experimental values, indicating that the simulation as whole is physically sensible (Figure 2.18).

The drug release rate is quite consistent for each magnetic state throughout the simulation: despite the uncertainty in deciding the magnitude of P_{PDMS}, the behavior of the drug delivery and transport rate can be matched and show that with reasonable application of pressure by the osmotic chamber, constant drug delivery can be achieve with the complete device setup. While numerical smoothing requires some linear increase and decrease of pressure at the start and end of the osmotic pumping, the pressure profile of the complete device setup is approximately constant throughout the simulation, based on the assumption that the second pressure term in Eqn. (2-3) is the dominating term.

While experimentally there is a sharp increase in osmotic pressure in the first few hours once the pumping starts, the general trend of osmotic pressure is to stay at the same pressure, assuming the saturation concentration stays constant. This reasoning is based on the calculation of osmotic pressure using Morse's Law for an ideal, diluted solution. While under the same saturation concentration, introduction of water should not increase osmotic pressure. If there is no undissolved salt precipitate, introduction of water will decrease molarity of salt water in osmotic chamber, decreasing osmotic pressure. If there is undissolved salt precipitate, introduction of water will hold the osmotic pressure in place as more salt is dissolved up to saturation concentration. Thus, the general trend of a rectangular osmotic pressure profile agrees with physical sensibility under Morse's Law of osmotic pressure with an ideal solution. The balance of pressures on the PDMS membrane of the pump supports this pressure profile (see Appendix A for discussion of net forces).

Progress of parameter derivation and estimated values associated with the composite membrane are summarized in a Table 2.8 along with average RhB transport rates as compared with experimental data.

Table 2.8 Simulation-derived values of porosity and permeability for the cyanoacrylate treated ethyl cellulose-PNIPAm-SPIO composite membrane, RhB transport rate of simulated and experimental data.

State	Determined Property	Simulated Avg. RhB transport (ng/hr)	Experimental Ave. RhB transport (ng/hr)
No Pump, Magnetic Activation	Porosity: 9.70E-5 Permeability: 1.00E-21 m^2	18.457	18.894
Pump, Magnetic Activation	Porosity: 9.70E-5 Permeability: 1.00E-21 m^2	39.389	37.464
Pump, No Magnetic Activation	Porosity: 7.40E-5 Permeability: 0.75E-21 m^2	28.343	27.753
All off	Porosity: 7.40E-5 Permeability: 0.75E-21 m^2	13.699	11.569

Porosity and permeability values apply whether or not the pump is active, and as would be expected, shrinking of the hydrogel when heated by magnetic activation causes the porosity and permeability values to increase. However, the simulation results in Figure 2.18 and Table 2.8 show deviations when compared to experimental data since these values are derived from simulation using governing physics and equation that are simplified for simulation efficiency. The methods used for simulating this device can help in future optimization of device components by allowing for a quantification of membrane properties which can then be compared to each other for determining appropriate material, composition, and dimension selection.

Regarding RhB transport rates and parameter determination, simulation results indicate the drug transport rate seems consistently linear, with constant rate of drug

transport per stage. Each determined parameter is a constant value for each prescribed state (Table 2.8), also making sense physically, as it is likely for values of porosity and permeability to stay constant over time for a given magnetic state, owing to the reversible nature of SPIO heating and PNIPAm size changing, and regardless of the pumping state.

Calculations of the bending rigidity (D) of both the semi-permeable EC membrane (D_{EC}=9.5x10^{-7} N·m) and the flexible PDMS membrane (D_{PDMS}=2x10^{-8} N·m) used in the pump, show that the EC membrane is 46 times more rigid in bending rigidity than the PDMS membrane. Therefore the vast majority of the pressure generated by the osmotic pump goes into the pressurization of the donor chamber above the PDMS, as opposed to bending of the semi-permeable membrane. This is evidenced in experiments where, in an individually activated pump, the PDMS membrane is deflected while the semi-permeable membrane appears to be perfectly flat. The composite membrane has approximately the rigidity of the bottom membrane, and as such, resists deflection in the face of the pressure transferred to the donor via the PDMS membrane, allowing increased pressure for the forced convection process (as opposed to the pressure going into bending the composite membrane).

2.3.4 Device Discussion

The most noticeable difference between the types of membranes used in our system is with regards to the order of magnitude of the delivery rates observed when comparing that of the untreated CA and EC membrane devices (micrograms per hour) and that of the cyanoacrylate treated EC membrane device (tens of nanograms per hour). Vibrating sample magnetometer (VSM) measurements (Figure 2.19) confirm that samples from both membrane types, used in each of the two devices, contain approximately equal amounts of magnetic SPIO material, as expected from the fabrication procedure. Small differences in M_s may be attributed to difference in VSM sample size (a result of error during manual slicing), as well as local non-homogeneity of the SPIO distribution within the initial uncut membranes, whose effects are aggravated when sampling very small pieces.

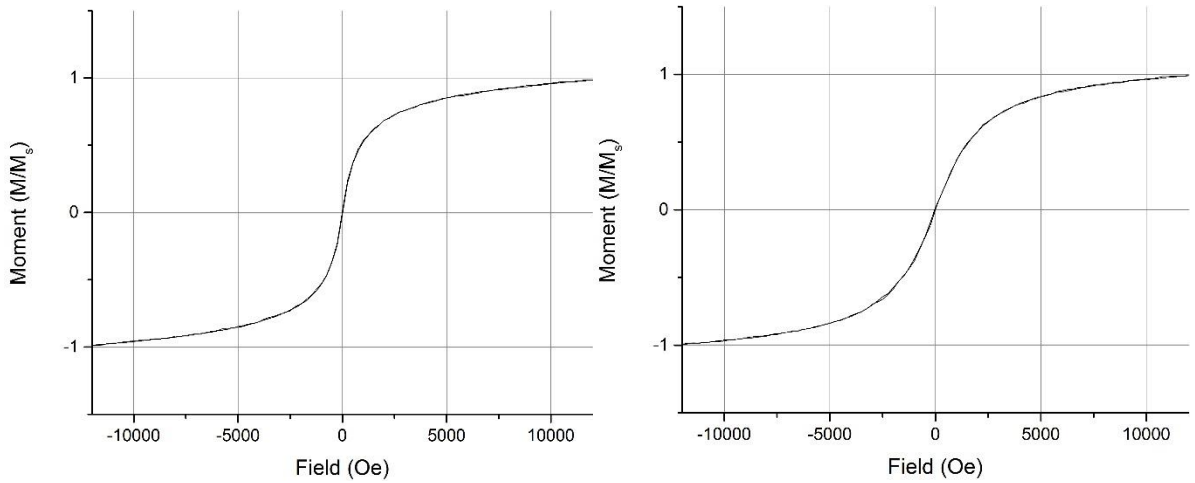

Figure 2.19 Vibrating sample magnetometer (M/M$_s$) measurements of 2 to 3 millimeter square pieces of (a) CA magnetic membrane (M$_s$ = 5.40 memu) and (b) EC magnetic membrane (M$_s$ = 4.26 memu). Small differences in M$_s$ may be attributed to difference in sample size, a result of error during manual slicing, as well as local non-homogeneity of the iron oxide distribution within the initial membrane, whose effects are aggravated when sampling very small pieces.

The difference in diffusion rates (heating versus room temperature with no osmotic pumping) are around 23-24 times when both EC and CA membrane types are tested for their diffusion profiles (Figure 2.14b, Figure 2.14c), and only 2.9 times for the CA membrane device when heated by SPIO particles (Figure 2.17, points A and B), 1.6 times for the treated EC membrane device when heated by SPIO particles (Figure 2.18, points A and H), and 2 times for the untreated EC membrane device when heated by SPIO particles (Figure 2.15, points A and B). With direct heating, heat is transferred to the entire membrane, affecting all incorporated hydrogel particles. Furthermore, both the donor and receptor cells reach the same temperature as the tested membrane, since they are submerged in the same water bath, and hence do not act as heat sinks that cool down the membrane. Therefore, two possible reasons contribute to this observation: (1) the donor and receptor cells of the devices are not heated during the inductive heating tests such that they continuously draw out energy from the membranes, unlike with the direct heating of all solutions surrounding membranes tested in diffusion cells; (2) the distribution of heat supply originating from each magnetic particles (i.e. distributed "points" in space in the membrane) can cause less-uniform shrinkage of PNIPAM hydrogel particles when compared to direct overall heating in diffusion cells. This

effect is also present in the stages consisting of osmotic pumping coupled with magnetic heating.

The diffusion cell (i) room temperature and (ii) direct heating test results for the CA-PNIPAm-SPIO membrane indicate that there is a difference of a factor of (i) 5.47 and (ii) 5.13 when compared to those results for the untreated EC-PNIPAm-SPIO membrane, respectively (Figure 2.14b, Figure 2.14c). Therefore the EC-PNIPAm-SPIO membrane design was selected for treatment using cyanoacrylate vapor deposition for even further reduction of its delivery rates (Figure 2.14d). This control layer reduces the delivery rates through the EC-PNIPAm-SPIO membrane during all device states. In this study, the thin layer of material is used for partially blocking pores at the top surface of the membrane, hence increasing the time required for permeating RhB molecules to find their way through the composite membrane and to diffuse into the receptor; the thicker the deposited cyanoacrylate material, the slower the rate. Such an approach to tuning the magnetic membrane allows for modification of drug delivery rates by changing the effective permeability of the membrane, based on patient or research requirements, without more drastic modifications to already mass-cast membranes. Results from the untreated CA and EC membrane devices (Figure 2.17 and Figure 2.15) indicate that magnetic actuation can result in higher drug delivery rate changes than osmotic pumping alone (points A to B and B to C for each device). This is desirable in practice since the osmotic pump is likely to be continuously pumping in real operation to provide a baseline dose, while the magnetic field is externally controlled, such that the variation of the delivered dose can be adjusted by the external magnetic fields.

Deviation between delivery rates in stage B, D and F in Figure 2.18 may be due to experimental error caused by slight differences in total power output of the inductive heater while generating the magnetic field. In each on-off cycle, when the field is applied, the power is modulated to a certain percentage of the power output of the machine, and this value stabilizes in slightly different times for each cycle. Such deviation does not apply to stages where the magnetic heating state is not pertinent (which is why stages C, E, and G are closer to each other). Another possible reason for the higher level of fluctuation for points B, D, and F when compared to C, E and G, is

that during ramp up and cool down of the membrane, it's temperature is more susceptible to fluctuations associated with the temperature changes and air motion within the lab setting. C, E, and G are measured at room temperature and well below the PNIPAm LCST, therefore not being as affected as B, D, and F, where a few degrees of fluctuation may result in measurable differences between the three points. That said, the temperature of the human body is a much more stable setting when using such a device in practice, and one would expect such fluctuations to diminish.

The use of a cyanoacrylate treatment allows for thin depositions from a vapor that have significant impact on drug release while bypassing limitations regarding casting a membrane at any arbitrarily large thickness, or small hydrogel content, in an attempt to reduce delivery rates. Such limitations include the following: (i) gravity and surface tension on a cast surface will limit the maximum thickness of the membrane during curing (assuming one cannot use walls because the use of a precise casting knife is in order); (ii) the thicker the membrane the more magnetic and hydrogel material is required in order to maintain appropriate heating and pore opening in the z-direction across the entirety of a thicker membrane, while simply treating the membrane with cyanoacrylate can achieve a very large amount of impedance without increasing any other materials; (iii) attempting to decrease the drug delivery rate in a highly fine tuning manner by reducing the porosity of, for example, an already low permeability membrane (i.e. reducing PNIPAm hydrogel content), is potentially more complicated than a cyanoacrylate treatment because of the risk of dropping below the required PNIPAm hydrogel percolation for having any flux across the membrane to begin with, while a very thin treatment of cyanoacrylate bypasses any concerns associated with PNIPAM percolation across the membrane.

2.4 Chapter Summary

This study demonstrates osmotically driven drug delivery devices that can provide reversible dosing states controlled remotely by electromagnetic fields. This is achieved in both the higher (μg/hr) and the reduced-rate (ng/hr) devices, consisting of components and packaging with biocompatibility in mind. Superparamagnetic iron oxide particles, internal to the valve-control membranes, provide magnetically-induced local heating that is sufficient for the volume change in the membranes' PNIPAM hydrogel particles, which occupy the pathways of diffusion and flow for the

RhB test drug, while providing no measurable heating of either the devices' packaging or drug solutions. When tested in the device configuration, the relationship between the CA (μg/hr rates), EC (μg/hr rates), and cyanoacrylate treated EC membranes (ng/hr rates) is similar to the relationship between the three membranes characterized individually for RhB flux in large volume diffusion cells, when no osmotic pumping is applied, (with the exception of the CA and EC untreated membranes in the device configuration). This suggests overall that further miniaturization of the system is possible while maintaining constant drug delivery rates within each magnetic field/pump state, as long as the drug concentration on the receiving end (patient side) remains less than 1% of the drug chamber's concentration. The origin of the differences between the delivery rates in the two setups (i.e. components that are actually heated, and the homogeneity of heating) are discussed. Modeling and simulation results confirm constant drug delivery within each device state. It is found that the contributions of the pump and the membrane change depending on the type of membrane used, and that the EC membrane device has a 23% larger ON/OFF ratio than the CA membrane device. The cyanoacrylate treatment used on the EC membrane reduces RhB diffusion by a factor of 21.4 for the room temperature condition of the device. Furthermore, despite the 23% lower ON/OFF ratio observed for the CA membrane device, the potential of replacing the more commonly used EC membrane matrix with the mechanically more robust CA matrix is shown. Calculations of rigidity, as well as experimental confirmation, show the appropriateness of the selection of PDMS and EC as the flexible membrane and semi-permeable membrane in the osmotic pump, respectively (the latter being 46 times more rigid than the former), thus providing a simple means of fabricating reliable osmotic pressure sources.

The magnetically controlled devices presented, with their wide range of delivery rates and repeatable nature, could have numerous biomedical applications, such as in treatments for patients suffering from Alzheimer's disease, diabetes, cancer, and other chronically debilitating diseases. Such designs can be implanted by minimally invasive surgery to deliver a specific drug, in the right dosage, at the right time, for the treatment of chronic debilitating diseases, while allowing for the long-term and repeatable release of small, highly

concentrated doses, depending on treatment needs. For human patients, the preferred site of implantation of osmotic devices is subcutaneous placement in the inside of the upper arm [43]. Our system lends itself well to implantation in human limbs, which can then be surrounded by a portable-sized magnetic coil when magnetic dosage control is required. In addition, such devices will significantly facilitate research relying on animal testing using osmotic drug delivery, as the added controllability and tunability of the composite membranes provides flexibility during testing. Devices can be implanted in locations under thicker layers of tissue or bone, since these would be penetrated by the magnetic field, regardless of the species. Furthermore, in mass fabrication of drug delivery devices, costs are greatly reduced if, for several device designs, the same components can be used; fixing the parameters of thickness, hydrogel type, magnetic particle type, and magnetic field of actuation, while solely tuning the cyanoacrylate control layer as done in this study, allows for a very cost effective method of designing drug delivery rates by controlling how all these components are utilized, without modifying any of them or their final dimensions. We have modeled the behavior of a cyanoacrylate treated device in two ways, using a fluidic circuit analogy, and a COMSOL simulation. The modelling matches well with experimental results, and the two approaches employed can be used for further design optimization prior to device production, including increasing the difference between the contribution of device mechanisms/components while in the "on" state and the "off" state. So far, studies have focused only on different PNIPAm hydrogel types and membrane thicknesses as membrane design parameters. These magnetically triggerable designs are not limited to coupling with osmotically induced pressure, but can be implemented with other controllable pressure sources such as RF pumps [276, 277], which may require stronger membranes such as those made with CA. For example, Appendix E demonstrates related work using PNIPAm as a mezzo-scale valve, heated via inductive heating of iron microparticles, coupled with electrolytic pumping [278, 279]. It is envisioned that several combinations using such magnetic valving, the permeability membranes discussed in this chapter, and any number of pumping sources (osmotic, electrolytic, etc.), may enable researchers and medical professionals to achieve desired arbitrary drug delivery profile control, depending on treatment needs.

Chapter 3 Magnetic Nanowires in PNIPAm Microdroplets for Drug Delivery

3.1 Synopsis

This chapter compares nanocomposite microdroplets composed of PNIPAm with embedded iron oxide nanoparticles or iron NWs for magnetically controlled release of a liquid test drug. As with the composite PNIPAm membranes work, this line of research also uses RhB as the model test drug. The microdroplets are fabricated by two phase droplet generation, with a high monodispersity distribution of size within each size population. Fabricated droplets range from monodisperse 20 μm populations to monodisperse 500 μm populations. Droplet generation in the microfluidic system occurs at frequencies up to 1 kHz. The PNIPAm microdroplets are heated by magnetically induced losses, which allows for remote controllability of the drug release from the microdroplet drug carriers. The mechanism of heat generated from losses differs depending on the type of magnetic component used; iron oxide nanoparticles undergo magnetic losses through magnetic hysteresis while iron NWs are found to generate vibrational friction in the medium of the microdroplet.

It was found that the crosslinker used to polymerize the PNIPAm microdroplets, must have a concentration of more than 2.5% for a wider range of iron oxide nanoparticles and iron NWs to be incorporated into the droplets while maintaining structural integrity.

Two modes of magnetic field application were used for the iron oxide nanoparticle and iron NW loaded microdroplets; continuous and pulsatile. A higher percent release of RhB is achieved via the pulsatile application of the field (70% versus 6.5%). NW loaded microdroplets are tested under a very low power magnetic field (low amplitude and frequency), relative to that of the iron oxide loaded microdroplets.

Magnetic triggering of the microdroplets, regardless of the magnetic component used, results in localized heating, internal to the droplets, that avoids the need for direct external heating of an entire system or surroundings of a local area in a patient injected with the droplets for drug delivery, or in a device with these droplets integrated in a valve membrane as discussed in Chapter 2. This latter secondary use of the droplets in magnetic membranes would allow for highly localized heating of the PNIPAM component in the membrane valve

system, potentially reducing response time and power requirements for the applied magnetic field.

Superparamagnetic iron oxide nanoparticles become demagnetized when no magnetic field is present, preventing magnetic PNIPAm microdroplets (MPMs) from agglomerating. If the medical treatment in question requires a high dispersion of the MPMs, this is an advantage in vivo, though one can envision localized treatments in which a tight agglomeration of injectable MPMs is desirable. Furthermore, this superparamagnetic behavior prevents the iron oxide from agglomerating within the MPMs themselves, resulting in an internal homogeneous distribution. On the other hand, this research shows that MPMs containing iron NWs are triggerable at a minute fraction of the required magnetic field strength and frequency used to generate comparable heat via superparamagnetism. Compared to the latter, less than 1.4 % of the magnetic field and 3.3 % of the frequency are needed for the NWs, which is an essential advantage for integrating and implanting devices in clinical and healthcare applications. In addition, this same field and frequency fails to trigger the superparamagnetic MPMs, which require high field strength and frequency for the phenomenon to be measurable. Compared to the values typically reported in literature for iron oxide nanoparticles, the drug release from NW filled particles is achieved with a magnetic field that is about three orders of magnitude lower in power. This difference is explained by the mechanical motion of the magnetically saturated ferromagnetic iron NWs embedded in a fluid environment, and the observations are corroborated with mathematical modeling. The microfluidic synthesis and fabrication process used for MPM production is both simple and fast, providing control over droplet size, rate of droplet generation, and the concentration of either of the aforementioned magnetic materials.

MPMs are formed and synthesized in a glass capillary microfluidic system which allows for the control of the MPM size with up to 1 kHz of droplet generation (Figure 3.1). Droplet sizes range from 20 to 500 µm, and the results reported focus on MPMs of 100 µm diameter and 2.54% v/v and 0.175% v/v magnetic metal concentrations for NW and iron oxide composite MPMs, respectively. The latter iron oxide concentration is required for heating MPMs within the same timescale/comparable heating power using a high-power 73 mT and 600 kHz field, as the NW loaded MPMs at a concentration of 2.54% v/v and a low-power magnetic field of 1 mT and 20 kHz. Results are obtained for MPMs that contain

magnetic material and synthesize properly during fabrication, as some MPMs did not respond to any applied magnetic field.

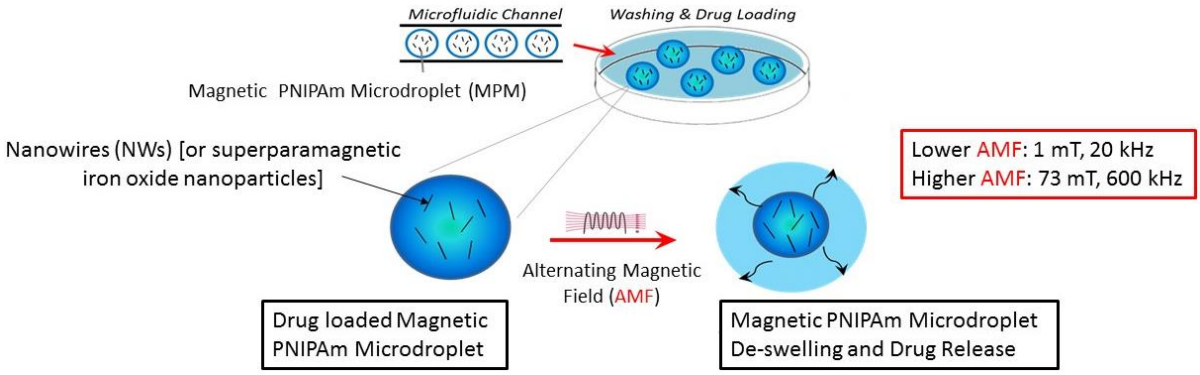

Figure 3.1 Schematic of the fabrication and drug release actuation principles for remotely triggered magnetic PNIPAM microdroplets (MPMs) with embedded iron nanowires or iron oxide nanoparticles (nanowires illustrated here). The MPMs are synthesized in a glass capillary microfluidic system and are loaded with the test drug by diffusion in an aqueous solution after post-synthesis washing. The heat generated by the nanowires or nanoparticles upon application of an alternating magnetic field AMF triggers the PNIPAm hydrogel structure, causing it to shrink and expel the aqueous drug content. Two AMFs are mainly used, one significantly lower than the other and resulting in comparable release rates.

3.2 Methods

3.2.1 Chemical Components of Magnetic PNIPAm Microdroplets

Two aqueous solutions are prepared for the synthesis of the PNIPAm hydrogel microdroplets. Solution 1 consists of 20 wt% of the monomer N-isopropylacrylamide (NIPAM), 2 mL of N,N,N',N'-tetramethylenediamine (TEMED) used as the accelerator for the reaction, 6 wt% of N,N-methylene(bis)acrylamide (BIS) used as the crosslinker, and 0.5 mL of 2-(methacryloyloxy) ethyltrimethyl ammonium chloride (METAC). The crosslinker, as previously discussed in Chapter 1, serves as a polymer bonding molecule. Solution 2 consists of 4 wt% ammonium persulfate (APS) and the magnetic particles (either iron oxide nanoparticles or iron NWs). Solution 3 consists of silicone oil (for the oil phase). All chemicals are purchased from Sigma Aldrich. Table 3.1 summarizes the constituents used in each solution described here.

Table 3.1 List of constituents of the solution phases used in the microfluidic droplet generation process.

Solution 1	Solution 2	Solution 3
20 wt% NIPAM monomer	4 wt% APS	Silicone oil (for oil phase)
2 mL TEMED accelerator	Iron nanowires or iron oxide nanoparticles	
6 wt% BIS crosslinker		
0.5 mL METAC		

3.2.1.1 Selection of Crosslinker Concentration

Experimental findings indicate that while changes in the ratios of the chemical components used to synthesize PNIPAm affected the consistency of the hydrogel, only changes in the concentration of the crosslinker resulted in a considerable effect on the MPM thermoresponsive behavior. Figure 3.2 shows the maximum percent shrinkage of MPM volume given a particular crosslinker concentration, and while under an AMF. The max percent shrinkage increases with increasing crosslinker concentrations and saturates at around 2.5%, corresponding to roughly 90% volume shrinkage. Based on the literature [81, 106, 280, 281], the hydrogel's pore sizes are affected by the crosslinker concentration; pore size increases with decreasing crosslinker concentration, thus increasing the structure's branched polymer network, while higher concentrations result in a denser, more compact gel. It is assumed that the different structures affect the distribution of magnetic material inside the MPM, with a more uniform distribution resulting from a denser polymer network, which in turn allows for a more homogenous heating of the MPM, and hence a higher max volume change. Based on these findings, experiments were conducted using a crosslinker concentration of >3 wt% to ensure the most effective thermal response from the MPMs.

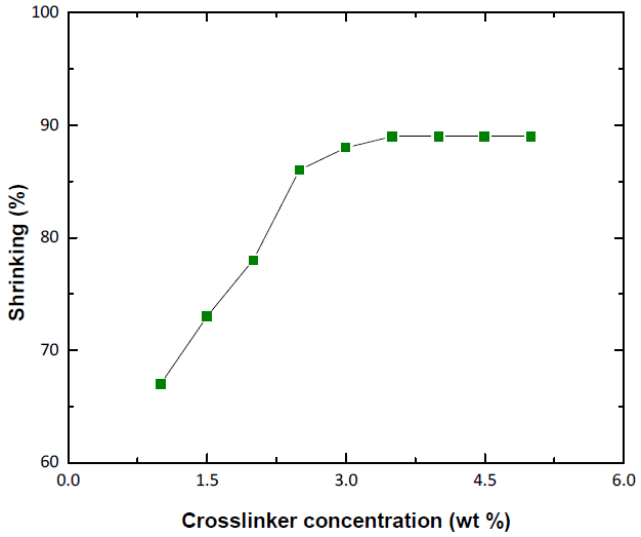

Figure 3.2 Maximum percentage shrinkage of MPM volume during magnetic triggering with respect to PNIPAm hydrogel crosslinker concentration.

3.2.2 Fabrication of Magnetic PNIPAm Microdroplets

Microfluidic systems that take advantage of tapered-capillary flow focusing and continuous multi-phase flow, can produce streams of continuous flow that generate capillary-diameter-tuned droplets, and can be used in chemical and biological applications and research [282-288].

Here, MPMs are synthesized using flow focusing, in which oil-water-water emulsions are formed (O/W/W). In O/W/W, an oil stream contains droplets generated from the two aqueous phases, one of which contains the magnetic material, both of which contain the chemicals used to synthesize the PNIPAm hydrogel. The MPM polymerization process occurs within only 2 minutes, when the PNIPAM white cloudiness is visibly observed.

The design of the microfluidic system used in this research is based on the use of tapered glass microcapillaries attached to glass slide substrates [289]. These are first well cleaned by ultrasonication in acetone, isopropanol, and ethanol for 10 minutes in each solution to remove any debris, contaminants, and organic materials. Next, two 75x25x1 mm^3 slides are taped onto a larger 75x50x1 mm^3 slide to form the main channel using double sided tape. A micro-capillary puller (P-1000, Sutter Instrument) is used to heat and pull the 800 μm diameter glass capillaries, forming the necessary tapered ends with orifice sizes for the desired droplet diameter (from 30 to several hundred μm orifices). The surface wettability

of the capillaries and the channel was modified using a coating agent (FluoroPel PFC 801A, Cytonix Corporation or Glaco Mirror Coat 'Zero', Soft 99 Co.), 0.2 mL was flushed through the channels for 5 seconds then dried by nitrogen, rendering them water-repellent [289]. Two tapered capillaries, with one slightly entering the opening of the other, are bonded to the inside of the channel by epoxy (HP 250, ITWDevcon, Inc.). This affixes both capillaries in place while separating the different solution flows. The current assembly is then covered by another 75x25x1 mm^3 slide taped onto it, again using double sided tape, sealing the channel and enclosing the tapered glass capillaries. Diamond core drilled (Eternal Tools) 1.7 mm diameter inlets in the cover are used for injecting the fluids through bonded syringe needles. Figure 3.3a shows a schematic of the completed system in operation with scale bars.

The generation of monodisperse O/W/W emulsions uses solution 3, solution 2 and solution 1 as the inner, the middle, and the outer phases, respectively. Solution 1 is injected into the channel through the first capillary on the left side, encountering solution 2 at the outlet of this first capillary (Figure 3.3a). Flow rates used in these experiments are Q_1 = 20 μL/min (solution 1), Q_2 = 2 μL/min (solution 2) and Q_3 = 120 μL/min (solution 3). Since the viscosities of solution 1 and solution 2 are similar, resulting in a very low local shear stress which does not pinch off solution 1 into droplets within solution 2 (Figure 3.3b). The laminar flow prevents the two first solutions from mixing and polymerizing in the first capillary. The shear stress from solution 3 pinches off the solution 1 and solution 2 streams when they reach the outlet of the second tapered capillary (located under the inlet of solution three with Q_3 flow rate, Figure 3.3a), generating the desired monodisperse droplets (Figure 3.3d). The MPMs are dropped into a glass container at the microfluidic outlet, filled with 100 mL of water. The MPMs are collected by filtration using a 40 μm pore size film (Fisher scientific), then re-suspended in 100 mL of water, and collected again. This washing process is performed three times to remove any unreacted and unnecessary components or chemicals. The MPMs are stored at room temperature while suspended in DI water to maintain full hydration before use in subsequent experiments.

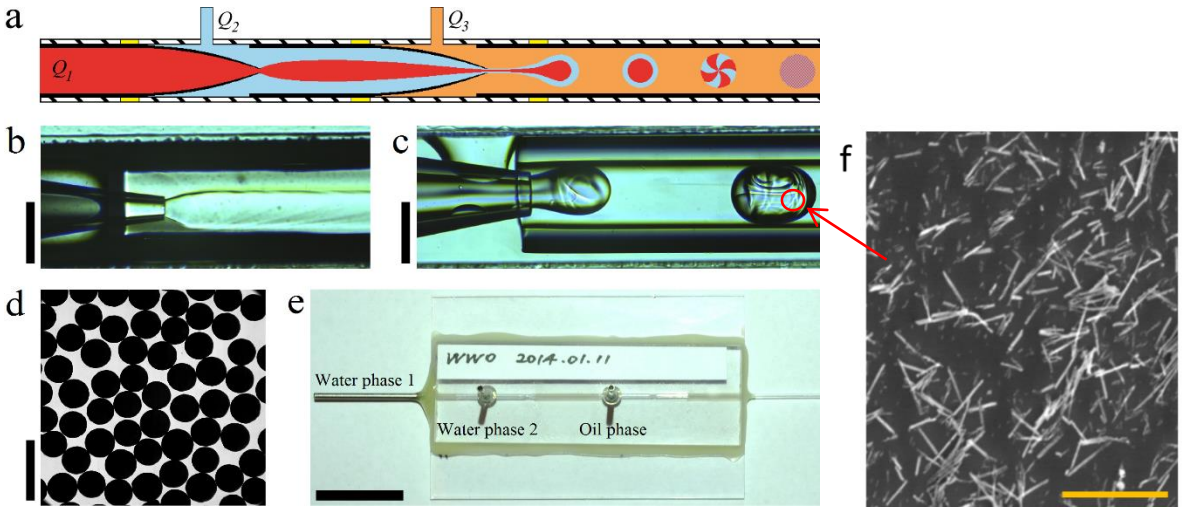

Figure 3.3 (a) Schematic the microfluidic system and synthesis process of MPMs. The inner and middle water phase and the outer oil phase flow rates are Q1 (20 µL/min), Q2 (20 µL/min) and Q3 (120 µL/min), respectively. (b) Image of the outlet of the first capillary as it generates a continuous laminar flow of the two streams Q1 and Q2. (c) Image of flow focus generation of the microdroplets. (d) Microscope image of several MPMs after fabrication. The MPM size distribution can be described by a PDI index, defined as PDI = (δ/d_{av} x 100) %, where δ is the standard deviation and d_{av} is the MPM diameter average. Over 500 MPMs are imaged and a PDI value of 3.9 % is found, indicating high monodispersity of droplet generated MPMs. (e) Image of the microfluidic system. (f) Scanning electron microscopy imaging of iron nanowires. Scale bars are 400 µm in (b) and (c), 200 µm in (d) 2 cm in (e) and 2 µm in (f).

3.2.3 Fabrication of Magnetic Iron Nanowires

Iron NWs of approximately 5.5 µm in length and 45 nm in diameter are fabricated by pulsed electrodeposition in porous anodized aluminum oxide templates, as previously discussed in Chapter 1 [214, 216, 217], and summarized as follows for convenience. Further details regarding the author's constructed fabrication system, as well as component blueprints and images associated with each step in detail, can be found in Appendix C. High purity aluminum disc substrates (99.999%, Goodfellow) are rinsed and sonicated in acetone, then isopropanol, and finally distilled water, with the sequence repeated three times, and each solution sonication lasting 5 minutes. Next, discs are electropolished for 3 min at 25 V (2 A current limit), with the discs connected to the negative terminal and submerged in a stirred electropolishing solution (25% perchloric acid and 75% ethanol concentrations), along with a positive electrode (Pt mesh). This process breaks down surface defects, smoothening the surface and promoting nanopore ordering (next step). This electropolishing solution is kept at 4°C prior to use; the cooler the temperature, the more efficient the electropolishing process.

The polished substrates are then anodized in 0.3M oxalic acid at 2-4°C, using an applied voltage of 40 V (positive electrode Pt mesh, negatively charged Al substrates, both in acid), for the first anodization step (24 hr). This generates slightly ordered nanopores whose ordering increases with depth of the grown anodized aluminum oxide layer. The aluminum oxide layer is dissolving at 37°C well within 12 hr using a slow acting solution (1.8 g chromium VI oxide, 7.1 g phosphoric acid, 100 mL distilled water), leaving the bottom aluminum substrate with highly ordered indentations used as seeds for the second anodization process.

The second anodization (10 hr) uses the same conditions as the first anodization and results in an approximately continuous level of ordering from top to bottom of the second anodized aluminum oxide layer. In this work, nanopores are approximately 45 nm in diameter and are hexagonally ordered.

An exponentially decaying applied voltage (40 V down to 4.5 V) using oxalic acid at 2-4°C results in dendritic openings at the bottom of the pores, which allow for electrical contact between any solution placed in the pores, and the substrate's un-oxidized and conductive aluminum bottom (required for electrodeposition of metal).

Finally, pulsed electrodeposition (-60 mA for 2 ms, 5 V for 2 ms, 1 s rest time), graphed in Figure 3.4, is used to deposit Fe NWs from a pH 4 electrodeposition solution (45 g/L of $FeSO_4 \cdot 7H_2O$, 30 g/L of H_3BO_3, 1 g/L of $C_6H_8O_6$ ascorbic acid). The NW length can be tailored using the deposition time. The amount of deposited material is related to the electric charge that flows through the system by Faraday's law, which states that the mass of deposited material and the charge that passes through the deposition area are proportional:

$$m = \frac{M}{n\, e\, N_A} \int_0^t I dt \tag{3-1}$$

where I is the current, t is the deposition time, N_A is Avogadro's number (6.022×10^{23} [1/mol]), n is the valence of the deposited ion, M is the molar mass and e is the electron charge (1.602×10^{-19} C). NWs are released from the aluminum oxide nanoporous membrane using fast acting 1M NaOH, and collected in plastic tubes (Eppendorf) using a magnetic rack (DynaMag-2, Invitrogen) for cleaning in ethanol and storage prior to use.

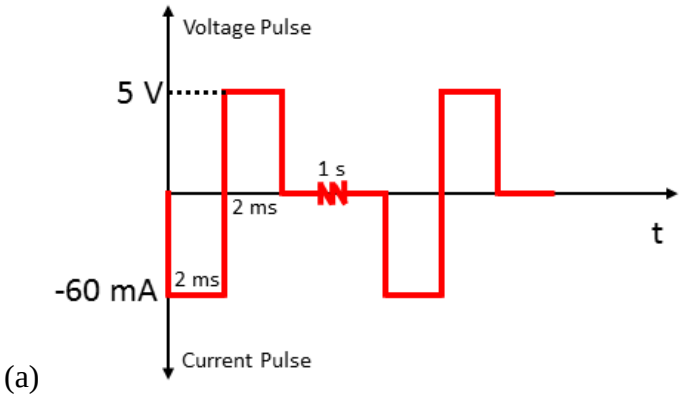

(a)

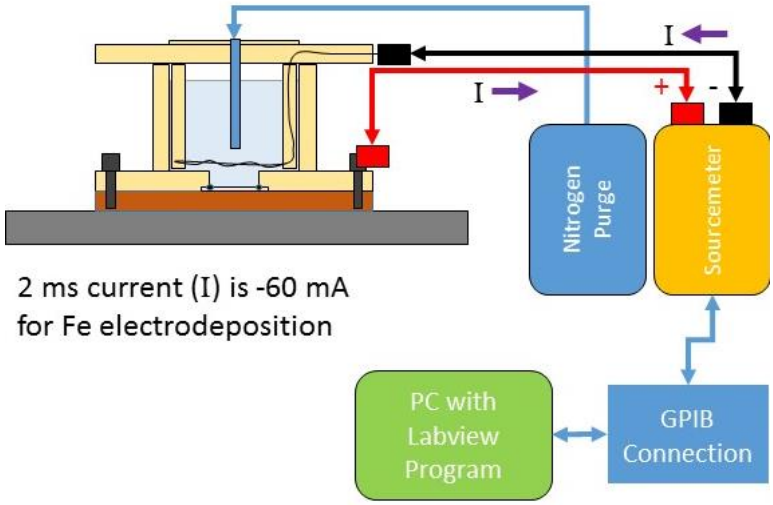

(b)

Figure 3.4 (a) Voltage and current profiles for electrodeposition of iron nanowires in aluminum oxide templates. (b) Schematic of electrodeposition process, nitrogen purge protects oxidation of iron electrodeposition solution.

The 5.5 μm NWs are ultrasonicated to average lengths of approximately 500 nm (Figure 3.3f), followed by sonication within solution 2, prior to microdroplet fabrication. To compare the effects of shape on nano-scale particles made of iron, VSM measurements of iron particles and fabricated iron NWs and are shown in Figure 3.5.The curves suggest that a set of wire shapes will experience larger magnetic torque due to its overall higher magnetization for any applied field strength. This is due to the single domain state of the nanowires which allows them to undergo large torque without switching magnetization, as the experimentally applied field does not exceed H_{sw}. The measurements taken for 5.5 μm NWs represent the shape of the hysteresis curve of sonicated wires, since the latter have an aspect ratio of 10 or greater, namely approximately 500 nm / 45 nm (see section 1.4.3).

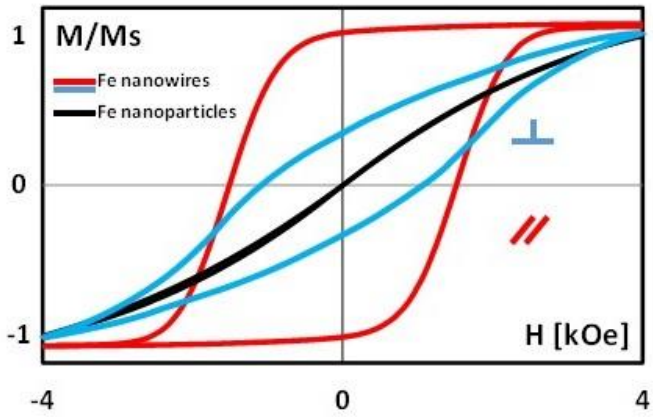

Figure 3.5 Magnetization of ~500 nm – 2 µm iron nanoparticles (not iron oxide) and un-sonicated 5.5 µm iron nanowires. Nanowires are measured with applied field parallel (red) and perpendicular (blue) to the wires. Due to shape anisotropy, regardless of the orientation of the nanowires relative the applied field, the remanent magnetization M_r will always be higher than that of the spherical particles, and the average of which for some disordered dispersion of nanowires will lie between the M_r values for aligned iron nanowires parallel to the field and iron nanoparticles (y-intercept of red and black curves here).

3.2.4 Characterization of Magnetic PNIPAm Microdroplets

3.2.4.1 Normalized Swelling-deswelling Ratio

The normalized swelling-deswelling ratio, defined below, is used to characterize the thermoresponsive behavior of magnetically triggered MPMs.

$$SR = (W_w - W_d)/W_d \tag{3-2}$$

W_w is the mass of the fully hydrated wet MPM, while W_d is the mass of the MPM when dehydrated and hence deswollen to a certain degree [290-292]. The literature uses the terms "degree of swelling," "equilibrium degree of swelling," (EDS) or "swelling ratio" (SR) for such measurements. To study the effect of embedding nano materials in PNIPAm, a comparison is made between the SR of pure PNIPAm microdroplets, and the SR of MPMs of different size and magnetic material concentrations. All direct heating (i.e. non-magnetically induced MPM activity) measurements were recorded at temperature between 28 ºC and 42 ºC in a temperature-controlled water bath.

The SR ratio is calculated using gravimetrically measured values of mass. A simple example of gravimetric analysis is that of suspended solids in a sample of a known volume of water; filtering the water results in a measurable mass of the remaining solids. For the

MPMs, the fully wet and subsequently drier states are measured after excess water is eliminated by filtration using 40 μm pore size films (Fisher scientific). To measure the fully dried mass, samples are filtered and dried in vacuum. Plots and data of SR reported here are normalized with respect to room temperature SR values.

3.2.4.2 Drug Loading

MPM loading and release procedures are as follows. The loading of the hydrophilic Rhodamine-B (RhB) dye is achieved by physical diffusion into the PNIPAm hydrogel polymer network by immersion and suspension in water with 1 mg/mL concentration of RhB at room temperature for 96 hr.

The MPMs are washed twice by water/filtration, to eliminate any unabsorbed RhB which would affect UV spectroscopy measurements. Calculation of the loading efficiency entails sampling 10 mL of an aqueous RhB solution both before and after the MPM loading process, and measuring the RhB content using UV spectroscopy (Picodrop 200, Bioneer).

The loading efficiency is calculated using UV spectroscopy results for 10mL of RhB-water solution (before and after loading), using the following equation.

$$Load_{eff} = \frac{initial\ RhB\ mass - remaining\ RhB\ mass}{initial\ RhB\ mass} \tag{3-3}$$

3.2.4.3 Drug Release

The release measurements are performed by placing an amount of RhB loaded MPMs contained in 100 mL of water in the container used for magnetic stimulation testing. During the experiments, 10 mL of water are sampled both before and after each AMF application and the RhB content is measured using UV spectroscopy.

The applied AMF used for magnetic stimulation of iron oxide nanoparticles in MPMs is generated using a 3 kW inductive heater (Induktive Erwärmungsanlagen GmbH, Austria), producing a 72 mT, 600 kHz field. The inductive heater is cooled by a chiller system, which prevents heating of the magnetic field generating coil. The MPMs are placed in a plastic non-conductive container (2.5 cm diameter, 12 cm height), in the inductive heater's coil's center (coil is 50 mm in height, 42 mm inner diameter, 4 turns, air core), and insulated using a PDMS cover [293].

The applied AMF used to magnetically trigger iron NW filled MPMs is generated using a 2 mm diameter air core 48 turn coil (6 layers of 8 turns per layer) made of a Litz wire (40 µm diameter strands, 60 conductive stands within the single Litz wire coil), producing a 1 mT, 20 kHz magnetic field. An advantage with regards to ensuring that heat generation is limited to the heat generated by the NWs is the coil's size, distance from microdroplets, and most importantly minimal power usage, making it unnecessary to use a cooling system with such power requirements as that used to cool the inductive heater experiment.

3.3 Results and Discussion

3.3.1 Thermoresponsive Behavior Magnetic PNIPAm Microdroplets

In Figure 3.6, the SR for different MPMs with respect to temperature are normalized by dividing each microdroplet's SR values by its maximum SR value, prior to any shrinking, such that each data set begins with $SR/SR_{max} = SR_{max}/SR_{max} = SR_{normalized} = 1$. A similar behavior is recorded for pure PNIPAm and MPMs regardless of magnetic material type or concentration. From this we conclude that the integration of magnetic content in the PNIPAm microdroplets has negligible effect on the thermoresponsive nature of the microdroplets.

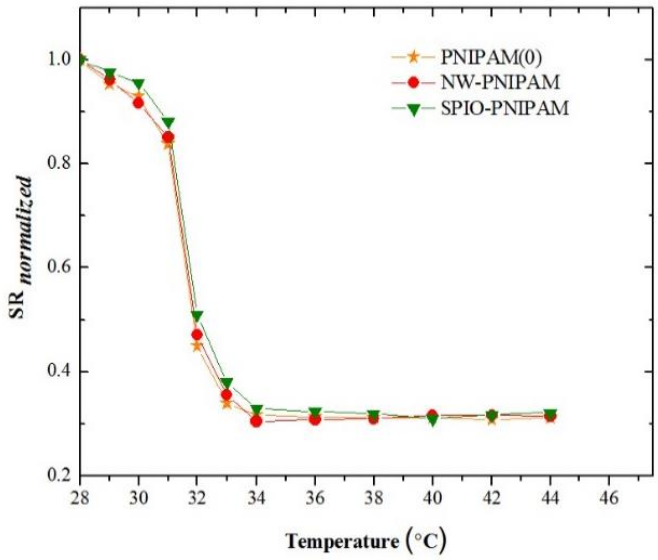

Figure 3.6 Under direct heating, normalized swelling-deswelling ratio (SR) of pure PNIPAm [PNIPAM(0)] microdroplets containing no magnetic material as well as that of magnetic PNIPAm microdroplets (MPMs) magnetic compositions using superparamagnetic iron oxide nanoparticles and (SPIO) iron nanowires (NW). Measurements are taken while MPMs are under direct external heating in a temperature controlled water bath with no magnetic field application.

This finding contrasts with previously reported synthesis methods in which the chemical grafting of nanoparticles and PNIPAm hydrogel networks results in a decrease in the thermosensitivity of the PNIPAm structure under direct heating [294]. This can be explained by the fact that the non-grafted materials used in this research only negligibly interfere with the changes in the 3D hydrogel polymer chains and, despite not being chemically attached to the chains, can still act as effective heat sources through their respective mechanism. This is particularly true in the case of NWs in PNIPAm, for which the more unrestrained the motion, the higher the level of vibration and heat generation. From Figure 3.6, the LCST can be confirmed to be approximately 31 ºC [295, 296], which is in line with typical values reported [75, 148, 172, 297, 298].

3.3.2 Magneto-Thermoresponsive Behavior Magnetic PNIPAm Microdroplets

To induce an MPM response to magnetic stimuli, the SR is measured when a 72 mT, 600 kHz alternating magnetic field (AMF) is applied to the superparamagnetic iron oxide (SPIO) nanoparticle filled MPMs, and when a 1 mT, 20 kHz AMF is applied to the iron NW filled MPMs. Figure 3.7a shows the SR as a function of the AMF duration for the nanoparticle filled MPMs. A small decrease in SR is observed in the first two minutes of AMF application, followed by a rapid decrease in SR around 200 seconds, before reaching maximum shrinkage at 400 seconds. Figure 3.7a also shows the SR as a function of the AMF duration for the NW filled MPMs. A small decrease in SR is observed in the first 3 to 4 minutes of AMF application, followed by a rapid decrease in SR around 550 seconds, before reaching maximum shrinkage at 850 seconds. The overall magnetically controlled thermoresponsive behavior of the MPMs is quite similar to the behavior resulting from direct thermal heating of the microdroplets (Figure 3.6). These results indicate that the LCST of nanoparticle and NW filled MPMs occur near 200 and 550 seconds after AMF application, respectively. The maximum shrinkage obtained after saturation is close to SR values previously reported in a work with the specific intent of increasing the thermosensitivity of PNIPAm microdroplets [299]. Furthermore, when applying the lower AMF to pure PNIPAm and SPIO filled MPMs, almost no SR change is observed, indicating that the change in SR at such a field is attributed to the special mechanism of heating generated by the vibrating NWs, and that magnetization losses in iron oxide are not high enough to induce shrinkage under these conditions. Figure 3.7b shows the average changes in temperature, ΔT, for the two

types of MPMs responding to an applied AMF, and these are derived from direct thermal heating (Figure 3.6) and magnetic triggering results (Figure 3.7a).

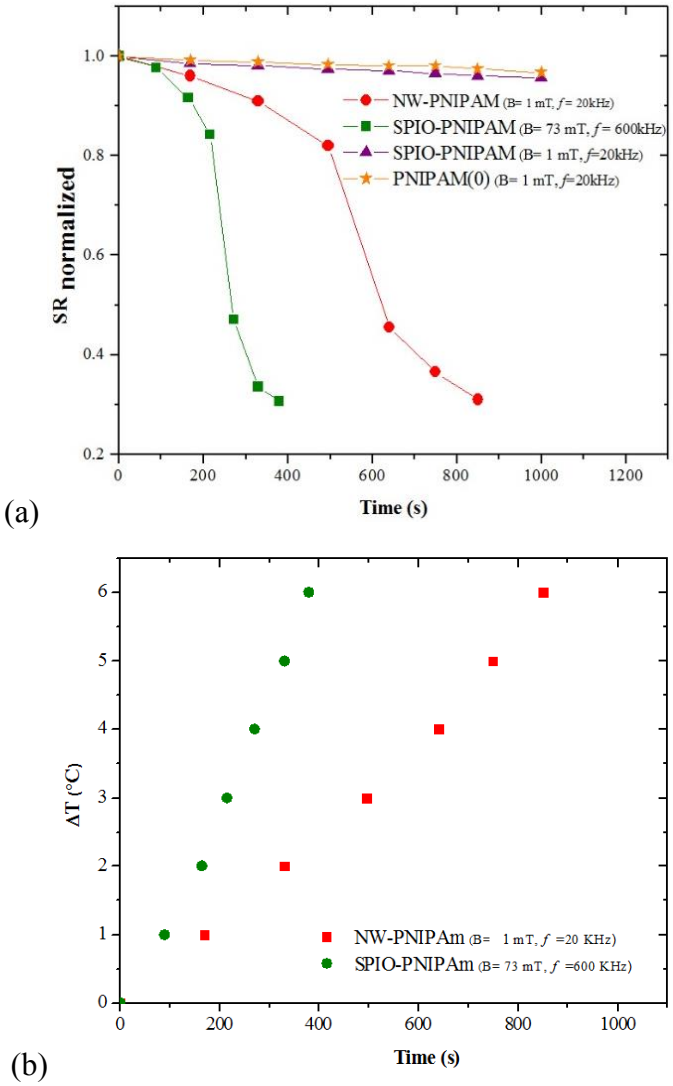

Figure 3.7 (a) Normalized swelling-deswelling SR ratio of superparamagnetic iron oxide (SPIO) nanoparticle filled MPMs (higher field, 73 mT 600 kHz) and iron nanowire (NW) filled MPMs (lower field, 1 mT 20 kHz), responding to applied alternating magnetic fields (AMF), along with control tests including pure PNIPAm [PNIPAM(0)]. The rapid decrease near 200 seconds and 550 seconds, respectively, corresponds to the time required for the lower critical solution temperature to be achieved. (b) Average temperature of the MPMs caused by NW and SPIO heating, at lower power and higher power AMFs as indicated, over time.

Figure 3.8a shows up to 25 min of attempting to trigger a size change in SPIO filled MPMs using the lower AMF condition; no change is observed, while Figure 3.8b-d shows the shrinking MPMs of all types.

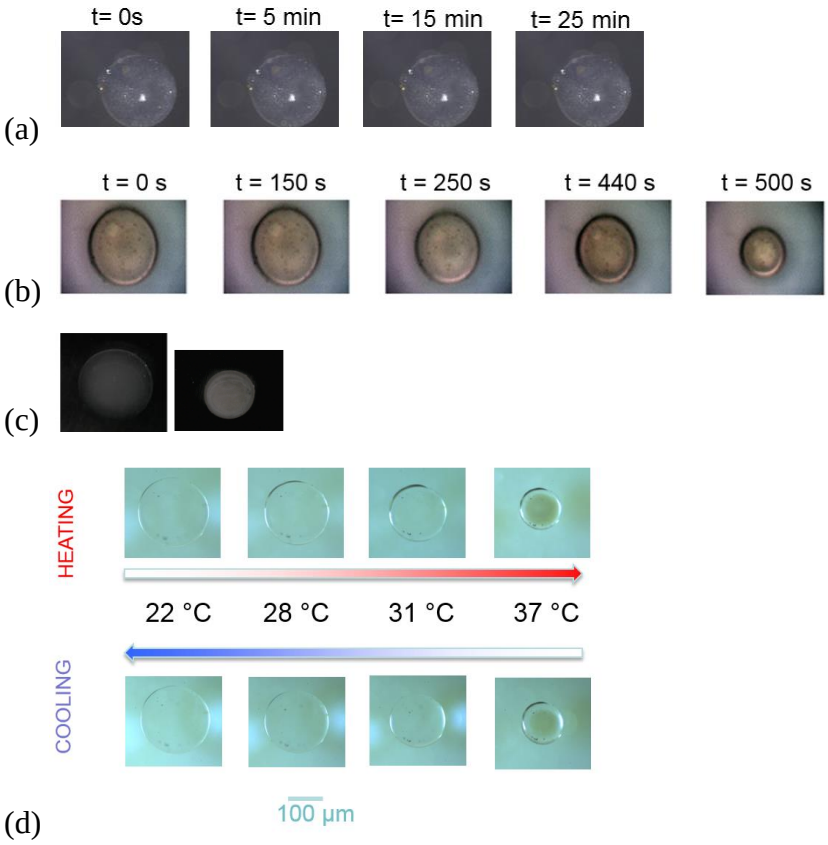

Figure 3.8 (a) Time-dependent imaging of SPIO filled MPM under the lower AMF condition, showing no notable shrinkage and hence the negligible SR change in Fig. 3.7a. (b) Time-dependent imaging of NW filled MPMs under the lower AMF condition, showing shrinkage. (c) Unheated and heated SPIO filled MPMs under the higher AMF condition, showing shrinkage. (d) Imaging of heated and cooled pure PNIPAm microdroplets.

Considering specifically locally the magnetic field and frequency at the SPIO filled MPM or the NW filled MPM particle, under the high power or low power magnetic field condition, the efficiency of each composite type can be calculated then compared, using Figure 3.7a which provides the total shrinkage time for each particle type, and the fact that the local power P is given by P = IU, where the voltage U $\propto$ dB/dt, and the current I $\propto$ H $\propto$ B. U and I are the voltage and current required to produce such local fields B or H. Given these proportionalities, the following is deduced:

$$P \propto B^2/t \quad \text{or} \quad P \propto B^2 f \tag{3-4}$$

where f is the frequency of the applied fields. For each case, the applied field and frequency values are the same locally to the particles as around them, and it is the total power of each

coil (which includes the field outside the coil) that is being neglected. However, since a researcher may design a coil in any number of ways to achieve the values reported here for both high and low power fields, by switching our focus to the local field power, we generalize the comparison.

Since it is desirable to reduce the shrinkage time as well as the value of B^2f, Table 3.2 shows effectiveness E_{NW} and E_{SPIO}, acquired by multiplying B^2f by shrinkage time and volume ratio of magnetic material to PNIPAm, and taking the inverse. For example, if the shrinkage time is large (undesirable), and B^2f is large (undesirable), then their product is large, and the effectiveness E is small. It is found that, given the parameters used here, E_{NW} is over 5000 times more effective when considering the local magnetic field. Considering the total magnetic field may increase this value even further.

Table 3.2 Efficiencies of NW and SPIO microdroplets with respect to max shrinkage time and local field power.

Symbolic Expressions	Mathematical Expressions	Values
Effectiveness of Iron Nanowires: E_{NW}	1/[0.0254 x 850s x 20kHz x $(1mT)^2$]	2.32 x 10^{-6} [1/mT^2]
Effectiveness of Iron Oxide Particles: E_{SPIO}	1/[0.00175 x 400s x 600kHz x $(73mT)^2$]	4.47 x 10^{-10} [1/mT^2]
Effectiveness ratio: E_{NW} / E_{SPIO}	5.88 x 10^{-8} / 7.89 x 10^{-13}	5.18 x 10^3

3.3.3 Modeling of Nanowire Vibration in PNIPAm Microdroplet

To explain the mechanism of NW heating, the power density (referred to as PD in mathematical equations of this chapter) required for triggering particle shrinkage is first determined by modeling SPIO power generation. The heat generated by the superparamagnetic SPIOs, when exposed to an alternating magnetic field, is a result of magnetic losses that occur due to the aforementioned two mechanisms: Neel relaxation and Brownian relaxation. τ_N and τ_B are calculated using Eqn. (1-20) and Eqn. (1-21) [166]. The

viscosity of the environment in which a SPIO filled MPM is suspended was estimated to be that of its surrounding aqueous solution contained in the hydrogel.

The volumetric power dissipated by SPIOs is obtained using Eqn. (1-30) [168], where χ_i is dependent on the frequency, effective relaxation τ, and the static susceptibility $\chi_0=\partial M/\partial H$ (which is obtained from the magnetization curves of the SPIO nanoparticles):

$$\chi_i = \frac{2\pi f\tau}{1+(2\pi f\tau)^2}\chi_0, \tag{3-5}$$

where the effective relaxation time τ is calculated as:

$$\frac{1}{\tau} = \frac{1}{\tau_N} + \frac{1}{\tau_B}, \tag{3-6}$$

The volumetric power dissipation of SPIO filled MPMs can now be calculated. Using Eqn. (3-6), an alternating magnetic field of 73 mT in amplitude and 600 kHz in frequency, χ_0 = 5.34, K = 13.5 kJ m^{-3}, and τ_0 = 1 ns, the total power dissipated inside an SPIO filled MPM is PD_{SPIO} = 5.8x10^5 W/m^3. PD_{SPIO} therefore causes the microparticle to exhibit the experimentally observed shrinkage.

Supported by previous work on rotating bodies in fluid media [210, 211, 213], the 2nd order non-linear ordinary differential equation reported is used, and simplified for the case of a fixed direction AC magnetic field. The equation (Eqn. (1-33)) is solved using Matlab (code included in Appendix D) to determine the angle of rotation θ_l of one Fe NW in PNIPAm during one cycle of the magnetic field. Here $\theta_l(t)$ is the angle between the NW and the fixed magnetic field direction with respect to time, C is a geometric factor (see below), η is the viscosity of PNIPAm (see below), r is the radius of a the NW (22.5 nm approximately, measured via SEM imaging), ρ is the density of iron (7870 kg/m^3), **H** is the sinusoidal applied AMF (1 mT approximately), M_s is the magnetic saturation value for iron NWs (1.71x10^6 A/m), since the NWs are brought to magnetic saturation prior to droplet fabrication, and L is the length of the NW (500 nm average length after repeated heavy sonication). A value of the geometric constant is calculated, C = 0.1443 [213], determined for a two segment NW with a 500 nm to 45 nm aspect ratio. C, N, and the relationship between C and the N segments of the wire, are described in section 1.4.5.3.

The total angle traveled by one NW in one full cycle, denoted by K (rad), is simply 2 times the absolute value difference between $\theta_l(0)$ at the beginning of a cycle, and $\theta_l(t/2)$ halfway through the cycle. The initial position of $\pi/4$ best represents the average NW position with respect to the fixed direction of the AMF, since each NW lies at an angle between 0 and $\pi/2$ with respect to the field, regardless of physical or magnetic orientation. The situation present under a 20 kHz AMF with fixed direction is similar to the extreme case discussed by Keshoju *et al* [213], in which the NW oscillates around its position, without fully rotating, while under a fast rotating magnetic field, with the difference being that the angle between the field direction and the NW start position in this study remains fixed.

The viscosity of PNIPAm environment surrounding a nanoscale wire is estimated to be approximately that of water, with the assumption that frequency and force from NWs as so high as to rupture the PNIPAm network surrounding them, and interact with contact to water, given additionally that the droplet is over 90 %v/v water.

The work in the first half of a cycle, W_1 [N·m], required to achieve an angular displacement K/2 for one NW, is found by integrating magnetic torque over the displaced angle (using the form of Eqn.(1-35)).

It is found that K = 31.91º (K/2 = 15.96º per half cycle). The total work is the sum of W_1, and W_2 (the work done during the second half of the cycle), which are equal, therefore $W_{total} = 2 \cdot M_s VH \cdot \cos(\theta_f - \theta_i)$. Work input into the PNIPAm-NW system is converted to heat generation; energy from the magnetic field converts to kinetic energy in the internal NW in the form of magnetic torque over angular displacement, which in turn converts to energy loss that is transferred from the NW to its surroundings via hydrodynamic friction. Other forms of loss, such as radiation, are negligible in such a system.

Finally, the power generated by the NW, P_{NW} [W/s, or N·m/s, per NW], is found by multiplying W_{total} with the magnetic field frequency (20 kHz), $P_{NW} = W_{total} \cdot f$. With a 2.54 %v/v concentration of Fe NWs in PNIPAm, and a total volume of a droplet $V_{droplet}$, the total number of NWs N_{NW} in a droplet is determined, $N_{NW} = (0.0254 V_{droplet})/V_{NW}$, and the total power of a NW loaded droplet is then $P_{droplet} = P_{NW} \cdot N_{NW} = 1.58E\text{-}6$ W. The power density is then simply $PD_{NW} = P_{droplet} / V_{droplet} = 4.84 \times 10^5$ W/m^3, which is compared to the PD_{SPIO} reported above. The difference in PD values may account for the difference in maximum shrinkage time in Figure 3.7.

3.3.4 Drug Release

The loading efficiency L_{eff} is found to be 30%, after MPMs are loaded with RhB by physical diffusion. Drug release is reported below for continuous AMF application (magnetic field on for specified duration of time) and for pulsatile AMF application (magnetic field cyclically applied in the form of pulses with rest times).

3.3.4.1 Continuous Drug Release

The MPMs are first tested for continuous release with the AMF applied continuously while the drug release is measured over time. The percent release profiles with respect to time for the two kinds of MPMs are shown in Figure 3.9a, which correlate well with the shrinkage and temperature change results found with the application of the same AMFs (Figure 3.7a).

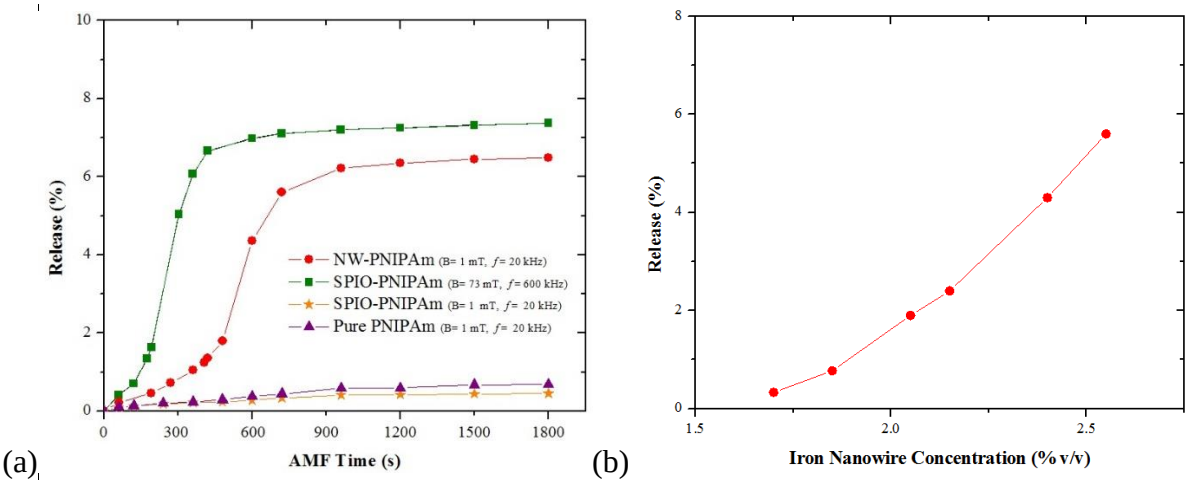

Figure 3.9 (a) Release profile of RhB with respect to time from control non-magnetic pure PNIPAm microdroplet, iron oxide nanoparticle loaded MPM, and iron nanowire loaded MPM, when a low power and high power alternating magnetic field is applied for continuous release (as indicated in legend). (b) Effect of nanowire concentration on the time required to release 4% of RhB using low-power AMF conditions (B = 1 mT, f = 20 kHz).

Control tests are also done by applying the lower field to pure PNIPAm microdroplet and SPIO loaded MPM. Under this condition, pure PNIPAm droplets and SPIO MPMs release only about 0.5 % within 30 minutes. In the case of NW MPMs at low-power field and SPIO MPMs at high-power field, the release is slow at first (before reaching LCST), then increases sharply from approximately 2% to 6%, when the MPMs shrink dramatically and the gel begins to collapse, expelling an equal amount of reduced volume in the form of RhB solution. Finally, the release saturates at around 6% and 7% in the case of NW and SPIO

MPMs, respectively. It should be noted that the AMF time is over 100 minutes, yet only a very slow increase was observed beyond the release rate level off. This may be due to the normal diffusion of RhB, estimated to be around 0.3 to 0.5 % per hour. The faster release rate of the SPIO MPM corresponds to the MPM's faster SR responsiveness at a higher power AMF (Figure 3.7a). When the release rate levels off and the profile saturates, the maximum shrinkage is achieved (as in Figure 3.7a), and the hydrogel's inner pores significantly decrease in size or close [295] during the process of MPM temperature stabilization.

The effect of the concentration of NWs is shown in (Figure 3.9b), when the lower power AMF of B = 1 mT and f = 20 kHz is applied continuously for 15 minutes. Below 1.7 % v/v of NWs, no significant release is observed; the total heat produced by the lower number of NWs is not sufficient to generate a response in the MPM. Between 1.7 and 2.3 % v/v, the release is small, with values below 3 %. Within the concentration range of 2.4 and 2.54 % v/v, the temperature reaches the LCST, causing an increased release due to pronounced shrinking. While maximum shrinking is obtained with a concentration of 2.54 % v/v, the release continues to increase with concentration, though at slower rates. Further increase of the NW concentration beyond this range adversely affects the polymerization of the gel and the integrity of the microparticles.

Similarly to the control experiment, no notable release was observed experimentally when the SPIO nanoparticle concentration was reduced below 4 mg/mL, as the associated power does not generate a sufficient temperature change due to heat dissipation, which counteracts the effects of magnetic heating.

3.3.4.2 Pulsatile Actuation Drug Release

This study explores the effects of pulsatile AMF generated release, an important application for several types of drug delivery, including successive release pulses of insulin [300]. The pulsatile RhB release mode is achieved by applying an AMF pulse for 12 minutes (720s, to allow for MPM collapse beyond PNIPAm LCST), followed by a 5 minute period with no stimulus (to allow for re-swelling), and repeating the process. Pulse duration is selected based on Figure 3.7a findings. Figure 3.10a shows that the NW MPM maintains a relatively constant release for each pulse, even after 16 cycles, and a total release of nearly 70% was achieved in less than 3.5 hr (lower power field). Similar results are found for the SPIO MPM using the higher power field, with a total release of 80 % obtained. Figure 3.10 also shows

that negligible release is obtained from pure PNIPAm and SPIO MPM under the pulsatile lower power AMF. Again, the small release may be due to RhB normal diffusion. Unlike the continuous AMF mode in which the gel can collapse (leading to a decrease of the pore dimensions or clogging of the pores), the pulsatile AMF application mode enables the gel to re-swell, resulting in an opening of the pores for the next cycle [301]. The difference in release profiles and performance when compared to continuous AMF application can be explained by the fact that a 70 % drop in SR (in weight percentage) of the droplet (Figure 3.7a) does not correspond to a 70 % expulsion of the aqueous-loaded RhB for the continuous AMF application mode, and therefore the loaded RhB must be adsorbed to the PNIPAm polymer network, and undergoes a small release for a single continuous pulse actuation (6% to 7%, Figure 3.9a).

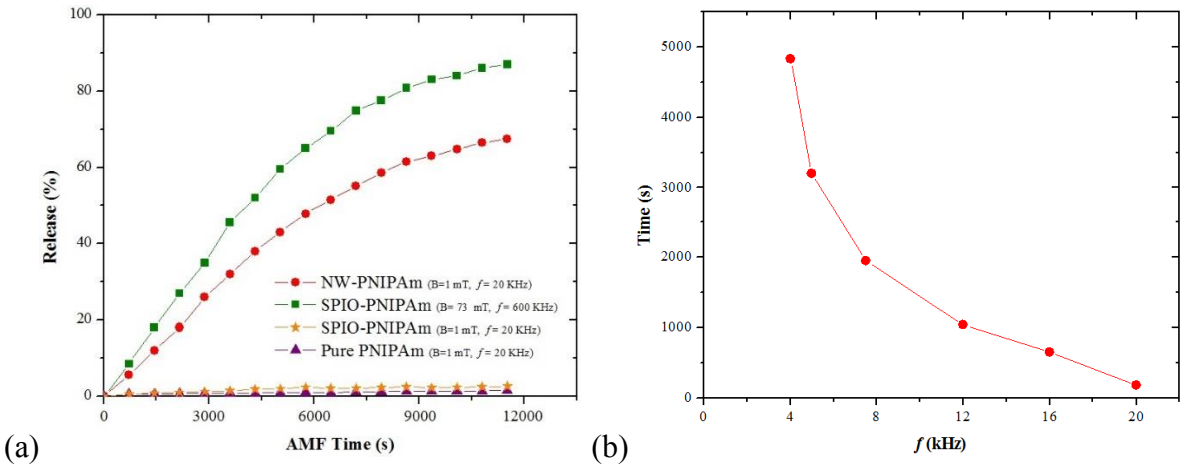

(a) (b)

Figure 3.10 (a) Pulsatile AMF generated release profiles of RhB from non-magnetic control pure PNIPAm, iron oxide nanoparticle loaded MPM, iron nanowire loaded MPM, by consecutive alternating magnetic field (AMF) applications. MPMs are exposed to an AMF for 12 minutes separated by 5 minute intervals. (b) Effect of AMF frequency on time required for 4% RhB release using lower power AMF (B = 1 mT, f = 20 kHz).

In contrast to the continuous AMF mode, the pulsatile AMF process allows for the re-dilution and de-adsorption of the RhB dye that has been adsorbed in the MPMs' PNIPAm hydrogel network, into the newly introduced volume of water; this is possible because the RhB molecules do not simply remain in the aqueous phase with surrounding water within the PNIPAm, but can get adsorbed into the PNIPAm after loading [302]. The concentration of RhB decreases with time as more and more loaded RhB molecules are ejected, which

explains the logarithmic behavior towards the end of the pulsed release profiles in Figure 3.10a. Furthermore, this adsorption/de-adsorption phenomenon explains the large difference between SR values and release percentages, namely the 6-7% release for a ~70% SR change in the continuous AMF application mode which does not allow for pulsatile actuation. This also suggests that MPMs can be overloaded with RhB (or another drug) by taking advantage of adsorption in the PNIPAm hydrogel, not requiring the loaded drug to remain in the aqueous phase while within the PNIPAm hydrogel, and permitting more cycles of efficiently deliverable drug in the pulsatile actuation AMF mode.

The effect of frequency change on the release response of NW MPMs is determined by maintaining a constant field of 1 mT, and varying the frequency from 20 kHz down to 5 kHz. The measured time is the time necessary to achieve a 4% release of RhB. As shown in Figure 3.10b, at 20 kHz this release amount can be achieved within approximately 500 seconds. By decreasing the frequency, the release time increases steadily until 12 kHz. A decrease below this value till 5 kHz or less, increases the release time dramatically, and the release time can reach around 5000 seconds. Although $P \propto B^2 f$ as discussed in Eqn. (3-4), time for release is not expected to be linearly proportional to f, because release time is associated with total heat generated in the system, versus total heat dissipating. Therefore, it is obviously expected that as P heads to 0, t heads to infinity. This is the equivalent of the fact that as f heads to 0, t heads to infinity (Figure 3.10b), while neglecting other causes of drug release (e.g. diffusion, small thermal fluctuations). Furthermore, it appears from Figure 3.10b that as f heads to infinity, t heads to 0, which is also expected.

3.4 Nanowire and Nanoparticle SAR Measurements

A SAR study of different NWs is one possible selection process for the magnetic materials used in the heating of drug delivery systems, such as the MPMs discussed in this chapter, when vibration is not the source, or not a possible source, of power generation (e.g. solid medium). SAR experiments for different NW materials and geometries were conducted in an attempt to explore NW magnetization losses as a viable form of heating. However, since it was found that power generation was primarily due to the vibrational losses of NWs, and due to the high complexity of mass fabricating NWs with 180 nm diameters (the most efficient at generating high SAR values), thinner NWs were used for the material presented in this

chapter. The details of these experiments were less applicable to this study, but can be found in Appendix B.

3.5 Chapter Summary

This chapter demonstrates the effectiveness of using iron NWs for the low power magnetic triggering of magnetic PNIPAm microdroplets, as compared to that of iron oxide nanoparticles. Calculations of the power density required to trigger a microdroplet using iron oxide nanoparticles, along with modeling of the physical vibrational motion of iron NWs in PNIPAm, corroborate the experimental observations of a droplet's volume change with known magnetic material concentration and magnetic field settings. Due to the nature of the physical motion of the higher aspect ratio NWs, compared to iron oxide particles, loss through the form of friction can be tapped into, permitting a drastic reduction in the necessary amplitude and frequency of the applied magnetic field that drives the heat generation (over one order of magnitude of reduction for each of these variable). Continuous application and pulsatile application of the magnetic field were studied for both types of microdroplets, which resulted in different release profiles over longer periods of time, as the pulsatile mode includes a rest period in which the microdroplets cool down, re-swell, and the newly internalized water mixes with the remaining dye prior to subsequent pulses.

The magnetic microdroplets covered in Chapter 3 can be implemented in the magnetic membranes discussed in Chapter 2 to improve on device performance and efficiency, allowing for highly localized heating of the PNIPAm component in the membrane valve system, potentially reducing response time and power requirements for the applied magnetic field. Furthermore, the low power permits the design of truly portable magnetic field supplies due to minimal power and small coil size requirements, which in the case of MPMs here amounts to a tabletop power supply and a 25 mm by 12 mm Litz wire coil, in contrast to a chiller cooled inductive heater that powers a 50 mm height and 42 mm inner diameter copper coil (typical setup for superparamagnetic heating) and cannot be easily transported. In hyperthermia research, safe levels of magnetic field and frequency combinations are determined by comparing those used with a previous study by Atkinson et al [306]. According to the study, 4.85×10^8 A/ms can be thermally tolerated for extended periods of time when tested on numerous persons. The magnetic membranes are operated at 2.22×10^{10} A/ms, while the magnetic microdroplets are operated at 1.59×10^7 A/ms

(achieved by multiplying the value of the field in A/m with the frequency), well below the safety threshold. Typical particles made of PNIPAm alone have not been reported to be biodegradable (an advantage for its long term use). Alternatively, they may be chemically synthesized specifically to be degradable by enzymes in the human body [303-305].

Chapter 4 Conclusion

4.1 Summary

This research develops technologies that provide alternative drug delivery mechanisms with magnetic control techniques. These new approaches provide remote controllability of membrane permeability for osmotic pump-based drug delivery devices, as well as decrease power requirements for injectable particle drug carriers, by tapping into the power generation of vibrating magnetic NWs.

The drug delivery device designs presented in this research focused on adding a controllable valve mechanism to currently uncontrollable, state-of-the-art applied, osmotic pumping, and focused on the modulation of the drug delivery rate both at the fabrication level (choice of membrane treatment) and at the experimental/application level (magnetic field application). A low cost treatment of the valve membrane allowed for the potential for fine tuning the drug delivery rate of the device in both the magnetically triggered and un-triggered states. Treated membranes exhibited release rates on the order of nanograms per hour of the test drug, while untreated membranes exhibited rates on the order of micrograms per hour. The behavior translates from individually tested membranes to membranes implemented and tested with osmotic pumps as the pressure source. The device design is simulated and modeled using a circuit analogy, an approach which can be used for assisting in the parameter selection of future designs that combine pressure sources with permeability controlled membranes. The components used in the devices are selected with medical applications in mind, as each material has been previously reported as biocompatible in at least certain applications.

The PNIPAm microparticles presented in this research were fabricated as composites with either magnetic iron NWs, or iron oxide nanoparticles for comparison, and it was found that the power requirements for magneto-thermally triggering a drug release and a size change in the shrinkage of PNIPAm, was significantly lower when taking advantage of losses induced by the vibration of the iron NWs embedded in the PNIPAm network of the microparticles. This was observed in both the cases of applied field strength (1 mT vs 73 mT) and field frequency (20 kHz vs 600 kHz). Iron oxide was used for comparison as it is the traditionally selected material for biocompatible medical applications using magnetic

heating. Iron, an element found in food, has the potential for meeting biocompatibility requirements. It was found that a pulsatile AC magnetic field application regime induced larger and faster test drug release over time when compared to continuous AC magnetic field application cases. These microparticles are envisioned to replace those used in the magnetically controlled membranes which act as valves for the reported osmotically pumped devices, enabling a much more efficient triggering of the valves, and permitting the design of truly portable magnetic field supplies due to minimal power and small coil size requirements.

4.2 Contributions

4.2.1 Journal Publications

First author publications

Zaher, A., Li, S., Wolf, K. T., Pirmoradi, F. N., Yassine, O., Lin, L., Khashab, N.M, & Kosel, J., ”Osmotically driven drug delivery through remote-controlled magnetic nanocomposite membranes.” *Biomicrofluidics*, 2015. *9*(5): p. 054113.

Yassine, O., Zaher, A., Li, E.Q., Alfadhel, A., Perez, J.E., Kavaldzhiev, M., Contreras, M.F., Thoroddsen, S.T., Khashab, N.M., & Kosel, J., “Highly Efficient Thermoresponsive Nanocomposite for Controlled Release Applications,” under review, *Nature Scientific Reports*, 2016.

Contreras, M.F., Zaher, A., Perez, J.E., Alfadhel, A., de Oliveira, L.A.S., Pirota, K.R., Ravasi, T., Kosel, J., “Magnetic Nanowires and Hyperthermia: the Influence of Geometry on and Material on Heat Production Efficiency,” (in preparation).

Second author publications

Yi, Y., Zaher, A., Yassine, O., Kosel, J., & Foulds, I. G., "A remotely operated drug delivery system with an electrolytic pump and a thermo-responsive valve." *Biomicrofluidics* 9.5 (2015): 052608.

Supporting author publications in related work

Alfadhel, A., Li, B., Zaher, A., Yassine, O., & Kosel, J., “A magnetic nanocomposite for biomimetic flow sensing.” *Lab on a Chip*, 2014. *14*(22), 4362-4369.

Contreras, M. F., Sougrat, R., Zaher, A., Ravasi, T., & Kosel, J., “Non-chemotoxic induction of cancer cell death using magnetic nanowires.” *International journal of nanomedicine*, 2015. *10*, 2141.

O. Yassine, Q. Li, A. Alfadhel, A. Zaher, M. Kavaldzhiev, S. Thoroddsen, J. Kosel, "Magnetically Controlled Nanocomposite Particles for Drug Delivery," under review, *International journal of polymer science*, 2016.

4.2.2 Conferences

4.2.2.1 Conference Oral Presentations

M. Contreras*, A. Zaher, J.E. Pérez, A. Alfadhel, L.A.S. de Oliveira, K.R. Pirota, T. Ravasi, and J. Kosel "Specific Absorption Rate Magnetic Nanowires: How Geometry and Material Affect Heat Production Efficiency", ASME 2015 4th Global Congress on Nano Engineering for Medicine and Biology.

A. Zaher*, S. Li, A. Alfadhel, O. Yassine, N. Khashab, J. Kosel, "Magnetically Controlled Release in an Osmotically Powered Drug Delivery Device", ASME 2014 3rd Global Congress on Nano Engineering for Medicine and Biology, San Francisco, CA (Feb 2014), (NEMB2014-93211 in book of abstracts).

A. Zaher*, S. Li, N. Khashab, J. Kosel, "Magnetic Nanocomposite Valve Membrane for the Control of an Osmotically Powered Drug Delivery Device", 58th MMM, Denver, CO, 2013.

O. Yassine, A. Zaher*, Q. Li , A. Alfadhel , S. Thoroddsen , J. Kosel, "Magnetically Controlled Droplets of Thermosensitive Microgel as Advanced Agent Carriers", 58th MMM, Denver, CO, 2013.

Y. Yi*, A. Zaher, O. Yassine, U. Buttner, J. Kosel, I.G. Foulds, "Electromagnetically powered electrolytic pump and thermo-responsive valve for drug delivery," in *Nano/Micro Engineered and Molecular Systems (NEMS), 2015 IEEE 10th International Conference on* , vol., no., pp.5-8, 7-11 April 2015. Winner of the CM HO Best Paper Award in Micro/Nano Fluidics.
IEEE published paper and oral presentation.

* Authors are oral presenters.
Underlined authors contributed equally to the presented work.

4.2.2.2 Conference Paper and Poster Contributions

Contreras, M.F., Zaher, A., Perez, J.E., Alfadhel, A., de Oliveira, L.A.S., Pirota, K.R., Ravasi, T., Kosel, J., "Magnetic Nanowires and Hyperthermia: the Influence of Geometry and Material on Heat Production Efficiency." 20th International Conference on Magnetism, Barcelona, 2015.

Y. Yi, A. Zaher, O. Yassine, U. Buttner, J. Kosel, I. G. Foulds: "A remotely operated drug delivery system with an electrolytic pump and magnetically triggered thermosensitive valve", AMN 2014.

O. Yassine, M. Kavaldzhiev, J. Kosel, Q. Li, A. Alfadhel, A. Zaher, "FEM Simulation of Magnetically Triggered Hydrogel Micro Particles As Advanced Drug Carriers", COMSOL 2014.

O. Yassine, A. Zaher, E. Li, A. Alfadhel, S. Thoroddsen, J. Kosel: "Magnetically Controlled Droplets of Thermosensitive Microgel as Advanced Agent Carriers", AMN 2013.

A. Alfadhel, A. Zaher, O. Yassine, R. Sougrat, and J. Kosel "Incorporation of Iron Nanowires into A PDMS Membrane", poster presentation, AMN 2013.

A. Alfadhel, A. Zaher, O. Yassine, and J. Kosel "Iron Nanowires Incorporated Into a PDMS Membrane", oral presentation, JEMS 2013, Greece.

D. Conchouso, A. Arevalo, D. Castro, E. Rawashdeh, M. Valencia, A. Zaher, J. Kosel, I. G. Foulds, "Simulation of SU-8 Frequency-Driven Scratch Drive Actuators," UKSim Conference 2013.

A. Arevalo, D. Conchouso, Amir Zaher, I. G. Foulds, J. Kosel, "Simulation of a Low Frequency Z-axis SU-8 Accelerometer in CoventorWare and MEMS+," UKSim Conference 2013.

M. Valencia, T. Atallah, D. Castro, D. Conchouso, M. Dosari, R. Hammad, E. Rawashdeh, A. Zaher, J. Kosel, I. G. Foulds "Development of untethered SU-8 polymer scratch drive microrobots," MEMS 2011 IEEE 24th Intl. Conference.

4.2.3 Patent

J. Kosel, N. Khashab, A. Zaher, Magnetically Controlled Permeability Membranes, US Patent App. 13/800,564

4.3 Recommendations and Future Directions

The findings in this research should pave the way for many interesting lower power drug delivery approaches that can further increase the controllability of pressure driven reservoir based drug delivery devices and particle drug carriers.

Devices that are valved using a magnetically controlled membrane will become more efficient if implemented with the reported microparticle drug carriers within the valve membrane (not loaded with a drug), such that the porosity controlling element (PNIPAm particle) is itself internally heated by vibrating NWs that require lower magnetic field strength and frequency in order to trigger a size change in the PNIPAm microparticle and an increase in porosity of the membrane. This not only would significantly reduce power requirements, but would also increase the efficiency of heating of the PNIPAm particles, as the heat source would be internal to the PNIPAm particles and not surrounding the particles in the membrane matrix polymer. Performing energy-dispersive X-ray spectroscopy (EDS) on the membrane matrix or PNIPAm particles may help image the magnetic materials when embedded, providing information on particle dispersion. Furthermore, not only can such a valve membrane be used to control the drug delivery port of a pressurized device, but also can be implemented as a controllable element at the water interface of an osmotic pump, such that the water flux intake of the pump can be temporarily changed magnetically.

Standalone microparticle drug carriers should offer excellent solutions for rapidly injectable localized treatments. The tradeoff here when compared to reservoir-based or infusion pump-based micro devices is an increase in ease of implantation versus long term use of the delivery solution. The size difference between particles and devices is already apparent, yet appropriate sizes must be determined in order to ensure the particles remain local to the injection site (i.e. too large to move within a patient, such as in the case of devices), and are not absorbed into the patient's internal tissue (i.e. microns large enough in radius), all while being small enough for the use of traditional syringe-based injection for implantation. Typical particles made of PNIPAm alone have not been reported to be biodegradable, which is an advantage for its long term use in membranes and microparticle carriers, though the later may need to be locally injected with care/precision for future ease of removal if necessary or, alternatively, chemically synthesized specifically to be degradable by enzymes in the human body.

It has been identified that by tapping into the power generation mechanism of vibrating magnetic NWs, any of these approaches can benefit from significant power reductions, making the drug delivery solutions more economical and practical (e.g. portability of magnetic field source). This increases the number of applications of the technologies arising from the field of implantable drug delivery, bearing in mind that the product H·f (magnetic field times frequency) in the case of the NW loaded microparticles used here is 30 times smaller than acceptable safety threshold levels of magnetic field exposure typically used in hyperthermia research, as discussed in Chapter 3. Furthermore, as covered in Appendix E, the possibility of applying PNIPAm as a mezzo-scale valve, heated via inductive heating of iron microparticles, coupled with electrolytic pumping, permits several combinations using such magnetic valving, the permeability membranes discussed in Chapter 2, and any number of pumping sources (osmotic, electrolytic, etc.), enabling researchers and medical professionals to achieve desired arbitrary drug delivery profile control, depending on treatment needs.

4.4 Final Word

The work presented in this research not only diversifies the possible drug delivery solutions to be pursued for production in this field, implemented in conjunction with low cost and state-of-the-art technology, but also demonstrates drastic improvements in power transfer from magnetic fields to targeted localized heat sites within the presented drug delivery systems. Iron nanowires within thermoresponsive PNIPAm polymer gels can achieve this, not only while enhancing the efficiency of PNIPAm micro-carriers, but also having the evident potential to replace polymers in PNIPAm permeability controlled membranes. In the race to achieve maximum control, with the highest efficiency, and at the lowest cost, such lines of work must be further explored.

Bibliography or References

1. Kohane, D.S. and R. Langer, *Biocompatibility and drug delivery systems.* Chemical Science, 2010. **1**(4): p. 441.
2. Cohen-Karni, T., R. Langer, and D.S. Kohane, *The Smartest Materials The Future of Nanoelctronics in Medicine.* ACS Nano, 2012.
3. Langer, R. and M. Chasin, *Biodegradable polymers as drug delivery systems*, 1990, Marcel Dekker, New York.
4. Stevenson, C.L., J.T. Santini, Jr., and R. Langer, *Reservoir-based drug delivery systems utilizing microtechnology.* Adv Drug Deliv Rev, 2012. **64**(14): p. 1590-602.
5. Paice, J.A., R.D. Penn, and S. Shott, *Intraspinal morphine for chronic pain: A retrospective, multicenter study.* Journal of Pain and Symptom Management, 1996. **11**(2): p. 71-80.
6. Smith, T.J., et al., *Randomized Clinical Trial of an Implantable Drug Delivery System Compared With Comprehensive Medical Management for Refractory Cancer Pain: Impact on Pain, Drug-Related Toxicity, and Survival.* Journal of Clinical Oncology, 2002. **20**(19): p. 4040-4049.
7. Poletti, C.E., et al., *Cancer pain relieved by long-term epidural morphine with permanent indwelling systems for self-administration.* Journal of Neurosurgery, 1981. **55**(4): p. 581-584.
8. Gardner, B., et al., *Intrathecal baclofen--a multicentre clinical comparison of the Medtronics Programmable, Cordis Secor and Constant Infusion Infusaid drug delivery systems.* Paraplegia, 1995. **33**(10): p. 551-4.
9. Penn, R. and J. Kroin, *CONTINUOUS INTRATHECAL BACLOFEN FOR SEVERE SPASTICITY.* The Lancet, 1985. **326**(8447): p. 125-127.
10. Joe I. Ordia, et al., *Chronic intrathecal delivery of baclofen by a programmable pump for the treatment of severe spasticity.* Journal of Neurosurgery, 1996. **85**(3): p. 452-457.
11. LaVan, D.A., T. McGuire, and R. Langer, *Small-scale systems for in vivo drug delivery.* Nat Biotech, 2003. **21**(10): p. 1184-1191.
12. McKinnon, W., M.C. Lee, and P. Kanev, *Mortality from Intrathecal Baclofen Withdrawal Following Posterior Spinal Fusion.* A Case Report, 2012. **2**(3): p. e32.
13. Meng, E. and T. Hoang, *MEMS-enabled implantable drug infusion pumps for laboratory animal research, preclinical, and clinical applications.* Advanced drug delivery reviews, 2012. **64**(14): p. 1628-1638.
14. Li, Y., et al., *In vivo delivery of BCNU from a MEMS device to a tumor model.* Journal of controlled release, 2005. **106**(1): p. 138-145.
15. Smeets, N.M.B. and T. Hoare, *Designing responsive microgels for drug delivery applications.* Journal of Polymer Science Part A: Polymer Chemistry, 2013. **51**(14): p. 3027-3043.
16. Hu, S.H., et al., *Remotely nano-rupturable yolk/shell capsules for magnetically-triggered drug release.* Chem Commun (Camb), 2011. **47**(6): p. 1776-8.
17. Baeza, A., et al., *Magnetically Triggered Multidrug Release by Hybrid Mesoporous Silica Nanoparticles.* Chemistry of Materials, 2012. **24**(3): p. 517-524.

18. Ma, W.-F., et al., *Magnetic drug carrier with a smart pH-responsive polymer network shell for controlled delivery of doxorubicin.* Journal of Materials Chemistry, 2012. **22**(30): p. 15206.
19. Seung-Ki, B., et al., *A wireless sequentially actuated microvalve system.* Journal of Micromechanics and Microengineering, 2013. **23**(4): p. 045006.
20. Jeon, G., S.Y. Yang, and J.K. Kim, *Functional nanoporous membranes for drug delivery.* Journal of Materials Chemistry, 2012. **22**(30): p. 14814.
21. Bäcker, M., et al., *Microfluidic chip with integrated microvalves based on temperature- and pH-responsive hydrogel thin films.* physica status solidi (a), 2012. **209**(5): p. 839-845.
22. Pirmoradi, F.N., et al., *A magnetically controlled MEMS device for drug delivery: design, fabrication, and testing.* Lab on a Chip, 2011. **11**(18): p. 3072-3080.
23. Zadražil, A., V. Tokárová, and F. Štěpánek, *Remotely triggered release from composite hydrogel sponges.* Soft Matter, 2012. **8**(6): p. 1811-1816.
24. Zhang, F. and C.C. Wang, *Preparation of P(NIPAM-co-AA) microcontainers surface-anchored with magnetic nanoparticles.* Langmuir, 2009. **25**(14): p. 8255-62.
25. Zhang, F., G.-H. Hou, and C.-C. Wang, *Preparation of wormlike PNIPAM microcontainers with magnetic nanoparticle inclusions.* Materials Letters, 2012. **89**(0): p. 97-100.
26. Murtaza, G., *Ethylcellulose microparticles: a review.* Acta Pol Pharm, 2012. **69**(1): p. 11-22.
27. Herrlich, S., et al., *Osmotic micropumps for drug delivery.* Adv Drug Deliv Rev, 2012. **64**(14): p. 1617-27.
28. Nuxoll, E., *BioMEMS in drug delivery.* Adv Drug Deliv Rev, 2013. **65**(11-12): p. 1611-25.
29. Sharma, S., et al., *Controlled-release microchips.* Expert Opin Drug Deliv, 2006. **3**(3): p. 379-94.
30. Santini, J.T., M.J. Cima, and R. Langer, *A controlled-release microchip.* Nature, 1999. **397**: p. 335-338.
31. Sershen, S., et al., *Temperature-sensitive polymer–nanoshell composites for photothermally modulated drug delivery.* Journal of biomedical materials research, 2000. **51**(3): p. 293-298.
32. Edelman, E., et al., *Regulation of drug release from polymer matrices by oscillating magnetic fields.* Journal of biomedical materials research, 1985. **19**(1): p. 67-83.
33. Müller-Schulte, D., *Thermosensitive, biocompatible polymer carriers with changeable physical structure for therapy, diagnostics and analytics*, 2004, Google Patents.
34. Müller-Schulte, D. and T. Schmitz-Rode, *Thermosensitive magnetic polymer particles as contactless controllable drug carriers.* Journal of Magnetism and Magnetic Materials, 2006. **302**(1): p. 267-271.
35. Zhang, K. and X.Y. Wu, *Temperature and pH-responsive polymeric composite membranes for controlled delivery of proteins and peptides.* Biomaterials, 2004. **25**(22): p. 5281-5291.
36. Hu, S.-H., et al., *Controlled rupture of magnetic polyelectrolyte microcapsules for drug delivery.* Langmuir, 2008. **24**(20): p. 11811-11818.

37. Sukhorukov, G.B., et al., *Multifunctionalized polymer microcapsules: novel tools for biological and pharmacological applications.* Small, 2007. **3**(6): p. 944-955.
38. Hu, S.H., et al., *Core/Single-Crystal-Shell Nanospheres for Controlled Drug Release via a Magnetically Triggered Rupturing Mechanism.* Advanced Materials, 2008. **20**(14): p. 2690-2695.
39. Hu, S.-H., et al., *Magnetic-sensitive silica nanospheres for controlled drug release.* Langmuir, 2008. **24**(1): p. 239-244.
40. Liu, T.-Y., et al., *Biomedical nanoparticle carriers with combined thermal and magnetic responses.* Nano Today, 2009. **4**(1): p. 52-65.
41. Hill, A., et al., *How do in-vitro release profiles of nanosuspensions from Alzet(R) pumps correspond to the in-vivo situation? A case study on radiolabeled fenofibrate.* J Control Release, 2013. **168**(1): p. 77-87.
42. Hill, A., et al., *In vitro-in vivo evaluation of nanosuspension release from subcutaneously implantable osmotic pumps.* Int J Pharm, 2013. **451**(1-2): p. 57-66.
43. Stuti Gupta, et al., *Osmotic Pumps: A Review.* IJCP, 2011. **6**(01): p. 1-8.
44. Theeuwes, F. and S.I. Yum, *Principles of the design and operation of generic osmotic pumps for the delivery of semisolid or liquid drug formulations.* Ann Biomed Eng, 1976. **4**(4): p. 343-53.
45. Farra, R., et al., *First-in-human testing of a wirelessly controlled drug delivery microchip.* Sci Transl Med, 2012. **4**(122): p. 122ra21.
46. Patra, C.N., et al., *Osmotic drug delivery systems: basics and design approaches.* Recent patents on drug delivery & formulation, 2013. **7**(2): p. 150-61.
47. Zhang, X., et al., *Controlled release of cyclosporine A self-nanoemulsifying systems from osmotic pump tablets: near zero-order release and pharmacokinetics in dogs.* Int J Pharm, 2013. **452**(1-2): p. 233-40.
48. Kost, J., *Pulsed and self-regulated drug delivery*. 1990: CRC Press.
49. Wu, J., et al., *Programmable transdermal drug delivery of nicotine using carbon nanotube membranes.* Proceedings of the National Academy of Sciences, 2010. **107**(26): p. 11698-11702.
50. Group, N.D.D., *Classification and diagnosis of diabetes mellitus and other categories of glucose intolerance.* Diabetes, 1979. **28**(12): p. 1039-1057.
51. Mellitus, D., *Diagnosis and classification of diabetes mellitus.* Diabetes care, 2005. **28**: p. S37.
52. Bray, G., et al., *A multicenter study of recombinant factor VIII (recombinate): safety, efficacy, and inhibitor risk in previously untreated patients with hemophilia A. The Recombinate Study Group.* Blood, 1994. **83**(9): p. 2428-2435.
53. White, G.C., et al., *Definitions in hemophilia.* THROMBOSIS AND HAEMOSTASIS-STUTTGART-, 2001. **85**(3): p. 560-560.
54. Wolf-Maier, K., et al., *Hypertension treatment and control in five European countries, Canada, and the United States.* Hypertension, 2004. **43**(1): p. 10-17.
55. Expert Panel on Detection, E., *Executive summary of the third report of the National Cholesterol Education Program (NCEP) expert panel on Detection, Evaluation, and Treatment of high blood cholesterol in adults (Adult Treatment Panel III).* Jama, 2001. **285**(19): p. 2486.
56. Heart, N. and B.I.N.A.E.P.E.P.o.t.M.o. Asthma, *Guidelines for the diagnosis and management of asthma*. 1991: National Asthma Education Program, Office of

Prevention, Education, and Control, National Heart, Lung, and Blood Institute, National Institutes of Health.
57. Asher, M., et al., *International Study of Asthma and Allergies in Childhood (ISAAC): rationale and methods.* European respiratory journal, 1995. **8**(3): p. 483-491.
58. Fisher, R.S., et al., *Epileptic seizures and epilepsy: definitions proposed by the International League Against Epilepsy (ILAE) and the International Bureau for Epilepsy (IBE).* Epilepsia, 2005. **46**(4): p. 470-472.
59. Patra, C.N., et al., *Osmotic drug delivery systems: basics and design approaches.* Recent Pat Drug Deliv Formul, 2013. **7**(2): p. 150-61.
60. Theeuwes, F., *Elementary osmotic pump.* J Pharm Sci, 1975. **64**(12): p. 1987-91.
61. Tresco, P.A. and B.D. Winslow, *The challenge of integrating devices into the central nervous system.* Crit Rev Biomed Eng, 2011. **39**(1): p. 29-44.
62. DeVos, S.L. and T.M. Miller, *Direct intraventricular delivery of drugs to the rodent central nervous system.* J Vis Exp, 2013(75).
63. Martin Bauknight, W., et al., *Convection enhanced drug delivery of BDNF through a microcannula in a rodent model to strengthen connectivity of a peripheral motor nerve bridge model to bypass spinal cord injury.* J Clin Neurosci, 2012. **19**(4): p. 563-9.
64. Martins, Y.C., et al., *Slow and continuous delivery of a low dose of nimodipine improves survival and electrocardiogram parameters in rescue therapy of mice with experimental cerebral malaria.* Malar J, 2013. **12**: p. 138-148.
65. Liu, X., et al., *Osmotic drug delivery to ischemic hindlimbs and perfusion of vasculature with microfil for micro-computed tomography imaging.* J Vis Exp, 2013(76).
66. Mulcahy, P., et al., *The behavioural and neuropathological impact of intranigral AAV-alpha-synuclein is exacerbated by systemic infusion of the Parkinson's disease-associated pesticide, rotenone, in rats.* Behav Brain Res, 2013. **243**: p. 6-15.
67. de las Heras Alarcón, C., S. Pennadam, and C. Alexander, *Stimuli responsive polymers for biomedical applications.* Chemical Society Reviews, 2005. **34**(3): p. 276-285.
68. Auslander, S., M. Wieland, and M. Fussenegger, *Smart medication through combination of synthetic biology and cell microencapsulation.* Metab Eng, 2012. **14**(3): p. 252-60.
69. Pirmoradi, F.N., et al., *A magnetically controlled MEMS device for drug delivery: design, fabrication, and testing.* Lab Chip, 2011. **11**(18): p. 3072-80.
70. Yu-Chuan, S. and L. Lin, *A water-powered micro drug delivery system.* Microelectromechanical Systems, Journal of, 2004. **13**(1): p. 75-82.
71. Rivero, R.E., et al., *Pressure and microwave sensors/actuators based on smart hydrogel/conductive polymer nanocomposite.* Sensors and Actuators B: Chemical, 2014. **190**: p. 270-278.
72. Matsuguchi, M., N. Harada, and S. Omori, *Poly (N-isopropylacrylamide) nanoparticles for QCM-based gas sensing of HCl.* Sensors and Actuators B: Chemical, 2014. **190**: p. 446-450.
73. Efrati, A., et al., *Electrochemical switching of photoelectrochemical processes at CdS QDs and photosystem I-modified electrodes.* ACS nano, 2012. **6**(10): p. 9258-9266.

74. Mihut, A.M., et al., *Tunable Adsorption of Soft Colloids on Model Biomembranes.* ACS nano, 2013. **7**(12): p. 10752-10763.
75. Nash, M.E., et al., *Cell and cell sheet recovery from pNIPAm coatings; motivation and history to present day approaches.* Journal of Materials Chemistry, 2012. **22**(37): p. 19376-19389.
76. Liu, D., et al., *Cell proliferation and cell sheet detachment from the positively and negatively charged nanocomposite hydrogels.* Biopolymers, 2014. **101**(1): p. 58-65.
77. Peroglio, M., et al., *Thermoreversible hyaluronan-based hydrogel supports in vitro and ex vivo disc-like differentiation of human mesenchymal stem cells.* The Spine Journal, 2013. **13**(11): p. 1627-1639.
78. Sorrell, C.D., M.C. Carter, and M.J. Serpe, *Color Tunable Poly (N-Isopropylacrylamide)-co-Acrylic Acid Microgel–Au Hybrid Assemblies.* Advanced Functional Materials, 2011. **21**(3): p. 425-433.
79. Karir, T., et al., *Preparation and evaluation of radioiodinated thermoresponsive polymer based on poly (N-isopropyl acrylamide) for radiotherapy.* Journal of Applied Polymer Science, 2013. **130**(2): p. 860-868.
80. Jones, C.D., et al., *Microlens formation in microgel/gold colloid composite materials via photothermal patterning.* Journal of the American Chemical Society, 2003. **125**(18): p. 5292-5293.
81. Carregal-Romero, S., et al., *Catalysis by Au@ pNIPAM nanocomposites: effect of the cross-linking density.* Chemistry of Materials, 2010. **22**(10): p. 3051-3059.
82. Zhao, Q., et al., *Thermoresponsive magnetic nanoparticles for seawater desalination.* ACS applied materials & interfaces, 2013. **5**(21): p. 11453-11461.
83. Saikia, A.K., S. Aggarwal, and U.K. Mandal, *Preparation and Controlled Drug Release Characteristics of Thermoresponsive PEG/Poly (NIPAM-co-AMPS) Hydrogels.* Int. J. Polym. Mater. Polym. Biomater., 2013. **62**(1): p. 39-44.
84. Qian, J. and F. Wu, *Thermosensitive PNIPAM semi-hollow spheres for controlled drug release.* J. Mater. Chem. B, 2013. **1**(28): p. 3464-3469.
85. Li, G., et al., *Complex micelles formed from two diblock copolymers for applications in controlled drug release.* J. Polym. Sci., Part A Polym. Chem., 2009. **47**(7): p. 1804-1810.
86. Nayak, S., et al., *Hollow thermoresponsive microgels.* Small, 2005. **1**(4): p. 416-421.
87. Lien, Y.-H., et al., *In vitro evaluation of the thermosensitive and magnetic nanoparticles for the controlled drug delivery of vitamin D3.* Macromol. Res., 2013. **21**(5): p. 511-518.
88. Vasani, R.B., et al., *Stimulus-Responsiveness and Drug Release from Porous Silicon Films ATRP-Grafted with Poly(N-isopropylacrylamide).* Langmuir, 2011. **27**(12): p. 7843-7853.
89. Pan, Y.-Z., et al., *Water-Soluble Poly(N-isopropylacrylamide)-Graphene Sheets Synthesized via Click Chemistry for Drug Delivery.* Adv. Funct. Mater., 2011. **21**(14): p. 2754-2763.
90. Lien, Y.-H., et al., *Cytotoxicity and drug release behavior of PNIPAM grafted on silica-coated iron oxide nanoparticles.* J. Nanopart. Res., 2011. **13**(10): p. 5065-5075.
91. Wang, W., et al., *A Novel Thermo-Induced Self-Bursting Microcapsule with Magnetic-Targeting Property.* ChemPhysChem, 2009. **10**(14): p. 2405-2409.

92. You, Y.-Z., et al., *Temperature-Controlled Uptake and Release in PNIPAM-Modified Porous Silica Nanoparticles.* Chem. Mater., 2008. **20**(10): p. 3354-3359.
93. Rubio-Retama, J., et al., *Synthesis and Characterization of Thermosensitive PNIPAM Microgels Covered with Superparamagnetic γ-Fe2O3 Nanoparticles.* Langmuir, 2007. **23**(20): p. 10280-10285.
94. Zhu, Z., et al., *Temperature-triggered on-demand drug release enabled by hydrogen-bonded multilayers of block copolymer micelles.* J. Controlled Release, 2013. **171**(1): p. 73-80.
95. Yu, Y.-L., et al., *Thermo-responsive monodisperse core-shell microspheres with PNIPAM core and biocompatible porous ethyl cellulose shell embedded with PNIPAM gates.* J. Colloid Interface Sci., 2012. **376**(1): p. 97-106.
96. Purushotham, S., et al., *Thermoresponsive core-shell magnetic nanoparticles for combined modalities of cancer therapy.* Nanotechnology, 2009. **20**(30): p. 305101/1-305101/11.
97. Han, H.D., B.C. Shin, and H.S. Choi, *Doxorubicin-encapsulated thermosensitive liposomes modified with poly(N-isopropylacrylamide-co-acrylamide): Drug release behavior and stability in the presence of serum.* Eur. J. Pharm. Biopharm., 2006. **62**(1): p. 110-116.
98. Han, H.D., et al., *Hyperthermia-induced antitumor activity of thermosensitive polymer modified temperature-sensitive liposomes.* J. Pharm. Sci., 2006. **95**(9): p. 1909-1917.
99. Cai, Y. and Y.-Y. Liu, *Amphiphilic uimolecular nanoparticles based on a hyperbranched polyacrylate core and a PNIPAm shell: Synthesis via ATRP and properties.* Macromol. Chem. Phys., 2013. **214**(8): p. 882-891.
100. Huang, G., et al., *Controlled drug release from hydrogel nanoparticle networks.* J. Controlled Release, 2004. **94**(2-3): p. 303-311.
101. Lu, N., et al., *Controlled Drug Loading and Release of a Stimuli-Responsive Lipogel Consisting of Poly(N-isopropylacrylamide) Particles and Lipids.* J. Phys. Chem. B, 2013. **117**(33): p. 9677-9682.
102. Guan, Y. and Y. Zhang, *PNIPAM microgels for biomedical applications: from dispersed particles to 3D assemblies.* Soft Matter, 2011. **7**(14): p. 6375.
103. Hu, L., et al., *Poly (N-isopropylacrylamide) microgel-based assemblies.* Journal of Polymer Science Part A: Polymer Chemistry, 2013. **51**(14): p. 3004-3020.
104. Doring, A., W. Birnbaum, and D. Kuckling, *Responsive hydrogels - structurally and dimensionally optimized smart frameworks for applications in catalysis, micro-system technology and material science.* Chemical Society Reviews, 2013. **42**(17): p. 7391-7420.
105. Meng, Z., M.H. Smith, and L.A. Lyon, *Temperature-programmed synthesis of micron-sized multi-responsive microgels.* Colloid and Polymer Science, 2009. **287**(3): p. 277-285.
106. Varga, I., et al., *Effect of cross-link density on the internal structure of poly (N-isopropylacrylamide) microgels.* The Journal of Physical Chemistry B, 2001. **105**(38): p. 9071-9076.
107. Blackburn, W.H. and L.A. Lyon, *Size-controlled synthesis of monodisperse core/shell nanogels.* Colloid and polymer science, 2008. **286**(5): p. 563-569.

108. McPhee, W., K.C. Tam, and R. Pelton, *Poly (N-isopropylacrylamide) latices prepared with sodium dodecyl sulfate.* Journal of colloid and interface science, 1993. **156**(1): p. 24-30.
109. Hoare, T., et al., *Magnetically triggered nanocomposite membranes: a versatile platform for triggered drug release.* Nano Lett, 2011. **11**(3): p. 1395-400.
110. Xu, F.J., et al., *Thermo-responsive porous membranes of controllable porous morphology from triblock copolymers of polycaprolactone and Poly(N-isopropylacrylamide) prepared by atom transfer radical polymerization.* Biomacromolecules, 2008. **9**(1): p. 331-339.
111. Lue, S.J., et al., *Thermally on-off switching membranes of poly(N-isopropylacrylamide) immobilized in track-etched polycarbonate films.* Journal of Membrane Science, 2007. **301**(1-2): p. 142-150.
112. Guilherme, M.R., et al., *Thermo-responsive sandwiched-like membranes of IPN-PNIPAAm/PAAm hydrogels.* Journal of Membrane Science, 2006. **275**(1-2): p. 187-194.
113. Shaikh, R.P., et al., *A Review of Multi-Responsive Membranous Systems for Rate-Modulated Drug Delivery.* Aaps Pharmscitech, 2010. **11**(1): p. 441-459.
114. Wang, G., et al., *Thermo-Responsive Polyethersulfone Composite Membranes Blended with Poly(N-isopropylacrylamide) Nanogels.* Chemical Engineering & Technology, 2012. **35**(11): p. 2015-2022.
115. Li, P.-F., et al., *Thermo-responsive membranes with cross-linked poly(N-isopropylacrylamide) hydrogels inside porous substrates.* Chemical Engineering & Technology, 2006. **29**(11): p. 1333-1339.
116. Zhang, Y., S. Sinha-Ray, and A.L. Yarin, *Mechanoresponsive polymer nanoparticles, nanofibers and coatings as drug carriers and components of microfluidic devices.* Journal of Materials Chemistry, 2011. **21**(23): p. 8269-8281.
117. Hoare, T., et al., *A Magnetically Triggered Composite Membrane for On-Demand Drug Delivery.* Nano Letters, 2009. **9**(10): p. 3651-3657.
118. Lue, S.J., J.-J. Hsu, and T.-C. Wei, *Drug permeation modeling through the thermo-sensitive membranes of poly(N-isopropylacrylamide) brushes grafted onto micro-porous films.* Journal of Membrane Science, 2008. **321**(2): p. 146-154.
119. Kato, K., et al., *Polymer surface with graft chains.* Progress in Polymer Science, 2003. **28**(2): p. 209-259.
120. Iwata, H., et al., *PREPARATION OF TEMPERATURE-SENSITIVE MEMBRANES BY GRAFT-POLYMERIZATION ONTO A POROUS MEMBRANE.* Journal of Membrane Science, 1991. **55**(1-2): p. 119-130.
121. Ying, L., E.T. Kang, and K.G. Neoh, *Synthesis and characterization of poly(N-isopropylacrylamide)-graft-poly(vinylidene fluoride) copolymers and temperature-sensitive membranes.* Langmuir, 2002. **18**(16): p. 6416-6423.
122. Huang, J., et al., *Temperature-sensitive membranes prepared by the plasma-induced graft polymerization of N-isopropylacrylamide into porous polyethylene membranes.* Journal of Applied Polymer Science, 2003. **89**(12): p. 3180-3187.
123. Wan, L.-S., et al., *Construction of comb-like poly(N-isopropylacrylamide) layers on microporous polypropylene membrane by surface-initiated atom transfer radical polymerization.* Journal of Membrane Science, 2009. **327**(1-2): p. 174-181.

124. Wang, W. and L. Chen, *"'Smart" membrane materials: Preparation and characterization of PVDF-g-PNIPAAm graft copolymer.* Journal of Applied Polymer Science, 2007. **104**(3): p. 1482-1486.
125. Hu, L., et al., *A Composite Thermo-Responsive Membrane System for Improved Controlled-Release.* Chemical Engineering & Technology, 2007. **30**(4): p. 523-529.
126. Nasef, M.M. and E.S.A. Hegazy, *Preparation and applications of ion exchange membranes by radiation-induced graft copolymerization of polar monomers onto non-polar films.* Progress in Polymer Science, 2004. **29**(6): p. 499-561.
127. Rosiak, J.M., et al., *Nano-, micro- and macroscopic hydrogels synthesized by radiation technique.* Nuclear Instruments & Methods in Physics Research Section B-Beam Interactions with Materials and Atoms, 2003. **208**: p. 325-330.
128. Ulanski, P., et al., *Polymeric biomaterials synthesized by radiation techniques - Current studies at IARC, Poland.* Polymers for Advanced Technologies, 2002. **13**(10-12): p. 951-959.
129. Wu, G., et al., *Novel thermo-sensitive membranes prepared by rapid bulk photo-grafting polymerization of N,N-diethylacrylamide onto the microfiltration membranes Nylon.* Journal of Membrane Science, 2006. **283**(1-2): p. 13-20.
130. Vertommen, M.A.M.E., et al., *Pore-covered thermoresponsive membranes for repeated on-demand drug release.* Journal of Membrane Science, 2008. **322**(1): p. 243-248.
131. Wu, D., et al., *Modification of aromatic polyamide thin-film composite reverse osmosis membranes by surface coating of thermo-responsive copolymers P(NIPAM-co-Am). I: Preparation and characterization.* Journal of Membrane Science, 2010. **352**(1-2): p. 76-85.
132. Ying, L., et al., *Drug permeation through temperature-sensitive membranes prepared from poly(vinylidene fluoride) with grafted poly(N-isopropylacrylamide) chains.* Journal of Membrane Science, 2004. **243**(1-2): p. 253-262.
133. Sun, Y.M. and T.L. Huang, *Pervaporation of ethanol-water mixtures through temperature-sensitive poly(vinyl alcohol-g-N-isopropyacrylamide) membranes.* Journal of Membrane Science, 1996. **110**(2): p. 211-218.
134. Yu, J.-Z., et al., *Poly(N-isopropylacrylamide) grafted poly(vinylidene fluoride) copolymers for temperature-sensitive membranes.* Journal of Membrane Science, 2011. **366**(1-2): p. 176-183.
135. Feng, X., et al., *Membrane formation process and mechanism of PVDF-g-PNIPAAm thermo-sensitive membrane.* Desalination, 2012. **290**: p. 89-98.
136. Svarfvar, B.L., et al., *Electron-beam graft-modified membranes with externally controlled flux.* Polymers for Advanced Technologies, 1996. **7**(11): p. 839-846.
137. Feng, X., et al., *Influence of Coagulant Temperature on the Membrane Formation Process and Properties of PVDF-g-PNIPAAm Temperature-sensitive Membranes.* Chemical Journal of Chinese Universities-Chinese, 2011. **32**(6): p. 1424-1430.
138. Zhao, Y., et al., *Properties of poly(vinylidene fluoride)-graft-poly (N-isopropylacrylamide) membranes prepared by alkali treatment.* Journal of Polymer Research, 2013. **20**(2).
139. Chen, X., et al., *Temperature-sensitive membranes prepared from blends of poly(vinylidene fluoride) and poly(N-isopropylacrylamides) microgels.* Colloid and Polymer Science, 2013. **291**(10): p. 2419-2428.

140. Zhang, Y. and A.L. Yarin, *Thermo-responsive copolymer coatings for flow regulation on demand in glass microcapillaries.* European Physical Journal E, 2010. **33**(3): p. 211-218.
141. Chu, L.Y., et al., *Negatively thermoresponsive membranes with functional gates driven by zipper-type hydrogen-bonding interactions.* Angewandte Chemie-International Edition, 2005. **44**(14): p. 2124-2127.
142. Chen, Y.-C., et al., *Gating Characteristics of Thermo-Responsive Membranes with Grafted Linear and Crosslinked Poly(N-isopropylacrylamide) Gates.* Chemical Engineering & Technology, 2009. **32**(4): p. 622-631.
143. Wang, W., et al., *Thermally On-Off Switching Membranes Prepared by Pore-Filling Poly(N-isopropylacrylamide) Hydrogels.* Industrial & Engineering Chemistry Research, 2010. **49**(4): p. 1684-1690.
144. Teixeira, F., Jr., et al., *Synthesis of poly(oligo(ethylene glycol)methacrylate)-functionalized membranes for thermally controlled drug delivery.* Journal of Applied Polymer Science, 2013. **129**(2): p. 636-643.
145. Liang, L., et al., *Surfaces with reversible hydrophilic/hydrophobic characteristics on cross-linked poly(N-isopropylacrylamide) hydrogels.* Langmuir, 2000. **16**(21): p. 8016-8023.
146. Liang, L., et al., *Temperature-sensitive membranes prepared by UV photopolymerization of N-isopropylacrylamide on a surface of porous hydrophilic polypropylene membranes.* Journal of Membrane Science, 1999. **162**(1-2): p. 235-246.
147. Rahimi, S., et al., *Implantable drug delivery device using frequency-controlled wireless hydrogel microvalves.* Biomed Microdevices, 2011. **13**(2): p. 267-77.
148. Hirokawa, Y. and T. Tanaka, *Volume phase transition in a nonionic gel.* The Journal of chemical physics, 1984. **81**(12): p. 6379-6380.
149. Saunders, B.R. and B. Vincent, *Microgel particles as model colloids: theory, properties and applications.* Advances in colloid and interface science, 1999. **80**(1): p. 1-25.
150. Zhu, Z., et al., *Programmable light-controlled shape changes in layered polymer nanocomposites.* Acs Nano, 2012. **6**(4): p. 3152-3162.
151. Suwa, K., et al., *Synthesis and functionalities of poly (N-vinylalkylamide). V. Control of a lower critical solution temperature of poly (N-vinylalkylamide).* Journal of Polymer Science Part A: Polymer Chemistry, 1997. **35**(15): p. 3087-3094.
152. Ghosh, S., et al., *Oscillating magnetic field-actuated microvalves for micro- and nanofluidics.* Journal of Physics D: Applied Physics, 2009. **42**(13): p. 135501.
153. Pelton, R. and P. Chibante, *Preparation of aqueous latices with N-isopropylacrylamide.* Colloids and Surfaces, 1986. **20**(3): p. 247-256.
154. Pan, Y., et al., *Water-Soluble Poly (N-isopropylacrylamide)–Graphene Sheets Synthesized via Click Chemistry for Drug Delivery.* Advanced Functional Materials, 2011. **21**(14): p. 2754-2763.
155. Liu, R., M. Fraylich, and B.R. Saunders, *Thermoresponsive copolymers: from fundamental studies to applications.* Colloid and Polymer Science, 2009. **287**(6): p. 627-643.
156. Ding, X.B., et al., *Preparation of thermosensitive magnetic particles by dispersion polymerization.* Reactive and Functional Polymers, 1998. **38**(1): p. 11-15.

157. Sauzedde, F., A. Elaissari, and C. Pichot, *Hydrophilic magnetic polymer latexes. 2. Encapsulation of adsorbed iron oxide nanoparticles.* Colloid and Polymer Science, 1999. **277**(11): p. 1041-1050.
158. Purushotham, S., et al., *Thermoresponsive core–shell magnetic nanoparticles for combined modalities of cancer therapy.* Nanotechnology, 2009. **20**(30): p. 305101.
159. Cullity, B.D. and C.D. Graham, *Introduction to magnetic materials*. 2011: John Wiley & Sons.
160. Coey, J.M., *Magnetism and magnetic materials*. 2010: Cambridge University Press.
161. Vázquez, M., et al., *Magnetic behaviour of densely packed hexagonal arrays of Ni nanowires: Influence of geometric characteristics.* Journal of Magnetism and Magnetic Materials, 2005. **294**(2): p. 174-181.
162. Kittel, C., P. McEuen, and P. McEuen, *Introduction to solid state physics*. Vol. 8. 1976: Wiley New York.
163. Sun, L., et al., *Tuning the properties of magnetic nanowires.* IBM Journal of Research and Development, 2005. **49**(1): p. 79-102.
164. Ivanov, Y.P., M. Vázquez, and O. Chubykalo-Fesenko, *Magnetic reversal modes in cylindrical nanowires.* Journal of Physics D: Applied Physics, 2013. **46**(48): p. 485001.
165. Vidal, E.V., et al., *A detailed study of magnetization reversal in individual Ni nanowires.* Applied Physics Letters, 2015. **106**(3): p. 032403.
166. Brown Jr, W.F., *Thermal fluctuations of a single-domain particle.* Journal of Applied Physics, 1963. **34**(4): p. 1319-1320.
167. Néel, L. and C. HEBD, *Seances Acad. Sci. 228, 664 1949.* Ann. Geophys. CNRS, 1949. **5**: p. 99.
168. Rosensweig, R.E., *Heating magnetic fluid with alternating magnetic field.* Journal of magnetism and magnetic materials, 2002. **252**: p. 370-374.
169. Tabatabaei, S.N., J. Lapointe, and S. Martel. *Hydrogel encapsulated magnetic nanoparticles as hyperthermic actuators for microrobots designed to operate in the vascular network*. in *Intelligent Robots and Systems, 2009. IROS 2009. IEEE/RSJ International Conference on*. 2009.
170. Sun, S.H., et al., *Monodisperse MFe2O4 (M = Fe, Co, Mn) nanoparticles.* Journal of the American Chemical Society, 2004. **126**(1): p. 273-279.
171. Krishnan, K.M., *Biomedical Nanomagnetics: A Spin Through Possibilities in Imaging, Diagnostics, and Therapy.* Ieee Transactions on Magnetics, 2010. **46**(7): p. 2523-2558.
172. Kang, X., et al., *Design and Synthesis of Multifunctional Drug Carriers Based on Luminescent Rattle-Type Mesoporous Silica Microspheres with a Thermosensitive Hydrogel as a Controlled Switch.* Advanced Functional Materials, 2012. **22**(7): p. 1470-1481.
173. Taha, M., et al., *Interactions of biological buffers with macromolecules: The ubiquitous "smart" polymer PNIPAM and the biological buffers MES, MOPS, and MOPSO.* Macromolecules, 2011. **44**(21): p. 8575-8589.
174. Cavalieri, F., et al., *Assembly and Functionalization of DNA− Polymer Microcapsules.* Acs Nano, 2009. **3**(1): p. 234-240.
175. Jordan, A., et al., *Effects of magnetic fluid hyperthermia (MFH) on C3H mammary carcinoma in vivo.* International Journal of Hyperthermia, 1997. **13**(6): p. 587-605.

176. Ito, A., et al., *Tumor regression by combined immunotherapy and hyperthermia using magnetic nanoparticles in an experimental subcutaneous murine melanoma.* Cancer science, 2003. **94**(3): p. 308-313.
177. Ito, A., et al., *Complete regression of mouse mammary carcinoma with a size greater than 15 mm by frequent repeated hyperthermia using magnetite nanoparticles.* Journal of bioscience and bioengineering, 2003. **96**(4): p. 364-369.
178. Billotey, C., et al., *Cell internalization of anionic maghemite nanoparticles: quantitative effect on magnetic resonance imaging.* Magnetic resonance in medicine, 2003. **49**(4): p. 646-654.
179. Giouroudi, I. and J. Kosel, *Recent progress in biomedical applications of magnetic nanoparticles.* Recent patents on nanotechnology, 2010. **4**(2): p. 111-118.
180. Li, F., I. Giouroudi, and J. Kosel, *A biodetection method using magnetic particles and micro traps.* Journal of Applied Physics, 2012. **111**(7): p. 07B328.
181. Jiao, A., et al., *Thermoresponsive Nanofabricated Substratum for the Engineering of Three-Dimensional Tissues with Layer-by-Layer Architectural Control.* ACS nano, 2014. **8**(5): p. 4430-4439.
182. Mönch, I., et al., *Synthesis and characteristics of Fe-filled multi-walled carbon nanotubes for biomedical application.* Journal of Physics: Conference Series, 2007. **61**(1): p. 820.
183. Chen, J., et al., *Au-Silica Nanowire Nanohybrid as a Hyperthermia Agent for Photothermal Therapy in the Near-Infrared Region.* Langmuir, 2014. **30**(31): p. 9514-9523.
184. Liu, L., et al., *Highly localized heat generation by femtosecond laser induced plasmon excitation in Ag nanowires.* Applied Physics Letters, 2013. **102**(7): p. 073107.
185. Su, Y., et al., *Silicon nanowire-based therapeutic agents for in vivo tumor near-infrared photothermal ablation.* Journal of Materials Chemistry B, 2014. **2**(19): p. 2892-2898.
186. Hochbaum, A.I., et al., *Enhanced thermoelectric performance of rough silicon nanowires.* Nature, 2008. **451**(7175): p. 163-167.
187. Fangohr, H., et al., *Joule heating in nanowires.* Physical Review B, 2011. **84**(5): p. 054437.
188. Kocakaplan, Y. and E. Kantar, *An effective-field theory study of hexagonal Ising nanowire: Thermal and magnetic properties.* Chinese Physics B, 2014. **23**(4).
189. Boukai, A.I., et al., *Silicon nanowires as efficient thermoelectric materials.* Nature, 2008. **451**(7175): p. 168-171.
190. Bauer, G.E.W., et al., *Nanoscale magnetic heat pumps and engines.* Physical Review B, 2010. **81**(2).
191. Chen, R., et al., *Nanowires for Enhanced Boiling Heat Transfer.* Nano Letters, 2009. **9**(2): p. 548-553.
192. Choi, D.S., et al., *Hyperthermia with Magnetic Nanowires for Inactivating Living Cells.* Journal of Nanoscience and Nanotechnology, 2008. **8**(5): p. 2323-2327.
193. Lin, W.-S., et al., *Shape Effects of Iron Nanowires on Hyperthermia Treatment.* Journal of Nanomaterials, 2013. **2013**: p. 1-6.
194. Armijo, L.M., et al., *Iron Oxide Nanocrystals for Magnetic Hyperthermia Applications.* Nanomaterials, 2012. **2**(2): p. 134-146.

195. Ang, K.L., S. Venkatraman, and R.V. Ramanujan, *Magnetic PNIPA hydrogels for hyperthermia applications in cancer therapy.* Materials Science and Engineering: C, 2007. **27**(3): p. 347-351.
196. Gao, N., H. Wang, and E.H. Yang, *An experimental study on ferromagnetic nickel nanowires functionalized with antibodies for cell separation.* Nanotechnology, 2010. **21**(10): p. 105107.
197. Hultgren, A., et al., *Cell manipulation using magnetic nanowires.* Journal of applied physics, 2003. **93**(10): p. 7554-7556.
198. Hultgren, A., et al., *Optimization of yield in magnetic cell separations using nickel nanowires of different lengths.* Biotechnology progress, 2005. **21**(2): p. 509-515.
199. Choi, D., et al., *Transport of living cells with magnetically assembled nanowires.* Biomedical microdevices, 2007. **9**(2): p. 143-148.
200. Hultgren, A., et al., *High-yield cell separations using magnetic nanowires.* Magnetics, IEEE Transactions on, 2004. **40**(4): p. 2988-2990.
201. Gao, N., et al. *Antibody-functionalized magnetic nanowires for cell purification*. in *SPIE Defense, Security, and Sensing*. 2009. International Society for Optics and Photonics.
202. Zhao, Y. and H. Zeng, *Rotational maneuver of ferromagnetic nanowires for cell manipulation.* NanoBioscience, IEEE Transactions on, 2009. **8**(3): p. 226-236.
203. Zhang, L., et al., *Targeted cargo delivery using a rotating nickel nanowire.* Nanomedicine: Nanotechnology, Biology and Medicine, 2012. **8**(7): p. 1074-1080.
204. Choi, D.S., et al., *Magnetically driven spinning nanowires as effective materials for eradicating living cells.* Journal of Applied Physics, 2012. **111**(7): p. 07B329.
205. Hossain, M.Z. and M.G. Kleve, *Nickel nanowires induced and reactive oxygen species mediated apoptosis in human pancreatic adenocarcinoma cells.* International journal of nanomedicine, 2011. **6**: p. 1475.
206. Wang, W., et al., *Acoustic Propulsion of Nanorod Motors Inside Living Cells.* Angewandte Chemie, 2014. **126**(12): p. 3265-3268.
207. Zhang, L., et al., *Controlled propulsion and cargo transport of rotating nickel nanowires near a patterned solid surface.* ACS Nano, 2010. **4**(10): p. 6228-34.
208. Garcia-Gradilla, V., et al., *Functionalized Ultrasound-Propelled Magnetically Guided Nanomotors: Toward Practical Biomedical Applications.* ACS Nano, 2013. **7**(10): p. 9232-9240.
209. Castillo, M., et al., *Local mechanical response of cells to the controlled rotation of magnetic nanorods.* J Biomed Mater Res B Appl Biomater, 2014.
210. Sun, L., K. Keshoju, and H. Xing, *Magnetic field mediated nanowire alignment in liquids for nanocomposite synthesis.* Nanotechnology, 2008. **19**(40): p. 405603.
211. Kim, K., et al., *Ultrahigh-speed rotating nanoelectromechanical system devices assembled from nanoscale building blocks.* Nat Commun, 2014. **5**: p. 3632.
212. Fung, A.O., et al., *Induction of Cell Death by Magnetic Actuation of Nickel Nanowires Internalized by Fibroblasts.* The Journal of Physical Chemistry C, 2008. **112**(39): p. 15085-15088.
213. Keshoju, K., H. Xing, and L. Sun, *Magnetic field driven nanowire rotation in suspension.* Applied Physics Letters, 2007. **91**(12): p. 123114.

214. Masuda, H. and K. Fukuda, *Ordered metal nanohole arrays made by a two-step replication of honeycomb structures of anodic alumina.* Science, 1995. **268**(5216): p. 1466-8.
215. Nielsch, K., et al., *Hexagonally ordered 100 nm period nickel nanowire arrays.* Applied Physics Letters, 2001. **79**(9): p. 1360-1362.
216. Pirota, K., et al., *Novel magnetic materials prepared by electrodeposition techniques: arrays of nanowires and multi-layered microwires.* Journal of alloys and compounds, 2004. **369**(1): p. 18-26.
217. Nielsch, K., et al., *Uniform Nickel Deposition into Ordered Alumina Pores by Pulsed Electrodeposition.* Advanced Materials, 2000. **12**(8): p. 582-586.
218. Vázquez, M., et al., *Magnetic properties of densely packed arrays of Ni nanowires as a function of their diameter and lattice parameter.* Journal of Applied Physics, 2004. **95**(11): p. 6642-6644.
219. Vivas, L.G., et al., *Coercivity of ordered arrays of magnetic Co nanowires with controlled variable lengths.* Applied Physics Letters, 2011. **98**(23): p. 232507-232507-3.
220. Thurn-Albrecht, T., et al., *Ultrahigh-density nanowire arrays grown in self-assembled diblock copolymer templates.* Science, 2000. **290**(5499): p. 2126-2129.
221. Chen, R., et al., *Silver telluride nanowires prepared by dc electrodeposition in porous anodic alumina templates.* Journal of Materials Chemistry, 2002. **12**(8): p. 2435-2438.
222. Xu, D., et al., *Preparation and characterization of CdS nanowire arrays by dc electrodeposit in porous anodic aluminum oxide templates.* Chemical Physics Letters, 2000. **325**(4): p. 340-344.
223. Timko, B.P., T. Dvir, and D.S. Kohane, *Remotely triggerable drug delivery systems.* Advanced materials, 2010. **22**(44): p. 4925-4943.
224. Ghosh, S., et al., *Alternating Magnetic Field Controlled, Multifunctional Nano-Reservoirs: Intracellular Uptake and Improved Biocompatibility.* Nanoscale Res Lett, 2009. **5**(1): p. 195-204.
225. Yang, C., et al., *Thermo-responsive Mn–Zn ferrite/poly (N, N'-isopropyl acrylamide-co-N-hydroxymethylacrylamide) core/shell nanocomposites for drug-delivery systems.* Journal of Biomaterials Science, Polymer Edition, 2011. **22**(11): p. 1473-1486.
226. Yao, A., et al., *Preparation and characterization of temperature-responsive magnetic composite particles for multi-modal cancer therapy.* Journal of Materials Science: Materials in Medicine, 2011. **22**(10): p. 2239-2247.
227. Liu, X.L., et al., *Magnetic nanoparticle-loaded polymer nanospheres as magnetic hyperthermia agents.* Journal of Materials Chemistry B, 2014. **2**(1): p. 120-128.
228. Zaher, A., et al., *Osmotically driven drug delivery through remote-controlled magnetic nanocomposite membranes.* Biomicrofluidics, 2015. **9**(5): p. 054113.
229. Desai, T.A., D. Hansford, and M. Ferrari, *Characterization of micromachined silicon membranes for immunoisolation and bioseparation applications.* Journal of Membrane Science, 1999. **159**(1): p. 221-231.
230. Santini, J.T., et al., *Microchip technology in drug delivery.* Annals of Medicine, 2000. **32**(6): p. 377-379.

231. Maloney, J.M., et al., *Electrothermally activated microchips for implantable drug delivery and biosensing.* Journal of Controlled Release, 2005. **109**(1): p. 244-255.
232. Prescott, J.H., et al., *Chronic, programmed polypeptide delivery from an implanted, multireservoir microchip device.* Nature biotechnology, 2006. **24**(4): p. 437-438.
233. Grayson, A.C.R., et al., *Multi-pulse drug delivery from a resorbable polymeric microchip device.* Nature materials, 2003. **2**(11): p. 767-772.
234. Chung, A.J., Y.S. Huh, and D. Erickson, *A robust, electrochemically driven microwell drug delivery system for controlled vasopressin release.* Biomedical microdevices, 2009. **11**(4): p. 861-867.
235. Elman, N., H.H. Duc, and M. Cima, *An implantable MEMS drug delivery device for rapid delivery in ambulatory emergency care.* Biomedical microdevices, 2009. **11**(3): p. 625-631.
236. Pirmoradi, F.N., et al., *On-demand controlled release of docetaxel from a battery-less MEMS drug delivery device.* Lab Chip, 2011. **11**(16): p. 2744-52.
237. Su, Y.-C., L. Lin, and A.P. Pisano, *A water-powered osmotic microactuator.* Microelectromechanical Systems, Journal of, 2002. **11**(6): p. 736-742.
238. Li, Y.-H. and Y.-C. Su, *Miniature osmotic actuators for controlled maxillofacial distraction osteogenesis.* Journal of Micromechanics and Microengineering, 2010. **20**(6): p. 065013.
239. Ryu, W., et al., *Biodegradable micro-osmotic pump for long-term and controlled release of basic fibroblast growth factor.* Journal of Controlled Release, 2007. **124**(1): p. 98-105.
240. Evans, A.T., S. Chiravuri, and Y.B. Gianchandani, *Transdermal power transfer for recharging implanted drug delivery devices via the refill port.* Biomedical microdevices, 2010. **12**(2): p. 179-185.
241. Evans, A.T., et al., *A low power, microvalve regulated architecture for drug delivery systems.* Biomedical microdevices, 2010. **12**(1): p. 159-168.
242. Evans, A.T., S. Chiravuri, and Y.B. Gianchandani, *A multidrug delivery system using a piezoelectrically actuated silicon valve manifold with embedded sensors.* Microelectromechanical Systems, Journal of, 2011. **20**(1): p. 231-238.
243. Bourouina, T., A. Bosseb, and J.-P. Grandchamp, *Design and simulation of an electrostatic micropump for drug-delivery applications.* Journal of Micromechanics and Microengineering, 1997. **7**(3): p. 186.
244. Teymoori, M.M. and E. Abbaspour-Sani, *Design and simulation of a novel electrostatic peristaltic micromachined pump for drug delivery applications.* Sensors and Actuators A: Physical, 2005. **117**(2): p. 222-229.
245. Schneeberger, N., et al., *Drug delivery micropump with built-in monitoring.* Procedia Chemistry, 2009. **1**(1): p. 1339-1342.
246. Geipel, A., et al., *Design of an implantable active microport system for patient specific drug release.* Biomedical microdevices, 2008. **10**(4): p. 469-478.
247. Li, P.-Y., et al., *An electrochemical intraocular drug delivery device.* Sensors and Actuators A: Physical, 2008. **143**(1): p. 41-48.
248. Li, P.-Y., et al., *A parylene bellows electrochemical actuator.* Microelectromechanical Systems, Journal of, 2010. **19**(1): p. 215-228.
249. Gensler, H., et al., *An implantable MEMS micropump system for drug delivery in small animals.* Biomedical microdevices, 2012. **14**(3): p. 483-496.

250. Sheybani, R., H. Gensler, and E. Meng. *Rapid and repeated bolus drug delivery enabled by high efficiency electrochemical bellows actuators*. in *Proc. IEEE Int. Conf. TRANSDUCERS*. 2011.
251. Sheybani, R. and E. Meng. *High efficiency wireless electrochemical actuators: design, fabrication and characterization by electrochemical impedance spectroscopy*. in *Micro Electro Mechanical Systems (MEMS), 2011 IEEE 24th International Conference on*. 2011. IEEE.
252. Sheybani, R. and E. Meng, *High-efficiency MEMS electrochemical actuators and electrochemical impedance spectroscopy characterization.* Microelectromechanical Systems, Journal of, 2012. **21**(5): p. 1197-1208.
253. Cooney, C.G. and B.C. Towe, *A thermopneumatic dispensing micropump.* Sensors and Actuators A: Physical, 2004. **116**(3): p. 519-524.
254. Samel, B., P. Griss, and G. Stemme, *A thermally responsive PDMS composite and its microfluidic applications.* Microelectromechanical Systems, Journal of, 2007. **16**(1): p. 50-57.
255. Reynolds, A.F. and J.Z. Hilt, *Poly(n-isopropylacrylamide)-based hydrogel coatings on magnetite nanoparticles via atom transfer radical polymerization.* Nanotechnology, 2008. **19**(17): p. 175101.
256. Regmi, R., et al., *Hyperthermia controlled rapid drug release from thermosensitive magnetic microgels.* Journal of Materials Chemistry, 2010. **20**(29): p. 6158.
257. Qi, W., et al., *Triggered release of insulin from glucose-sensitive enzyme multilayer shells.* Biomaterials, 2009. **30**(14): p. 2799-2806.
258. Mamada, A., et al., *Photoinduced phase transition of gels.* Macromolecules, 1990. **23**(5): p. 1517-1519.
259. Lee, Y.J., et al., *Biocompatibility of a Novel Cyanoacrylate Based Tissue Adhesive: Cytotoxicity and Biochemical Property Evaluation.* PLoS ONE, 2013. **8**(11): p. e79761.
260. Moretti Neto, R.T., et al., *In vivo qualitative analysis of the biocompatibility of different cyanoacrylate-based adhesives.* Braz Oral Res, 2008. **22**(1): p. 43-7.
261. Hyeon, T., et al., *Synthesis of Highly Crystalline and Monodisperse Maghemite Nanocrystallites without a Size-Selection Process.* Journal of the American Chemical Society, 2001. **123**(51): p. 12798-12801.
262. Sun, S. and H. Zeng, *Size-Controlled Synthesis of Magnetite Nanoparticles.* Journal of the American Chemical Society, 2002. **124**(28): p. 8204-8205.
263. Goya, G.F., et al., *Magnetic Hyperthermia With Fe3O4 Nanoparticles: The Influence of Particle Size on Energy Absorption.* Ieee Transactions on Magnetics, 2008. **44**(11): p. 4444-4447.
264. Timoshenko, S., S. Woinowsky-Krieger, and S. Woinowsky-Krieger, *Theory of plates and shells*. Vol. 2. 1959: McGraw-Hill New York.
265. Whitaker, S., *Flow in porous media I: A theoretical derivation of Darcy's law.* Transport in Porous Media, 1986. **1**(1): p. 3-25.
266. Teng, O.K., *Influence of Additives on Ethylcellulose Coatings*, 2006: National University of Singapore.
267. Lien, Y.-H., et al., *Cytotoxicity and drug release behavior of PNIPAM grafted on silica-coated iron oxide nanoparticles.* Journal of Nanoparticle Research, 2011. **13**(10): p. 5065-5075.

268. Lien, Y.-H., et al., *In vitro evaluation of the thermosensitive and magnetic nanoparticles for the controlled drug delivery of vitamin D3.* Macromolecular Research, 2013. **21**(5): p. 511-518.
269. Cai, Y. and Y.-Y. Liu, *Amphiphilic Unimolecular Nanoparticles Based on a Hyperbranched Polyacrylate Core and a PNIPAm Shell: Synthesis via ATRP and Properties.* Macromolecular Chemistry and Physics, 2013. **214**(8): p. 882-891.
270. Lu, N., et al., *Controlled Drug Loading and Release of a Stimuli-Responsive Lipogel Consisting of Poly(N-isopropylacrylamide) Particles and Lipids.* The Journal of Physical Chemistry B, 2013. **117**(33): p. 9677-9682.
271. Zhu, Z., et al., *Temperature-triggered on-demand drug release enabled by hydrogen-bonded multilayers of block copolymer micelles.* Journal of Controlled Release, 2013. **171**(1): p. 73-80.
272. Han, H.D., B.C. Shin, and H.S. Choi, *Doxorubicin-encapsulated thermosensitive liposomes modified with poly(N-isopropylacrylamide-co-acrylamide): Drug release behavior and stability in the presence of serum.* European Journal of Pharmaceutics and Biopharmaceutics, 2006. **62**(1): p. 110-116.
273. Han, H.D., et al., *Hyperthermia-induced antitumor activity of thermosensitive polymer modified temperature-sensitive liposomes.* Journal of Pharmaceutical Sciences, 2006. **95**(9): p. 1909-1917.
274. Yu, Y.-L., et al., *Thermo-responsive monodisperse core–shell microspheres with PNIPAM core and biocompatible porous ethyl cellulose shell embedded with PNIPAM gates.* Journal of Colloid and Interface Science, 2012. **376**(1): p. 97-106.
275. Randall, G.C. and P.S. Doyle, *Permeation-driven flow in poly(dimethylsiloxane) microfluidic devices.* Proceedings of the National Academy of Sciences of the United States of America, 2005. **102**(31): p. 10813-10818.
276. Yi, Y., U. Buttner, and I.G. Foulds, *Towards an Implantable Pulsed Mode Electrolytic Drug Delivery System.* MicroTas, 2013: p. pp. 527-529.
277. Fong, J., Z. Xiao, and K. Takahata, *Wireless implantable chip with integrated nitinol-based pump for radio-controlled local drug delivery.* Lab on a Chip, 2015. **15**(4): p. 1050-1058.
278. Ying, Y., et al. *Electromagnetically powered electrolytic pump and thermo-responsive valve for drug delivery*. in *Nano/Micro Engineered and Molecular Systems (NEMS), 2015 IEEE 10th International Conference on*. 2015.
279. Yi, Y., et al., *A remotely operated drug delivery system with an electrolytic pump and a thermo-responsive valve.* Biomicrofluidics, 2015. **9**(5): p. 052608.
280. Bradley, M. and B. Vincent, *Interaction of nonionic surfactants with copolymer microgel particles of NIPAM and acrylic acid.* Langmuir, 2005. **21**(19): p. 8630-8634.
281. Harmon, M.E., et al., *Photo-cross-linkable PNIPAAm copolymers. 4. Effects of copolymerization and cross-linking on the volume-phase transition in constrained hydrogel layers.* Langmuir, 2003. **19**(26): p. 10947-10956.
282. Yassine, O., et al., *Electrophoresis PDMS/glass chips with continuous on-chip derivatization and analysis of amino acids using naphthalene-2, 3-dicarboxaldehyde as fluorogenic agent.* Analytica chimica acta, 2008. **609**(2): p. 215-222.
283. Gooneratne, C.P., et al., *Selective Manipulation of Superparamagnetic Beads by a Magnetic Microchip.* Magnetics, IEEE Transactions on, 2013. **49**(7): p. 3418-3421.

284. Renaud, L., et al., *Electrophoresis Poly (Dimethylsiloxane)/Glass Chips with Integrated Active Cooling for Quantification of Amino Acids.* Experimental Heat Transfer, 2009. **23**(1): p. 63-72.
285. Faure, K., et al., *Electrochromatography in poly (dimethyl) siloxane microchips using organic monolithic stationary phases.* Electrophoresis, 2007. **28**(11): p. 1668-1673.
286. Seo, M., et al., *Microfluidic consecutive flow-focusing droplet generators.* Soft Matter, 2007. **3**(8): p. 986-992.
287. Gongora-Rubio, M.R., et al., *LTCC-3D Coaxial Flow Focusing Microfluidic Reactor for Micro and Nanoparticle Fabrication and Production Scale-Out.* Journal of microelectronics and electronic packaging, 2013. **10**(3): p. 102-108.
288. Yassine, O., et al., *Isolation of cells for selective treatment and analysis using a magnetic microfluidic chip.* Biomicrofluidics, 2014. **8**(3): p. 034114.
289. Li, E.Q., J.M. Zhang, and S.T. Thoroddsen, *Simple and inexpensive microfluidic devices for the generation of monodisperse multiple emulsions.* Journal of Micromechanics and Microengineering, 2014. **24**(1): p. 015019.
290. Valles, E., et al., *Equilibrium swelling and mechanical properties of hydrogels of acrylamide and itaconic acid or its esters.* Polymer bulletin, 2000. **44**(1): p. 109-114.
291. Liu, P., et al., *Radiation preparation and swelling behavior of sodium carboxymethyl cellulose hydrogels.* Radiation Physics and Chemistry, 2002. **63**(3): p. 525-528.
292. Liu, P., et al., *Radiation crosslinking of CMC-Na at low dose and its application as substitute for hydrogel.* Radiation Physics and Chemistry, 2005. **72**(5): p. 635-638.
293. Li, B., O. Yassine, and J. Kosel. *Integrated passive and wireless sensor for magnetic fields, temperature and humidity*. in *SENSORS, 2013 IEEE*. 2013. IEEE.
294. Chu, L.Y., et al., *Monodisperse Thermoresponsive Microgels with Tunable Volume-Phase Transition Kinetics.* Advanced Functional Materials, 2007. **17**(17): p. 3499-3504.
295. Schild, H., *Poly (N-isopropylacrylamide): experiment, theory and application.* Progress in polymer science, 1992. **17**(2): p. 163-249.
296. Xiao, X., *Effect of the initiator on thermosensitive rate of poly (N-isopropylacrylamide) hydrogels.* Exp. Polym. Lett., 2007. **1**(4): p. 232-235.
297. Nagase, K., J. Kobayashi, and T. Okano, *Temperature-responsive intelligent interfaces for biomolecular separation and cell sheet engineering.* Journal of The Royal Society Interface, 2009: p. rsif. 2008.0499. focus.
298. Zhang, Y., et al., *A novel route to thermosensitive polymeric core–shell aggregates and hollow spheres in aqueous media.* Advanced Functional Materials, 2005. **15**(4): p. 695-699.
299. Xia, L.-W., et al., *Nano-structured smart hydrogels with rapid response and high elasticity.* Nature communications, 2013. **4**.
300. Sershen, S. and J. West, *Implantable, polymeric systems for modulated drug delivery.* Advanced Drug Delivery Reviews, 2002. **54**(9): p. 1225-1235.
301. Zhang, J.-T., et al., *A novel two-level microstructured poly (N-isopropylacrylamide) hydrogel for controlled release.* Acta biomaterialia, 2010. **6**(10): p. 3890-3898.
302. Quinn, J.F. and F. Caruso, *Facile Tailoring of Film Morphology and Release Properties Using Layer-by-Layer Assembly of Thermoresponsive Materials.* Langmuir, 2004. **20**(1): p. 20-22.

303. Mizuntani, M., K. Satoh, and M. Kamigaito, *Degradable poly (N-isopropylacrylamide) with tunable thermosensitivity by simultaneous chain-and step-growth radical polymerization.* Macromolecules, 2011. **44**(7): p. 2382-2386.
304. Zhang, B.-y., et al., *Reducibly degradable hydrogels of PNIPAM and PDMAEMA: Synthesis, stimulus-response and drug release.* Journal of Polymer Science Part A: Polymer Chemistry, 2010. **48**(16): p. 3604-3612.
305. Galperin, A., et al., *Synthesis and fabrication of a degradable poly(N-isopropyl acrylamide) scaffold for tissue engineering applications.* Journal of Biomedical Materials Research Part A, 2013. **101A**(3): p. 775-786.
306. Atkinson, W.J., I.A. Brezovich, and D.P. Chakraborty, *Usable frequencies in hyperthermia with thermal seeds.* Biomedical Engineering, IEEE Transactions on, 1984(1): p. 70-75.
307. Millington, R. and J. Quirk, *Permeability of porous solids.* Transactions of the Faraday Society, 1961. **57**: p. 1200-1207.
308. Ma, M., et al., *Facile synthesis of ultrathin magnetic iron oxide nanoplates by Schikorr reaction.* Nanoscale Research Letters, 2013. **8**(1): p. 16.
309. Müller, R., et al., *Preparation of magnetic nanoparticles with large specific loss power for heating applications.* Journal of magnetism and magnetic materials, 2005. **289**: p. 13-16.
310. Shiba, K., et al., *Analysis of specific absorption rate in biological tissue surrounding transcutaneous transformer for an artificial heart.* Journal of Artificial Organs, 2002. **5**(2): p. 91-96.
311. Katscher, U., et al., *Determination of electric conductivity and local SAR via B1 mapping.* Medical Imaging, IEEE Transactions on, 2009. **28**(9): p. 1365-1374.
312. Buzdugan, M.I., et al., *The Electromagnetic Threat in the Today's Environment*, in *International Conference on Advancements of Medicine and Health Care through Technology*, S. Vlad, R. Ciupa, and A. Nicu, Editors. 2009, Springer Berlin Heidelberg. p. 355-358.
313. Ferré, R., et al., *Magnetization processes in nickel and cobalt electrodeposited nanowires.* Physical Review B, 1997. **56**(21): p. 14066-14075.
314. Pirmoradi, F.N., et al., *On-demand controlled release of docetaxel from a battery-less MEMS drug delivery device.* Lab on a Chip, 2011. **11**(16): p. 2744-2752.
315. Kim, J.W., et al., *Fabrication of monodisperse gel shells and functional microgels in microfluidic devices.* Angewandte Chemie, 2007. **119**(11): p. 1851-1854.

Appendices

Appendix A Modeling and Numerical Simulation of Osmotically Driven Drug Delivery through Remote-Controlled Magnetic Nanocomposite Membranes

This section covers the details associated with the simulation results presented in Figure 2.18a, for which the author had some theoretical contributions, and for which the collaborator at the University of California Berkeley conducted the simulations and most of the theoretical aspects.

A.1 Modeling and Numerical Simulations

Modeling and simulation can provide design and experimental insight for further understanding the drug delivery system used in experiments. COMSOL is used in this work using 2D axis-symmetric conditions with the focus on the cyanoacrylate treated EC membrane with PNIPAm hydrogel and SPIO particles, which is then compared with experimental results. Three unknown parameters are studied in the modeling/simulation process: (1) magnitude and behavior of osmotic pressure, (2) membrane porosity, and (3) permeability of magnetic membrane with and without the magnetic field. The numerical model is developed based on three key modules in the software: fluid-structure interaction (FSI), free flow and flow through porous media, and species transport through free and porous media. The FSI module simply combines the Navier-Stokes equation that applies to water (incompressible, Newtonian flow) with the structural mechanics equation for isotropic linearly elastic material that is nearly incompressible (PDMS), while the Brinkman equation is utilized for porous regions. The transport of species (RhB solution) through free and porous media can be solved with Free and Porous Media Flow module in COMSOL. In this work, the governing equation of the module is transferred to a mathematical module and simplified for the simulation. The setting of the governing equation has been emulated to the built-in equations and simplified (see next paragraph), for the purpose of computability, to:

$$\varepsilon \frac{\partial c}{\partial t} + \nabla \cdot (c\boldsymbol{u}) = \nabla \cdot \left(\left(\varepsilon^{\frac{4}{3}} D \right) \nabla c \right) \qquad [A\text{-}1]$$

where ε is the porosity; c is the concentration of the diffusing species (RhB); **u** is the velocity profile, and D is the diffusion coefficient of the diffusing species.

In order to reach this form of the governing equation used for simulation, first the osmotic pressure profile parameter is selected as the controlling parameter, or independent input variable, due to the complexity of the osmotic pump system. In this complex process, osmosis drives the initial PDMS deflection. The resistive force from the PDMS membrane and donor chamber will ultimately affect the water inflow from osmosis, causing the osmosis pressure and the resistive pressure from the PDMS and donor chamber to affect each other. Modeling of all parameters that fully describe the osmotic process causes difficulties in simulation by introducing rather complex physical and chemical interactions. Furthermore, they are not all directly linked to the PDMS membrane's deflection. Therefore, instead of the osmotic process itself, it is more appropriate for the osmotic pressure profile to be simulated, as it can be closely related to the PDMS deflection and the consequential coupled relationship between resistive forces from the PDMS membrane, and the donor chamber and magnetic composite membrane. Using certain physical conditions and assumptions that happen over long periods of time, a compromise between efficiency and accuracy over predicting PDMS water volume displacement and deflection can be achieved in the simulation: (i) the amount of drug delivery from the donor chamber to the receptor chamber per stage of osmotic pumping cycling is assumed to be linear. (ii) the osmotic pressure will stay the same as more water is introduced to the osmotic chamber by assuming that the saturation concentration of salt stays the same throughout the pumping. The introduction of more water into the osmotic chamber over time will keep the salt concentration the same, since there are always undissolved salt precipitate in the osmotic chamber throughout the experiments.

To define the boundaries between fluidic and solid regions, the FSI module in COMSOL combines the Navier-Stokes equation that applies to water (incompressible, Newtonian flow) with a structural mechanics equation for isotropic and linear elastic material that is nearly incompressible (describes PDMS). With some adjustment of the fluidic frame of reference with the solid frame of reference, the FSI module is solved:

$$\mathbf{f} = \mathbf{n} \cdot \{-p\mathrm{I} + \left(\mu\left(\nabla \mathrm{u}_{\mathrm{fluid}} + (\nabla \mathrm{u}_{\mathrm{fluid}})^{\mathrm{T}}\right) - \frac{2}{3}\mu(\nabla \cdot \mathrm{u}_{\mathrm{fluid}})\mathbf{I}\right)\} \qquad [A\text{-}2]$$

- **f** is the reaction force from the fluidic force
- **n** is the outward normal vector in fluid-structure boundary
- p is the pressure
- μ is the dynamic viscosity of the fluid
- u_{fluid} is the fluidic velocity vector
- **I** is the identity vector

Next, the Free Flow and Flow through Porous Media COMSOL module, used to simulate the magnetic membrane, is discussed. The Free Flow and Flow through Porous Media module is governed by two equations: the Navier-Stokes equation for water (incompressible, Newtonian) for open flow, and the Brinkman equation for porous regions. The Brinkman equation is a modification of Darcy's Law for porous flow, adding additional importance to momentum transport in fluid due to shear stress. Typically, the Brinkman equation is in the form $\beta\nabla^2 q + q = -K\nabla P$, where q is the Darcy velocity (q = v*n, where v is fluid velocity, and n is porosity), P is pressure, β and K are effective viscosity and permeability, respectively. COMSOL utilizes a more complex form of the Brinkman equation, accounting for various source/sink flux, conservation of mass and momentum, while accounting for viscous effects in porous media flow.

And finally, the following covers the steps and assumptions required in order to reach the simplification of the governing equation for transport through free and porous media, Eqn. (2-2). The governing equation for the transport of RhB is derived from the equation describing porous media and a single fluid (from built-in COMSOL equation) which is of the form:

$$\left(\varepsilon + \rho_b k_{P,i}\right)\frac{\partial c_i}{\partial t} + \left(c_i - \rho_P c_{P,i}\right)\frac{\partial \varepsilon}{\partial t} + \nabla \cdot (c_i u) = \nabla \cdot \left[\left(D_{D,i} + \theta\tau_{F,i}D_{F,i}\right)\nabla c_i\right] + R_i + S_i \qquad [A\text{-}3]$$

where ε is porosity, ρ_b is bulk density, $k_{P,i} = \frac{\partial c_{P,i}}{\partial c_i}$ is the adsorption isotherm ($c_{P,i}$ is the solute mass sorbed into the solid, i.e. the membrane), ρ_P is the solid phase density, **u** is the fluid velocity, $D_{D,i}$ is the dispersion tensor (mechanical mixing), θ is the liquid fraction for specified species, $\tau_{F,i}$ is the tortuosity factor, $D_{F,i}$ is the effective diffusion coefficient of the specified species, R_i is the reaction rate of the species, and S_i is the

production rate of the species. Several facts are used to simplify the governing equations. First, the index i is removed, as RhB is the only element in consideration during the transport process. Second, it is assumed that there is no air pocket in the process as the membrane is saturated in water and the liquid fraction θ reduces to porosity ε. Third, it is assumed that little or no RhB is adsorbed to the nanocomposite membrane, and the term that deals with adsorption is neglected, i.e. $\rho_b k_{P,i} \frac{\partial c_i}{\partial t} \to 0$. Fourth, the porosity of the nanocomposite membrane is constant during stage-wise operation (i.e. it is constant within each stage of operation, except when magnetically changing the temperature and porosity when changing to a different stage), i.e. $\left(c_i - \rho_P c_{P,i}\right) \frac{\partial \varepsilon}{\partial t} \to 0$. Fifth, mechanical mixing can be neglected, thus $D_{D,i} \to 0$ for very low fluid flows in thin membranes, such that dispersion is expected to play small role. Sixth, the tortuosity factor is derived from default model used in COMSOL Multiphysics, which is called the Millington and Quirk model [307]. This makes $\tau_{F,i} = \varepsilon^{\frac{1}{3}} \to\to \theta\tau_{F,i} = \varepsilon^{\frac{4}{3}}$. Seventh, $D_{F,i}$ is the diffusivity of RhB in liquid water, which is calculated as $300\left(\frac{\mu m^2}{s}\right) = 3 * 10^{-10}(m^2/s)$. Finally, the model is assumed to have no internal reaction and creation of species during simulation. These lead to Eqn. (2-2) above. This indicates that the transport process depends mainly on the porosity of the nanocomposite membrane.

This approximate analytical equation provides a good baseline for the simulation-based investigation of the complete device's operation. Furthermore, elements difficult to measure experimentally are approximated and supported by the analytical approximation, and used in simulation. Approximation particularly focuses on the applied pressure by the osmotic chamber on the flexible PDMS membrane, P_{PDMS} (Figure S1).

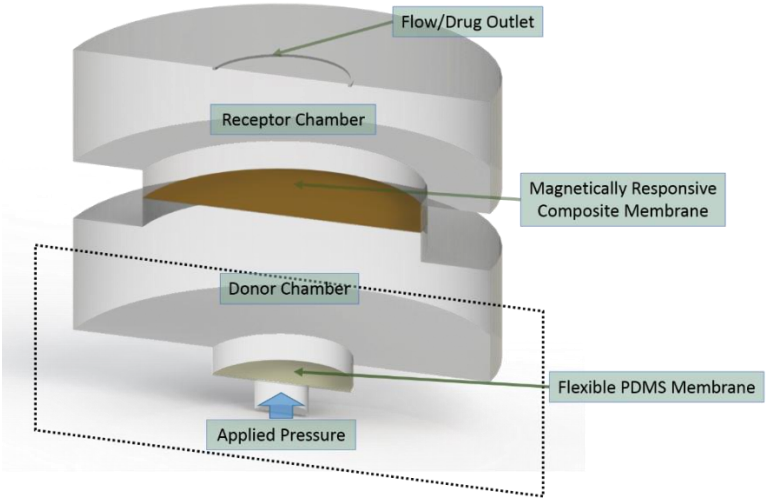

(a)

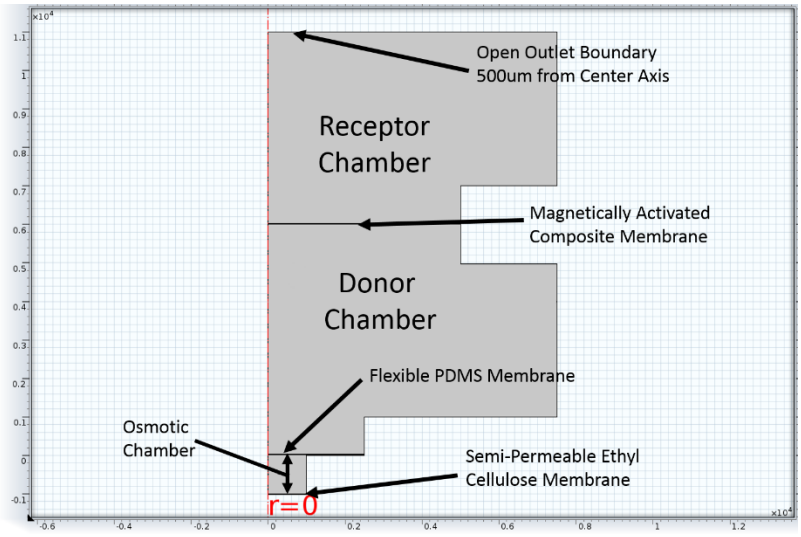

(b)

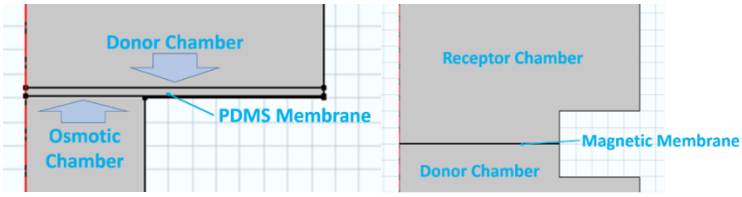

(c)

Figure S1 (a) Diagram of simulated device assembly with osmotic pump, with components used summarized as follows: (i) donor chamber houses test drug to be transferred to receptor chamber, (ii) the osmotic chamber under the PDMS membrane is replaced by applied fluid pressure profile for simplicity, (iii) the relief at the top of the assembly marked as "Flow/Drug Outlet" indicates the atmospheric boundary, (iv) dotted parallelogram indicates the part of the full osmotic pump assembly examined in a separate simulation model for closer understanding of flexible PDMS membrane's behavior (applied pressure test). (b) 2D axisymmetric model of the device. (c) Close up views of PDMS membrane and inlet membrane. Reprinted with permission from [228]. Copyright 2015, AIP Publishing LLC.

The analytical equation for this applied pressure on the PDMS membrane is derived from two basic equations that describe the elastic deflection of a membrane and the fluid flow through a semi-permeable membrane, namely the equation of deflection of a circular plate with clamped edges and under uniform lateral load (valid for any deflection) [264], and Darcy's Law [265]. By combining these and the boundary conditions, an approximation of the applied pressure on the PDMS membrane is derived (see section A2):

$$P_{PDMS} = \alpha V^3 + \frac{\mu h}{kA}\dot{V} \qquad [A\text{-}4]$$

- P_{PDMS} is the applied pressure on the PDMS membrane by the osmotic chamber in the pump
- α is a parameter determined when solely examining PDMS membrane deflection
- V is the fluid volume displaced due to PDMS deflection
- μ is the dynamic viscosity of the fluid
- h is the thickness of the magnetically responsive membrane
- k is the mechanical permeability of the magnetically responsive membrane
- A is the cross-sectional area of the magnetically responsive membrane
- $\dot{V}$ is the rate of volume displacement over time

The second term appears only with the existence of the magnetically responsive membrane, while the first term represents the contribution of the osmotic pump's displaced volume via the deflection of the PDMS membrane.

An approximated applied pressure on the PDMS, used to simulate the behavior of the PDMS membrane alone, shows an interesting behavior of the input pressure profile. Since the magnetic membrane's permeability is low in general, the small displacement of the PDMS membrane reduces the influence of the αV^3 term in P_{PDMS}, causing the applied pressure profile onto the donor chamber to be dominated by the volume displacement rate $\dot{V}$ through the magnetic membrane and the permeability k of the magnetic membrane in the second term. Because volume displacement is directly linked to the drug delivery rate to the receptor chamber, a small volume displacement also indicates a reduced drug delivery rate.

Furthermore, experimental data indicates a fairly constant drug transport rate. Under the assumption of a large drug reservoir donor chamber during osmotic pumping, a constant drug transport rate through the magnetic membrane with low permeability indicates a constant P_{PDMS} profile, one that is simple and almost time-independent. This pressure profile's dependency on the magnetic membrane's permeability makes it difficult to estimate the magnitude of the applied pressure during low drug transport, as the permeability of the magnetic membrane can be rather difficult to measure accurately. However, other crucial values and relations such as drug transport rates, applied pressure profile, and the magnetic membrane's permeability variation (by the external magnetic field) can still be evaluated with good accuracy and support, and are not affected by P_{PDMS}.

The simulation relies on three governing physics modules, namely (1) fluid-structure interaction for flexible PDMS, (2) fluid through open/free and semi-permeable media for the magnetically responsive magnetic membrane, and (3) convection-diffusion equation for drug (RhB) transport from the donor chamber to the receptor chamber. The approximation of the permeability of the magnetic membrane is based on work done on fluid transport and permeability of water vapor through EC [266]. From such a basis, the magnitude of P_{donor} is determined (see section A3). The permeability of the magnetic membrane is calibrated with this applied pressure, and the permeability difference between the magnetically activated and deactivated states is approximated by comparing the two states (magnetic field on and off), which gives a ratio of the magnetic membrane's permeability values for the two states (see section A4). Knowing this ratio, permeability difference can be determined.

The simulation process is divided into four parts, namely (1) direct pressure test, (2) magnetic membrane porosity calibration, (3) magnetic membrane permeability calibration, and (4) simulation of the full osmotic pump and magnetic membrane assembly. In the direct pressure test, only a certain segment of the osmotic pump is tested to investigate the flexible PDMS membrane's behavior (i.e. the osmotic process itself is not simulated). In the magnetic membrane porosity and permeability calibrations, the full osmotic pump and magnetic membrane assembly is simulated only for the magnetic on and off states (without osmotic pumping) in order

to calibrate the magnetic membrane's permeability and porosity during its magnetically activated and deactivated states. Finally, simulation of the full osmotic pump and nanocomposite magnetic membrane assembly follows the same osmotic pumping and magnetic activation regimes as the experiment, and the resulting simulation data is compared to and plotted with the experimental data.

A.2 Derivation of Pressure Applied to PDMS Membrane by Osmotic Process

To derive the P_{PDMS} formula of Eqn. [A-4], we start with the simple configuration between the PDMS membrane; the osmotic chamber on one side, and the donor chamber on the other side. Two properties can be noted from this. First, when considering the effect on the PDMS membrane, pressure retained in the donor chamber due to the magnetic membrane's low permeability, and pressure applied to the PDMS membrane due to osmosis in osmotic chamber, will counteract each other at the PDMS membrane, reaching equilibrium and holding it in a position at any given time. Second, the magnitude of the pressure in the osmotic chamber is always greater than or equal to the pressure in the donor chamber. Aside from the gravitational effect (which can be and is neglected), the only source of *external* pressure application is from the osmotic chamber. When the magnetic membrane is impermeable (i.e. permeability of magnetic membrane=0), the donor chamber pressure and osmotic chamber pressure will be equal over time, resulting in a stationary state for the PDMS membrane once pressure equilibrium is reached.

This creates a simple pressure equation, $P_{Net} = P_{PDMS} - P_{Donor}$, where P_{Net} is the net pressure applied onto the PDMS membrane, P_{PDMS} is the pressure applied to the PDMS membrane only from osmosis, and P_{Donor} is the back pressure from donor chamber. Note that P_{Net} will always be greater than or equal to zero to make physical sense with regards to the definition of the simulation parameters, as $P_{PDMS} \geq P_{Donor}$.

Of course, this condition does not initially work since the initial contact area of pressure for pressure from osmosis is not same as the area of PDMS membrane that donor chamber can apply pressure to, due to difference in osmotic and donor chamber cross-sectional areas (an assembly requirement). However, the initial pressure created by the osmotic chamber and the resulting deflection of the PDMS membrane allows the salt water in the osmotic chamber to be in contact with the entire PDMS surface (The resulting differential

pressure can thus be approximated as a step function). This causes the area of applied pressures from donor chamber and osmotic chamber to quickly become equal (with negligible changes in areas of pressure application on the PDMS membrane due to its deflection).

From $\mathrm{F_{Net}} = F_{PDMS} - F_{Donor}$, where $\mathrm{F_{Net}}$ is the net force applied to the PDMS membrane, $\mathrm{F_{PDMS}}$ is the force applied to PDMS membrane from osmosis, and $\mathrm{F_{Donor}}$ is the force applied to PDMS membrane from donor chamber. After a relatively short period of time, areas of PDMS membrane with pressure applied from donor chamber and osmotic chamber are the same as A.

Thus, $\frac{\mathrm{F_{Net}}}{A} = P_{Net} = \frac{F_{PDMS}}{A} - \frac{F_{Donor}}{A} = P_{PDMS} - P_{Donor} \gg P_{Net} = P_{PDMS} - P_{Donor}$.

From Timoshenko's work for large deflection of circular plates [264], the equation of deflection as a function of radial distance is defined as $\mathrm{w(r)} = \mathrm{w_0}\left(1 - \frac{r^2}{a^2}\right)^2$, where w is the deflection as a function of radial distance, $\mathrm{w_0}$ is the maximum deflection or the deflection at the center of the membrane, r is the radial distance, and a is the radius of the flexible membrane.

According to the work, $\mathrm{w_0} = 0.662a\sqrt[3]{\frac{qa}{Eh}}$, where q is the applied load on the membrane, E is the Young's modulus of the membrane, and h is the thickness of the membrane. However, the value for maximum deflection is based on when Poisson's ratio of the membrane is approximately 0.3, not 0.5 of the PDMS in this work. Asides from the relationship $\mathrm{w_0} \propto \sqrt[3]{q}$, which is supported by this work's simulation result during the direct pressure test on the PDMS membrane without the existence of the magnetic membrane, the coefficient term $0.662\mathrm{a}\sqrt[3]{\frac{a}{Eh}}$ should be re-determined.

Using the definition of w(r), volume of deflection can be determined using the shell method.

$$\mathrm{V} = 2\pi \int_0^a rw(r)dr = 2\pi w_0 \int_0^a \left(r - \frac{2r^3}{a^2} + \frac{r^5}{a^4}\right)dr = 2\pi w_0 \left(\frac{r^2}{2} - \frac{2r^4}{4a^2} + \frac{r^6}{6a^4}\right)\Big|_0^a$$

$$\mathrm{V} = 2\pi w_0 \left(\frac{a^2}{2} - \frac{a^2}{2} + \frac{a^2}{6}\right) = \frac{\pi w_0}{3}a^2.$$

If w_0 is defined as $w_0 = \beta\sqrt[3]{q}$, where β is a coefficient that can be approximated via simulation for a simple PDMS membrane, then:

$V = \frac{\pi}{3}a^2\beta\sqrt[3]{q}$. We can combine $\frac{\pi}{3}a^2\beta$ as η, and let $V = \eta\sqrt[3]{q}$.

Note that Timoshenko's examination is of a membrane under uniform load in a single direction (perpendicular to initial membrane configuration). Under uniform pressure, as in the case of the PDMS membrane, the pressure is normal to the surface of the PDMS, which changes direction with deflection, creating a more complex pressure application direction profile. However, considering the relatively small deflection of the PDMS membrane's area, a simulation of membrane deflection under uniform load is a good approximation. Thus, $V = \eta\sqrt[3]{q} = \eta\sqrt[3]{p}$.

Since the PDMS membrane's deflection is determined by the net pressure from the donor chamber and the osmotic chamber, $V = \eta\sqrt[3]{P_{Net}} \gg P_{Net} = \frac{V^3}{\eta^3}$. Since η is also some constant, we can let $\alpha = \frac{1}{\eta^3}$, making $P_{Net} = \alpha V^3$.

Given $P_{Net} = P_{PDMS} - P_{Donor} \gg \alpha V^3 = P_{PDMS} - P_{Donor}$.

$P_{PDMS} = \alpha V^3 + P_{Donor}$. We can determine P_{Donor} using the setup of the magnetic membrane, with the receptor chamber on one side and the donor chamber on the other (Figure S1).

The receptor chamber pressure is set to 0 relative to atmospheric pressure. Using Darcy's Law [265], this gives

$$Q = -\frac{kA}{\mu}\frac{(p_{receptor} - p_{donor})}{L} = \frac{kA}{\mu L}(p_{donor} - p_{receptor}) = \frac{kA}{\mu L}p_{donor},$$

where Q is the volumetric flow rate, k is the permeability of magnetic membrane, A is the area of magnetic membrane, μ is the dynamic viscosity of fluid, and L is the thickness of magnetic membrane.

Under the assumption that the fluid is incompressible, and wall-bending due to water pressure is negligible, Q can be determined as the time derivative of V derived from Timoshenko's work. Thus,

$Q = \dot{V} = \frac{kA}{\mu L}p_{donor} \gg p_{donor} = \frac{\mu L}{kA}\dot{V}$. Combining the relations for different pressures together, $P_{PDMS} = \alpha V^3 + P_{Donor} = \alpha V^3 + \frac{\mu L}{kA}\dot{V}$.

Thus, $P_{PDMS} = \alpha V^3 + \frac{\mu L}{kA}\dot{V}$. The second term appears only with the existence of the magnetic membrane, while the first term represents the contribution of the osmotic pump's displaced volume via the deflection of the PDMS membrane.

A.3 Determining Magnitude of Donor Chamber Pressure

The usage of P_{PDMS} comes from the inspection of the equation defined as $P_{PDMS} = \alpha V^3 + \frac{\mu L}{kA}\dot{V}$. Under the condition where there is no magnetic membrane, the second term of the equation disappears, becoming $P_{PDMS} = \alpha V^3$.

When the magnetic membrane is included in the simulation, however, the second term becomes the dominant term, due to the low volume fluid displacement amount caused by the low permeability of the magnetic membrane (regardless of its magnetic state), making $P_{PDMS} \cong \frac{\mu L}{kA}\dot{V}$.

The process of determining p_{donor} utilizes a linearization under the low-permeability condition. The experimental data of the drug release rate, and the ensuing approximation of the fluid flow rate in the low-permeability magnetic membrane state, indicate that the porous membrane with low permeability underwent a pressure that yielded a low fluid release when compared to the amount of fluid in donor chamber.

Several clarifications have to be made in defining "low" fluid flow and permeability. First, the "low" *permeability* of the magnetic membrane can be determined by comparing the theoretical governing equation of the osmotic pump flow. The complete osmotic pump and magnetic membrane assembly requires an almost constant P_{PDMS} to achieve a constant drug delivery rate (in both the theoretical prediction and the simulation results). This would suggest that the governing equation, $P_{PDMS} = \alpha V^3 + \frac{\mu L}{kA}\dot{V}$ would need to be converted to $P_{PDMS} \cong \frac{\mu L}{kA}\dot{V}$ for the complete osmotic pump and magnetic membrane assembly. This in turn indicates that the $\frac{\mu L}{kA}\dot{V}$ term becomes a much more dominant factor compared to the αV^3 term. Several factors can affect changes in P_{PDMS} over the experimental time.

One option could be an increase in the value of $\dot{V}$. However, change in the volume displacement rate, especially under constant fluidic volume displacement rate, would indicate a linear correlation with V^3. And with displaced volume in higher order of relevance, $\dot{V}$

would be an unlikely candidate for the change in P_{PDMS}. Another option could be the dimensions of the magnetic membrane. However, note that L and A are well within the characteristic length/area dimensions for micro-scale flow (10s of micrometers for thickness L and order of mm^2 for area of magnetic membrane), also making for an unlikely possibility that the dimensions of the magnetic membrane are the major cause for the change in P_{PDMS}. Since the dynamic viscosity of the fluid (water) used in the simulation is the same value used for water in macro-scale, this would also be an unlikely cause for the change in P_{PDMS}. This only leaves k, the permeability of magnetic membrane, to be the major contributor of P_{PDMS} behavior change. And in order for $\frac{\mu L}{kA}\dot{V}$ to become a dominant term in P_{PDMS}, k would necessarily be have to be much smaller than typical characteristic dimensions for micro-scale flow (μm^2). Thus, theoretical suggestion of the full osmotic pump and magnetic membrane assembly's behavior indicates that the permeability of the magnetic membrane has to be relatively "small" or "low" (which in line with the fact that the simulated membrane is treated with a cyanoacrylate layer for reducing the drug delivery rates from µg/hr to ng/hr).

Another important point is with regards to the definition of "low" fluid flow: the largest volume displaced under full osmotic assembly is around $1.1 mm^3$. Note, however, that volume of the drug source, the donor chamber, is much bigger. Specifically, the volume of the donor chamber is approximately $V_{Donor} \cong 2.5^2 * 1 * \pi[mm^3] + 7.5^2 * 4 * \pi[mm^3] + 5^2 * 1 * \pi[mm^3] = 256.25\pi[mm^3] = 805.0331[mm^3]$. This means that $\frac{1.1}{805.0331} * 100 = 0.1366\ \%$ of the fluid available in donor chamber is displaced to receptor chamber. This relatively small percentage of fluid flow allows the fluid flow in the full osmotic pump and magnetic membrane setup to be defined as relatively "low".

With these two definitions of "low" permeability and flow defined, linearization of the low-permeability flow can be made (i.e. for full osmotic pump and magnetic membrane assembly). The Darcy's law is first approximated as $Q = \dot{V} = -\frac{kA}{\mu L}\Delta p = -\frac{kA}{\mu}\frac{p_{end} - p_{start}}{L}$. If p_{end} is assumed to be 0, then $Q = \frac{kA}{\mu L}p_{start}$.

The linearization of low-permeability flow assumes $\frac{Q}{k} = \frac{A}{\mu L}p_{start}$ is some constant c for various membranes of low-permeability and low flow rate (as long as p_{end} is defined to be 0). This statement is unlikely to be physically exact as p_{start}, Q, and k are all unknowns

(A, μ, and L are assumed constant) and may not necessarily have such a relation as described. Even a simple explanation that relates flow rate (or velocity, assuming that average velocity over cross-sectional area multiplied by flow cross-sectional area is the flow rate) and $\mathrm{p_{start}}$, such as Bernoulli's principle, indicates a relationship much more complex than a simple linear ratio relation as shown above. However, by simplifying and assuming that fluid flow and pressure varies with varying permeability in a linear scale, we achieve a very simple correlation that allows for a reasonable approximation of the simulated input pressure. (Furthermore, this linearization is sensible in low-permeability and low-fluid flow conditions).

Using this relationship, another membrane test with low permeability could be used as a reference to approximate the input pressure for the full osmotic pump and membrane assembly. An EC membrane's permeability study with atmospheric humidity is used as a reference [266].

Under the above mentioned assumption of constant $\frac{\mathrm{Q}}{\mathrm{k}} = c$,

$$\frac{A_{reference}}{\mu_{reference} L_{reference}} \Delta p_{reference} = \frac{A_{pump}}{\mu_{pump} L_{pump}} \Delta p_{pump}.$$

Note that both the reference and the complete osmotic pump and magnetic membrane assembly utilizes water, making $\mu_{reference} = \mu_{pump}$.

Thus, $\frac{A_{reference}}{L_{reference}} \Delta p_{reference} = \frac{A_{pump}}{L_{pump}} \Delta p_{pump}$. The reference uses a water vapor pressure difference across EC membrane of 75% of relative humidity (75% RH).

The pressure of the complete osmotic pump and magnetic membrane assembly at the receptor, by design, is set at 0. This makes the pressure difference across the osmotic pump the same as the pressure of the donor chamber. Furthermore, the reference paper sets only one side of the membrane at 75% RH while setting the other side of the membrane at a dry condition. Since the dry condition side of the membrane makes water vapor pressure on that side 0, this sets the pressure difference across the EC membrane equal to the vapor pressure on wet side. Thus,

$\frac{A_{reference}}{L_{reference}} p_{wet} = \frac{A_{pump}}{L_{pump}} p_{donor}$, where

$A_{reference}$, A_{pump} are the surface areas of membranes across fluid flow in the reference paper and that of the complete osmotic pump and magnetic membrane assembly, respectively.

$L_{reference}$, L_{pump} are the thicknesses of the membranes in the reference paper and the complete osmotic pump and magnetic membrane assembly, respectively.

p_{wet}, p_{donor} are pressures on the wet side of the EC membrane in the reference paper and the donor chamber in the complete osmotic pump and magnetic membrane assembly, respectively.

This makes $p_{donor} = \frac{L_{pump}}{A_{pump}} * \frac{A_{reference}}{L_{reference}} p_{wet}$.

Given $L_{pump} = 20\mu m$, $A_{pump} = (5^2 * \pi) mm^2$ from magnetic membrane above the pump, while the reference paper gives $A_{reference} = 5cm^2$, $L_{reference} = 200\mu m$, $p_{wet} = 23.8\ mmHg$.

Since 1mmHg ≅ 0.01934 psi → $p_{wet} = 23.8 mmHg = 0.4603\ psi$,

$p_{donor} = \frac{20\mu m}{78.5398 mm^2} * \frac{5cm^2}{200\mu m} * 0.4603 \text{ psi} = \frac{20\mu m}{78.5398 mm^2} * \frac{500 mm^2}{200\mu m} * 0.4603 \text{ psi} =$ 0.2930psi~0.3psi.

In Pascal, since 1psi ≅ 6894.75729 Pa, 0.3psi ≅ 2068.4272Pa~2070 Pa.

Thus, p_{donor} is set around $0.3 psi$ or $2070 Pa$.

Note that the p_{donor} value is rounded to the first decimal for pressure in psi and ten digit places for pressure in pascal for simplicity, since the magnitude of the input pressure of the complete osmotic pump and magnetic membrane assembly is not required to be exact for the purposes of simulation.

A.4 Approximation of Ratio of Permeability Values of Magnetically Triggered Membrane (Magnetic Field ON/OFF)

To determine the ratio of permeability values for the two magnetic states, the theoretical setup of Δp needs to be examined, $\Delta p = p_{donor} - p_{receptor}$. But $p_{receptor}$ is 0 relative to atmospheric pressure, therefore $\Delta p = p_{donor}$. Under the low permeability condition for the magnetic membrane however, we can assume that p_{donor} is very close to P_{PDMS} (we can assume that the magnetic membrane is more like a wall boundary with low leakage). This

means that, Δp can be approximated as P_{PDMS} for both magnetic and non-magnetically activated cases, resulting in:

$$\frac{k_{mag}}{k_{non}} = \frac{\dot{V}_{mag}}{\dot{V}_{non}} \cdot \frac{\Delta p\ non}{\Delta p\ mag} = \frac{\dot{V}_{mag}}{\dot{V}_{non}} \cdot \frac{P_{PDMS}}{P_{PDMS}} = \frac{\dot{V}_{mag}}{\dot{V}_{non}}$$

$$\frac{k_{mag}}{k_{non}} = \frac{\dot{V}_{mag}}{\dot{V}_{non}} = \frac{c_{mag}}{c_{non}} \cong 1.15$$

Note that this assumption is a physical approximation. P_{donor} will in reality vary for the two different magnetic field states. Some of the variables must be fixed in order to determine the relationships of the other variables, to show that constant drug delivery with osmotic pumping can be achieved in simulation.

Letting $P_{donor} = P_{PDMS}$ for both magnetically and non-magnetically activated states creates a physically inexact ratio of permeability values of the magnetic membrane in these two states. However, despite this, the osmotic pump can still be shown to provide constant drug delivery rates. Furthermore, this uncertainty does not influence the constant drug delivery behavior of the osmotic pump with relatively constant P_{PDMS} as any discrepancy can be adjusted using varied magnetic membrane's permeability by either varying the ratio of permeability between magnetic states or the magnitude of permeability. Thus, the simulation result is reliable as long as the magnitude of the permeability is not interpreted as exact.

Direct pressure test simulation results are shown as plots of simulated applied pressure to PDMS from the water inlet side over time, and the resulting volume deflection of the PDMS membrane over time. Discussion of the significance will follow.

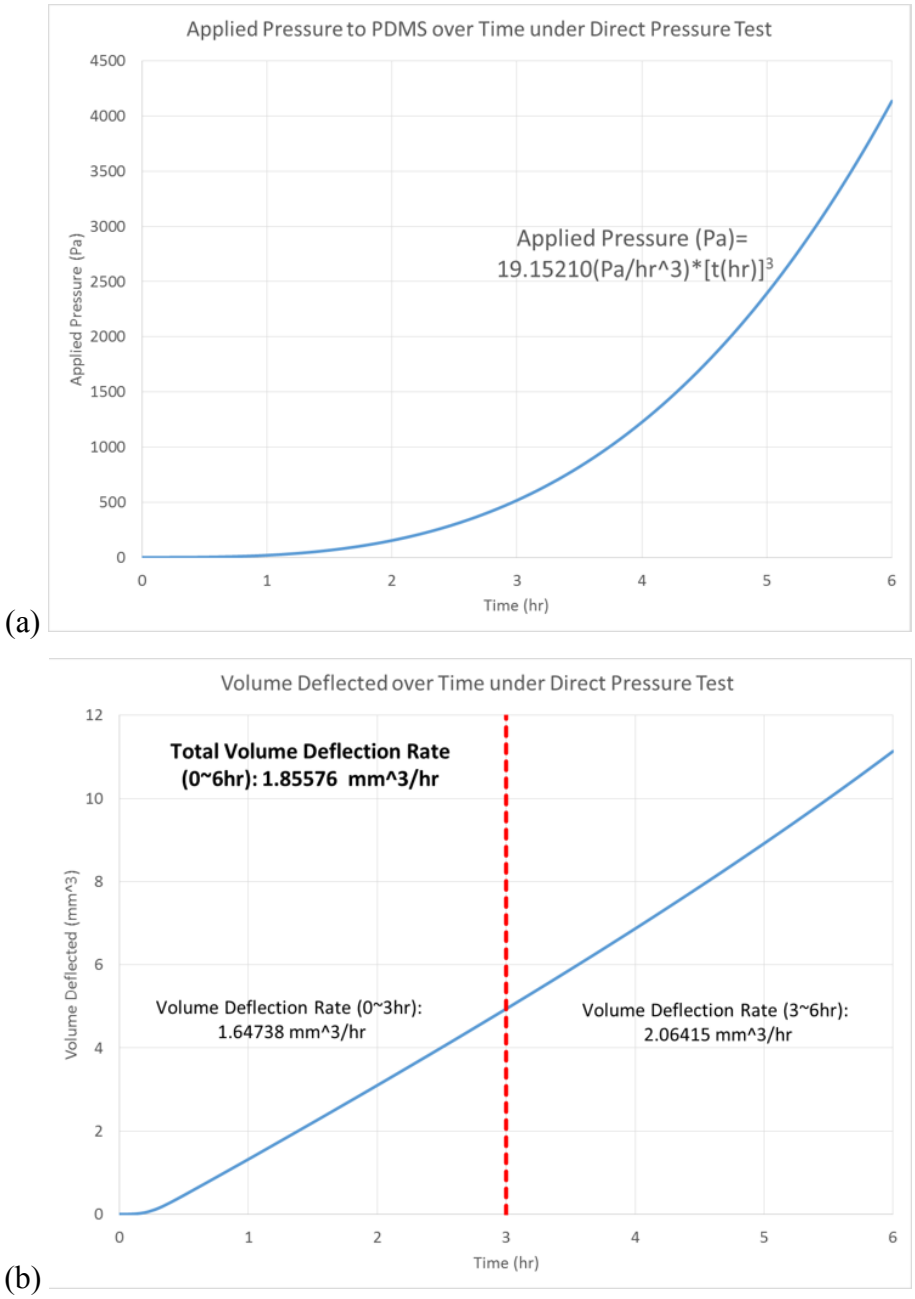

Figure S2: Simulated applied pressure on PDMS membrane (a) and volume deflected by PDMS membrane (b) over time. Note that the applied pressure plot is cubic over time, while the resulting volume deflection in almost linear. Reprinted with permission from [228]. Copyright 2015, AIP Publishing LLC.

With no magnetic membrane present during this direct pressure test, an almost-linear volume deflection under cubic pressure over time supports the αV^3 term in Eqn. [A-4] with reliable accuracy (Figure S2). Under the same condition, Figure S2a shows the relation Pressure $\propto$

Time^3, from plotting the applied pressure to the PDMS membrane over time, and Figure S2b shows the relation Volume $\propto$ Time, from plotting volume deflection of PDMS over time. These two result in the relation Pressure $\propto$ Volume^3. Note that these results from the direct pressure test, used to support the analytical approximation, represent the simulation of the osmotic pump only, without the inclusion of the magnetic membrane, and therefore the pressures shown do not represent those that occur with the inclusion of the magnetic membrane in the complete simulated assembly.

A.5 Summary of Simulation Specific Settings

- For the mesh type, the general overlay is a triangular mesh, with the exception being around the boundaries where a pre-built to COMSOL mesh for boundaries is used. For the boundaries and domains near the areas of PDMS deflections, mesh refinement was used. The total element size after refinement is numbered around 15000.
- For the boundary conditions, a typical no slip, no penetration boundary condition for fluid and species, respectively, is used. As for the porous magnetic membrane, the governing equations associated with the boundary conditions are a combination of Brinkman's equation, Navier-Stokes equation, and typical convection-diffusion equation for species transport. For the remaining domains, the Navier-Stokes and convection-diffusion equations are used, while the regions near the deflecting membrane rely on the Fluid-Structure Interaction model to combine fluid and solid motion instead of the Navier-Stokes equation.
- For the input of the inlet flow, a pressure is applied to the elastic membrane, triggering the transport process, which results in the output of mass transport of species into the region beyond the porous magnetic membrane.
- Finally, in the convection-diffusion equation, a model is created using a COMSOL mathematics module and is used instead of the COMSOL convection-diffusion model, since the pre-built convection-diffusion model provided some unrealistic values due to some built in boundary condition issue.

Appendix B Nanowire and Nanoparticle SAR Measurements

B.1 Specific Absorption Rate of Magnetic Materials

The specific absorption rate (SAR) is defined as the amount of power per unit mass that is absorbed during a power transfer process from an AC electromagnetic source to the volume of material receiving the power [182, 308, 309]. It is also referred to as specific loss power (SLP) [309]. The typical unit for SAR is W/kg, and its values are calculated as follows for a specific AC field frequency and amplitude.

$$SAR = \left(\frac{C_P}{mass}\right)\left(\frac{dT}{dt}\right), \qquad \text{[B-1]}$$

The mass is that of the magnetic material, nanoparticles or NWs, used to transfer power from the AC field to the material absorbing the power. C_p [J/K] is the heat capacity of the material that the nano materials are heating. The term dT/dt is the rate at which the temperature of the heated material changes. The SAR value of the system containing the power transferring material and the heated material is therefore only "specific" insofar as the mass of the power transferring material [W/kg], and is determined for a fixed field power, field frequency, material being heated and its amount (e.g. ethanol), and power transferring material (e.g. iron oxide). This is important, as the primary approach for controlling the total power transfer to a drug delivery system would be to tune the amount of power transferring material, and not the material surrounding it. This rate can be measured using a temperature probe submerged in a solution of known C_p along with nano materials of known mass, inside of an AC field.

SAR calculation are critical in the selection of optimal nano materials and geometries. For example, previous work has shown the potential for NWs to be more effective power transfer agents than widely used nanoparticles. This was done for the case of iron specifically, with both nano material geometries having the same concentrations in solution during comparison [193]. Of course, solution type and viscosity must be appropriately selected in a study used to determine the material and geometry to be used in a specific fluid application, such as human body fluid environments or drug delivery system materials using PNIPAm (e.g. magnetic PNIPAm microdroplets, MPMs).

The SAR is used for quantifying the effectiveness of materials used in heat related therapies, such as hyperthermia treatments, but is also used in other fields such as for the

determination and monitoring of safe levels of power emissions from transformers [310], MRI machines [311], and cellular devices [312], to materials such as human tissue, as these emissions are undesired side effects that may result in unhealthy SAR levels.

A comparative SAR study of various magnetic materials, in the form of iron oxide nanoparticles and different NWs, is described in this Appendix. The material primarily shows findings regarding losses from the magnetization of NWs that generate power in a low viscosity medium, and since this is not directly exploited in the work present in Chapters 2 and Chapter 3, it is not included in the main text but may still be viewed by the reader.

For consistency of comparison, all SAR measurements are performed using a 60 mT, 425 kHz magnetic field on all samples being compared, namely ~35 nm diameter Fe, Co, and Ni "thin" NWs, thicker NWs of Fe, and Fe_3O_4 iron oxide nanoparticles, though it was later found that the NWs can be used for heat generation via physical vibration with a much lower power magnetic field application. Nevertheless, the SAR comparison serves as a good starting point for material selection when seeking to generate heat in an aqueous based hydrogel, or in other applications, to mimic a biological cellular environment.

B.2 Methods

Characterization of Magnetic Nanowires

Scanning and tunneling electron microscopy (SEM and TEM) are used for determining NW diameters, lengths, and morphological structures (Quanta 3D and Tecnai BioTWIN, FEI Company, USA). These images are assessed using ImageJ analytical software for accurate on-screen measurements. X-ray spectroscopy (Tecnai BioTWIN, FEI Company) is used for studying magnetic material compositions. Imaging is done on freshly fabricated and ethanol cleaned/sonicated samples for best results and dispersion in solution prior to drying on sample holder wafers.

The quantity of magnetic material in a sample is determined by inductively coupled plasma mass spectrometry (ICP-MS). A small volume (5-20 µl) is taken from each sample and diluted to a 7 mL volume with 2% HNO_3 for analysis by ICP-MS (Quadrupole, Elan DRC II, PerkinElmer, USA). By measuring each sample's most abundant isotope, the concentration of each element is determined.

Unreleased NW samples in aluminum oxide membranes (used in NW fabrication) are measured for their magnetization loops at room temperature using a vibrating sample magnetometer, or VSM (MicroMag 3900, Princeton Measurement Corporation, USA). The maximum applied field is 1 T with a sensitivity of 0.5 μemu and a standard deviation of 1 second at each measurement point.

SAR Measurements

SAR measurements are taken over periods of 30 minutes for different NW samples placed inside the coil of an AMF inductive heater (IEW GmbH, Austria) producing a 60 mT, 425 kHz magnetic field. NWs are placed in an airtight inner bottle with a known volume of ethanol (1 mL), inside a vacuum assisted thermal isolation external bottle (Figure S3). The inner tube is physically suspended in low-pressure space by the fluoroptic cable, the only physical contact between this inner sample holder bottle and the low pressure external bottle. The external bottle is positioned and centered in the inductive heater coil, both separated by an air gap. The NW-ethanol solution temperature is measured over time by the connected fluoroptic thermometer with an accuracy of ±0.5°C (Luxtron 812, LumaSense Technologies, USA).

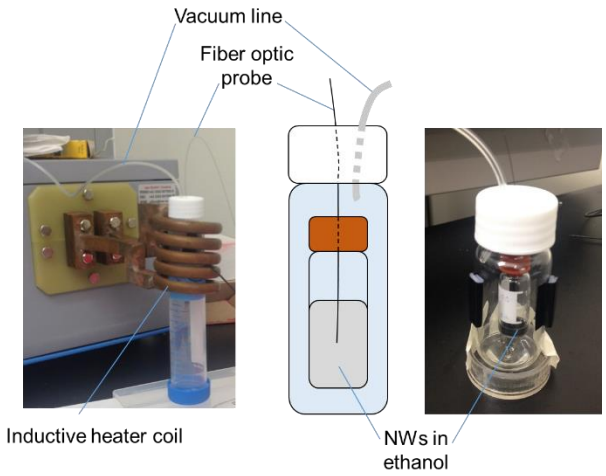

Figure S3 Experimental setup for SAR measurements.

B.3 Results

Properties of Magnetic Nanowires

SEM images of anodized aluminum oxide templates with well-organized and parallel pores, used for NW fabrication, are shown in Figure S4a-b, for two different pore sizes. NWs released from templates are shown in Figure S4c-d.

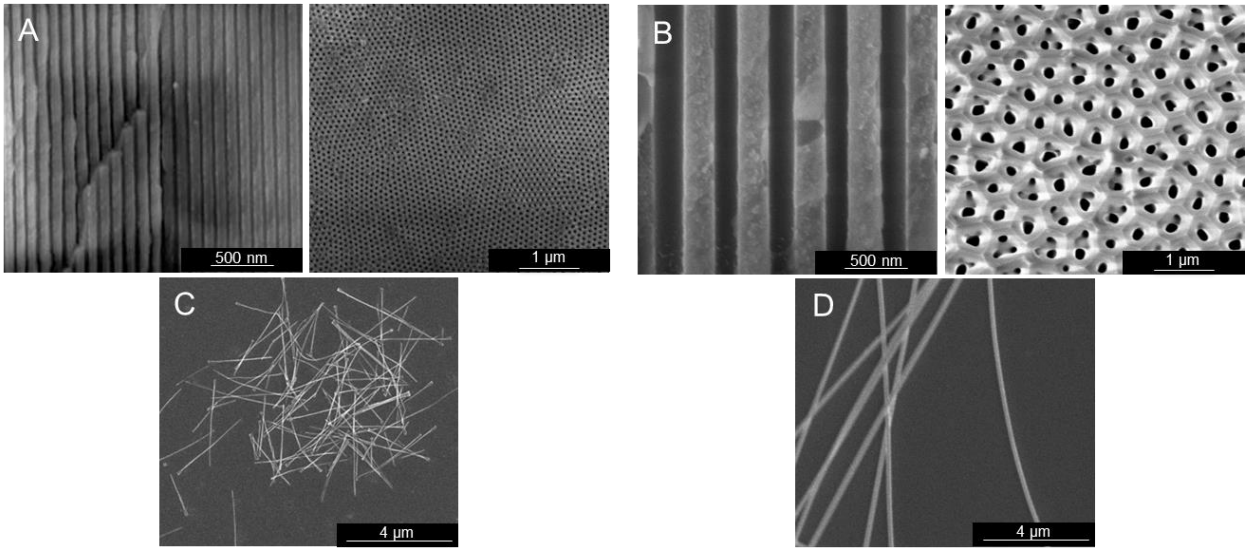

Figure S4 Morphology of magnetic nanowires. Cross-section and top SEM images of the anodized aluminum oxide templates used to later deposit NWs. Pore size is determined by the acid used, averaging 35 nm for oxalic acid (A) and 190 nm for phosphoric acid (B). SEM images of released magnetic NWs on top of a silicon wafer with an average diameter of 35 nm (C) and 180 nm (D).

The geometric information for each material used in this study is tabulated in Table S1 after analyzing SEM imagery. Superparamagnetic iron oxide nanoparticles (NPs) of ~60 nm diameter (Spherotech, USA) are included for comparison.

Table S1 Magnetic nanowires and nanoparticles used in the experiments.

Sample	Diameter (nm)	Length (µm)
Fe35	35	50
Fe180	180	14.5
Ni35	35	50
Ni300	323	7.9
Co35	35	50
Fe_3O_4 NPs	60	---

Magnetization loops for all NW and nanoparticle samples are shown in Figure S5. Measurements of NWs are taken prior to release from aluminum oxide templates, allowing for the positioning of the NWs to be parallel (along the easy axis) or perpendicular (along the hard axis) to the VSM magnetic field. Magnetization loops are ordered based on highest to lowest SAR efficiency, as labeled. The amplitude of the applied AMF used in SAR measurements is 600 Oe (60 mT). Loops in black and loops in red indicate easy and hard axis measurements for NWs, respectively.

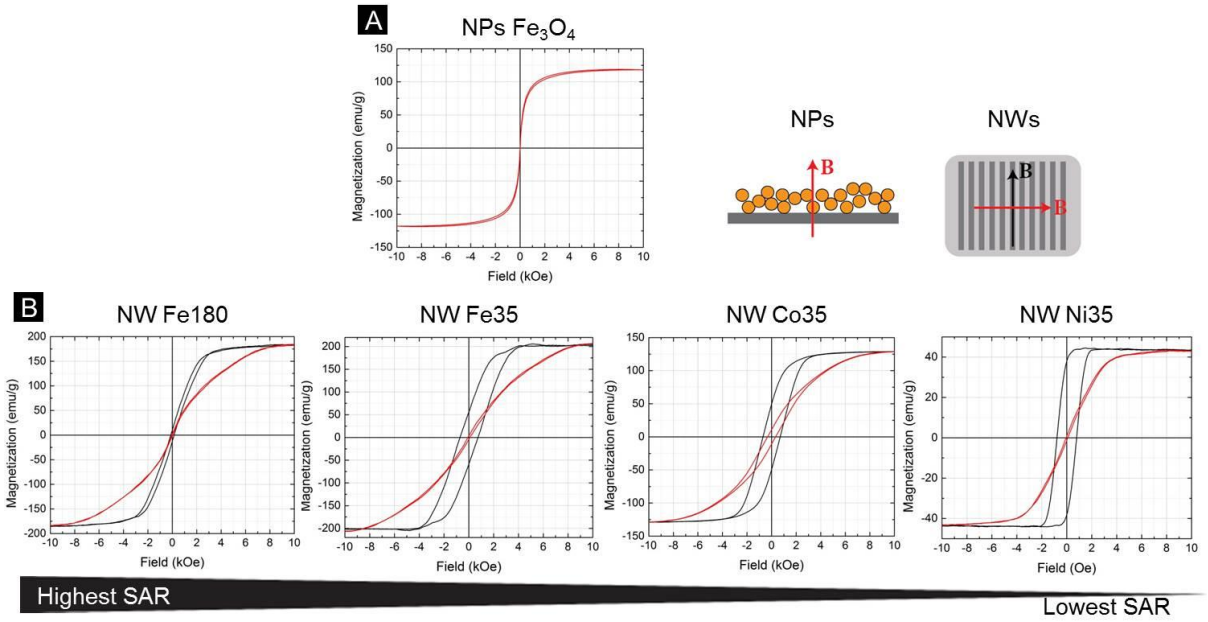

Figure S5 Magnetization loops of arrays of nanowires (NWs) embedded in the anodized aluminum oxide template. For all NW measurements the field is applied parallel the NWs (black curves) and perpendicular to the NWs (red curves). In the case of the iron oxide nanoparticles, only one curve is shown as the particle-solution suspensions are isotropic during measurement.

Magnetic properties of the samples are tabulated in Table S2, where materials are again ordered according to heating efficiency.

Table S2 Relevant magnetic quantities of the studied samples Abbreviations: M_R, remanence magnetization; M_S saturation magnetization; $H_{C\parallel}$, in-plane coercive field; $H_{C\perp}$, out-of-plane coercive field. * Observed trend for NWs was not observed for the iron oxide nanoparticles. $^{+}H_{SW}$ is the coercive field of single nanowires as reported elsewhere [164].

Sample	M_S (emu/g)	M_R (emu/g)	M_R/M_S	$H_{C\parallel}$ (Oe)	$H_{C\perp}$ (Oe)	H_{SW} (Oe) $^{+}$ [single NW]
Fe180	185.1	10.1	0.0401	131.4	30.3	455
Fe_3O_4 NPs*	87.6	2.3	0.045	7.87		
Fe35	207.4	56.1	0.23	704.6	96.3	1245
Co35	130.4	49.3	0.39	694.1	326.4	1790
Ni35	43.4	37.9	0.94	773.5	79.4	1350

Temperature Measurements and SAR Calculations

All samples share the same initial temperature of 24 °C during fluoroptic temperature measurements. Figure S6 shows the temperature curves for each sample over time (each measured for a total of 1800 minutes). Despite the vacuum assisted insulation used with the external bottle, the system cannot be assumed perfectly adiabatic for such sensitive measurements, and therefore a control measurement is taken for pure ethanol containing no magnetic material, and subtracted from all curves shown, such that temperatures can be attributed solely to magnetic heating. The control measurement showed a bias temperature rise of approximately 4.5°C. The difference in initial slopes and final temperatures at saturation can be attributes to the heating efficiency of the magnetic material itself.

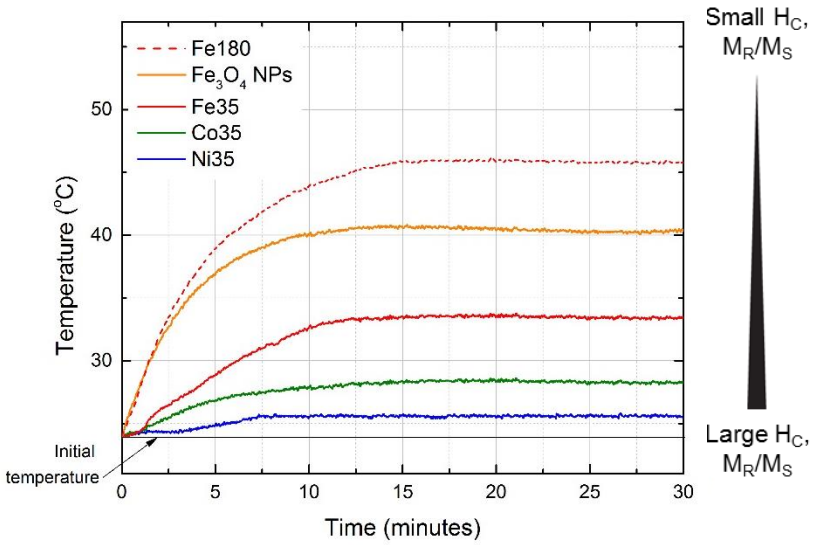

Figure S6 Temperature curves for nanowire and nanoparticles under a 60 mT, 425 kHz AMF over time.

Final temperatures correlate with values of M_R/M_s of materials and their H_C values. Samples with low coercivity (<16 mT) are more efficient at heating than samples with higher coercivity (>70 mT), with the applied field being 60 mT. SAR for each material is calculated using Eqn. [B-1], and tabulated in Table S3. The value of dT/dt is extracted from the slope of the temperature plots during the first 10 seconds of temperature increase.

Table S3 SAR values of the samples tested, along with temperature and concentration information.

Sample	SAR (W/g NWs or NPs)	T_{sat} (°C)	t_{sat} (minutes)	NW/NP concentration (mg/ml)
Fe180 thick	3924.7	47.0	14.9	0.05
Fe_3O_4 NPs	2101.5	40.4	11.6	0.17
Fe35 thin	195.3	33.4	12.1	1.00
Co35 thin	88.0	28.3	14.5	1.00
Ni35 thin	35.5	25.7	7.3	1.00

These findings show that the heating power of NWs depends on the magnetic material and associated properties and geometry. The lower the coercivity (less than or equal to the applied field), the higher the SAR measured. This correlation is particularly notable for Fe and Ni NWs, due to their single domain magnetic behavior [216], which results in no

hysteresis losses for applied fields that are lower than the material's coercive field. The coercivity depends heavily on the material's geometry [313], therefore the temperature change ΔT of thin Fe NWs is observed to be lower (< 10℃ for Fe) than that of thicker Fe NWs. Co NWs exhibit a smaller coercivity than Fe and Ni NWs. Because of this, cobalt's ΔT has a slightly higher value when comparing with thin Ni NWs.

Although thick NWs would seem to exhibit the best heating efficiencies, their fabrication procedure using aluminum oxide templates that are anodized with phosphoric acid (as opposed to oxalic acid for~ 35 nm pores) becomes a concern when it comes to mass fabrication of NWs. The fabrication of phosphoric acid aluminum oxide templates is found to have a high failure rate, as the process is very sensitive to small temperature fluctuations and overall temperature set point, the deviations of which can easily disrupt the proper growth of pores in the membrane. Among the thin NWs, Fe NWs exhibit the more efficient heating, and the preparation of aluminum oxide membranes using oxalic acid is relatively easy with very low instances of membrane damage or pore growth failure. Therefore, Fe NWs would be selected for study and comparison with superparamagnetic iron oxide particles, if heat generation from magnetization losses were to have been relevant in the shrinking of the MPMs reported in Chapter 3.

B.4 Summary

Characterization of iron, cobalt, and nickel NWs, as well as iron oxide nanoparticles, for their specific absorption rates in solution, shows insight into the proper selection of material and geometry for the production of heat in liquid or viscous media, such as inside of a PNIPAm microdroplet. However, due to the large difference in effectiveness and efficiency of fabrication techniques for different NW diameters (thin versus thick), and the need for mass fabrication of NWs when synthesizing microdroplets, more advanced fabrication equipment is required if thicker NWs are to be implemented. Nonetheless, the comparison of widely used iron oxide nanoparticles and thin NWs, as done in this work, serves as a good starting point for heading towards a diversification of heat generation methods, potentially combining both magnetization losses with magnetically induced vibrational losses.

Appendix C Nanowire Fabrication System

C.1 Details of Constructed Nanowire Fabrication System

The protocol used for the fabrication of porous AAO templates with 35 to 45 nm pore diameter, and the subsequent electrodeposition of wires therein, is introduced in Chapter 1 section 1.4.5.4. Below are details of the NW fabrication system (see Figure 1.14), assembled and constructed for the production of magnetic NWs, associated with each step of the fabrication process (see Figure 1.15) where applicable.

1. Ultrapure 0.5 mm thick aluminum substrates are rinsed with acetone, isopropanol, and distilled water, followed by a 10 min sonication to remove any organic contamination. This is achieved using a Branson B-200 Ultrasonic cleaner, shown below, and placing the samples in beakers in the water filled sonication bath.

Figure S7 Branson B-200 Ultrasonic cleaner used in the initial cleaning process of aluminum substrates.

2. Each sample is then electropolished for 2 minutes in 25% perchloric acid, 75% ethanol solution kept at 4°C, ensuring surface quality and homogeneity. Below is a photograph of the 0.25 mm 99.99+% purity Pt wire mesh (Goodfellow Corporation, USA) in a 75 mm by 100 mm by 2 mm Teflon plates, used in this step. The sample and the mesh are submerged in the magnetically agitated solution at a distance of approximately 75 mm. The mesh is suspended in the solution by a retort stand, while the sample is held by hand by a conductive tweezer connected to the power supply, allowing for further agitation of the sample around the 75 mm distance.

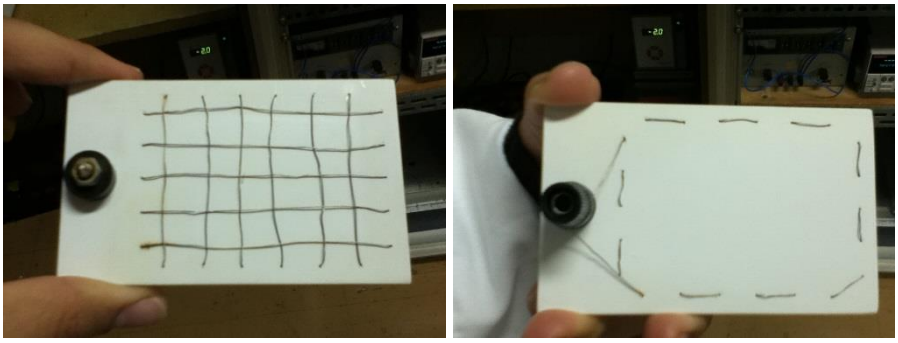

Figure S8 Electropolishing platinum mesh on Teflon plate.

3. The first anodization step is performed in 0.3M oxalic acid held at 4°C in an anodization cell (Figure 1.14 shows schematic and dimensions), under a constant voltage of 40V for 24 hours. This grows approximately 60 μm (2.5 μm/hr) of oxide for a given sample. Pore ordering increases with time/oxide growth. Below is the experimental setup for anodization of aluminum. The refrigeration circuit (Phoenix II recirculating chiller, Thermo Scientific) runs under the cooling plate, which is in contact with the Cu plate. Depending on the laboratory environment, the temperature

of the chiller may be adjusted accordingly in order to maintain 4°C at the anodization cell (in this work, the chiller typically ran at -10°C). Between the Cu plate and the Teflon container, the aluminum is secured with an O-ring to prevent leaking. The container is filled with the acid, into which a Pt wire mesh (supported with Teflon) is submerged as well as a stirrer to avoid freezing. The Pt is the anode and the Cu/Al is the cathode in the electric circuit shown in (Figure 1.14). The distance between the Pt mesh and the sample is approximately 5 mm. A Keithley 2400c Sourcemeter provides the voltage, while and Agilent E3648A DC power supply powers the stirrer motors.

Figure S9 Images of custom Teflon cell on Thermo Scientific cooled cooling plate, chiller, Keithley sourcemeter used for anodization and electrodeposition, and Agilent DC power supply for stirrer.

Alternatively, a multi-hole cell may be used for preparing multiple samples in parallel, allow for up to 8 samples being simultaneously anodized (by using 2 cells on the cooling plate.

Figure S10 Images of 4-hole Teflon cell with O-rings and aluminum substrates. Diameter of exposure of holes is ~15 mm (depending on O-ring design).

4. The anodization solution is then removed, the cell and sample are rinsed with distilled water, and the sample is subjected to a chromium oxide and phosphoric acid solution etch at 30°C for 12 hours under magnetic agitation, removing the first anodization's

oxide layer and leaving behind a highly ordered set of indentations on the Al surface.

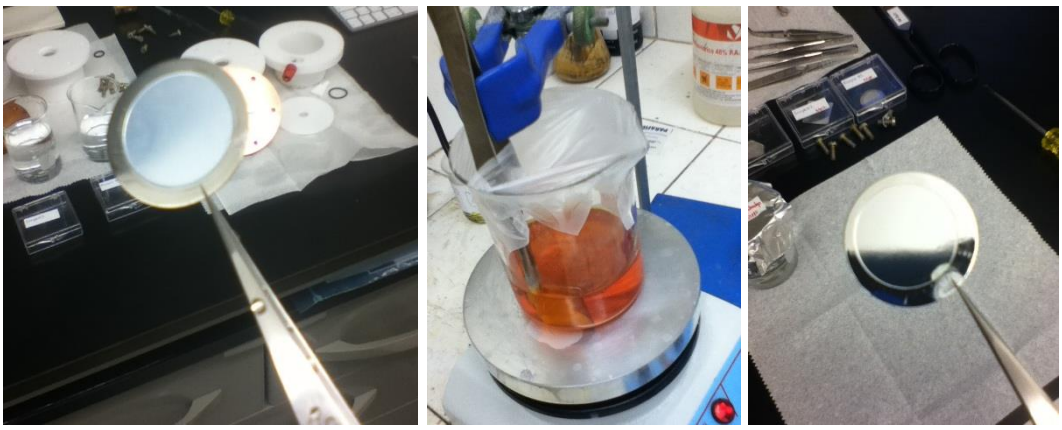

Figure S11 The opaque cloudy aluminum oxide layer on the initially mirror-like aluminum substrate is removed in a chromium oxide and phosphoric acid solution, rendering the surface mirror-like again, with nano indentations on the surface.

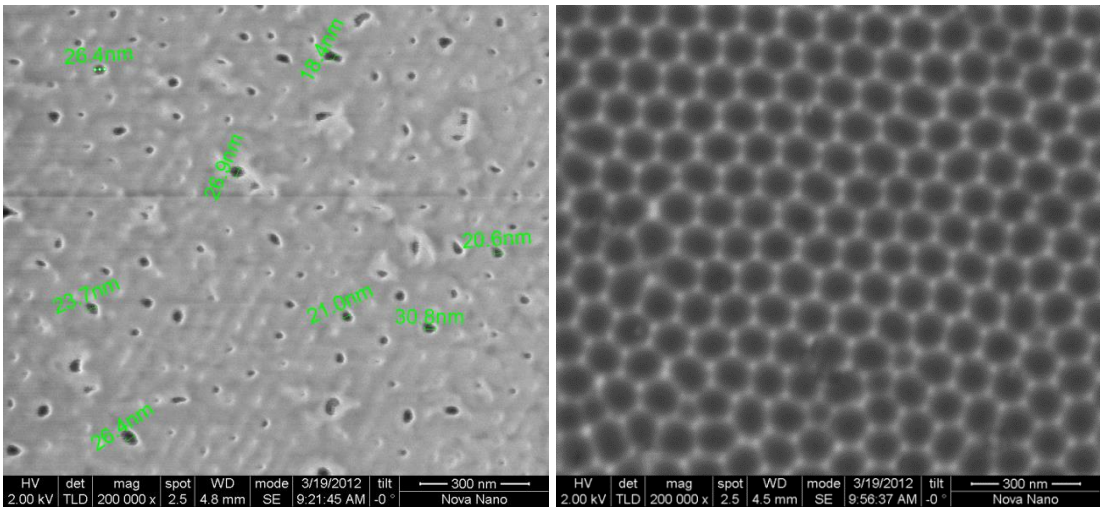

Figure S12 Scanning electron microscopy images before and after the removal of the 1st anodization oxide layer.

5. The second anodization step is performed under the exact same parameters as the first. This one takes advantages of the indentations to grow uniform highly ordered pores, and the anodization time determines the length of the pores.

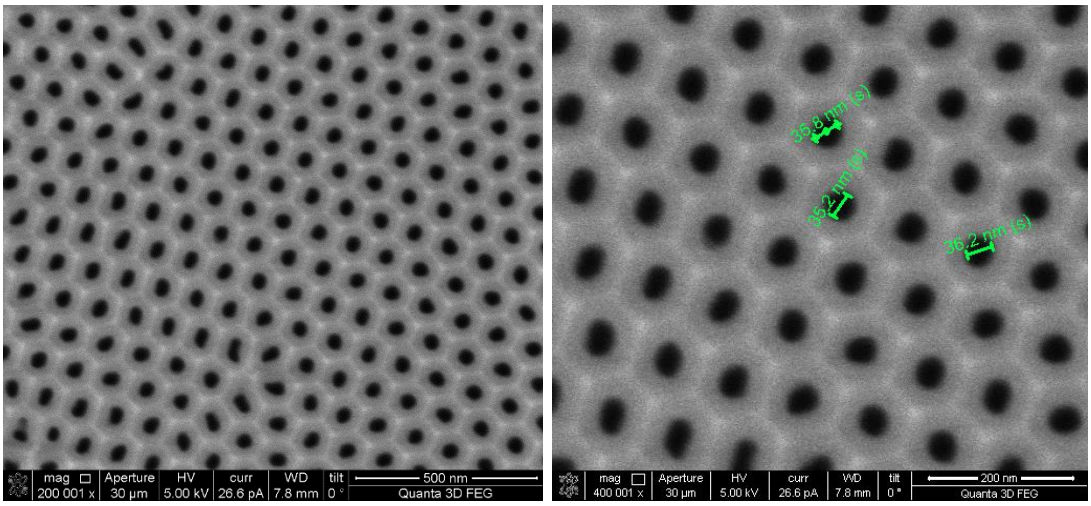

Figure S13 Scanning electron microscopy images taken after the second anodization, which use the nano indentations of the previous step, results in a more ordered array of pores.

6. A homogenization and reduction step is performed on the newly grown pores using a step-down voltage starting at 40V and ending at 5V, in the same solution, for approximately 1 hour. This step ensures the creation of dendrites through the oxide layer at the bottom of the pores, directly electrically linking any solution in the pores to the substrate's un-anodized Al material.

7. The anodization solution is removed again, the cell is cleaned, and the electrodeposition of wires is performed using one of the prepared electroplating solutions, kept at 40°C during the procedure for Co and Ni, and at room temperature for Fe. If additional precaution is desired, a different Teflon cell with a smaller hole can be used to ensure a smaller area of exposure to the electroplating solution, more isolated from the oxide layer/Al sidewall interface. By properly tuning the applied voltage/current profile, we ensure a higher quality of metal ion deposition.

Figure S14 The electrodeposition solution is heated during the deposition process for Co and Ni. For more precaution, a smaller hole of ~7 mm diameter (depending on O-ring design) exposure for the substrate may be used.

A negative current pulse attracts the positive metal ions to the cathode, its value depending on the deposited metal and the solution composition. We apply a current of -60 for Fe, and -30mA for Co and Ni, for 2ms (Figure 3.4). Following this, a voltage pulse of 5V removes accumulating charges on the oxide barrier layer, which behaves as a capacitor, and the pores are filled with fresh electroplating solution due to the polarity inversion. The applied voltage also helps repairs fissures that can occur during the first pulse. For a more homogeneous deposition, a final recovery time with no pulses is applied, allowing for the recovery of the ion concentration and pH at the pore bottoms.

8. When the process described is completed, the end result is an Al substrate, carrying an AAO membrane, filled with NWs grown from the bottom of the AAO pores up as far electrodeposition time allowed. To release the wires into solution, 20ml of 1M sodium hydroxide (NaOH) at room temperature dissolves the oxide layer within approximately 1 hour. Alternatively, the chromium oxide and phosphoric acid solution etch at 30°C described in step 4 is used for a slower and more controlled release of the oxide layer. To ensure a complete dissolution of aluminum oxide from the release NWs, a combination of NaOH until the reaction is visibly stopped, followed by chromium oxide and phosphoric acid solution treatment for 12 hr at 30ºC, is used in this work. The total number of wires grown in a given substrate piece can be found by calculating the total electroplated area and using the length of the wire growth. Samples may be diced into smaller pieces for experiments, imaging (Figure 3.3f), magnetic measurements (Figure 3.5), or storage, prior to release and use.

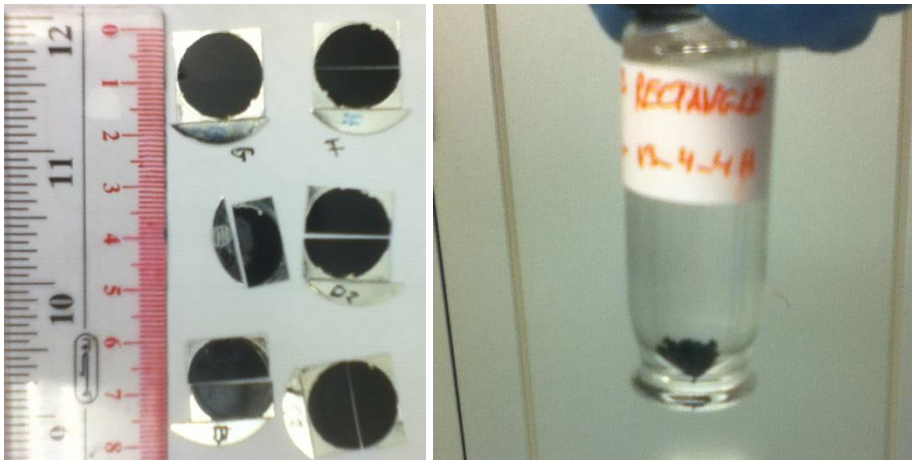

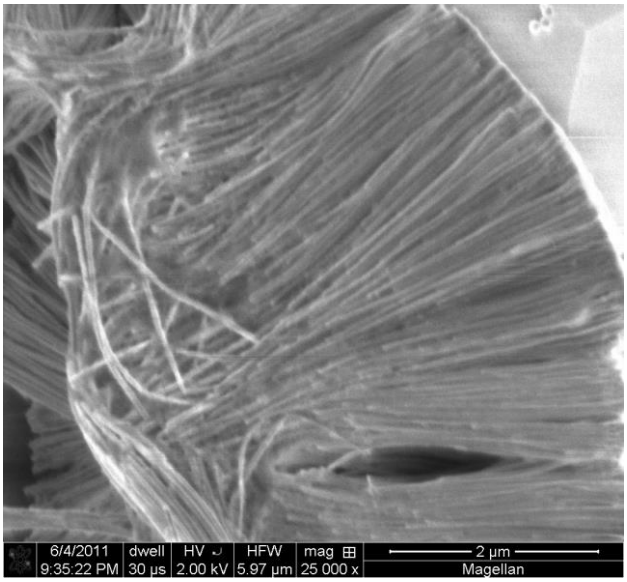

Figure S15 Electrodeposited samples may be diced into smaller pieces for experiments, imaging, magnetic measurements, or storage, prior to release and use. Partially released nanowires connected to aluminum oxide.

The following are blueprints for the anodization and electrodeposition devices that were machined and assembled for NW fabrication. These can be seen in use in Figure S9.

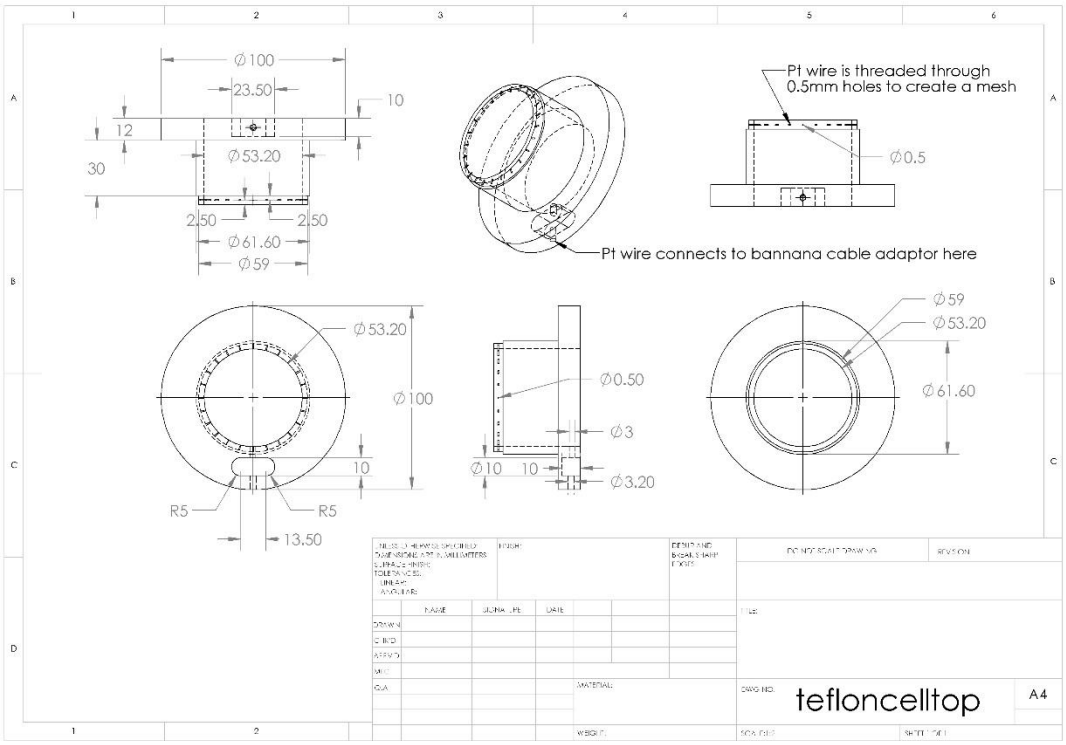
Ø100
23.50
10
12
Ø53.20
30
2.50
2.50
Ø61.60
Ø59
Pt wire is threaded through
0.5mm holes to create a mesh
Ø0.5
Pt wire connects to bannana cable adaptor here
Ø53.20
Ø100
10
R5
R5
13.50
Ø0.50
Ø3
Ø10
10
Ø3.20
Ø59
Ø53.20
Ø61.60
tefloncelltop
A4

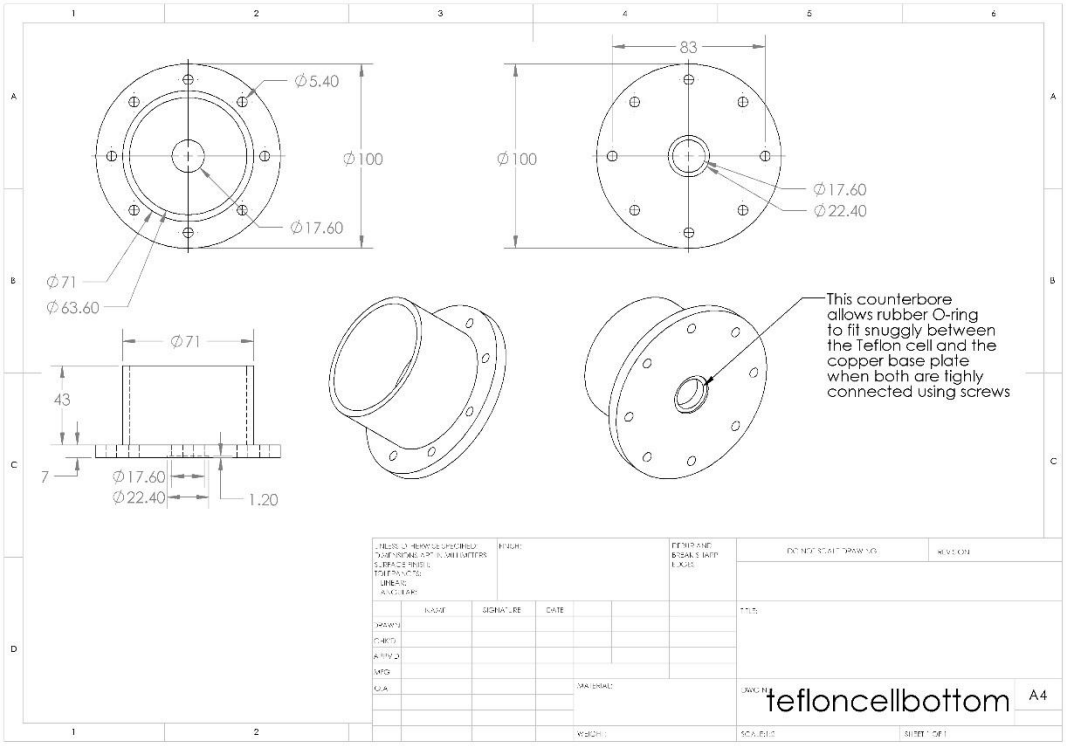
Ø5.40
Ø100
Ø17.60
Ø71
Ø63.60
83
Ø100
Ø17.60
Ø22.40
Ø71
43
7
Ø17.60
Ø22.40
1.20
This counterbore
allows rubber O-ring
to fit snuggly between
the Teflon cell and the
copper base plate
when both are tighly
connected using screws
tefloncellbottom
A4

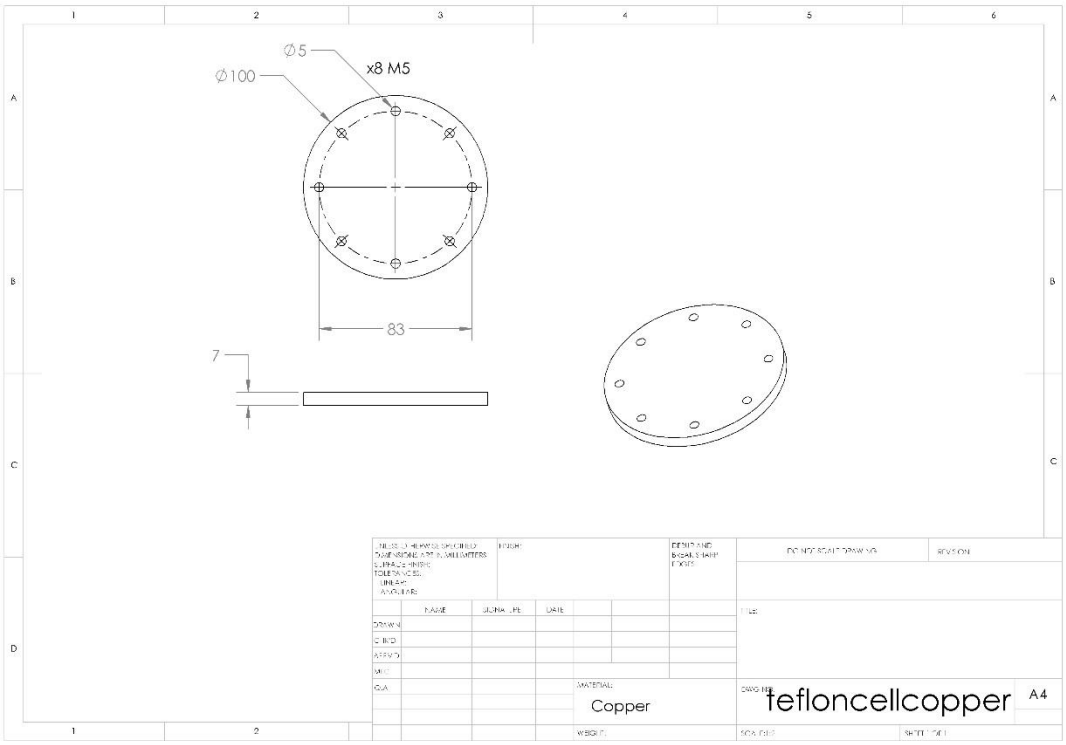
Ø5
x8 M5
Ø100
83
7
Copper
tefloncellcopper
A4

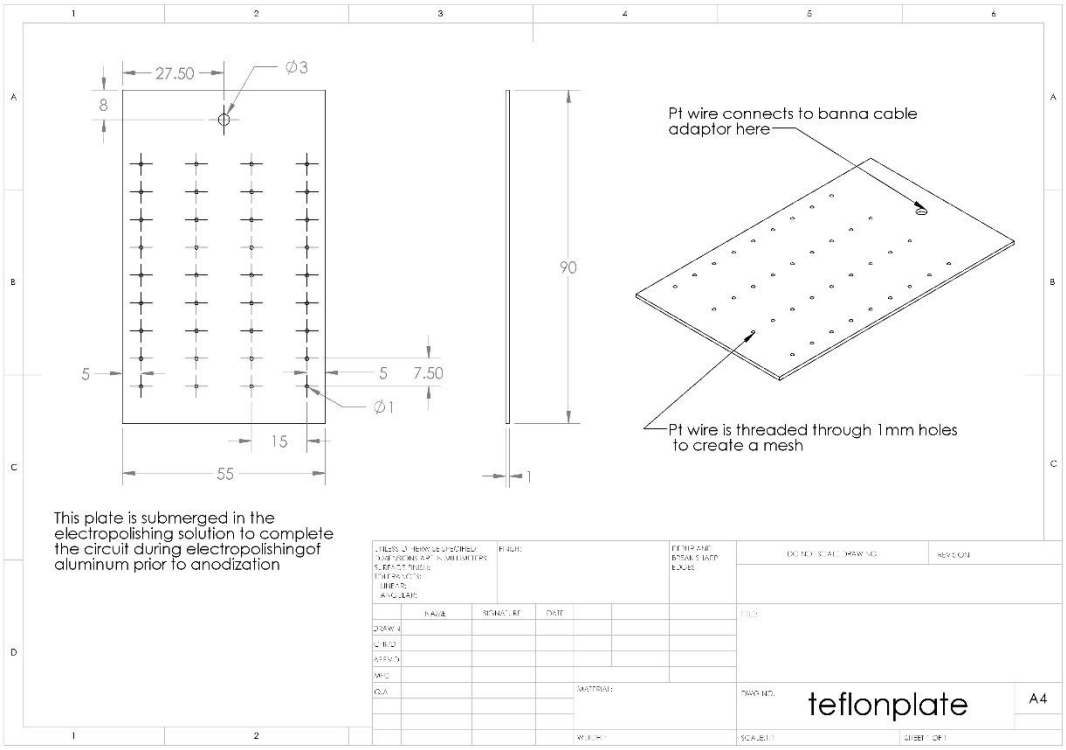
27.50
Ø3
8
5
5
7.50
Ø1
15
55
90
Pt wire connects to banna cable adaptor here
Pt wire is threaded through 1mm holes to create a mesh
This plate is submerged in the electropolishing solution to complete the circuit during electropolishingof aluminum prior to anodization
teflonplate
A4

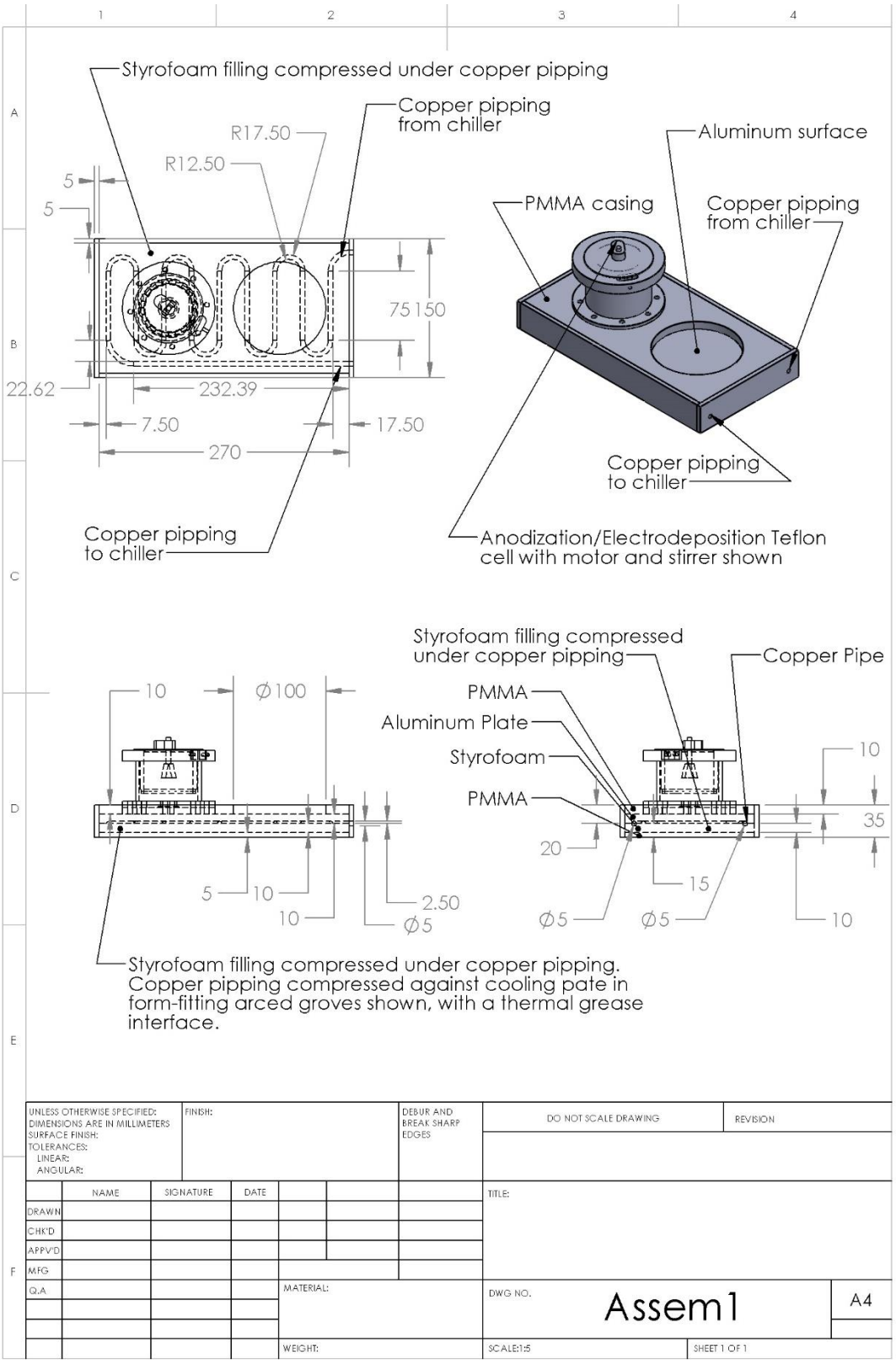
Styrofoam filling compressed under copper pipping
Copper pipping from chiller
R17.50
R12.50
5
5
75
150
22.62
232.39
7.50
17.50
270
Copper pipping to chiller
Aluminum surface
PMMA casing
Copper pipping from chiller
Copper pipping to chiller
Anodization/Electrodeposition Teflon cell with motor and stirrer shown
Styrofoam filling compressed under copper pipping
Copper Pipe
PMMA
Aluminum Plate
Styrofoam
PMMA
10
Ø100
10
35
20
15
5
10
2.50
10
Ø5
Ø5
Ø5
10
Styrofoam filling compressed under copper pipping. Copper pipping compressed against cooling pate in form-fitting arced groves shown, with a thermal grease interface.
UNLESS OTHERWISE SPECIFIED:
DIMENSIONS ARE IN MILLIMETERS
SURFACE FINISH:
TOLERANCES:
LINEAR:
ANGULAR:
FINISH:
DEBUR AND BREAK SHARP EDGES
DO NOT SCALE DRAWING
REVISION
NAME
SIGNATURE
DATE
DRAWN
CHK'D
APPV'D
M.FG
Q.A
MATERIAL:
WEIGHT:
TITLE:
DWG NO.
Assem1
A4
SCALE:1:5
SHEET 1 OF 1

Appendix D Modeling of Iron Nanowire Vibration in PNIPAM microdroplets

D.1 Matlab Script for Modeling the Vibration of Iron Nanowires

```
function [] = call_pend()

tspan=[0 1000*0.5*1/20000]; % set time interval. 1*0.5 shows one half cycle instead of
"1000", and "20000" is 20 kHz frequency

z0=[pi/4,0]; % set initial conditions of theta and d_theta/dt
[t,z]=ode23(@pend,tspan,z0);

figure(1)
plot(t,z(:,1))
function dzdt = pend(t,z)

G=-2628570266.84; L=-10429479034307.50; w=125663.7061;
% for nu PNIPAM, length=0.50um, r= 45/2 nm, H= 0.0010 T and C=0.1443

z1=z(1); % get z1
z2=z(2); % get z2

dzdt = [z2 ; G*z2+L*(sin(w*t))*(sin(z1));];
% sin(w*t) term comes from H field angle with NW.
 % x"+(2628570266.84)*x'+(10429479034307.50)*(sin(125663.7061*t))*(sin(x))
```

Appendix E Magnetic PNIPAm Microvalves for Electrolytic Drug Delivery

E.1 Synopsis

Electrolytic Pumps for Drug Delivery

Careful applications of micro electro mechanical systems (MEMS) allows for the miniaturization and optimization of effective controllable drug delivery by taking advantage of the properties that are characteristic of micro scale fluid flow, actuation, and power generation. As such, MEMS based electrolytic pumps are of particular interest in the field of drug delivery, given their capacity to transform electrical power into mechanical work through swelling of fluids and deformation of membranes [247-249, 252]. Electrolysis based pumping has the predominant advantages of ease of implementation, ease of operation, low power consumption and requirements, and reaction stability [252].

However, many electrolytic pumps are limited by the maximum deformation of their membranes and by ineffective applications of drug dosing in the long term, when the drug concentration or delivery profile no longer achieves similar levels those of initial dosages [249]. This is largely due to the use of purely liquid drugs, which become diluted over time. An alternative solid-form drug reservoir (SDR) approach has been pursued [22, 314], in which a renewable drug solution is generated after each delivered dose by dissolving a saturating solid-form drug, thus maintaining the desired drug concentration for the next dose. These reported devices were limited by factors of distance of operation of actuation mechanism and its alignment requirements. Previously an SDR and electrolytic pump were combined in a system designed to draw in fluid from the patient's internal environment through the device outlet, dissolve the solid drug, and cyclically pump out the formed concentration of liquid [276].

The use of a catalytic reformer in this research improves on this design by achieving a faster recombination rate of the oxygen and hydrogen bubbles formed during the electrolytic process, hence reducing the time required to prepare a dose pulse and increasing the number of pulses within any defined therapeutic time period. The pump is coupled with a valve system discussed below.

This research studies the effectiveness of combing a microfluidic channel that is flow-controlled by either of two PNIPAm monolith designs, and an electrolytic pump utilizing catalytic reformer technology. The pump and the valve are controlled using the same power supply, namely an externally applied AC magnetic field, while the catalytic reformer ensures fast recombination of bubbles (resulting in a reversal of the pump membrane deflection) and thus proper refilling for the SDR prior to the complete re-sealing of the valve.

E.2 Methods

Device Design

Figure S16 is a schematic of the device's primary components and functions. The efficiency of the platinum (Pt) electrode is increased by using a uniformly applied Nafion coating [252], the catalytic reformer is fully submerged in the solution of electrolytic chamber, which is sealed by a polydimethylsiloxane (PDMS) membrane. The PDMS membrane serves as the separator between the electrolytic chamber and the drug reservoir, as the pump actuator when deflecting into the drug chamber to pump the liquid drug, and as the refill aspirator when returning to its start position and drawing in new solution into the system.

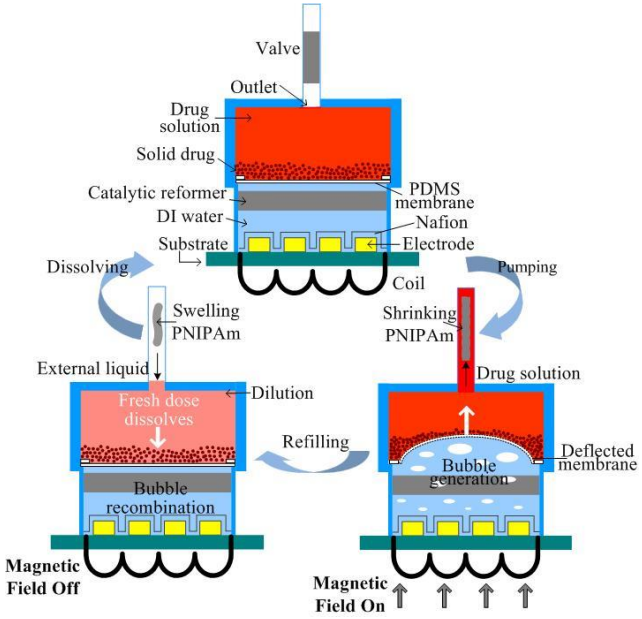

Figure S16 Schematic illustration of the solid drug in reservoir (SDR) based device and its cyclic operation. Reprinted with permission from [279]. Copyright 2015, AIP Publishing LLC.

When applying an AC magnetic field, the voltage induced in the pickup coil powers the electrode, which in turn runs the electrolytic reaction in the DI water. The oxygen and

hydrogen bubbles generated by the separation reaction of the water increase the pressure in the electrolytic chamber and deflect the PDMS membrane towards the PNIPAm valve. The valve consists of PNIPAm cast in a serpentine shape and mixed with iron microparticles, or cast in a glass capillary surrounded by iron microparticles. The application of an AC magnetic field induces magnetization losses in the form of heat from the iron microparticles, resulting in a temperature change in the PNIPAm and shrinkage when the temperature reaches and passes its LCST (around 41 ºC in this study). This change in PNIPAm volume creates an opening in the valve, allowing the solution to pass the PNIPAm. Turning off the magnetic field results in the non-instantaneous re-swelling of the PNIPAm, which eventually seals the outlet. At the same time, due to the recombination of oxygen and hydrogen gases into the water, the deflected PDMS membrane moves down towards its original position, pulling in fresh solution from the outside of the device and refilling the drug reservoir prior to the valve fully closing; for this reason, the non-instantaneous re-swelling of the PNIPAm is desired. A certain amount of the solid drug is dissolved by the entry of the fresh solution, which forms in turn the new drug solution, ready for the next dosing cycle. A Pt-coated carbon fiber mesh can be used to accelerate the recombination process by taking advantage of its catalytic property, increasing the amount of back flow, into the drug reservoir, used to dissolve more of the solid drug during the valve closing period. By cycling on and off the AC magnetic field, each consecutively produced drug solution is cyclically pumped out of the device.

Fabrication of Electrolytic Pump

Figure S17a shows the setup used for measuring the mounted prototype's drug delivery. Figure S17c shows Nafion coated platinum-titanium (Pt/Ti) interdigitated electrodes. Figure S17d shows an image of the catalytic reformer that resides below the PDMS membrane and above the interdigitated electrodes. The drug reservoir is a drilled cavity in a poly(methyl methacrylate) sheet (PMMA) with a 2.5 mm internal radius and a 3 mm depth. The electrolytic chamber is a PMMA cylinder of 2.6 mm internal radius and 2.7 mm height. To ensure the ability to repeat tests and interchange components, the electrolytic pump was assembled by mounting and tightening PMMA holders (2x2x2 cm). In actual drug delivery applications, permanent bonding of the drug reservoir to the actuator chamber replaces the need for the larger holder capable of disassembly.

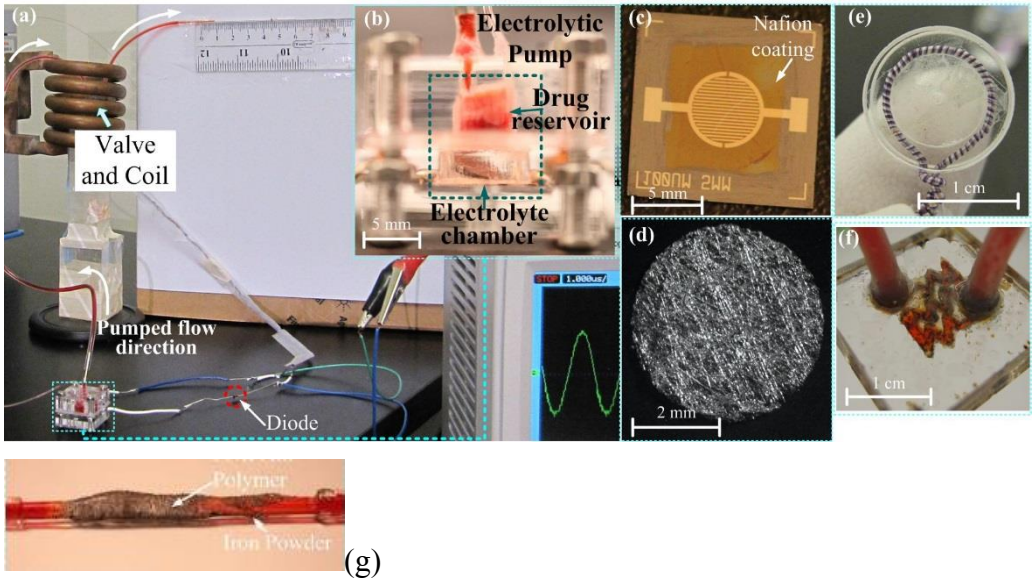

Figure S17 (a) photographs of the experimental apparatus and the prototypes of the major components: (b) assembled electrolytic pump; (c) image of Nafion coated Pt/Ti electrodes; (d) sputtered platinum coated carbon fiber mesh; (e) inductive coil; (f) the serpentine PNIPAm valve mixed with iron micro-particles (g) the glass capillary PNIPAm valve surrounded by iron micro-particles. Reprinted with permission from [279]. Copyright 2015, AIP Publishing LLC.

Pt/Ti electrodes are fabricated using photolithography. First a photoresist is deposited and an ultraviolet light exposure defines the pattern. Next is the sputtering of Ti followed by Pt, depositing onto the electrode pattern. Finally, a lift-off process removes the sacrificial layers, and the metal electrode remains. The Ti layer serves as an adhesion layer for Pt on the bottom silicon substrate.

The electrodes are 100 µm wide with 100 µm spaces between them and a height of 300 nm. This heights has a thickness ratio of 1/5 of Ti to Pt. Spin-coated Nafion on the surface of the electrodes, forms a 250 nm thin film.

The fabrication of the catalytic reformer components consists of taking a scaffold laser etched from carbon fiber paper (78% porosity of 5 mm diameter and 0.3 mm thickness), inert in the pump's electrolyte, and sputtering Pt onto it. The porous mesh structure of the carbon fiber results in a large surface of contact area between the Pt and the electrolysis generated gases, thus increasing the reformer's catalytic efficiency.

A 1 turn, 10mm diameter Litz wire coil (AWG 46 gauge, Figure S17e) is bonded to the electrode contact pads. A diode rectifies the AC magnetic field induced voltage to provide DC power to the pump. An Agilent DS01012A oscilloscope measures the voltage

induced in the pickup coil. The AC magnetic field is generated by a 3 kW inductive heater (Induktive Erwärmungsanlagen GmbH, Austria).

Fabrication of Serpentine and Capillary PNIPAm Microvalves

The serpentine PNIPAm valve (Figure S17f) consists of a serpentine shaped PMMA microchannel filled with a polymer composite of PNIPAm and iron microparticles (<10 μm, Sigma-Aldrich Co. LLC.). The microchannel (0.4 mm wide, 0.3 mm deep) is created using a laser cutter (Universal PLS6.75). 3 mg of iron microparticles are uniformly placed in the microchannel, and the PMMA sheet is bonded to another PMMA sheet by thermal-compression bonding (INSTRON Dual Column Testing Systems). The glass capillary PNIPAm valve (Figure S17g) consists of PNIPAm synthesized inside a 500 μm diameter capillary tube, which in turn is surrounded by 2-5 mg of iron microparticles attached to the capillary by mixing it with adhesive (LOCTITE 402). The PNIPAm hydrogel used in the two microvalve designs is synthesized from a mixture of two solutions of equal volumes [315]. The first consists of 20 wt% N-Isopropylacrylamide (NIPAAM), 4 wt% N, N, N, N-dimethylene bis (acrylamide) (BIS) used as the polymer crosslinker, and 2 %v/v TEMED (N, N, N', N'-tetramethylethylenediamine) used as the reaction accelerator, while the second solution consists of 4.5 wt % potassium persulfate (KPS) used as the reaction initiator. The two solutions are injected with equal rates into the valve using a Y-junction, and the polymerization of the PNIPAm hydrogel occurs shortly thereafter. Due to the non-serpentine shape of the glass capillary valve, a T-junction is formed using a sidewall-punctured Tygon tube (1mm internal diameter) at one end of the capillary, which prevents the release of the PNIPAm monolith from the capillary, while allowing fluid transfer from the capillary/around the PNIPAm and into one end of Tygon tube (while the other end is sealed off) and to the measuring setup.

E.3 Results and Discussion

Characterization of Electrolytic Pump

The PNIPAm valve is not included in the experiments focusing on the performance of the catalytic reformer, described as follows. A dyed solution substitutes the drug solution, and is easily tracked by a digital camera, placed in front of the test setup, used for recording the dye displacement inside of a glass capillary affixed at the device outlet. Dye displacement is

measured against a graduated ruler (Figure S17a), and displacement over time yields flow rate, which can be modulated by the magnetic field strength (Figure S18). Each measurement point is taken with the field on for 20 seconds, followed by the field off, until complete recombination of the gases, before the next measurement cycle is initiated. By increasing the magnetic field amplitude from 40.5 mT to 58.5 mT, the flow rate increased from 17 µL/min to 37 µL/min due to the increased voltage induced. Furthermore, the electrolytic pump utilizing a catalytic reformer component has a somewhat reduced dye flow rate due to an accelerated gas recombination into the water, even during the electrolysis-bubble generation step.

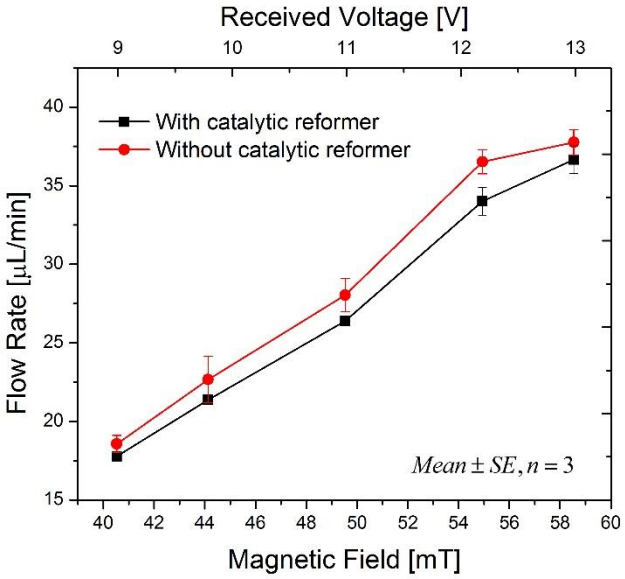

Figure S18 Magnetic field controlled flow rates (mean ± standard error, *n*=3) of the electrolytic pump with one catalytic reformer element and without a catalytic reformer under the same conditions. Reprinted with permission from [279]. Copyright 2015, AIP Publishing LLC.

To further assess the functionality of the catalytic reformer, dye displacement profiles are generated during the application of a 40.5 mT magnetic field in the "On/Off" mode for two pumps, one with and one without a catalytic reformer component (Figure S19). The field is left on until the PDMS membrane reaches a displacement that pumps approximately 2.5 µL, and this is done for two tested pumps. It takes a considerably longer time for the pump without the reformer to recombine the generated gasses, despite the slight difference in actuation time for both pumps. In particular, while using a catalytic reformer, the displacement is back to zero after 7.5 min, while and it remains at 1.2 µL after 18 min for the

other pump. Recombining of all generated gasses in the latter case takes over 1 hr, as previously reported [249], since this pump can rely only on the Pt electrode for catalysis. From these findings it is concluded that the pump utilizing a catalytic reformer is more suitable for the SDR application of drug delivery, due to its very fast recombination rate, which allows fresh fluid to rapidly refill the drug reservoir before the valve is sealed and the outlet closed off.

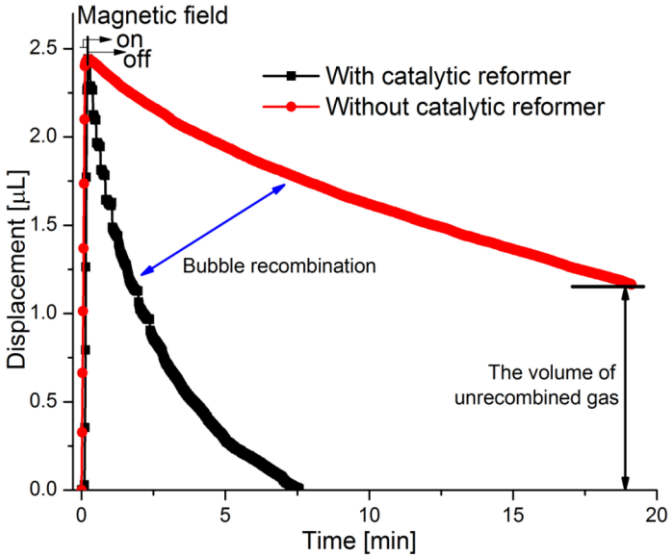

Figure S19 Dye displacement of electrolytic pump with one catalytic reformer element and without a catalytic reformer under the same conditions. An electromagnetic field of 40.5 mT is applied. Reprinted with permission from [279]. Copyright 2015, AIP Publishing LLC.

Controlled Release of Drug from Electrolytic Pump and PNIPAm Microvalve

- **Serpentine PNIPAm Microvalve**

This section discusses the integrated system that combines the electrolytic pump with the serpentine PNIPAm valve. Figure S17 shows the test setup used for measuring dye displacement across the opening valve. Three catalytic reformer components of the Pt coated carbon fiber mesh are added to further improve the recombination rate of the full system. The PNIPAm valve temperature is measured using an infrared thermometer (Fisher Scientific Inc.), and plotted against the corresponding time during which the valve is in actuation in response to a 40.5 mT field (Figure S20). Before an obvious opening of the valve, the PNIPAm polymer requires a few seconds of response time, after which a small volume of dye is displaced at a valve temperature of approximately 37 ºC. The valve is not fully open in this time, though a fraction of the valve has reacted in response to the heating by reaching

LCST, allowing for some dye to pass through the valve in response to the deflection of the PDMS. Following this state, the slope of the flow rate sharply rises and becomes constant, indicating a completed valve opening. At 3 μL of displacement, the valve temperature is found to be 41 ºC, at which point the PNIPAm valve is completely open, while the complete opening of the valve cannot be guaranteed at lower temperatures.

Recombination of gasses in the electrolytic chamber occurs after the field is switched off, allowing the deflected and stretched PDMS membrane to retract and draw liquid into the device and into the drug reservoir. The three catalytic reformer components rendered the recombination rate much faster, as seen by comparing Figure S20 and Figure S19. During the recombination of gasses, the PNIPAm cools down and swells, absorbing some of the water molecules that are being pulled in by the retracting PDMS, until the valve channel is sealed off. After approximately 1 min, the valve almost completely closed at 26 ºC. The temperature continues dropping until room temperature is reached, and at 22 ºC, the valve is completely closed. However, this occurs prior to compete recombination of the gasses, leaving a bias displacement of 0.5 μL of dye. Under the chosen experimental parameters, the valve's time to complete closure is shorter than that of the pump's complete recombination, demonstrating the valve's ability to properly seal the system even in light of negative pressure. A hypothetical leaky valve would allow fluid to flow back towards the drug reservoir under negative pressure due to the recombination process. If this were the case, the displaced volume should reach the zero position again after full recombination (such as in Figure S19).

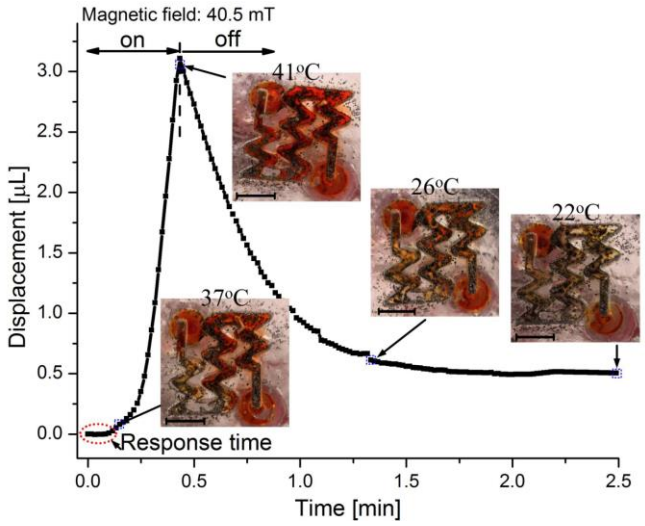

Figure S20 Pumping profile under an electromagnetic field of 40.5 mT when the thermo-responsive valve was used in combination with a pump with three catalytic reformer elements. The insets illustrate the states of the valve at different time points and the corresponding temperatures. Black particles are the iron micro-particles. Scale bars are 3 mm. Reprinted with permission from [279]. Copyright 2015, AIP Publishing LLC.

In Addition, the PNIPAm valve does not experience any hysteresis as it passes its LCST (either while heating up or cooling down past it); the PNIPAm volume change is completely reversible through its valve opening and closing transitions (Figure S20 steps 1-4). The increasing dye volume presence (1-2), and the following decreasing dye volume (2-4) until no dye flow is observable in the PNIPAm channel, also demonstrates that PNIPAm re-swells and properly seals the valve, preventing flow while below LCST, despite the device's negative pressure application from bubble recombination.

The magnetic field was cycled through on-off periods several times in order to demonstrate the device's stability and repeatability using the SDR approach for delivery of multiple drug doses. Figure S21 shows this cyclical device operation. In the case of the first pulse, the valve temperature increases from 20 ºC to above the PNIPAm LCST, which takes a longer time to show a response. Although the valve is closed effectively by the PNIPAm cooling to sub-LCST temperature in the following pulses, the total system temperature does not return back to 20 ºC, but rather somewhere around 22 (22 ºC is reached at 2.5 minutes in Figure S20, while the periods of on-off operation in Figure S21 last 2.5 min or 2 min). In this manner, the re-heating of the valve requires less time for the 2nd pulse and the following pulses, making the valve open faster than it does in the 1st pulse. To elaborate on this: the

system is never at a homogenous temperature but rather there is a temperature gradient from the PNIPAm monolith axis to the PNIPAm surface, and then through the surrounding moisture, and into the PMMA, and out to the PMMA surface of the device, especially in light of the pull in of room temperature fresh liquid from the outside of the device, which locally cools the PNIPAm. Yet, even though the PNIPAm may be effectively closed while below LCST, and cool enough at its core surface to do so, the application of the following pulse generates heat which accumulates more easily locally in the PNIPAm since the PMMA which is slightly above room temperature at 22 ºC and 2.5 min is acting as less of a heat sink as it did when it was at 20 ºC.

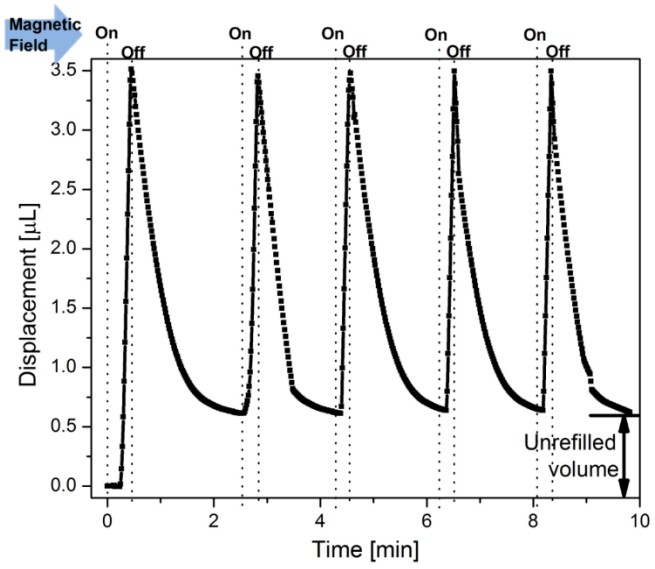

Figure S21 Cyclic liquid displacement of the dye when a device with a pump, three catalytic reformer elements and a PNIPAM valve is operated with an electromagnetic field of 40.5 mT that is periodically turned on and off. Reprinted with permission from [279]. Copyright 2015, AIP Publishing LLC.

Approximately 0.5 µL of the volume remains un-refilled after having pumped up to 3.5 µL (Figure S20). Furthermore, as can be seen in Figure S21, subsequent pulses do not change this un-refilled volume. This suggests that a maximum pumping reduction from 3.5 µl to 3 µl in each cycle would allow for refilling approximately all of the pumped 3 µl during the valve's closing time. This reduction may prevent measureable volume losses over time, yet still allow enough liquid to exit and then fully refill the drug reservoir, as such a condition must be met for long term continuous replenishing of the drug supply by dissolution the solid drug that saturates the fluid.

- **Glass capillary PNIPAm Microvalve**

This section discusses the glass capillary PNIPAm valve and the integrated system that combines it with the electrolytic pump. Figure S22 shows the PNIPAm as it changes shape above and below LCST in the capillary. The PNIPAm hydrogel is colored from contact with the test dye used during experimentation.

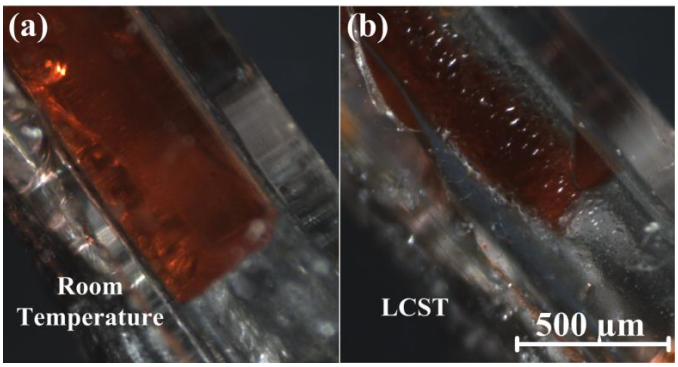

Figure S22 (a) PNIPAm polymer valve sealed at room temperature; (b) The valve opens under magnetic field, due to shrinking of PNIPAm. Figure reprinted with permission [278], © 2011 IEEE.

Again, a red dye was used to track the displacement of fluid during the experiments. The results show that by increasing the electromagnetic field strength, the time required to achieve maximum throughput through the polymer valve decreases, resulting from a faster heating of the iron powder and therefore a faster shrinking of PNIPAm. The throughput in Figure S23 is the total volume of fluid (µL) having passed through the valve at any time, after having turned on the electromagnetic field. Figure S23 shows the throughput of the tracking liquid through the PNIPAm valve under different electromagnetic fields (40.5 mT and 58.5 mT). In both cases, the PNIPAm valve reaches its terminal volume, beyond which it cannot shrink any further, and where it provides the largest throughput. However, the PNIPAm in the 58.5 mT test shrinks faster; thus, reaching this terminal volume sooner. Besides a faster opening of the PNIPAm valve, when the coil is placed in a larger electromagnetic field, the power received is also higher, causing a higher pumping rate. This allows a much faster delivery of the drug solution. Therefore, we studied the properties of the combined device, electrolytic pump plus PNIPAm valve, with a magnetic field of 58.5 mT. Figure S24 shows that the device achieves a maximum displacement of about 3 µL (the safe deflection limit of the PDMS membrane in this work) in about 18 seconds. This shows that

the fluid can pass the PNIPAm efficiently before the valve reaches its maximum throughput, and the delivery is not limited by the response time of the valve.

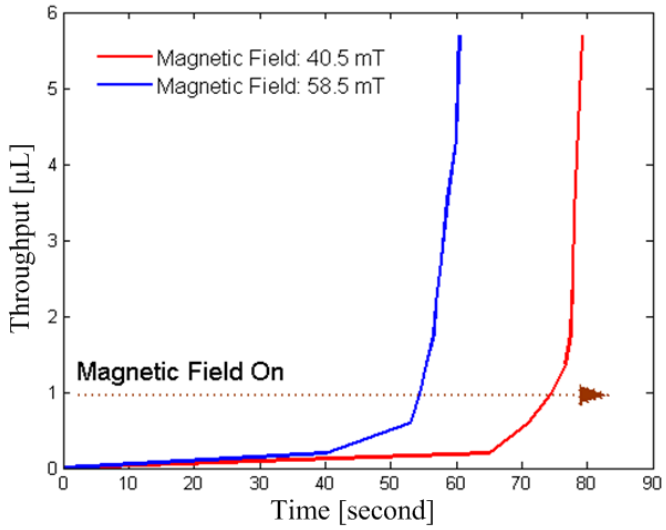

Figure S23 Throughput of the valve under different magnetic fields, used to calculate the corresponding valve opening time. Figure reprinted with permission [278], © 2011 IEEE.

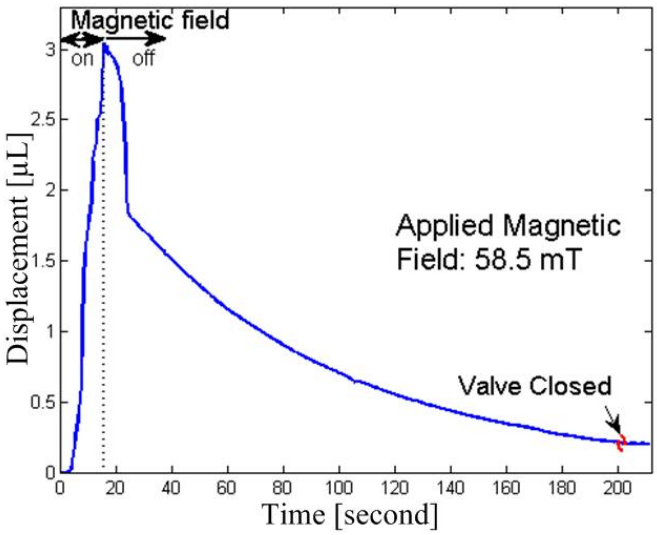

Figure S24 Single pumping pulse under magnetic field with PNIPAm polymer valve installed. Figure reprinted with permission [278], © 2011 IEEE.

Upon shutting off the electromagnetic field, the PNIPAm cools down and the valve closes. At the same time, the gas generated in the pump starts recombining, inducing a negative pressure. The negative pressure results in a drop in volume displaced. First, the liquid refills

the valve during the swelling of the PNIPAm, which is observed as a sharp drop at the beginning of the "magnetic field off state". Then, the reservoir is refilled with a continuously decreasing rate, until the valve is fully closed. As analyzed in Figure S19, the recombination rate is far slower in the pump without the catalytic reformer, which may eventually deplete the drug solution in the reservoir due to the lower volume of each refill during the valve's closing time. By using a catalytic reformer, more fresh liquid from outside the device flows back towards the drug reservoir. As shown in Figure S24, the backward flow stopped within approximately 3 minutes, indicating that the valve is completely closed at this time. A volume of nearly 2.8 μL was refilled before the valve sealed the outlet. Therefore, 2.8 μL is the maximum volume of drug released in this experiment that can be fully replenished by refilling.

As with the serpentine PNIPAm valve device, we observe a maximum pumping of around 5 μL, followed by an un-refilled volume of approximately 0.25 μL. The difference in unrecovered refilling liquid (0.025 μL versus 0.5 μL) is largely due to the difference in closing time, where the capillary PNIPAm valve takes a little less than 3.5 minutes to close, versus <2 min for the serpentine valve. Depending on the application of the device, and the equipment available for fabrication (serpentine valves requires expensive laser cutting tool), one may make an appropriate selection between the two valve designs, and control the closing time by adjusting maximum pumped volume (affects volume re-filling) and iron microparticle content (affects valve opening-closing speeds).

E.4 Summary

The research presented in this chapter demonstrates the remote and electromagnetic control of drug release from a drug delivery system using an electrolytically driven soluble solid drug, expelled through thermosensitive PNIPAm valves. Both the pumping source and the valving design used are controlled by the same externally applied electromagnetic field. The system can expel single doses of dissolved drug, as well as undergo repeatable delivery cycles, using the solid drug reservoir which continuously dissolves the drug in the presence of an aqueous solution. The PNIPAm valve controlled drug delivery port protects the user of the system against unwanted drug diffusion or leakage when the device is not in operation. In the "on" state of device operation, the PNIPAm valve is heated and opens, allowing for the electrolysis generated bubbles to pressurize the drug solution out of the device. The "off"

state consists of the recombination of these bubbles, which creates a back pressure that draws in fresh solution into the solid drug reservoir, while the PNIPAm valve cools and eventually fully closes, resealing the device. Cycling the device between the on and off states shows repeatable and reversible behavior of both the electrolytic process and the PNIPAm swelling and deswelling in the valve.

Furthermore, the rates of bubble generation and bubble recombination created in the pump can be tuned by selecting appropriate dimensions of the inductive source coil, the receiving coil, as well as changing the number of catalytic reformers used. An increase or decrease in the receiving coil, for example, results in an increase or decrease of the induced voltage powering the pump, and in turn, changes the flow rate accordingly.

While a PNIPAm valve functions as a diffusion and leakage prevention safety mechanism, it also requires that the rate of bubble recombination be as fast as possible to ensure refilling of the solid drug reservoir prior to the complete sealing of the device at the drug outlet.

For example, the more the pumping time is reduced (or the pumped volume is reduced), the smaller the volume of bubbles generated in the electrolytic pump, and the shorter the time for the system to recombine all the generated gas (well within the valve closing time). However, a reduction of the pumping time is not ideal. For this reason, the recombination rate should be accelerated as much as possible, which is the outcome achieved by using the three catalytic reformer components inside the electrolytic chamber. The catalytic reformer ensures the highest amount of refilling occurs during valve closing, and that, as much as possible, the refilled volume does not change over time. Speeding up the recombination allows for the potential to increase the pumping time (or the pumped volume), without any adverse effects during valve closing.

This device configuration is a suitable SDR system platform designed for remote and repeated on-demand drug delivery for long term therapeutic treatments of chronically debilitating diseases.